Overcoming Obstacles in the Aqueous Processing of Nickel-rich Layered Oxide Cathode Materials

Kumulative Dissertation
zur Erlangung des naturwissenschaftlichen Doktorgrades
an der Fakultät für Chemie und Pharmazie der
Julius-Maximilians-Universität Würzburg

durchgeführt am
Fraunhofer-Institut für Silicatforschung ISC
Würzburg

vorgelegt von

Michael Hofmann

aus Ellwangen (Jagst)

Würzburg, 2021

Eingereicht bei der Fakultät für Chemie und Pharmazie am 22.11.2021

Gutachter der schriftlichen Arbeit:

1. Gutachter: Prof. Dr. Gerhard Sextl

2. Gutachter: Prof. Dr. Volker Engel

Prüfer des öffentlichen Promotionskolloquiums:

1. Prüfer: Prof. Dr. Gerhard Sextl

2. Prüfer: Prof. Dr. Volker Engel

3. Prüfer: PD Dr. Florian Beuerle

Datum des öffentlichen Promotionskolloquiums:

18.03.2022

Doktorurkunde ausgehändigt am:

____

Die vorliegende Arbeit wurde im Zeitraum von April 2017 bis März 2021 am Fraunhofer-Institut für Silicatforschung ISC unter der Leitung von Herrn Prof. Dr. Gerhard Sextl, Lehrstuhl für Chemische Technologie der Materialsynthese der Julius-Maximilians-Universität Würzburg, angefertigt.

Bei der vorliegenden kumulativen Dissertation handelt es sich um eine verkürzte Darstellung der Forschungsergebnisse. Die ausführlichen Ergebnisse können den folgenden Veröffentlichungen entnommen werden:

1. M. Hofmann, M. Kapuschinski, U. Guntow, G. A. Giffin,
   Implications of Aqueous Processing for High Energy Density Cathode Materials: Part I. Ni-Rich Layered Oxides.
   J. Electrochem. Soc. **2020**, *167*, 140512.
   https://doi.org/10.1149/1945-7111/abc033, *Open Access* (CC BY 4.0)

2. M. Hofmann, M. Kapuschinski, U. Guntow, G. A. Giffin,
   Implications of Aqueous Processing for High Energy Density Cathode Materials: Part II. Water-Induced Surface Species on $LiNi_{0.8}Co_{0.15}Al_{0.05}O_2$.
   J. Electrochem. Soc. **2020**, *167*, 140535.
   https://doi.org/10.1149/1945-7111/abc6ca, *Open Access* (CC BY 4.0)

3. M. Hofmann, F. Nagler, M. Kapuschinski, U. Guntow, G. A. Giffin,
   Surface Modification of $LiNi_{0.8}Co_{0.15}Al_{0.05}O_2$ Particles via Li_3PO_4 Coating to Enable Aqueous Electrode Processing.
   ChemSusChem **2020**, *13*, 5962 – 5971.
   https://doi.org/10.1002/cssc.202001907, *Open Access* (CC BY 4.0)

4. M. Hofmann, F. Nagler, U. Guntow, G. Sextl, G. A. Giffin,
   Long-Term Cycling Performance of Aqueous Processed Ni-rich $LiNi_{0.8}Co_{0.15}Al_{0.05}O_2$ Cathodes.
   J. Electrochem. Soc. **2021**, *168*, 060511.
   https://doi.org/10.1149/1945-7111/ac054f, *Open Access* (CC BY 4.0)

Table of contents

1. Introduction

1.1. Motivation

Global warming and environmental degradation are some of the most serious challenges facing society in the 21st century. In recent years, great efforts have been made worldwide to combat these issues. For instance, the European Union (EU) has presented a concept that aims to reduce European greenhouse gas emissions by at least 50% by 2030 in comparison to 1990 levels and to make Europe the first climate neutral continent by 2050 ("European Green Deal", 2019).[1] For achieving these and similar goals, the transition to sustainable energy production by the use of renewable energy sources must be enforced continuously. However, the performance of e.g. solar or wind energy converters is highly contingent on the intermittent natural conditions. Therefore, balancing of energy supply and demand becomes increasingly challenging.[2] To compensate for such energy fluctuations, the installation of decentralized and centralized stationary energy storage systems is required.[3] Energy storage systems are considered to be a key element to pave the way to reduced emissions of greenhouse gases, not only in the energy sector, but also in the mobility sector, by enabling the widespread use of electric (EV) and hybrid electric (HEV) vehicles.[4]

Lithium-ion batteries (LIBs) are one of the most widely used energy storage devices in the energy and mobility sector due to their relatively high energy and power density as well as long cycle life.[4] In addition to these fields of application, LIBs power multiple portable electronic devices such as smartphones, tablets and laptops enabling wireless communication around the world.[5] Consequently, the inventors of lithium-ion batteries John B. Goodenough, M. Stanley Whittingham and Akira Yoshino were honored with the Nobel Prize in Chemistry 2019.[6] The first commercial LIB was introduced by Sony Corporation in 1991 and to date remarkable progress in terms of e.g. lifetime, energy, and power density has been made.[7] For example, in 2020, Contemporary Amperex Technology (CATL), one of the battery suppliers for the automobile manufacturer Tesla, announced that they are already able to produce batteries that allow electric vehicles to drive over one million miles.[8] However, as pointed out by Nobel Prize winner M. Stanley Whittingham very recently, researches have tended to neglect the sustainability of LIBs in the last years.[9] Therefore, future research has to focus on the development of new environmentally friendly LIB manufacturing methods and innovative recycling processes.[9,10] To enable a more sustainable LIB production, the implementation of a water-based cathode manufacturing process seems promising. Instead of the reproductive toxic and irritating organic solvent *N*-methyl-2-pyrrolidone (NMP) and poorly recyclable fluorinated binders like polyvinylidene fluoride (PVDF), this process uses water as a solvent and rather harmless binders like cellulose derivatives.[11] In addition, various studies also estimated lower greenhouse gas emissions and lower costs for this manufacturing method.[11–13]

Water-based electrode processing is already state-of-the-art for graphite-based anodes.[14] In contrast, aqueous cathode manufacturing is still problematic due to the water sensitivity of many cathode active materials that results in difficulties during electrode fabrication and the deterioration of the electrochemical performance.[11] For the successful implementation of a sustainable cathode manufacturing process it is therefore essential to overcome this obstacle.

1.2. Aim of the work

The aim of the present work is to elucidate the origin of the water sensitivity of cathode materials from the class of nickel-rich layered oxides in detail and to derive solutions to improve their suitability for an aqueous electrode manufacturing process. Nickel-rich layered oxide cathode materials are considered to be promising for batteries in EVs due to their relatively low price, high capacity and nominal voltage.[15,16] It is therefore assumed that they will be implemented in the majority of EVs in the coming next decade.[15,16]
Overall, this work shall contribute to an accelerated and successful implementation of a water-based cathode manufacturing process in the future and thus improve the sustainability of next-generation LIB production.

To achieve this goal, the following investigations have been carried out within the scope of this work:

1. To identify correlations between water sensitivity and cathode material composition, different layered oxide cathode materials have been evaluated in terms of water-induced metal leaching and time-dependent pH evolution in aqueous medium. Furthermore, electrochemical tests on cells containing electrodes made with a water-based

process have been conducted and the results have been compared to those of cells with conventional NMP/PVDF-electrodes (sub-chapter 3.1.1).

2. The most water-sensitive cathode material has been identified and further studies have been carried out to clarify the processes that take place upon water contact in detail. Especially, the focus is set on the detection and elucidation of changes at the active materials surface and the evaluation of their impact on the electrochemical performance (sub-chapter 3.1.2).
3. In a next step, the active material surface has been modified with a protective coating to reduce detrimental reactions during water contact and to improve the electrochemical performance of cells with aqueous manufactured electrodes. The influence of the coating amount has been evaluated in detail and a comparison of the cycling performance of cells with NMP-electrodes and cells with optimized water-based electrodes has been conducted (sub-chapter 3.2).
4. Finally, the scalability of the coating process has been investigated and the long-term cycling performance of full cells with aqueous processed cathode and a graphite anode has been evaluated (sub-chapter 3.3).

2. Theoretical background

2.1. Lithium-ion battery

2.1.1. Working principle of a lithium-ion battery

The configuration and working principle of a lithium-ion battery during the discharge process is illustrated in Figure 1. The cathode and anode are immersed in a lithium-ion conducting electrolyte that consists of a lithium salt in an organic solvent. Typical lithium salts are $LiPF_6$ and $LiN(SO_2F)_2$ (LiFSI), while alkyl carbonates such as dimethyl carbonate (DMC), diethyl carbonate (DEC) and ethylene carbonate (EC) are common organic solvents.[17] The cathode is defined as the electrode where electrochemical reduction takes place during discharge (= spontaneous electrochemical reaction), while the electrode where oxidation occurs, is defined as the anode. Although these processes change during charging, by convention the terms remain the same. To avoid the contact of both electrodes and thus prevent a short circuit, a separator (often polyolefin-based) is placed between the two electrodes.[18]

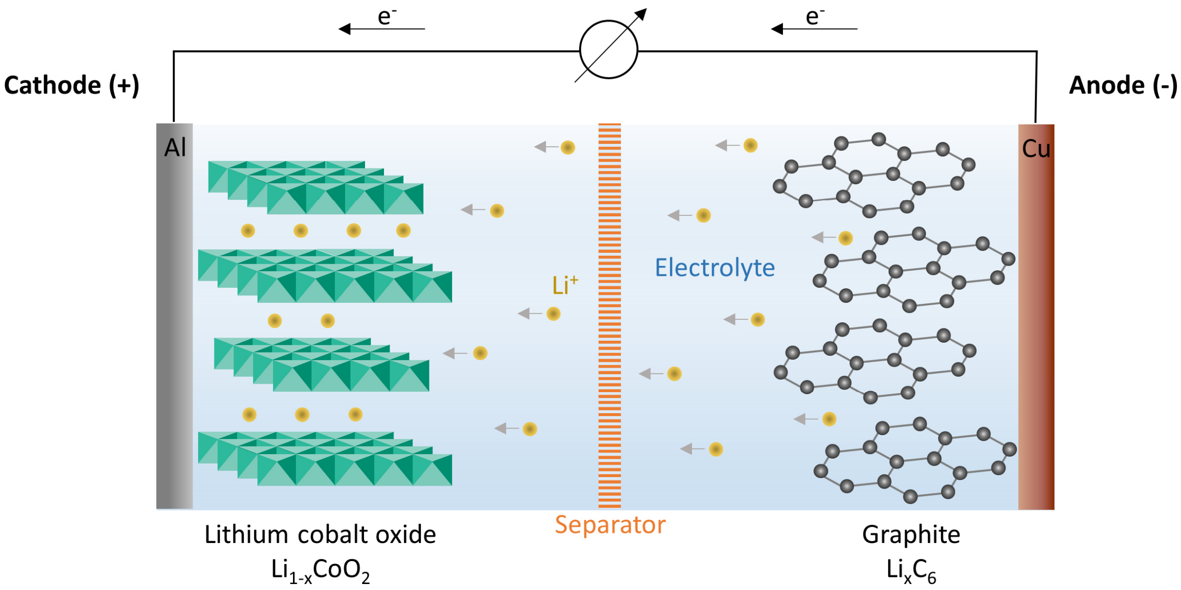

Figure 1: Illustration of the configuration and working principle of a lithium-ion battery during the discharge process.

During the discharge process, lithium ions migrate from the anode to the cathode and are stored within the cathode active material structure. Simultaneously, electrons are transferred between the two electrodes through the external circuit. The storage of lithium ions can occur via different processes such as alloying, conversion and intercalation, which depends on the nature of the active materials.[19] The first commercial lithium-ion battery, which was introduced by Sony in 1991, consisted of $LiCoO_2$ (LCO) as cathode active material and a petroleum coke-based anode material.[7,20] Shortly afterwards, the latter was replaced by a graphite anode.[20] LCO and graphite belong to the class of intercalation compounds. For these materials the reactions during discharge can be written as the following (Eq. 1-3):

Anode (oxidation): $Li_xC_6 \rightarrow x\ Li^+ + x\ e^- + C_6$ (Eq. 1)

Cathode (reduction): $Li_{1-x}CoO_2 + x\ Li^+ + x\ e^- \rightarrow LiCoO_2$ (Eq. 2)

Total reaction: $Li_xC_6 + Li_{1-x}CoO_2 \rightarrow LiCoO_2 + C_6$ (Eq. 3)

Other typical anode active materials are silicon, lithium or $Li_4Ti_5O_{12}$ (LTO). A detailed description of further cathode active materials is given in sub-chapter 2.2.

2.1.2. Important parameters to characterize a lithium-ion battery

The following section provides an overview of important parameters to characterize a lithium-ion battery. For the more detailed descriptions, reference is made to the associated specialist literature.[21–25]

Capacity

The theoretical capacity Q_t of an electrochemical cell is defined as the amount of charge that can be stored or released. It depends on the amount and nature of the electroactive species (number of electrons that are involved in the electrochemical reaction). Q_t can be calculated as follows (Eq. 4):

$$Q_t = n\ F \qquad \text{(Eq. 4)}$$

n is the number of moles of electrons involved and F is the Faraday constant. Its unit is typically given in ampere-hours [Ah]. The practical capacity Q_p is the actual capacity that can be obtained under given conditions. Q_p depends on various factors such as operating temperature, cutoff voltage, kinetic limitations and cell construction. The capacity calculated per mass of active material is called the specific capacity Q_s and has the unit ampere-hours per kilogram [Ah kg^{-1}].

Coulombic efficiency

The Coulombic efficiency (C. E.) is defined as the ratio of capacity obtained during the discharge process $Q_{discharge}$ over capacity obtained during the charge process Q_{charge} (Eq. 5):

$$\text{C. E.} = \frac{Q_{discharge}}{Q_{charge}} \tag{Eq. 5}$$

Its unit is percent [%]. A Coulombic efficiency close to 100% indicates a high reversibility of the electrochemical processes and the occurrence of only minor side reactions.[26]

Capacity retention

The capacity retention [%] is the remaining capacity of an electrochemical cell after N charge/discharge cycles (Q_N) in comparison to the capacity obtained in a previous cycle (e.g. first cycle capacity, Q_1) (Eq. 6):

$$\text{Capacity retention} = \frac{Q_N}{Q_1} \tag{Eq. 6}$$

A high capacity retention value indicates a stable cycling performance of an electrochemical cell. For batteries in electric vehicles, the widely accepted end-of-life (EoL) criterion is reached when the capacity retention drops below 80%.[27]

C-rate

The pace at which charging and discharging of an electrochemical cell is conducted is denoted as the C-rate. The unit of the C-rate is [h^{-1}] and can be calculated by the following equation, where t is the time in hours taken to completely charge (or discharge) the cell, i the applied current [A] and Q the battery capacity [Ah] (Eq. 7):

$$\text{C-rate} = \frac{1}{t} = \frac{i}{Q} \tag{Eq. 7}$$

Electrode potential and cell voltage

The equilibrium potential E of a redox electrode can be calculated with the Nernst equation (Eq. 8):

$$E = E^0 + \frac{RT}{zF} \ln \frac{a_{ox}}{a_{red}} \tag{Eq. 8}$$

E^0 is the standard electrode potential, R the universal gas constant, F the Faraday constant, z the number of transferred electrons, T the temperature and a the activity of the components involved in the electrochemical reaction.

The equilibrium voltage V_0 [V] of an electrochemical cell is given by the difference of the potentials of the two redox electrodes (Eq. 9).

$$V_0 = E_{cathode} - E_{anode} \qquad \text{(Eq. 9)}$$

Polarization and overpotential

When current flows, the actual cell voltage V deviates from the equilibrium voltage V_0. This phenomenon is called polarization. The extent of polarization is called the overpotential η, which is the difference between the actual voltage and the equilibrium voltage V_0 (Eq. 10):

$$\eta = V - V_0 \qquad \text{(Eq. 10)}$$

The total overpotential is the sum of different overpotentials, with some important ones being ohmic polarization η_{ohm} (= ohmic or internal resistances including e.g. electrolyte resistance and contact resistance of the cell components), concentration polarization η_{con} (= accumulation/depletion of reactive species causes a concentration gradient; as a consequence the reaction rate is limited by mass transport) and activation or charge transfer polarization η_{ct} (= reaction rate is limited by the passing of charge carriers through the electrode/electrolyte interface requiring activation energy). The latter one can be mathematically described with the Butler-Volmer equation that correlates the current density with the charge transfer polarization η_{ct}.[23,24]

The impact of these three polarization effects on the cell voltage as a function of the current density is shown in Figure 2.

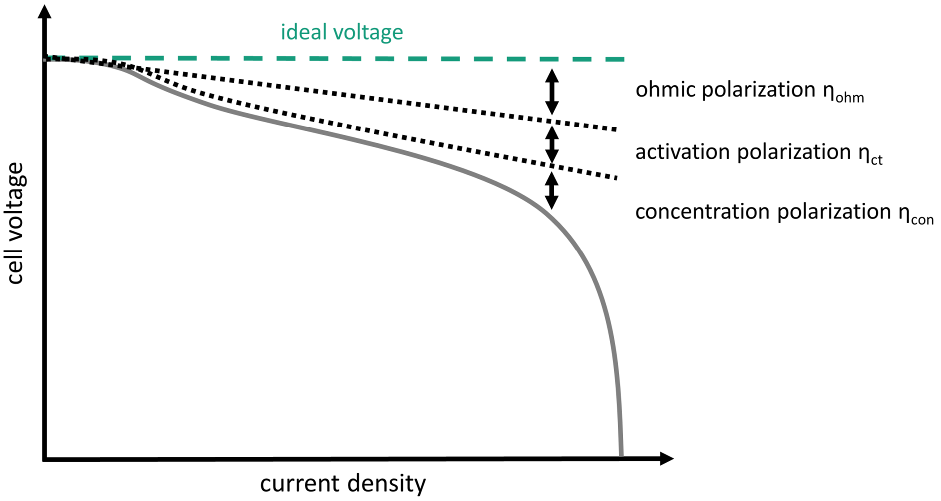

Figure 2: Impact of polarization effects on the cell voltage in dependency of the current density. The illustration was redrawn based on reference [25].

Mean voltage

The mean voltage $\tilde{V}$ (e.g. discharge mean voltage $\tilde{V}_{discharge}$) determines the nominal voltage of an electrochemical cell and is defined as (Eq. 11):[28]

$$\tilde{V}_{discharge} = \int V_{discharge} \frac{dQ_{discharge}}{\int dQ_{discharge}} \qquad \text{(Eq. 11)}$$

Energy Density

The term energy density refers to the amount of energy that can be stored in a battery. Its value is typically given per unit of mass (gravimetric energy density; [Wh kg^{-1}]) or volume (volumetric energy density; [Wh L^{-1}]). The energy density can be calculated as follows (Eq. 12-13):

$$\text{Gravimetric energy density} = \frac{1}{m} (Q\,\tilde{V}) \qquad \text{(Eq. 12)}$$

$$\text{Volumetric energy density} = \frac{1}{v} (Q\,\tilde{V}) \qquad \text{(Eq. 13)}$$

Here, m, v, Q and $\tilde{V}$ are the mass, volume, capacity and mean voltage of the battery, respectively.

2.2. Cathode materials: A huge variety of materials

Over the last decades, a large variety of cathode materials have been developed for lithium-ion batteries. Each cathode material has different characteristics in terms of electrochemical properties, safety, lifetime, and costs that must be considered for the field of application. Divisions can be made based on the crystal structure of the cathode materials.[29] Some common cathode materials (Table 1), which are already implemented in commercial batteries, are $LiCoO_2$ (LCO) and $LiNi_{0.33}Co_{0.33}Mn_{0.33}O_2$ (NCM111) both belonging to the class of layered oxides, $LiMn_2O_4$ (LMO) from the spinel class, and the olivine $LiFePO_4$ (LFP).[30]

Table 1: Practical capacity and nominal voltage of some common cathode materials, which are already implemented in commercial lithium-ion batteries. The data was taken from reference [21].

cathode material	practical capacity / mAh g^{-1}	nominal voltage / V
$LiCoO_2$ (LCO)	~ 150	3.9
$LiNi_{0.33}Co_{0.33}Mn_{0.33}O_2$ (NCM111)	~ 154	3.7
$LiMn_2O_4$ (LMO)	~ 130	4.0
$LiFePO_4$ (LFP)	~ 160	3.4

For the rapidly growing market of electric vehicles, improvements in terms of energy density are urgently needed to meet consumer demands for longer driving ranges. For these batteries nickel-rich layered oxides have been identified as promising cathode materials due to their high capacity, nominal voltage, and relatively low price.[15]

2.2.1. Ni-rich layered oxides – derivatives of $LiNiO_2$

2.2.1.1. Structure and synthesis of $LiNiO_2$

Ni-rich layered oxides with the formula $LiNi_{1-x}M_xO_2$ (M = Co, Al, Mn, Mg, etc.) are derived from $LiNiO_2$ (LNO). Ideal stoichiometric $LiNiO_2$ has a layered α-$NaFeO_2$ structure with $R\bar{3}m$ space group.[31,32] The oxygen anions (O^{2-}) form a face-centered cubic (fcc) lattice (AB CA BC stacking), where the octahedral sites are occupied with lithium (Li^+) or nickel (Ni^{3+}) cations resulting in the formation of alternating Li-O-Ni-O slabs (Figure 3a).[31,33,34]

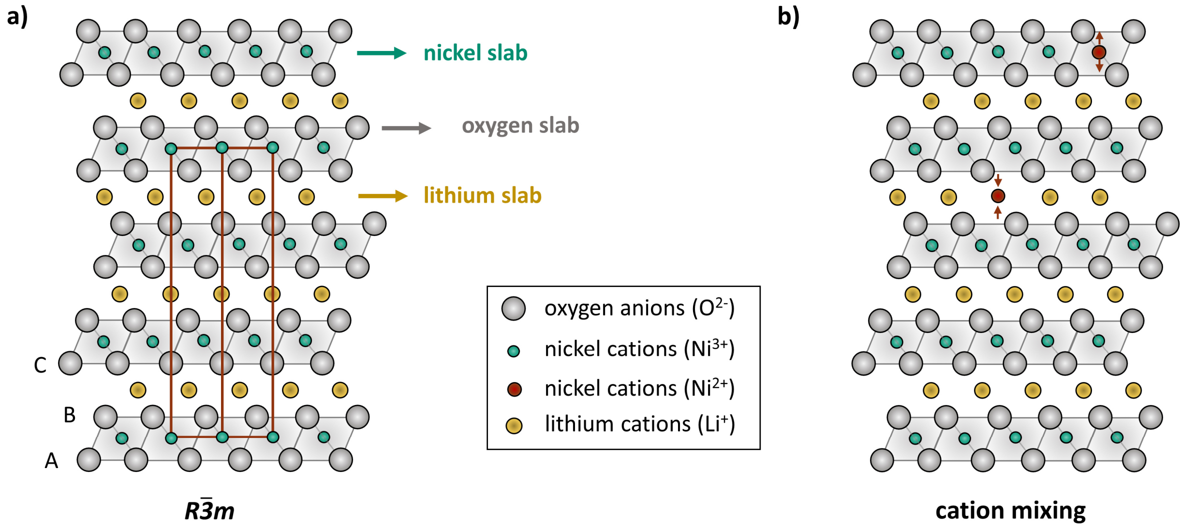

R$\bar{3}$m

cation mixing

Figure 3: Illustration of a well-ordered R$\bar{3}$m structure for $LiNiO_2$ (a, redrawn based on reference [35]) and partial cation mixing with Ni^{2+} in the lithium and nickel slab (b).

However, the synthesis of ideal stoichiometric $LiNiO_2$ is hard to achieve since the presence of some Ni^{2+} is practically inevitable, thus Bianchini et al.[36] proposed that ideal stoichiometric LNO has likely never been synthesized to date.[31,33,37] The actual formula is therefore better described as $Li_{1-z}Ni_{1+z}O_2$, where even for well controlled synthesis conditions z is on the order of 0.01 – 0.03.[31,34,36,38,39] In general, various aspects must be considered for the synthesis of LNO. The nickel precursor usually has the oxidation state +2.[33,36,40,41] For the successful oxidation of Ni^{2+} to Ni^{3+} the best results were achieved with a continuous oxygen flow during synthesis, where the gas flow additionally enables the removal of decomposition products such as CO_2 and H_2O.[33,36,40,41] Moreover, the sintering temperature is a decisive factor. While high temperatures generally enable the rapid synthesis of crystalline compounds, LNO is unstable at high temperatures and decomposes with the release of oxygen (Eq. 14) [36,42,43]:

$$LiNiO_2 \rightarrow \frac{1}{1+z} Li_{1-z}Ni_{1+z}O_2 + \frac{z}{1+z} Li_2O + \frac{z}{2(1+z)} O_2 \qquad \text{(Eq. 14)}$$

In a subsequent reaction, the lithium oxide formed can then be converted into volatile lithium peroxide (in the O_2-containing atmosphere).[42,44] To compensate for this lithium loss, a slight excess of lithium precursor can be used.[36] As a consequence, this can lead to the deposition of unreacted lithium salts such as Li_2CO_3 or LiOH on the surface of the cathode material that can detrimentally influence the electrochemical performance.[36,45] Common synthesis techniques include co-precipitation[46], sol-gel synthesis[47], micro-wave assisted synthesis[32], combustion[48], and hydrothermal synthesis[49].

Since the presence of some Ni^{2+} instead of Ni^{3+} is practically inevitable (see section above), there are some deviations from the ideal $LiNiO_2$ structure: In particular, Ni^{2+} can easily occupy positions in the lithium layer.[36,38] This phenomenon is often described as cation mixing. For charge compensation, Ni^{2+} is present not only in the lithium slab but also in an equal amount in the nickel slab.[36] As a result, the nickel slab expands ($r(Ni^{3+}) < r(Ni^{2+})$), while the lithium slab ($r(Ni^{2+}) < r(Li^{+})$) contracts (Figure 3b).[36,38] When Ni^{2+} is present in the lithium slab, the lithium diffusion during cell operation is impeded due to the contraction of the lithium slab and the repulsion of Li^+ by Ni^{2+}.[37] The mechanisms for lithium diffusion during cell operation are explained in more detail in the next section.

2.2.1.2. Electrochemical characteristics of $LiNiO_2$

The theoretical specific capacity of $LiNiO_2$ is 274 mAh g^{-1}.[50] This calculation is based on the assumption that LNO is ideally stoichiometric and Ni^{3+} is completely oxidized to Ni^{4+} during delithiation according to the following equation (Eq. 15):[36]

$$\mathrm{Li}\overset{+III}{\mathrm{Ni}}\mathrm{O_2} \rightarrow \overset{+IV}{\mathrm{Ni}}\mathrm{O_2} + \mathrm{Li^+} + \mathrm{e^-} \qquad \text{(Eq. 15)}$$

As described in the previous sub-chapter (2.2.1.1) stoichiometric LNO is hard to synthesize. Therefore, the practical achievable capacity is always lower. In recent years, discharge capacities of around 250 mAh g^{-1} in the first cycle have been reported due to improved synthesis conditions.[51,52] Combined with a mean voltage of $\sim$ 3.8 V, LNO is in principle a candidate for electrochemical cells with high energy density.[21,30]

During delithiation/lithiation several phase transitions can be observed for LNO (Figure 4), which have been investigated by various authors with ex situ and in situ x-ray diffraction (XRD) and can be correlated with the electrochemical characteristics.[50,53,54] The following phase transition sequence during the extraction of lithium ions is accepted in the literature:[36] Transition of a hexagonal phase (H1) to a monoclinic phase (M) followed by a second (H2) and third hexagonal phase (H3). During lithium insertion this sequence is reversed. While it is more common in literature to use H (for hexagonal), sometimes authors in the literature use R (for rhombohedral). Although this may seem contradictory, phases belonging to the $R\bar{3}m$ space group (as assumed in literature for H1, H2 and H3)[50] may be described either by a rhombohedral ($a = b = c$; $\alpha = \beta = \gamma \neq 90°$) or a hexagonal ($a = b \neq c$; $\alpha = \beta = 90°$ $\gamma = 120°$) unit cell.[55]

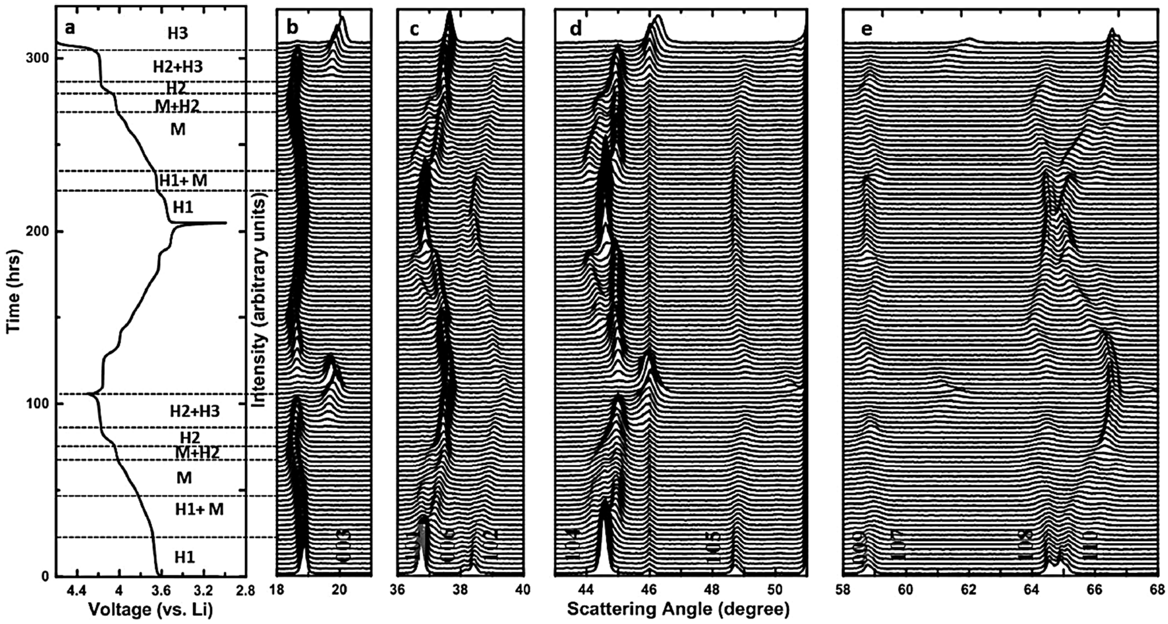

Figure 4: Phase transitions detected for $LiNiO_2$ during cycling. The figure was reproduced from reference [50] (open access article distributed under the terms of the Creative Commons Attribution 4.0 License (CC BY, http://creativecommons.org/licenses/by/4.0/)).

For lithium diffusion in layered oxide cathode materials such as $LiNiO_2$, in general, two main mechanisms – tetrahedral site hop (TSH) and oxygen dumbbell hop (ODH) – were described by van der Ven et al. (Figure 5).[56,57]

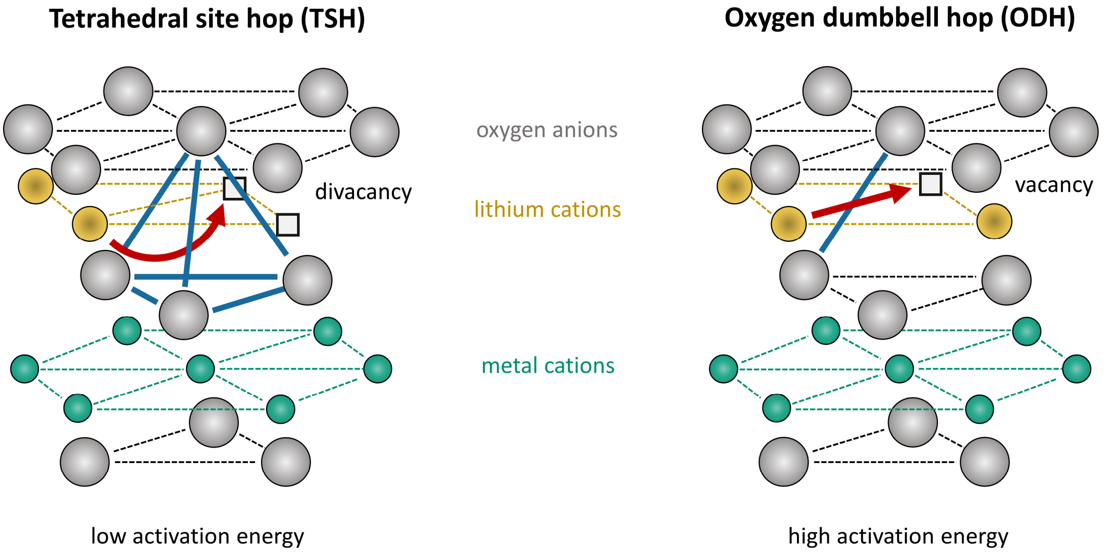

Figure 5: Lithium migration paths in layered oxides proposed by van der Ven et al.[56]: Tetrahedral site hop (TSH) and oxygen dumbbell hop (ODH). The illustration was redrawn based on reference [56].

The type of lithium diffusion mechanism depends on the number of lithium vacancies.[37,56,57] In the early state of lithium extraction (beginning of the charging process) only single vacancies are present, which is why the ODH mechanism dominates. The lithium cation migrates directly to the free octahedral site and passes a dumbbell of oxygen anions.

With a higher degree of extracted lithium ions, the number of divacancies increases, so that the TSH mechanism becomes possible. In this mechanism, the lithium ion migrates in a curved path via a tetrahedral site to the vacancy. The TSH mechanism has a lower activation barrier as compared to the ODH mechanism, and therefore becomes the predominant mechanism when divacancies are present.[56]

2.2.1.3. Degradation phenomena of $LiNiO_2$

LNO has not been commercialized so far due to various degradation phenomena which are discussed in this section.[43,53]

Mechanical stability

One issue is the phase transition from H2 to H3 at high state of charge (sub-chapter 2.2.1.2) since it is accompanied by an abrupt unit cell volume contraction of approx. 3.8%.[50,53,58] This mechanical stress can induce the formation of various cracks in the cathode particle as illustrated in Figure 6.[51,59] Harmful consequences are the disruption of lithium ion diffusion (a) and capacity loss due to electrical isolation (b, e).[59] If a crack increases the electrochemically active surface areas (c, d), then the effect may be beneficial, but may also accelerate side reactions with the electrolyte.[59,60] The formation of cracks progresses from cycle to cycle and thus drastically accelerates the cell degradation.[51,61] By lowering the higher cut-off voltage, the mechanical aging has been shown to be minimized, however, this limits the achievable specific capacity.[51]

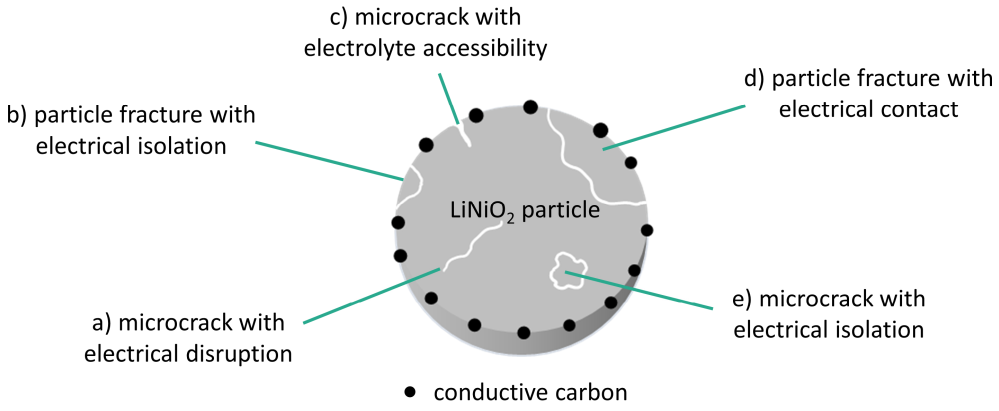

Figure 6: Formation of different cracks and their consequences. The illustration was redrawn based on reference [60].

Thermal stability

The thermal stability of cathode materials is a key aspect since it affects the safety of a lithium-ion cell. Dahn et al. reported that lithiated LNO is stable up to high temperatures, while it is unstable in a delithiated state.[62] By investigating Li_xNiO_2 with x = 0.3, 0.4 and 0.5 they found that oxygen can be released at a temperature of around 200 °C (a temperature that can be reached during a thermal runaway of a lithium-ion battery[63]). While no oxygen release was detected for $Li_{0.5}NiO_2$, the amount of oxygen increased when decreasing x from 0.4 to 0.3. As a consequence the release of oxygen into the electrolyte, which is heated above its flash point can lead to a violent reaction.[36,62,64]

Moisture stability

To date, various authors reported an extreme moisture-sensitivity of LNO, which results in the degradation of the cathode material and in turn accelerates the cell degradation.[64–66] A more detailed discussion of the moisture sensitivity of LNO and its Ni-rich derivatives will be given in sub-chapter 2.3.2.

Structural stability and electrolyte decomposition during electrochemical cycling

A well-known problem is that the structure of LNO is unstable during electrochemical cycling and a layered to rock-salt (NiO-like or $Li_nNi_{1-n}O$-like phase) transformation is induced.[36,67,68] The rock-salt structure is mainly detected on the particles surface and can be several nanometers thick.[51,69] The transformation is triggered by the reduction of the highly reactive Ni^{4+}, which is formed during delithiation.[36,67] The structural transformation proceeds with the release of oxygen, although it is still unclear whether the transformation to the rock-salt structure has a spinel intermediate.[67,70] Since a continuous increase in cathode impedance can be observed during cycling, many authors assume that this increase is correlated to a poorer ionic conductivity of the rock salt phase.[51,69,71] However, an exact characterization of the rock salt phase is very challenging, and another explanation might be also Ni^{4+}-induced electrolyte oxidation and the deposition of undesirable decomposition products on the particle surface.[16,72]

2.2.2. Element substitution in $LiNiO_2$ – NCA and NCM

In recent years, various strategies have been developed to minimize the degradation problems of $LiNiO_2$ (sub-chapter 2.2.1.3). A very successful approach is the substitution of nickel with elements such as cobalt, aluminum, manganese, titanium, and magnesium.[36,73,74] Two promising cathode material classes that can be obtained by element substitution are NCM ($LiNi_{1-x-y}Co_xMn_yO_2$) and NCA ($LiNi_{1-x-y}Co_xAl_yO_2$). Myung et al. even proposed that the majority of EVs coming up in the next decade, will contain Ni-rich NCM or NCA.[16] While it is common for NCM materials to add the ratio of Ni/Co/Mn in numbers in the name (e.g. NCM811 = $LiNi_{0.8}Co_{0.1}Mn_{0.1}O_2$), this additional description is normally missing for NCA materials, so that the exact composition is often not directly apparent. In the following section, some advantages reported for Co-, Al- and Mn-substitution will be discussed briefly.

Cobalt substitution

Due to the similar ionic radii of Co^{3+} (0.0545 nm) and Ni^{3+} (0.056 nm), nickel can be relatively easy substituted by cobalt.[75] The redox pair Co^{3+}/Co^{4+} is also electrochemical active and can therefore contribute to the achievable capacity.[75] Main beneficial effects reported for cobalt substitution are the stabilization of the structure by diminishing Li^+/Ni^{2+}-mixing (sub-chapter 2.2.1.1) and the effective suppression of the phase transitions during charging and discharging (sub-chapter 2.2.1.2).[38,73,76] However, the effective suppression of cation mixing, and phase transitions is highly dependent on the amount of substituted cobalt.[58] Interestingly, the group of Jeff Dahn reported in 2019 that for cathode materials with the general formula $LiNi_{0.95}M_{0.05}O_2$ (M = Co, Al, Mg or Mn), regardless of whether nickel is substituted with cobalt, magnesium or aluminum, Li^+/Ni^{2+}-cation mixing is nearly the same.[58] Moreover, they found that Mg-, Mn- or Al-substitution is even more effective in suppressing the phase transitions leading them to the conclusion that cobalt is not necessary in these materials. The complete exclusion of cobalt substitution would benefit the cathode material price and avoid children work in cobalt mining.[58] However, further studies must prove whether this would be compatible with a good electrochemical performance. Finally, it should be mentioned that it is also possible to synthesize $LiNi_xCo_{1-x}O_2$ compounds by doping $LiCoO_2$ with nickel.[77]

Aluminum substitution

The price of aluminum is relatively low as compared to cobalt. However, Al^{3+} is redox-inactive, which means that the achievable capacity decreases with increasing substitution. Different positive effects of Al-substitution such as increase of thermal stability of the delithitated cathode material and therefore enhancement in battery safety[78], suppression of phase transitions[58], diminishing particle cracking[36] and increase of mean cell voltage[79] have been reported so far.

Manganese substitution

Manganese substituted $LiNiO_2$ ($LiNi_{1-x}Mn_xO_2$) has been systematically investigated by Rossen et al. in 1992.[80] They reported that the incorporation of Mn is possible up to x = 0.5 and proposed that manganese in the oxidation state +4 is formed with increasing x. Koyama et al. calculated the oxidation states in $LiNi_{0.5}Mn_{0.5}O_2$ as Ni^{2+}/Mn^{4+} rather than Ni^{3+}/Mn^{3+}.[81] This can lead to an increase in Li^+/Ni^{2+} cation mixing, decrease of capacity and deterioration of the electrochemical performance.[75,80,82] However, advantages have been reported to be the low costs of manganese[75], lower synthesis temperature for the Mn-substituted cathode material than for pure $LiNiO_2$[82], increased thermal stability in a delithiated state[83] and suppression of phase transitions[58].

In summary, several improvements compared to pure LNO can be achieved by element substitution, although the exact amount and type of substituent is a decisive factor to reach the best electrochemical performance.

2.3. Electrode processing

Figure 7 shows the schematic structure of a LIB electrode. The electrode is a porous composite consisting of active material particles, conductive additives and binder.[84] The role of the binder is to ensure adhesion on the current collector and cohesion within the composite.[85,86] Conductive additives are integrated to ensure the formation of sufficient electron paths.[85,86] The ratio of the composite components is essential for the later performance of the battery.[87] In the case of energy density optimized electrodes, the amount of electrochemically inactive materials (binder and conductive additives) is kept as low as possible.[85,88]

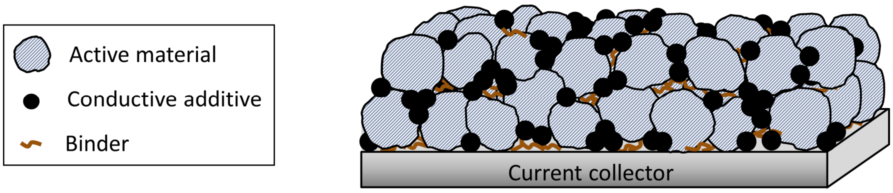

Figure 7: Illustration of a LIB electrode consisting of active material, conductive additives and binder coated on a current collector.

To manufacture an electrode, various process steps are required (Figure 8):[21,85,86] First, in order to prepare a homogenous electrode paste (slurry), the binder is dissolved in a solvent followed by admixing of active material and conductive additives. Then, the slurry is coated on the current collector in the desired pattern and thickness. A subsequent drying process ensures that the solvent and moisture are removed. Finally, the electrode is calendered to increase electrode density and cut in the desired shape. While slot-die coating is the most common process in the industry, electrodes can be easily prepared by the doctor blade technique on a lab scale.[88,89]

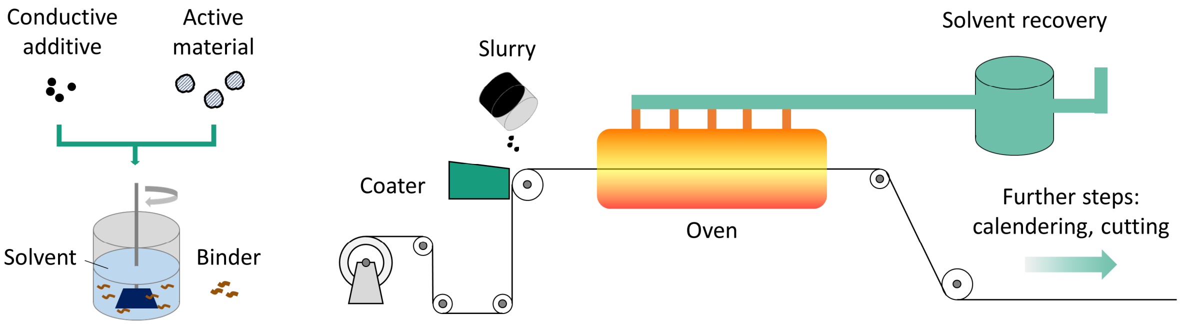

Figure 8: Illustration of the slurry preparation process and electrode manufacturing process. The illustration was redrawn based on reference [11].

For state-of-the-art cathodes mainly polyvinylidene fluoride (PVDF) as a binder and *N*-methyl-2-pyrrolidone (NMP) as a solvent are used. Contrary, state-of-the-art anodes are processed with water as a solvent and water-soluble binders such as carboxymethyl cellulose (CMC), styrene-butadiene rubber (SBR) or polyacrylic acid (PAA).[11,90] The reason for this will be explained in detail in sub-chapter 2.3.2.. However, the implementation of a water-based electrode manufacturing process also on the cathode side would have several advantages.

2.3.1. Advantages of aqueous electrode processing

In terms of environmental benignity, the use of water as a solvent allows the substitution of the reproductive toxic and irritating organic solvent NMP, which is included in the candidate list of substances of very high concern (SVHC) in the European Union that may have serious impact on human health or the environment since 2011.[91] Recently, on May 9th 2020, the use of NMP was limited in the EU.[92] According to this new REACH (Regulation concerning the Registration, Evaluation, Authorization and Restriction of chemicals) regulation, the sale and use of mixtures with a NMP content ≥ 0.3wt% is only permitted if certain exposure threshold values (derived no-effect levels (DNELs)) for workers are met. In detail, the values for exposure by inhalation have to be below 14.4 mg m^{-3} and for dermal exposure below 4.8 mg kg^{-1} per day. Not only in the EU, but also in countries such as the USA, Australia and Canada measures are taken to protect workers from NMP exposure.[93] In contrast, for some countries in the Asia Pacific region such as China, the existence of regulatory limits for NMP exposure is unclear.[93] In addition to the substitution of NMP by water, the replacement of the fluorinated, poorly recyclable PVDF-binder by suitable water-soluble binders would contribute to greener electrode production.[11] Concrete numbers regarding the environmental impact were reported by Zackrisson et al..[13] In their life cycle assessment they estimated the emissions of CO_2 equivalents for a 10 kWh battery pack made with NMP/PVDF-electrodes to be about 4,400 kg, while the emissions would be reduced to 3,400 kg CO_2 equivalents when switching to water and a water-soluble binder.

Another benefit of aqueous electrode processing is the forecast of reduced electrode manufacturing costs.[12,90,94,95] The contribution of the electrode manufacturing costs to the total battery pack costs are estimated to be around 8 – 9%.[90] The cost savings for aqueous electrode processing are seen in multiple aspects: The costs for the raw materials NMP

(1.25 \$ L^{-1}) and PVDF (5.5 \$ lb^{-1}) are significantly higher than the costs for water (0.015 \$ L^{-1}) and the commonly-used binder CMC (1.1 \$ lb^{-1}).[12] Moreover, for the electrode drying process, Susarla et al. calculated a nearly ten times less drying energy per kg solvent when using water instead of NMP.[95] In contrast the costs during the drying step were estimated to be nearly identical for both solvents in a report by Wood et al..[90] However, these authors found that significant cost savings (reduction of the costs by almost the half) can be made due to the fact that a water-based process does not require explosion protections for slurry mixers and other process equipment, a solvent emission control system, and a solvent recovery system. Their calculations estimated \$3 – 6 million cost savings in capital equipment when building a new plant producing 100,000 units of 10 kWh plug-in hybrid electric vehicle (PHEV) batteries per year.

In addition, using aqueous binders such as CMC[96,97], chitosan derivatives[98,99], xantham gum[100,101], alginate[102] and PAA[103] can also have an advantageous effect on the cell performance. Various authors reported increased adhesion to the aluminum current collector, a more uniform electrode microstructure and less electrode swelling by the electrolyte.[11,97–99] This in turn led to better de-/lithiation kinetics and lower internal cell resistance.

2.3.2. Challenges of aqueous cathode processing

As mentioned in sub-chapter 2.3, the implementation of an aqueous electrode manufacturing process for the cathode side is still under investigation, while an aqueous electrode processing for the anode side is already state of the art. The reason is the water sensitivity of cathode materials. Here, further distinctions regarding the water sensitivity must be made for the different cathode materials. For example, the cathode material LFP has proven to be relatively insensitive in water, which is attributed to its high structural stability due to the strong Fe-P-O bond.[11] Consequently, various studies reported excellent electrochemical performance of cells containing water-based LFP-electrodes which even outperformed cells made with NMP/PVDF-electrodes.[11,100,101,103] Nevertheless, also LFP has shown to be not completely water resistive. Porcher et al. observed the formation of a few nm-thick Li_3PO_4 layer together with the increase of Fe^{3+} percentage when LFP is soaked in water, which however had no significant impact on the electrochemical performance.[104]

Furthermore, it was reported that the degradation of LFP in water depends strongly on the mixing conditions.[105]

Contrary, lithium transition metal oxides such as NCM and NCA are, in general, much more prone to water-induced degradation.[11] The typical problems that arise when processing lithium transition metal oxides in water are the detection of metal ions (in particular lithium ions) in the aqueous medium, degradation of the active materials surface and a highly alkaline slurry pH.[11,66,106–108] The latter aspect can lead to the breakdown of the natural oxide layer on the aluminum current collector (slurry pH > 9) and initiate aluminum corrosion and the concomitant generation of hydrogen gas via the following mechanism (Eq. 16-17):[109,110]

$$Al_2O_3 + 2\,OH^- + 3\,H_2O \rightarrow 2\,[Al(OH)_4]^- \qquad \text{(Eq. 16)}$$

$$2\,Al + 2\,OH^- + 6\,H_2O \rightarrow 2\,[Al(OH)_4]^- + 3\,H_2 \qquad \text{(Eq. 17)}$$

The alkalinity is directly related to the presence of lithium ions. The exact origin of the detected lithium ions is still under discussion in literature. Some authors report residual alkaline lithium compounds, such as lithium hydroxide or lithium carbonate, on the cathode surface stemming from unreacted precursors of the production process that are dissolved when the cathode materials are immersed in water.[111] Others suggest the occurrence of a Li^+-/H^+-exchange mechanism in the aqueous medium and the concomitant formation of lithium hydroxide or lithium carbonate if CO_2 is present (Eq. 18-19):[65,112–114]

$$Li^+\,\text{(active material)} + H_2O \rightarrow H^+\,\text{(active material)} + LiOH \qquad \text{(Eq. 18)}$$

$$2\,LiOH + CO_2 \rightarrow Li_2CO_3 + H_2O \qquad \text{(Eq. 19)}$$

Another possible explanation is the formation of lithium species through the reaction of active oxygen species on the oxide surface with water and CO_2 molecules.[66,115] In detail, the formation of the active oxygen species and its further reactions were proposed by Liu et al. as the following (Eq. 20-24):[66]

$$Ni^{3+} + O^{2-}\,\text{(lattice)} \rightarrow Ni^{2+} + O^- \qquad \text{(Eq. 20)}$$

$$O^- + O^- \rightarrow O^{2-}\,\text{(active)} + O \qquad \text{(Eq. 21)}$$

$$O^{2-}\,\text{(active)} + CO_2/H_2O \rightarrow CO_3^{2-}/2\,OH^- \qquad \text{(Eq. 22)}$$

$$2\ Li^+ + CO_3^{2-}/2\ OH^- \rightarrow Li_2CO_3/2\ LiOH \qquad \text{(Eq. 23)}$$

$$O^- + O \rightarrow O_2^- \text{ or } O + O \rightarrow O_2 \qquad \text{(Eq. 24)}$$

The reaction is initiated by the spontaneous reduction of Ni^{3+} to Ni^{2+} accompanied by the oxidation of lattice oxygen to active oxygen (O^-). In the next step, active O^{2-} and neutral O is formed in a disproportionation reaction. Active O^{2-} can then react with carbon dioxide or water molecules to form OH^- and CO_3^{2-}, which in a follow up reaction together with surface Li^+ form Li_2CO_3 and LiOH. Neutral oxygen (O) either recombines to O_2 or reacts with active O^- forming O_2^-.

Surface changes induced by moisturized conditions during the storage of cathode materials have been already shown to dramatically worsen the cell performance.[116–118] However, in the context of aqueous processing water-induced surface changes are often neglected or not investigated in literature. Further research addressing this point is therefore urgently needed to clarify the implications of aqueous electrode processing on cathode materials in more detail.

2.3.3. Strategies to overcome obstacles of aqueous cathode processing

In recent years, various strategies have been developed to overcome the obstacles arising during a water-based cathode fabrication. In 2014, Doberdò et al. reported that by applying a few µm-thick carbon coating layer on the aluminum current collector the direct contact of the alkaline slurry with the current collector can be prevented and therefore aluminum corrosion be reduced.[109] In the following years this technique has been adopted in a huge number of reports.[99,119–122] However, this approach is disadvantageous insofar that an additional process step (coating of the current collector) is necessary and the energy density of the cell is decreased due to the higher mass of electrochemically inactive material.[11]

Other approaches addressing the alkalinity of the slurry, are the addition of acids[106,107,110,121,123–126] or amphoteric oxides[127] during electrode processing to shift the pH value into the region, where aluminum is passivated. However, it has been demonstrated that the addition of acids can simultaneously result in an accelerated dissolution of the transition metals of the active material.[107] Therefore a number of studies concluded that cathode materials are most stable at their native pH value.[106,121] Bauer et al. reported that the addition of acids can also have detrimental impacts on the slurry rheology and electrode adhesion on the current collector.[106] Nonetheless, very recently, promising results have been reported for even Ni-rich layered oxide cathode materials when PAA, which acts as acid and binder at the same time, is used.[106,124,125] For example in 2020, Kuo and Li investigated aqueous electrode processing with PAA as binder and NCM811 as cathode material. The slurry pH was nearly neutral and half cells with water-based electrodes showed a high initial capacity of 189.2 mAh g^{-1} and a high capacity retention of 84.2% (100 cycles, 0.2C).[125] However, the impact of the acidic PAA binder on the long-term performance still needs to be investigated in detail.

Beneficial effects by the addition of amphoteric oxides such as SiO_2 and Al_2O_3 have been reported by Memm et al..[127] Depending on the amount of additives they were able to reduce the pH value of a NCM111-slurry from 11.8 (without additives) down to 8.8 (13.6wt% Al_2O_3) and 8.6 (13.6wt% SiO_2), respectively. Analogous to the approach with carbon coated aluminum foil, this method introduces material which is not able to store lithium ions and thus lowers the energy density of the cell.

All the approaches described above attempt to mitigate the negative consequences of the contact between cathode material and water, rather than preventing the reaction of cathode material with water in the first place. The surface modification/coating of the cathode material particles therefore seems to be a more sustainable approach since it can prevent the contact of the active material with water and thus inhibit negative consequences of aqueous processing from the beginning. Here, when analyzing the literature, it is possible to differentiate between surface modification prior to or during aqueous electrode processing (in situ).

Surface modification prior to an aqueous electrode manufacturing was first reported by Laszczynski et al. in 2015.[128] By applying a vanadium oxide (VO_x) coating on Li-rich NCM particles, leaching of metals and therefore corrosion of the aluminum current collector upon water contact was reduced resulting in improved performance of cells with coated material as compared to cells with uncoated active material. In the following years various coating materials such as carbon, Al_2O_3, TiO_x, Nb_2O_5, VO_x have been investigated as protective surface layers during aqueous electrode processing on $LiCoPO_4$, Li-rich NCM, $LiNi_{0.5}Mn_{1.5}O_2$ and NCA, which all had a beneficial effect on the cell performance.[129]

For the in situ approach, so far two different methods can be found in literature. In 2016, Loeffler et al. reported that the addition of phosphoric acid to an aqueous NCM111 slurry lowers the pH value to the aluminum stable regime while simultaneously forming a protective metal phosphate coating on the active materials surface.[107] As a result, remarkable full cell performance with a capacity retention of 95.66% after 311 cycles was achieved. In the meantime, this method has been used several times for different active materials such as NCM111[107,130], NCM424[131], NCM523[123], Li-rich NCM[132] or LNMO[120,122,126,133,134], with further improvements such as the addition of citric acid[120,122,126,134] resulting in the crosslinking of the binder. An in situ surface coating can also be achieved by injection of CO_2 gas into the electrode slurry. This method was firstly reported by Kimura et al. in 2018.[135] There, a Li_2CO_3 coating was formed on NCA particles and was accompanied by a decrease of the slurry pH value from 12.2 to 8.3. Overall, this approach resulted in the improved performance of cells containing electrodes made with CO_2 gas injection compared to the variant without gas treatment.[135,136]

Comparing the two coating strategies – coating prior to electrode fabrication and in situ coating –, the in situ method has the advantage that no additional coating process is necessary. On the other hand, when using the in situ approach, the active material is unprotected at least for the short period until the protection layer is formed. Recently in 2020, both methods were combined by Watanabe et al..[137] By combining TiO_x-coated NCA particles prepared prior to electrode fabrication with CO_2 gas injection during aqueous slurry preparation surface double coated (TiO_x/Li_2CO_3) NCA particles have been obtained. As a result, half cells with water-based electrodes with double coated NCA delivered comparable performance in terms of cycling stability and C-rate dependency to half cells with uncoated NCA NMP/PVDF electrodes.

As many of the reports described above performed the tests in half cells (= lithium anode), the long-term performance still has to be proven as the lithium anode might compensate lithium loss that resulted from aqueous processing. To develop even better coating materials in the future, an even more intensive focus has to be set on the detailed investigation of the impact of water on the cathode material and the protection mechanism of the coating material.

2.4. Electrochemical methods

2.4.1. Galvanostatic measurements

Depending on the cell chemistry, each battery needs to be operated in a specific voltage window to guarantee safe cycling. Otherwise, overdischarge and overcharge can lead to severe safety issues such as thermal runaway or battery swelling.[138] Charging and discharging of a battery can be conducted by various techniques.[139,140] In this work, two different charge/discharge techniques were chosen (Figure 9). In the CC-CC technique, the cell is charged with constant current (CC) until the cell voltage reaches the specified charge cutoff voltage. Then the cell is discharged with constant current until the cell voltage drops to the discharge cutoff voltage. In the CCCV-CC technique the cell is first charged with constant current, but as soon as the charge voltage cutoff is reached, the cell voltage is held constant (CV) until the current drops to a specified value. Discharge is again conducted in the CC-mode. In general, using the CCCV-CC technique enables higher capacity values to be achieved.[140] Compared to the CC-CC technique, the disadvantage is that the charging time is significantly increased and the cell is held at a high voltage for a longer period of time, which might favor side reactions.

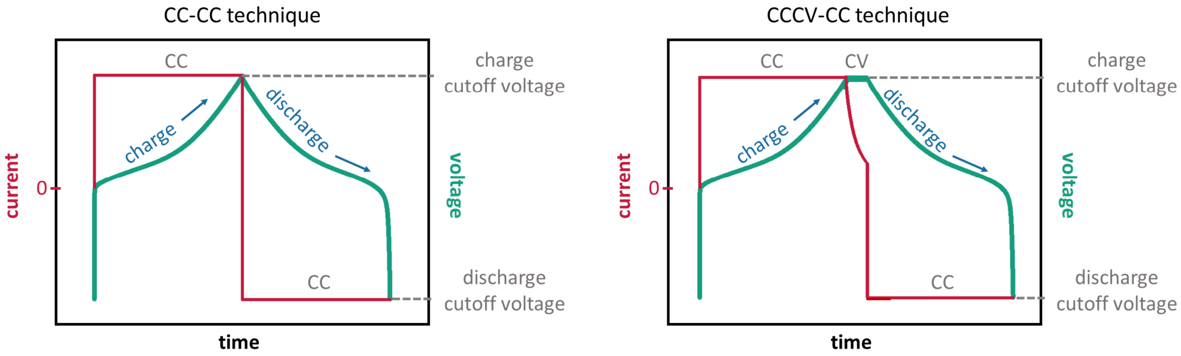

Figure 9: Illustration of different charge-/discharge techniques: CC-charge/CC-discharge (left) and CCCV-charge/CC-discharge (right).

In general, the shape of the voltage profile of a cell is dependent on the type of active material and loss mechanisms (polarization, see sub-chapter 2.1.2) that cause a divergence from an ideal voltage curve.

2.4.2. Cyclic voltammetry

Cyclic voltammetry is a potentiodynamic technique for investigating electrochemical processes.[23,141] A three-electrode setup, consisting of a working electrode (WE), counter electrode (CE), and reference electrode (RE) is typically used.[142] Metallic lithium is typically used as a reference electrode for cyclic voltammetry measurements with LIBs. However, it should be noted that lithium is better described as a quasi-reference electrode as its potential can be influenced by the electrolyte (formation of passivation layers).[143]

For a cyclic voltammetry experiment the potential of the WE is linearly swept between an initial value E_1 and value E_2 in a triangular form for as many times as needed (Figure 10).[142,144] The potential is measured against the reference electrode. When an electrochemical reaction takes place, current flows between WE and CE, which is recorded as a function of the potential. The resulting graph is called a cyclic voltammogram (Figure 10). The velocity of the potential change – the scan rate ($v = dE/dt$) – must be specified for each measurement.[141]

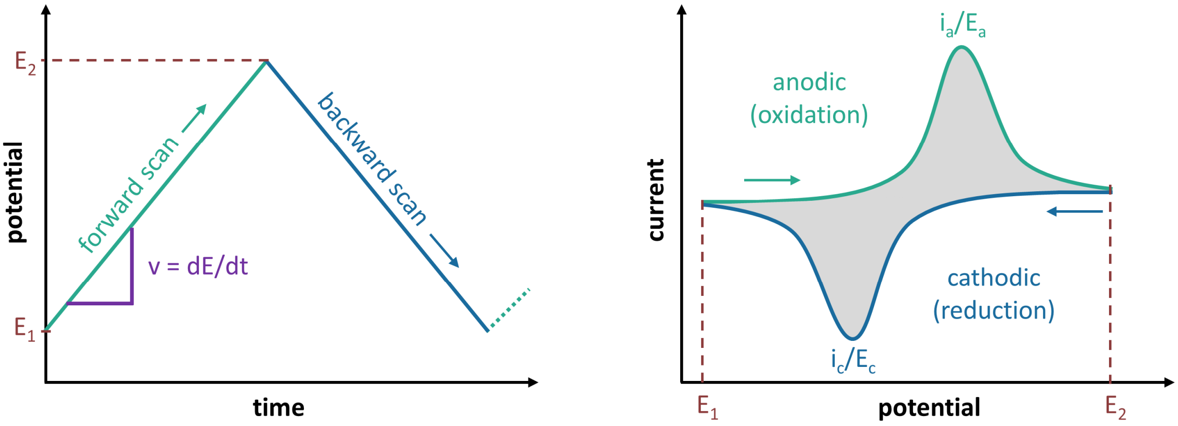

Figure 10: Applied potential as a function of time (left) and schematic voltammogram of a simple reversible process $R \leftrightarrows O + e^-$ with the start in anodic direction.

The schematic voltammogram in Figure 10 can be correlated to a simple reversible process ($R \leftrightarrows O + e^-$, where O is the oxidized species and R the reduced species). As the potential is scanned anodically (towards higher potentials), a non-faradaic current (double layer current) can be detected. As soon as the oxidation potential is reached, R is oxidized at the electrode/electrolyte interface.[24,145] With increasing potential, the current increases exponentially until an anodic current i_a and potential E_a is reached. Subsequently, the current begins to decrease due to the depletion of oxidizable species. During the backward scan (= reduction) the cathodic current i_c and potential E_c can be detected. The current at the beginning of the backward scan differs from zero since oxidation from R to O takes still place.[24]

In general, the shape of a voltammogram is highly dependent on the investigated system. For cyclic voltammetry measurements of lithium-ion cells, the voltammogram can be affected by various factors such as active material, particle size, electrolyte concentration, scan-rate, electrode thickness and temperature.[146]

2.4.3. Electrochemical impedance spectroscopy

Electrochemical impedance spectroscopy (EIS) is a widespread non-destructive technique, which allows for the detailed characterization of interface phenomena.[147,148] The basis of potentiostatic electrochemical impedance spectroscopy (PEIS) is the perturbation of a system with an alternating voltage and the analysis of the current response.[147,148] The time-dependent voltage V(t) and current signal i(t) can be mathematically represented as follows (Eq. 25-26):[21]

$$V(t) = V_m \sin(\omega t) \qquad \text{(Eq. 25)}$$

$$i(t) = i_m \sin(\omega t - \phi) \qquad \text{(Eq. 26)}$$

Here, V_m and i_m represent the maximum values of the voltage and current, respectively. The angular frequency ω is defined by $\omega = 2\pi f$, whereby f is the frequency in Hz. The signal of the current response is matching the voltage signal in frequency but can be shifted in phase (ϕ), which depends on the characteristics of the system (Figure 11).

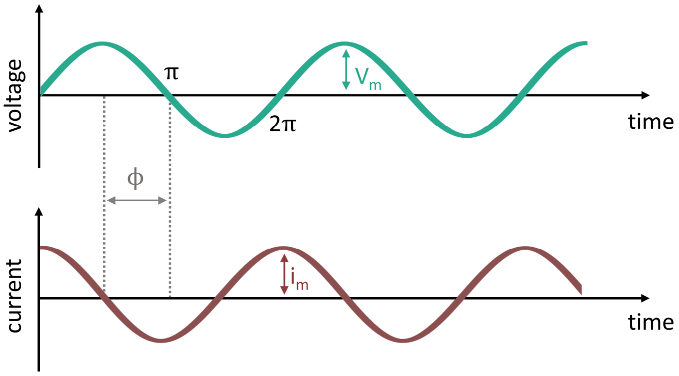

Figure 11: Illustration of a phase shift between alternating voltage signal and current response.

Voltage and current can be expressed as complex functions (Eq. 27-28):[21]

$$V(t) = V_m\, e^{j\omega t} \qquad \text{(Eq. 27)}$$

$$i(t) = i_m\, e^{j(\omega t - \phi)} \qquad \text{(Eq. 28)}$$

$$\text{with } j = \sqrt{-1} = e^{j\frac{\pi}{2}}$$

The impedance Z(ω), which is the analogue to resistance of the direct current (DC) technique, can then expressed by Ohm`s law as the following (Eq. 29):[21]

$$Z(\omega) = \frac{V(t)}{i(t)} = \frac{V_m e^{j\omega t}}{i_m e^{j\omega t - j\phi}} = \frac{V_m e^{j\phi}}{i_m} = |Z| e^{j\phi} \qquad \text{(Eq. 29)}$$

By using Euler`s formula $e^{j\phi} = \cos(\phi) + j\sin(\phi)$, equation (Eq. 29) can be simplified and divided into a real (Z`) and imaginary part (Z``):

$$Z(\omega) = |Z|(\cos(\phi) + j\sin(\phi)) = \text{Z`} + j\,\text{Z``} \qquad \text{(Eq. 30)}$$

$$\text{with } \text{Z`} = |Z|\cos(\phi),\ \text{Z``} = |Z|\sin(\phi),\ |Z| = \sqrt{\text{Z`}^2 + \text{Z``}^2}$$

A typical impedance spectrum is recorded by systematically varying the frequency of the applied alternating voltage perturbation (~1 mHz - 1 MHz).[148] The spectrum can be represented in different ways.[147] The Nyquist plot shows the imaginary part (Z``) on the y-axis and the real part (Z`) on the x-axis (Figure 12). Each data point belongs to a different frequency, whereby the frequency increases from right to left. The Bode plot represents the magnitude of impedance IZI and phase angle ϕ on the y-axis and the frequency f on the x-axis (Figure 12).

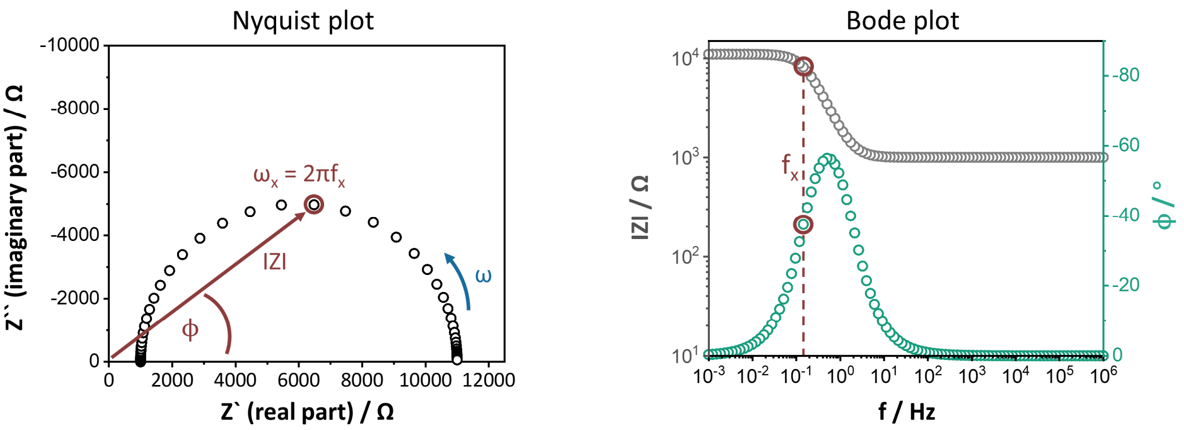

Figure 12: Impedance spectrum represented in the Nyquist plot (left) and Bode plot (right).

To gain information from the impedance spectrum, an equivalent circuit model must be created which describes the examined system.[148] The equivalent circuit model is created with fundamental components such as capacitors, resistors, inductors, constant phase elements, and diffusion elements. For example, to simulate the impedance spectra of Figure 12, an equivalent circuit model consisting of a resistor R_1 and a parallelly connected resistor R_2 and capacitor C would be used (Figure 13).

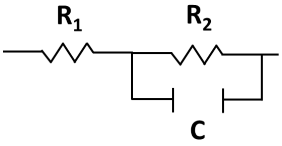

Figure 13: Equivalent circuit model used to simulate the impedance spectrum in Figure 12 (R_1 = 1000 Ω, R_2 = 10000 Ω, C = 0.0001 F).

In Table 2, the impedance of different fundamental elements that are typically used to create an equivalent circuit model for a lithium-ion battery, are listed.[21,147,148]

Table 2: Fundamental elements, which are typically used to create an equivalent circuit model for a lithium-ion battery.

element	formula	description
resistor R	$Z_R = R$	ohmic resistance, e.g. current collector resistance
capacitor C	$Z_C = (j\omega C)^{-1}$	capacitor, e.g. double layer capacitance
inductor L	$Z_L = j\omega L$	inductor, e.g. cables
constant phase element Q_{CPE}	$Z_{CPE} = Q(j\omega)^{\alpha}$ (α = 1 for ideal capacitor)	nonideal capacitor due to surface roughness, porosity etc.
Warburg impedance W	$Z_W = \sigma\omega^{-1/2} - j\sigma\omega^{-1/2}$ (σ = Warburg coefficient)	description of diffusion of mobile charge carriers

In general, to obtain meaningful impedance spectra, the following conditions must be fulfilled:[149]

1. Causality

The response signal is free of artifacts and can be solely attributed to the perturbation of the system.

2. Linearity

The applied voltage signal is linearly related to the responding current signal. Since an electrochemical cell is a non-linear system the amplitude of the current signal must be small enough to ensure pseudo-linear behavior.

3. Stability

The system is stable and does not change with time. After perturbation, the system returns to its original state.

4. Finiteness

The impedance values must be finite over the entire frequency range.

3. Results and discussion

The following chapter summarizes the manuscripts. The experimental parts and the detailed results along with extensive literature comparisons can be found in the manuscripts in the appendix or online. The data were reprinted or adapted from the associated manuscripts.

Table 3 correlates the manuscripts with the sub-chapter text:

Table 3: Correlation between manuscript text and sub-chapter.

Manuscript	**Sub-chapter**
Manuscript I: M. Hofmann, M. Kapuschinski, U. Guntow, G. A. Giffin, Implications of Aqueous Processing for High Energy Density Cathode Materials: Part I. Ni-Rich Layered Oxides. *J. Electrochem. Soc.* **2020**, *167*, 140512. https://doi.org/10.1149/1945-7111/abc033, CC BY 4.0	3.1 (3.1.1)
Manuscript II: M. Hofmann, M. Kapuschinski, U. Guntow, G. A. Giffin, Implications of Aqueous Processing for High Energy Density Cathode Materials: Part II. Water-Induced Surface Species on $LiNi_{0.8}Co_{0.15}Al_{0.05}O_2$. *J. Electrochem. Soc.* **2020**, *167*, 140535. https://doi.org/10.1149/1945-7111/abc6ca, CC BY 4.0	3.1 (3.1.2)
Manuscript III: M. Hofmann, F. Nagler, M. Kapuschinski, U. Guntow, G. A. Giffin, Surface Modification of $LiNi_{0.8}Co_{0.15}Al_{0.05}O_2$ Particles via Li_3PO_4 Coating to Enable Aqueous Electrode Processing. *ChemSusChem* **2020**, *13*, 5962 – 5971. https://doi.org/10.1002/cssc.202001907, CC BY 4.0	3.2
Manuscript IV: M. Hofmann, F. Nagler, U. Guntow, G. Sextl, G. A. Giffin, Long-Term Cycling Performance of Aqueous Processed Ni-rich $LiNi_{0.8}Co_{0.15}Al_{0.05}O_2$ Cathodes. *J. Electrochem. Soc.* **2021**, *168*, 060511. https://doi.org/10.1149/1945-7111/ac054f, CC BY 4.0	3.3

3.1. Implications of aqueous processing for high energy density cathode materials

The implementation of a water-based cathode manufacturing process is beneficial in terms of environmental benignity and costs of lithium-ion battery production (see section 2.3.1). By successfully combining this process with the use of Ni-rich layered oxide cathode materials, cells with higher energy density could be produced (see section 2.2). However, due to the high water sensitivity of this class of cathode materials, aqueous electrode processing remains challenging (see section 2.3.2). To overcome this obstacle, it is essential to first understand the origin of the water sensitivity in more detail.

3.1.1. Ni-rich layered oxide cathode materials

In recent years, a water-based electrode manufacturing process has already been investigated for various layered oxide cathode materials (see section 2.3). However, the direct comparison of these studies is difficult due to different treatment parameters. Therefore, four commercially available layered oxide cathode materials with different elemental compositions have been chosen and evaluated in terms of their response to an aqueous processing route to identify possible correlations between water sensitivity and cathode material composition. All materials have been treated with exactly the same conditions to allow the direct comparison.

The cathode material compositions were as follows:

- $LiNi_{0.33}Co_{0.33}Mn_{0.33}O_2$ (NCM111)
- $LiNi_{0.6}Co_{0.2}Mn_{0.2}O_2$ (NCM622)
- $LiNi_{0.8}Co_{0.1}Mn_{0.1}O_2$ (NCM811)
- $LiNi_{0.8}Co_{0.15}Al_{0.05}O_2$ (NCA)

Metal leaching

Metal leaching of layered oxide cathode materials in aqueous medium is known to be one of the major challenges of a water-based cathode manufacturing process (see section 2.3.2). To investigate water-induced metal leaching of NCM111, NCM622, NCM811 and NCA, aqueous cathode material suspensions with different water exposure durations were prepared separately. After a filtration step, the metal-ion content in the filtrate was investigated by means of inductively coupled plasma optical emission spectrometry (ICP-OES). Figure 14 depicts the mass concentration of lithium ions in the different filtrates.

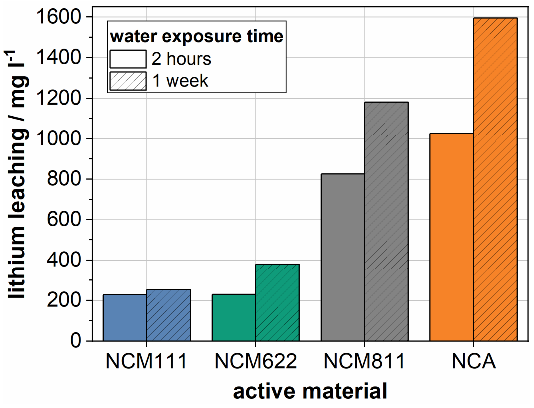

Figure 14: Mass concentration of lithium ions in the filtrate of aqueous cathode material suspensions after different water exposure durations. The figure was reprinted from reference [150] (open access article distributed under the terms of the Creative Commons Attribution 4.0 License (CC BY, http://creativecommons.org/licenses/by/4.0/)).

After two hours of water exposure the lithium content is lowest for NCM111 followed by NCM622, NCM811 and NCA. While the lithium content after one week increases only slightly for NCM111, it is remarkably higher for NCM622, NCM811 and NCA, respectively. Overall, the lithium content is highest in the filtrates of the aqueous NCA suspensions.

The origin of the detected lithium ions after water exposure is still under investigation in the literature and different mechanism are currently under discussion (see also section 2.3.2):

1. Dissolution of residual lithium precursors (e.g. Li_2CO_3) stemming from the cathode material production process.[111]
2. Lithium leaching induced by a mechanism starting with the spontaneous reduction of Ni^{3+} to Ni^{2+} and the subsequent formation of LiOH or Li_2CO_3 (detailed mechanism see section 2.3.2).[66]
3. Lithium ions liberated by a Li^+-/H^+-exchange mechanism in aqueous medium forming LiOH (and Li_2CO_3 if CO_2 is present). This mechanism would simultaneously imply the formation of e.g. NiOOH-like* compounds.[65,112–114]

---

*Assuming the occurrence of a Li^+-/H^+-exchange mechanism for the cathode material $LiNiO_2$ (NCM and NCA are derivatives of $LiNiO_2$, see section 2.2.2), where Li^+ is replaced by H^+, this would lead to the formation of NiOOH according to the following reaction: $H^+ + LiNiO_2 \rightarrow Li^+ + HNiO_2$ (= NiOOH).

When comparing the NCM-type materials, it is striking that a higher lithium content in the filtrate is associated with an increased nickel content in the cathode material structure (NCM111 < NCM622 < NCM811). It is therefore suggested that a main part of the detected lithium can be attributed to a nickel-driven lithium loss mechanism that likely follows at least one of the two later mechanisms (2./3.).

Interestingly, NCA ($LiNi_{0.8}Co_{0.15}Al_{0.05}O_2$) has the same nickel content as NCM811 ($LiNi_{0.8}Co_{0.1}Mn_{0.1}O_2$), but a clearly higher lithium content is detected in its filtrate. Despite the higher cobalt content in the NCA composition compared to that of NCM811, a cobalt associated lithium leaching mechanism as a main driving force may be excluded since NCM111 ($LiNi_{0.33}Co_{0.33}Mn_{0.33}O_2$) has the highest cobalt content in its structure but shows the lowest lithium content in the associated filtrates. A significant composition difference between NCA-type and NCM-type materials is the presence of aluminum and manganese, respectively. It is noteworthy that for both types of materials no nickel or cobalt ions could be detected in the filtrate of the aqueous suspensions. However, while no manganese ions were present for the NCM-type materials, aluminum ions were detected in the filtrates of the NCA suspensions (see manuscript I, Table I).

For lithium aluminate ($LiAlO_2$), which might be considered as a kind of substructure of NCA, there exists various literature reporting about its moisture sensitivity. For example, Lin et al. proposed a mechanism according to the following equations (Eq. 31-32):[151]

$$LiAlO_2 + H_2O \rightarrow AlO(OH) + LiOH \qquad \text{(Eq. 31)}$$

$$2\ AlO(OH) + (2+x)\ H_2O + LiOH \rightarrow LiAl_2(OH)_7 \cdot x\ H_2O \qquad \text{(Eq. 32)}$$

In the first step $LiAlO_2$ reacts with water forming AlO(OH) and lithium hydroxide. In a follow-up reaction AlO(OH) is converted to $LiAl_2(OH)_7 \cdot x\ H_2O$. The latter compound belongs to the class of layered double hydroxides (LDHs).[152] LDHs consist of positively charged metal hydroxide layers, where the positive charge is compensated by anions in the interlayers.[153] The majority of LDHs can be expressed by the formula $[M^{2+}_{1-y}M^{3+}_{y}(OH)_2]^{y+}\ A^{z-}_{y/z} \cdot x\ H_2O$, where M^{2+}/M^{3+} are divalent/trivalent cations and A^{z-} are interlayer anions.[153,155] Li/Al-LDHs represent a unique class of LDHs as they consist of monovalent and trivalent metal cations.[154] They can be described by the formula $[LiAl_2(OH)_6]^+ A^{z-}_{1/z} \cdot x H_2O$.[155] The positively charged layers of Li/Al-LDHs consist of gibbsite-like $Al(OH)_3$ layers, where the lithium ions are located in unfilled octrahedral sites.[153,154,156] Consequently, the formula $LiAl_2(OH)_7 \cdot x H_2O$ is better described by $[LiAl_2(OH)_6]^+ OH^- \cdot x H_2O$.[153]

Another mechanism was proposed by Beckerman et al., where $LiAlO_2$ reacts with moisture in the following manner (Eq. 33):[157]

$$4\ LiAlO_2 + 9\ H_2O + 2\ CO_2 \rightarrow Li_2Al_4(CO_3)(OH)_{12} \cdot 3\ H_2O + Li_2CO_3 \qquad \text{(Eq. 33)}$$

The formation of $Li_2Al_4(CO_3)(OH)_{12} \cdot 3 H_2O$, when $LiAlO_2$ is exposed to moisturized conditions, has also been demonstrated by Gao et al..[158]

Assuming similar reactions to occur for NCA, this would provide an explanation for the detection of aluminum ions, along with a comparatively higher amount of lithium ions in the filtrate of the NCA-suspensions.

Overall, for all cathode materials, significant amounts of lithium ions (highest for NCA) could be detected in the filtrate of aqueous cathode material suspensions. While no other metal ions from the active material structure were detected in the filtrate of the NCM-type materials, aluminum ions were present in the filtrates of NCA. The main part of the detected lithium is assumed to have its origin in nickel-driven lithium leaching mechanisms. This would mean that the detected lithium ions stem not only from the dissolution of lithium precursors (see mechanism 1.) but also from electrochemically active lithium from the active material structure itself (see mechanism 2. (with further details in section 2.3.2) and mechanism 3.). For NCA, the even higher lithium content in the filtrate is assumed to be induced by an additional aluminum-driven lithium leaching mechanism that is likely similar to the reactions described above (see Eq. 31-32 and Eq. 33). As aluminum-doping is used to stabilize the cathode material structure (see section 2.2.2), the loss of aluminum ions might lead to an enhanced structural instability of water-exposed NCA.

pH evolution

Metal leaching is accompanied by the increase of the pH value in the alkaline region due to the presence/formation of basic lithium species such as LiOH and Li_2CO_3 (see section above). If the pH value exceeds pH > 9, the corrosion of the current collector (consisting of aluminum) during the electrode manufacturing process can be expected (see section 2.3.2). To investigate the alkalinity of the different aqueous cathode material suspensions, the pH value was monitored over time (Figure 15).

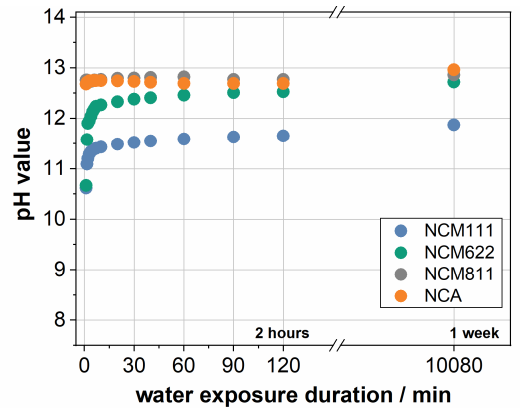

Figure 15: pH value of the different aqueous cathode material suspensions monitored over the water exposure time. The figure was adapted from reference [150] (open access article distributed under the terms of the Creative Commons Attribution 4.0 License (CC BY, http://creativecommons.org/licenses/by/4.0/)).

Immediately after bringing the cathode materials in contact with water, the pH value of all suspensions rises into the alkaline region. The pH value of the suspensions is lowest for NCM111 followed by NCM622, NCM811 and NCA. After around 60 min, a specific threshold value seems to be reached for each active material. This phenomenon might be interpreted as the establishment of an equilibrium of a Li^+-/H^+-exchange reaction (mechanism 3.). After one week of water exposure, a further, albeit minor, increase in the suspension pH value can be observed for all cathode materials (highest for NCA). As expected, the pH measurements therefore follow the trends of the metal leaching tests. As the pH value of all suspensions is above 9 and therefore beyond the aluminum passivation region, at least partial aluminum current collector corrosion is expected during aqueous electrode processing. Although techniques to modify the pH value exist, none of these were used in the following section, as they can impact the electrochemical tests (see section 2.3.3). Actually, in a work of Bauer et al., the cells with aqueous processed electrodes made without a pH modifier showed the best long-term performance.[106]

Electrochemical performance

To evaluate the implications of aqueous electrode processing on the electrochemical performance, water-based electrodes were prepared and tested in half cells (= lithium metal as anode). This configuration allows the electrochemical reactions of the cathode to be investigated in detail due to the known behavior of the lithium anode. Particular care was taken to ensure the same electrode processing time for all materials to avoid an additional impact of the water exposure time, as was observed in the previous section. As a reference, half cells with conventional NMP-based electrodes were built and tested in the same manner. The results obtained during electrochemical cycling are depicted in Figure 16. In this cycling test, the response of the cells to different current rates (C/10, C/4 and 1C) was evaluated. The data represent the average discharge capacity and the associated standard deviation of three cells. Prior to the cycling tests, the cells were conditioned with five charge/discharge cycles at a low current (= formation). For the results of the formation cycles and additional electrochemical characterization tests, reference is made to the manuscript text (see manuscript I).

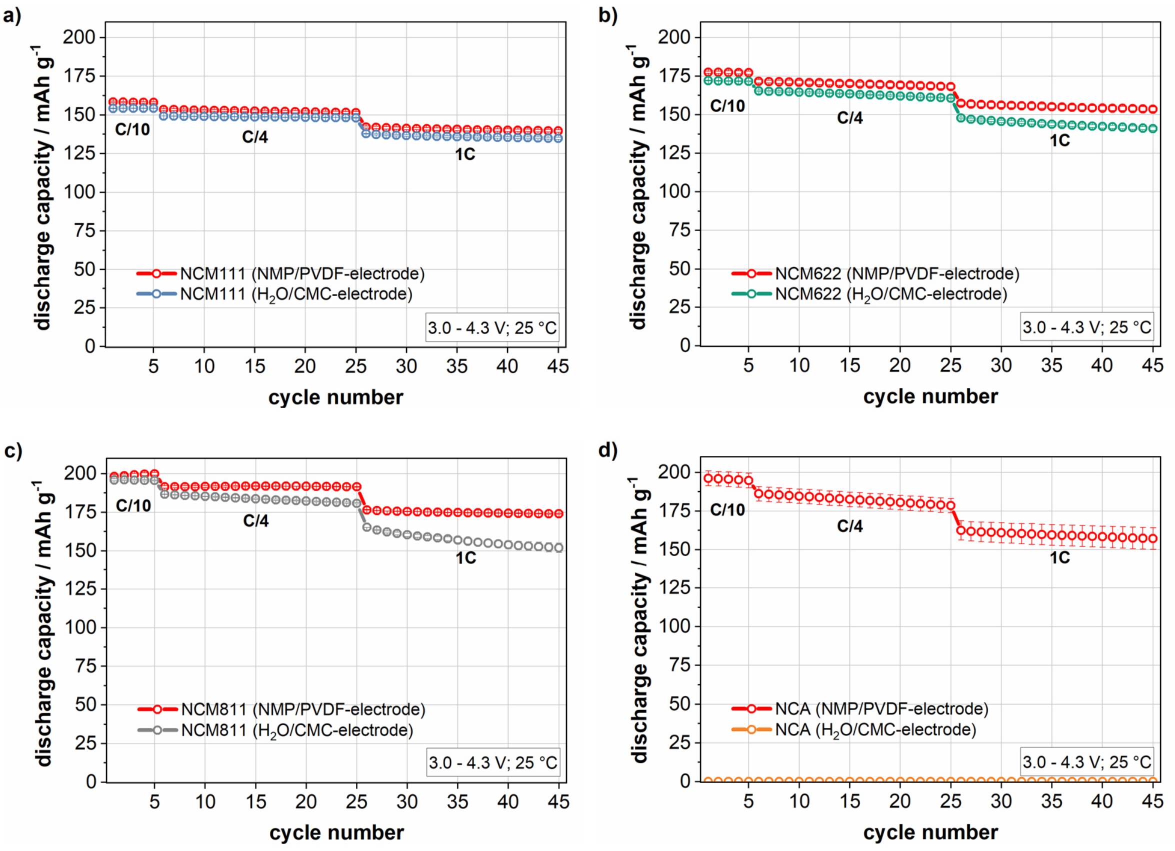

Figure 16: Specific discharge capacity obtained for cells containing NMP/PVDF- and H_2O/CMC-based electrodes (NCM111 (a), NCM622 (b), NCM811 (c) and NCA (d)) cycled at different C-rates. The data are the average values of three cells and the error bars represent the standard deviation between these cells. The figure was adapted from reference [150] (open access article distributed under the terms of the Creative Commons Attribution 4.0 License (CC BY, http://creativecommons.org/licenses/by/4.0/)).

Compared to the cells with reference NCM-electrodes (NMP/PVDF), the average discharge capacity is lower for the cells with water-based NCM-electrodes during the whole cycling procedure (Figure 16a, b, c). This strengthens the hypothesis that the loss of lithium during aqueous processing, at least partially, stems from the active materials structure (see sections above). When analyzing the response of these cells to the varying C-rates, differences can be observed dependent on the NCM composition. While both cell variants with NCM111 show a similar performance regardless of the applied current, the cells with water-based electrodes and cathode materials with a higher fraction of nickel (NCM622 and NCM811) show an increased capacity fading (especially at increasing C-rate) compared to their reference cells. Water exposure seems therefore not only lead to a reduced capacity but also to an enhanced degradation during electrochemical cycling that is more pronounced for the more water-sensitive Ni-rich (NCM622, NCM811) cathode materials. In contrast, it is striking that the cells with H_2O/CMC-electrodes with NCA are completely electrochemical inactive. To clarify the origin of the electrochemical inactivity in detail, further studies are needed that will be conducted in sub-chapter 3.1.2. A correlation between this observation and the results of the metal leaching tests (highest lithium leaching and detection aluminum ions in the filtrate of aqueous NCA suspensions) seems likely.

Based on the previous results it is clear that a water-based electrode manufacturing process is proving to be increasingly challenging when using especially Ni-rich NCM (NCM622, NCM811) cathode materials. For the Ni-rich NCA, the aluminum-doping seems to even exacerbate the water sensitivity as the cells with water-based NCA-electrodes were completely electrochemical inactive. To sum up, NCA has been shown to be the most water-sensitive cathode material at least from those tested. As such, the further focus was set on elucidating the processes in more detail that take place when NCA is exposed to water.

3.1.2. Water-induced surface species on $LiNi_{0.8}Co_{0.15}Al_{0.05}O_2$

To investigate the water-induced changes of NCA and their impact on the electrochemical performance in more detail, further studies were conducted with pristine (NCA-p) and water-exposed NCA. The water-exposed NCA samples are referred by the exposure time as NCA-2h (two hours) and NCA-1w (one week). These were obtained after the filtration of the aqueous NCA suspensions (see section 3.1.1) and a subsequent drying step (110 °C in air). Additional analyses were also conducted on the filtrate that is associated with NCA-2h and is denoted in the text as filtrate-2h.

Analysis of NCA-p, NCA-2h and NCA-1w

The analysis of the crystal structure of NCA-p, NCA-2h and NCA-1w revealed that water exposure does not affect the bulk structure (see manuscript II). This suggests that water-induced effects occur only on the surface of NCA. For the investigation of the NCA surface, the pristine and the water-exposed NCA particles were first examined by scanning electron microscopy (Figure 17). The magnified images show a smooth surface for NCA-p, while particulate species can be detected on the surface of NCA-2h and NCA-1w. Clearly, the amount of surface species increases with water exposure time (most pronounced for NCA-1w).

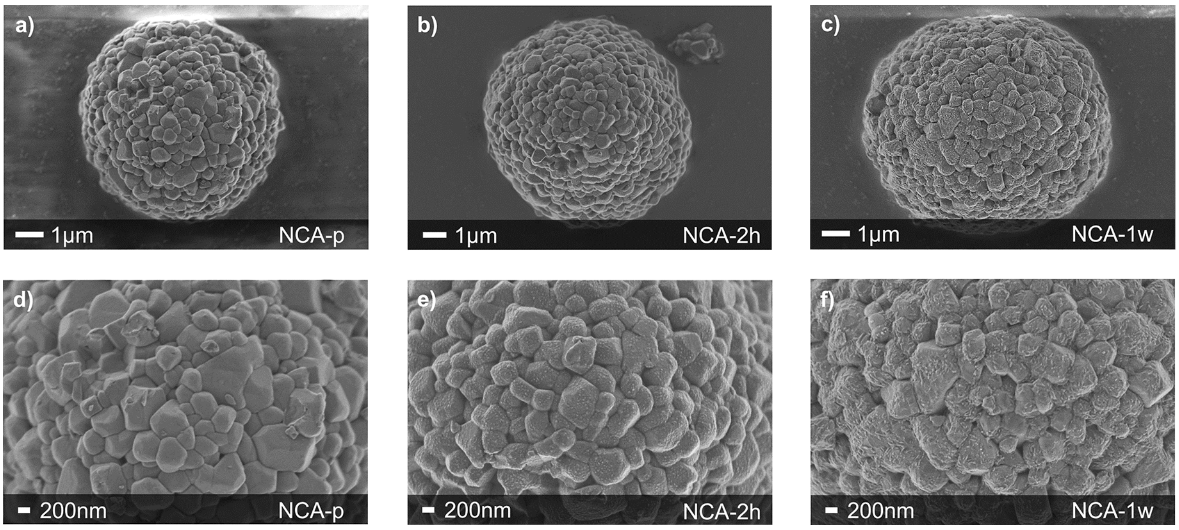

Figure 17: Scanning electron microscopy (SEM) images of pristine NCA (a, d), NCA-2h (b, e) and NCA-1w (c, f). The figure was reprinted from reference [159] (open access article distributed under the terms of the Creative Commons Attribution 4.0 License (CC BY, http://creativecommons.org/licenses/by/4.0/)).

Thermogravimetric analysis with coupled mass spectrometry (TG-MS) was performed with NCA-p, NCA-2h and NCA-1w in argon to examine the nature of these surface species (Figure 18). The mass signals m/z = 18, m/z = 32 and m/z = 44 were assigned to H_2O, O_2 and CO_2, respectively.

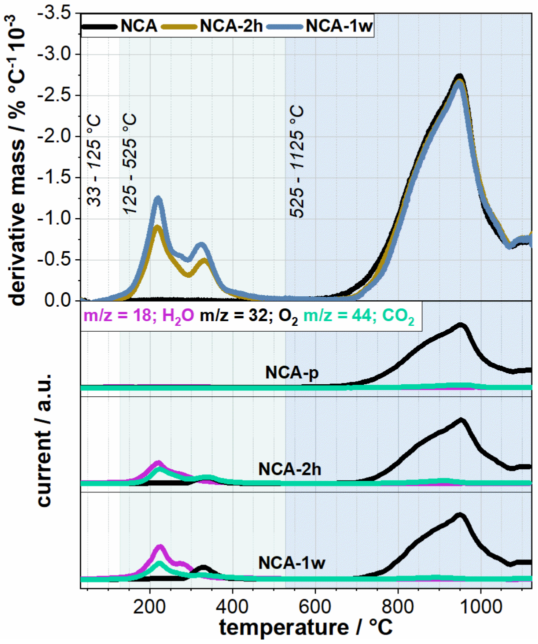

Figure 18: TG-MS analysis of NCA-p/NCA-2h/NCA-1w in argon in the temperature range 33°C – 1125°C. The mass signals m/z = 18, m/z = 32 and m/z = 44 were assigned to H_2O, O_2 and CO_2, respectively. The intensity of the CO_2-signal was multiplied by a factor of 1.5. The figure was reprinted from reference [159] (open access article distributed under the terms of the Creative Commons Attribution 4.0 License (CC BY, http://creativecommons.org/licenses/by/4.0/)).

All samples show a significant mass loss in the temperature range 525°C – 1125°C that goes along with the release of O_2 and reflects the thermal decomposition of NCA.[118] In the same temperature range, an additional, very small, CO_2 signal can be detected for all samples. Based on previous literature, this CO_2 signal was assigned to the decomposition of Li_2CO_3.[118,160] Lithium carbonate is often used as a precursor for the synthesis of NCA and might here represent a production residue as it can be already detected on the pristine NCA.[111] Alternatively, Li_2CO_3 might have formed via the reaction of lithium from NCA with H_2O/CO_2 out of the atmosphere before the material was received (e.g. due to improper storage of NCA).[116] The intensity of the CO_2 signal is almost negligible for NCA-1w. This result suggests that Li_2CO_3 dissolves, at least partially, from the particles surface during water contact.

The most significant difference between the pristine and water-exposed NCA samples can be seen in the temperature range 125°C – 525°C. Here, a mass loss can be only detected for the water-exposed NCAs (most pronounced for NCA-1w). This mass loss comes along with the evolution of several mass signals (CO_2, H_2O and O_2). Based on an extensive literature research, these signals are assigned to adsorbed CO_2, nickel carbonate- and

NiOOH-like species. For the detailed assignments, reference is made to the corresponding manuscript text (see manuscript II).

Based on the TG-MS analysis, the water-induced surface species are mainly assigned to nickel-containing species. However, the presence of newly formed Al- or Co-containing species cannot be excluded by the TG-MS analysis, as the intensity of associated signals might be simply too weak due the lower proportion of these elements in NCA. Actually, water-induced formation of new cobalt and aluminum species was observed by the more surface sensitive X-ray photoelectron spectroscopy analysis (XPS) that are assigned to the formation of $Co(OH)_2$ and $Al(OH)_3$ or AlOOH (see manuscript II). The latter compound has been proposed to be formed upon water contact in section 3.1.1. For the even more detailed assignments, reference is made to the corresponding manuscript text (see manuscript II).

Analysis of the Filtrate

As described in section 3.1.1, lithium and aluminum ions were detected in the filtrate of aqueous NCA suspensions by means of ICP-OES analysis. For further analysis, the filtrate that was obtained after a water exposure time of two hours (filtrate-2h) was dried at 110 °C in air and examined by means of TG-MS analysis (Figure 19). The results were compared with those of NCA-2h.

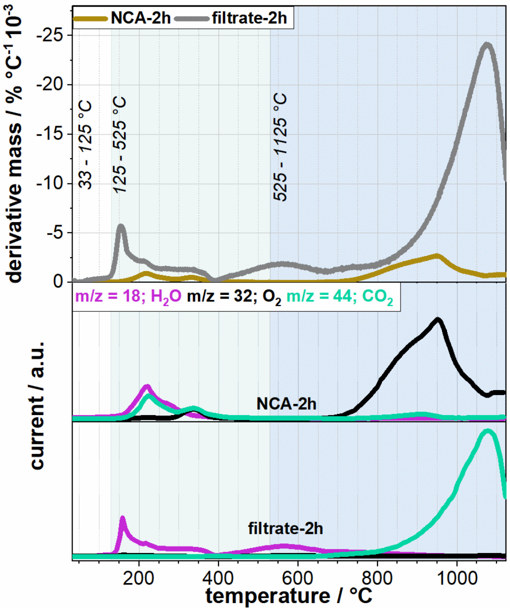

Figure 19: TG-MS analysis of NCA-2h/filtrate-2h in the temperature range 33°C – 1125°C. The mass signals m/z = 18, m/z = 32 and m/z = 44 were assigned to H_2O, O_2 and CO_2, respectively. The intensity of the CO_2-signal was multiplied by a factor of 1.5. The figure was reprinted from reference [159] (open access article distributed under the terms of the Creative Commons Attribution 4.0 License (CC BY, http://creativecommons.org/licenses/by/4.0/)).

It is striking that the decomposition temperatures (along with the mass signals) of NCA-2h and filtrate-2h differ completely. Based on literature and additional analysis techniques (SEM/EDS and XRD) it was demonstrated that the species in the filtrate are mainly lithium hydroxide and lithium carbonate (see manuscript II). However, it was suggested that also minor proportions of aluminum compounds such as $LiAl_2(OH)_7 \cdot x\ H_2O$ are present in the filtrate. This component might be related to the formation of AlOOH on the NCA surface (described above) and be formed in a follow up reaction via the mechanism described in section 3.1.1 (Eq. 31-32). For the detailed analysis, reference is made to the manuscript text (see manuscript II).

Conclusions of Physical and Chemical Characterization Results

Based on the previous results, the processes that occur when NCA is exposed to water can be summarized as the following:

1. Dissolution of surface impurities (e.g. Li_2CO_3) that are present on the pristine NCA.
2. Continuous leaching of lithium and aluminum ions from the NCA structure into water (forming e.g. Li_2CO_3, LiOH and $LiAl_2(OH)_7 \cdot x\ H_2O$).
3. Continuous formation of surface species (e.g. nickel carbonate and NiOOH-like species).

An illustration of these processes is depicted in Figure 20.

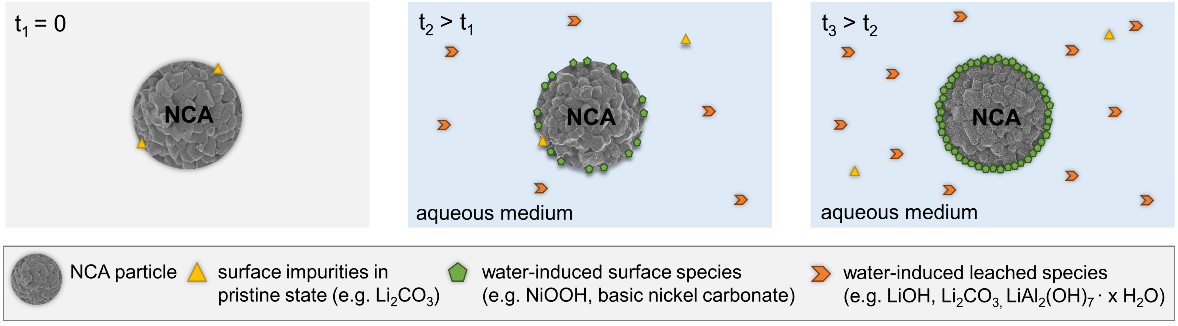

Figure 20: Illustration of the proposed processes that occur when NCA is exposed to water. The figure was adapted from reference [159] (open access article distributed under the terms of the Creative Commons Attribution 4.0 License (CC BY, http://creativecommons.org/licenses/by/4.0/)).

In particular the involvement of aluminum in the leaching process is assumed to destabilize the surface structure of NCA and exacerbate its water sensitivity compared to NCM-type materials.

Impact of Water-induced Surface Species on the Electrochemical Performance

To evaluate the impact of the water-induced surface species on the electrochemical performance, half cells containing pristine NCA and water-exposed NCA were built. The conventional NMP/PVDF-route was used to prepare electrodes as the manufacturing of water-based electrodes with NCA has been demonstrated to directly end in electrochemically inactive cells (see section 3.1.1). In addition to NCA-2h and NCA-1w, a further sample, denoted as NCA-8h (eight hours of water exposure), was prepared for the electrochemical characterization tests. The results obtained during the formation of the cells are depicted in Figure 21.

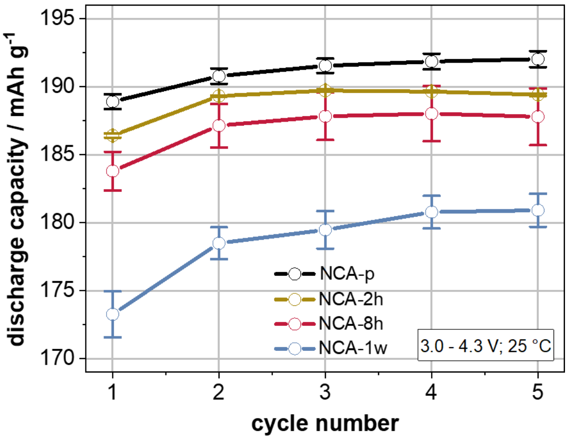

Figure 21: Average discharge capacity over cycle number obtained during the formation protocol of cells containing NMP-based electrodes with NCA-p, NCA-2h, NCA-8h and NCA-1w, respectively. The values represent the average discharge capacity of three cells of each variant and the associated standard deviation is indicated by the error bars. The figure was reprinted from reference [159] (open access article distributed under the terms of the Creative Commons Attribution 4.0 License (CC BY, http://creativecommons.org/licenses/by/4.0/)).

During the whole formation process, the average discharge capacity is highest for the cells with pristine NCA.* For the cells containing water-exposed NCA the discharge capacity decreases with increasing water exposure duration (NCA-2h > NCA-8h > NCA-1w). This result confirms the continuous water-induced modulation of the NCA surface that leads to a reduced storage capability of lithium ions. Over the five formation cycles, the average discharge capacity increases for all cells. As the increase can also be observed for the cell variant with pristine NCA, this might be at least partially attributed to the following point. During cycling (= lithium-ion deinsertion and insertion) it is known that NCA particles expand

---

*Note that all cells in this section contain NMP/PVDF-based electrodes. Cells with H_2O/CMC-based electrodes and pristine NCA have been demonstrated to be electrochemically inactive (see section 3.1.1).

and contract (see section 2.2.1). This mechanical stress might continuously enable the electrolyte to wet previously not accessible active material in the electrode and consequently increase the achievable capacity. In concrete numbers, the discharge capacity increase from the 1st to the 5th formation cycle is 3.1 mAh g^{-1}, 3.0 mAh g^{-1}, 4.0 mAh g^{-1} and 7.6 mAh g^{-1} for the cells with NCA-p, NCA-2h, NCA-8h and NCA-1w, respectively. As such, the increase seems to be more pronounced for prolonged water exposure durations. This result together with the detection of NiOOH-like surface species by means of TG-MS analysis suggests a regeneration of the cathode material via a reversed Li^+-/H^+-exchange mechanism as it was first proposed by Shkrob et al..[114] For NCA, this mechanism might be written as the following (Eq. 34):

$$Li_{1-x}H_xNi_{0.8}Co_{0.15}Al_{0.05}O_2 + x\ Li^+ \rightarrow LiNi_{0.8}Co_{0.15}Al_{0.05}O_2 + x\ H^+ \qquad \text{(Eq. 34)}$$

However, such a mechanism would simultaneously lead to the liberation of protons that might react with the lithium salt $LiPF_6$ and accelerate the cell degradation.[161] Despite this regeneration process, in the last formation cycle the average discharge capacity is still higher for the cells with NMP/PVDF-electrodes. This suggests that a full regeneration cannot be reached and water exposure also results in irreversible structural changes.

The voltage profiles of the first and second cycle of a representative cell of each variant are shown in Figure 22. For the cells with water-exposed NCA, a significant initial overvoltage can be detected in the 1st charge cycle (magnified in the inset of Figure 22a) that is more pronounced with increasing water exposure duration. A direct correlation to the amount of newly formed water-induced surface species seems likely, where the surface species act as a barrier layer and impede the extraction of lithium ions (illustrated in Figure 23). For the cells containing NCA-1w, it stands out that the initial overvoltage is quite close to the specified charge cut-off voltage limit of 4.3 V.* In fact, a slightly higher initial overvoltage that exceeds 4.3 V would render the cells practically electrochemical inactive.

---

*A charge cut-off voltage limit of 4.3 V was chosen for the electrochemical tests to guarantee safe cycling of the cells (see section 2.4.1).

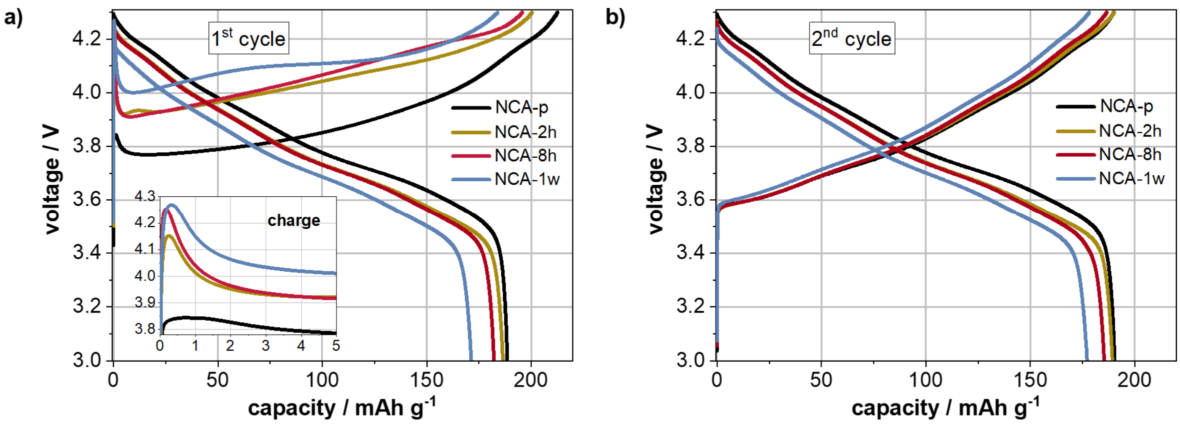

Figure 22: Voltage profile of the first (a) and second (b) formation cycle of a representative cell containing a NMP-based electrode with NCA-p, NCA-2h, NCA-8h and NCA-1w, respectively. The figure was reprinted from reference [159] (open access article distributed under the terms of the Creative Commons Attribution 4.0 License (CC BY, http://creativecommons.org/licenses/by/4.0/)).

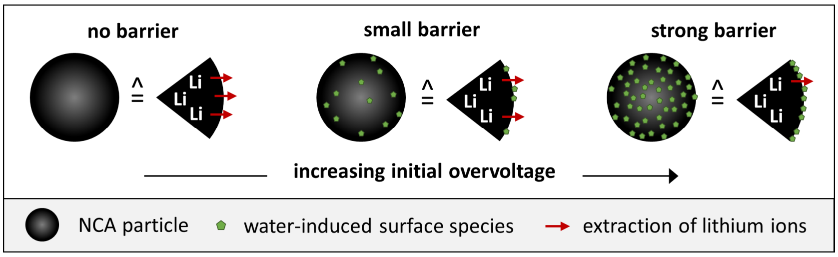

Figure 23: Illustration of the effect of the water-induced surface species on the initial overvoltage in the first charge cycle.

These results therefore provide an explanation for the electrochemical inactivity of the cells with water-based NCA electrodes as seen in section 3.1.1: For these cells, the formation of an even higher amount of water-induced surface species and in turn a more pronounced barrier layer is expected, which completely impedes the lithium-ion extraction in the tested voltage range.*

Interestingly, in the second cycle (Figure 22b), the initial overvoltage is significantly reduced, suggesting that the surface layer is at least partially removed or modified. After the formation protocol, the cells were cycled between 3.0 V – 4.3 V starting with an initial cycle at C/10 and followed by 49 cycles at 1C (Figure 24).

---

*Note that cells with water-based electrodes and pristine NCA were even electrochemically inactive in cyclic voltammetry tests, where the voltage window was extended to 4.5 V (see manuscript I). This suggests that the barrier layer is significantly more pronounced for these cells compared to the cells with the NMP-based variant with NCA-1w. For aqueous processed NCA electrodes it is likely that water-induced leached species can also deposit on the particle surface during electrode drying additionally to water-induced surface species. This might further increase the initial overvoltage and has to be investigated in further studies that are beyond the scope of this work.

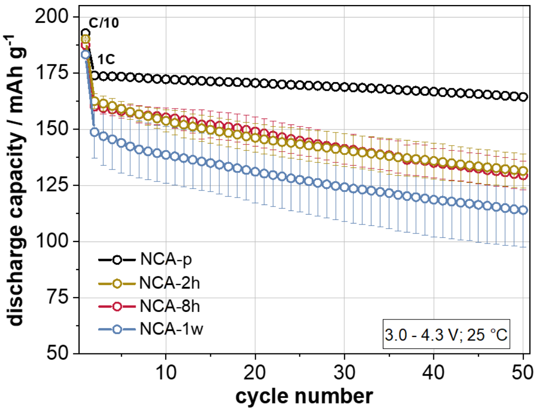

Figure 24: Average discharge capacity over cycle number obtained during the cycling protocol of cells containing NMP/PVDF-based electrodes with NCA-p, NCA-2h, NCA-8h and NCA-1w, respectively. The values represent the average discharge capacity of three cells of each variant and the associated standard deviation is indicated by the error bars. The figure was adapted from reference [159] (open access article distributed under the terms of the Creative Commons Attribution 4.0 License (CC BY, http://creativecommons.org/licenses/by/4.0/)).

As during the formation, the discharge capacity remains the highest for the cells with pristine NCA and lowest for these with NCA-1w. While the cycling of the cells with NCA-p is relatively stable (94.5% capacity retention between the first and last 1C cycle), the cells with water-exposed NCA degrade relatively fast (NCA-2h: 80.9%, NCA-8h: 80.8% and NCA-1w: 76.6%). This is at least partially attributed to the decomposition of the $LiPF_6$-containing electrolyte by protons liberated by a reversed Li^+-/H^+-exchange mechanism as described above. Moreover, in a report by Sicklinger et al., it has been demonstrated that nickel carbonate species, as also detected here on the surface of water-exposed NCA particles, can react with ethylene carbonate from the electrolyte and accelerate the capacity fade.[118]

The above results have shown that in the context of aqueous processing a clear differentiation has to be made between surface species already present on the pristine NCA, water-induced leached species and water-induced surface species. The water-induced surface species form a resistive surface layer that is continuously growing with an increasing water exposure time. The modulation of the NCA surface impacts not only the initial cycles, but also accelerates the cell degradation during cycling. For the successful implementation of a water-based electrode manufacturing process for this extremely water-sensitive material (and probably for Ni-rich cathode materials in general), it is therefore essential to overcome these obstacles. Here, the modification of the NCA surface by a protective coating to avoid the direct contact with water might provide a sufficient solution. This approach will be investigated in sub-chapter 3.2.

3.2. Surface modification of NCA particles via Li_3PO_4 coating

When considering the results in sub-chapter 3.1, it is obvious that aqueous processing is challenging for especially Ni-rich layered oxide cathode materials like NCA. An approach to overcome the previous identified obstacles, might be the protection of the core material by a surface coating. In the last years, various phosphate coatings have been successfully applied on the surface of NCA particles and could remarkably improve the cell performance.[162,163] This effect was often attributed to the strong P–O-bonding energy of the phosphate anion (PO_4^{3-}) protecting the NCA core from side reactions such as electrolyte decomposition during electrochemical cycling.[162,164] However, all the phosphate coated NCA particles were only used in the combination with a NMP-based electrode manufacturing process. As such, the suitability of a phosphate coated NCA for aqueous electrode processing has never been studied.

The ability of a phosphate coating to protect the NCA core against water attack during a water-based electrode manufacturing process was thoroughly examined in this work. Lithium phosphate was chosen as a coating material as it is relatively easy to synthesize and, compared to other phosphate coatings such as $AlPO_4$, $Ni_3(PO_4)_3$ and $Co_3(PO_4)_2$, a lithium-ion conductor.[165] The latter aspect is thought to be beneficial during electrochemical cycling in terms of a simplified lithium insertion and deinsertion.

For the coating process, ethanol (dried over molecular sieves) was used as a solvent to minimize any pre-damage to the NCA surface. The coating process is based on a Li_3PO_4 precipitation reaction and is assumed to occur as the following (Eq. 35):

$$3\,CH_3COOLi + H_3PO_4 \rightarrow Li_3PO_4\downarrow + 3\,CH_3COOH \qquad \text{(Eq. 35)}$$

Four different coating amounts were tested and the modified particles are denoted by increasing coating amount as c01-NCA (0.00625 mmol g^{-1}), c02-NCA (0.0125 mmol g^{-1}), c03-NCA (0.025 mmol g^{-1}) and c04-NCA (0.05 mmol g^{-1}), respectively.

The attenuated total reflection Fourier-transform infrared (ATR-FTIR) spectra of the pristine and coated NCA particles are shown in Figure 25. With increasing coating amount two additional peaks evolve at around 1027 cm^{-1} and 1117 cm^{-1} that were assigned to the asymmetric P–O stretching vibrations of the PO_4^{3-}-ion.[166] As a free PO_4^{3-} ion belongs to the T_d point group only one signal of the asymmetric P–O stretching vibration would be expected in this wavenumber range. However, if the symmetry is lowered due to the interaction of the phosphate ion with lithium or other metal cations from the NCA surface this can lead to the observed peak splitting. For more details of the interpretation of the spectra, reference is made to the manuscript text (see manuscript III).

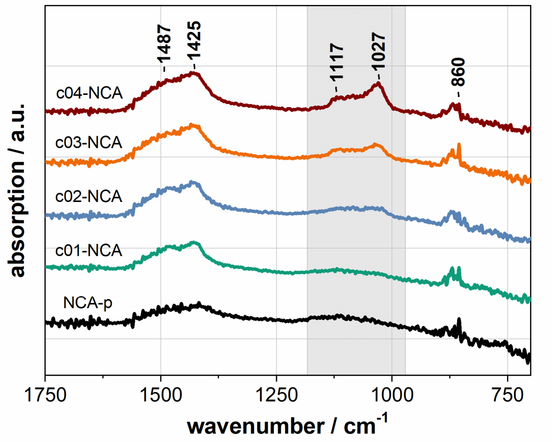

Figure 25: ATR-FTIR spectra of pristine NCA (NCA-p) and c01-NCA, c02-NCA, c03-NCA and c04-NCA. The figure was adapted from reference [167] (open access article distributed under the terms of the Creative Commons Attribution 4.0 License (CC BY, http://creativecommons.org/licenses/by/4.0/)).

The surface of the coated NCA particles was examined by SEM and EDS (Figure 26). As described in section 3.1.2, the surface of the uncoated NCA particles is smooth. The associated EDS mapping indicates a homogeneous distribution of aluminum, nickel and cobalt in the NCA particle. After the coating process the surface appears rather rough and the presence of the coating is additionally confirmed by the associated phosphorus EDS map.

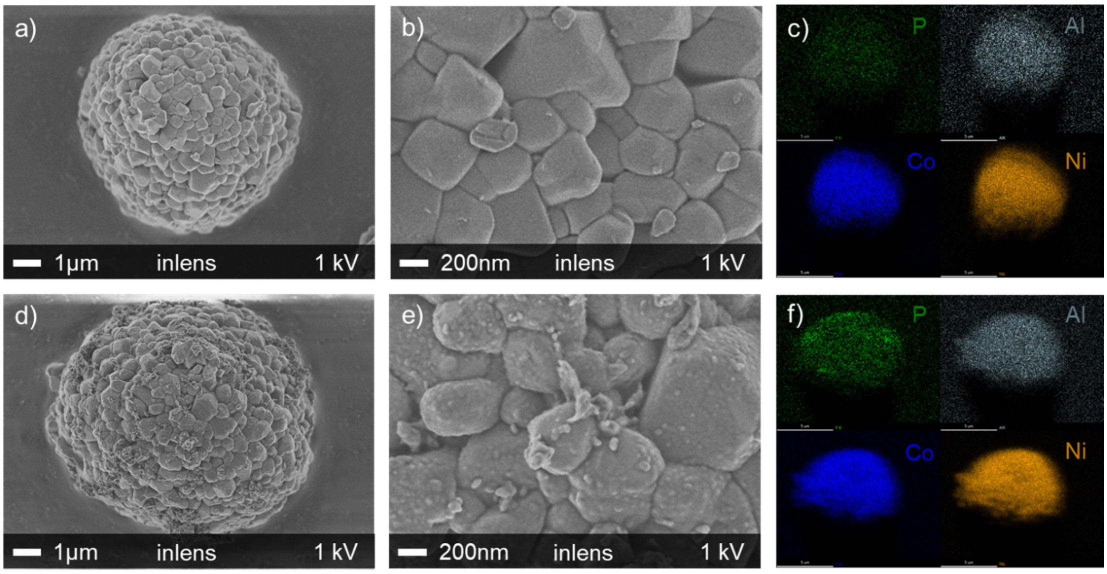

Figure 26: SEM images and EDS mapping of pristine NCA (a, b, c) and c04-NCA (d, e, f). The figure was reprinted from reference [167] (open access article distributed under the terms of the Creative Commons Attribution 4.0 License (CC BY, http://creativecommons.org/licenses/by/4.0/)).

As demonstrated in section 3.1.1, the pH value of an aqueous suspension with pristine NCA rises quickly in the highly alkaline region. To see if the coating has any beneficial effect on the pH value, analogous aqueous suspensions with coated NCA particles were prepared. The pH value was monitored over a period of two hours and compared to that of the aqueous suspension with pristine NCA (Figure 27).

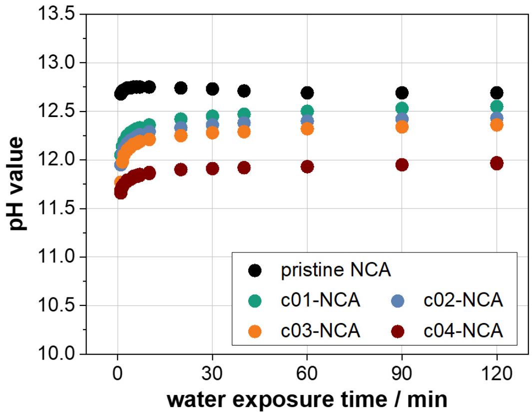

Figure 27: pH values of aqueous suspensions with pristine NCA and c01-NCA, c02-NCA, c03-NCA and c04-NCA. The figure was adapted from reference [167] (open access article distributed under the terms of the Creative Commons Attribution 4.0 License (CC BY, http://creativecommons.org/licenses/by/4.0/)).

As seen for the pristine NCA, the pH value rises quickly in the alkaline region for the suspensions with coated NCA. While the pH is 12.69 for the suspension with uncoated NCA after two hours of water exposure, it decreases with increasing coating amount to 12.55 (c01-NCA), 12.43 (c02-NCA), 12.36 (c03-NCA) and 11.97 (c04-NCA). At first glance, this decrease seems rather small, but when considering the logarithmic dependency of the pH value, the OH^--ion concentration could be reduced by a factor of more than 7 for the suspension with c04-NCA. Nevertheless, as all pH values are far beyond the aluminum passivation regime ($pH > 9$), only reduced aluminum corrosion during the water-based electrode manufacturing process is expected.

Photographs of aqueous processed electrodes with pristine NCA and coated NCA (c04-NCA) along with SEM images of the electrode top view are displayed in Figure 28. As expected from the pH measurements, both electrodes show holes and cracks that can be attributed to aluminum corrosion and the associated evolution of hydrogen gas (see equations in section 2.3.2). However, the number of holes and cracks is clearly reduced for the electrode with coated NCA demonstrating that aluminum corrosion was at least partially suppressed.

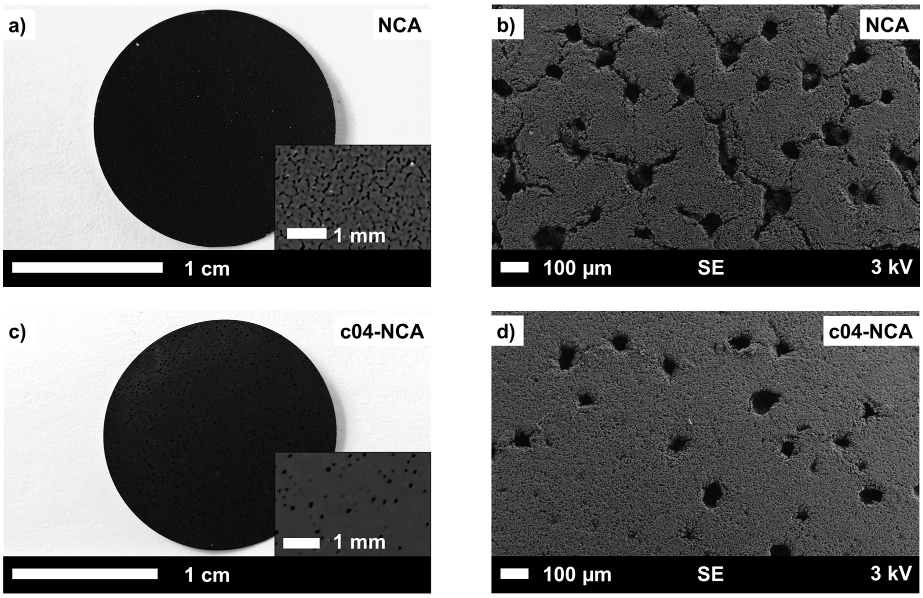

Figure 28: Photographs and SEM images of the top view of calendered aqueous processed electrodes containing pristine NCA (a, b) and c04-NCA (c, d). The figure was reprinted from reference [167] (open access article distributed under the terms of the Creative Commons Attribution 4.0 License (CC BY, http://creativecommons.org/licenses/by/4.0/)).

The impact of the coating on the electrochemical performance was evaluated in half cells containing water-based NCA electrodes. The same test protocol as in section 3.1.2 was applied to all cells. The average discharge capacity obtained during the last formation cycle is depicted in Figure 29a.

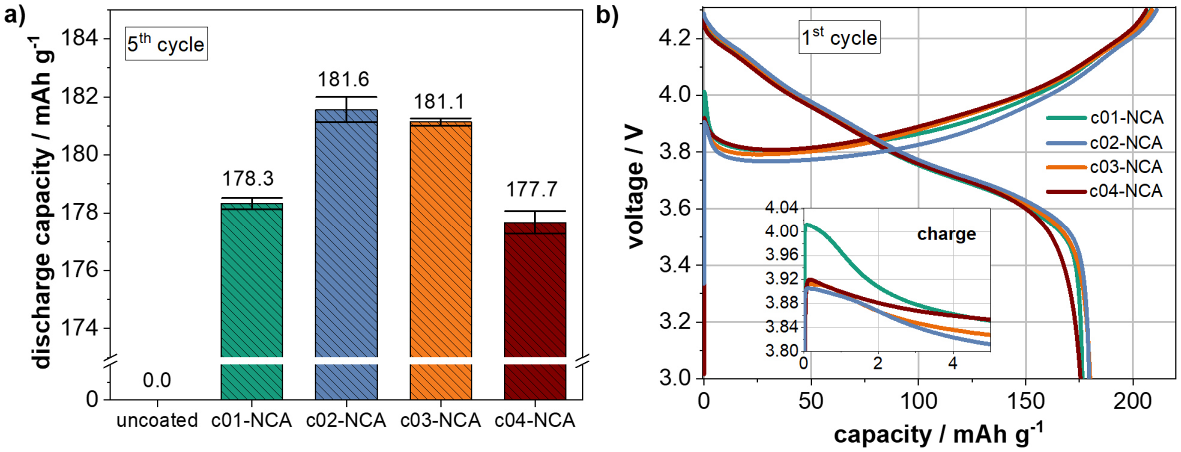

Figure 29: Average discharge capacity of the 5th formation cycle of cells with pristine NCA, c01-NCA, c02-NCA, c03-NCA and c04-NCA (a). The values represent the average discharge capacity of three cells of each variant and the standard deviation is indicated by the error bars. Voltage profile of the 1st formation cycle of a representative cell with c01-NCA, c02-NCA, c03-NCA and c04-NCA (b). The figure was adapted from reference [167] (open access article distributed under the terms of the Creative Commons Attribution 4.0 License (CC BY, http://creativecommons.org/licenses/by/4.0/)).

As shown in section 3.1.1, the cells containing water-based electrodes with uncoated NCA were electrochemically inactive and delivered negligible discharge capacity. This was attributed to a too high initial overvoltage of these cells that exceeds the charge cut-off voltage and is correlated with an extreme amount of water-induced surface species (see section 3.1.2).[*] In contrast, all cells with coated NCA are electrochemically active, thus demonstrating the protective effect of the coating. While the obtained discharge capacity in the last formation cycle is 178.3 mAh g^{-1} for the cells with c01-NCA (lowest coating amount), it increases to 181.6 mAh g^{-1} for cells with NCA particles that were coated with a slightly higher Li_3PO_4 amount (c02-NCA). A further increase of the coating amount, however, did not lead to a further improvement in discharge capacity.

The impact of the coating amount can be also seen in the voltage profile of the first formation cycle (Figure 29b). The initial overvoltage, which has been demonstrated to correlate with the amount of water-induced surface species (see section 3.1.2) is highest for the cells with c01-NCA and lowest for the cells with c02-NCA. This implies that a lower proportion of water-induced surface species is present on c02-NCA. However, for an increased coating amount the initial overvoltage rises again slightly. This aspect can be explained by the fact that lithium phosphate is a lithium-ion conductor, but a poor electron conductor. Therefore, a too thick or overly-dense coating can inhibit sufficient electron transfer, which might then lead to an increase of the overvoltage. This interpretation was also strengthened by cyclic voltammetry and impedance spectroscopy analysis (see manuscript III).

From the combination of these results, a picture of the effect of the coating starts to appear, as illustrated in Figure 30.

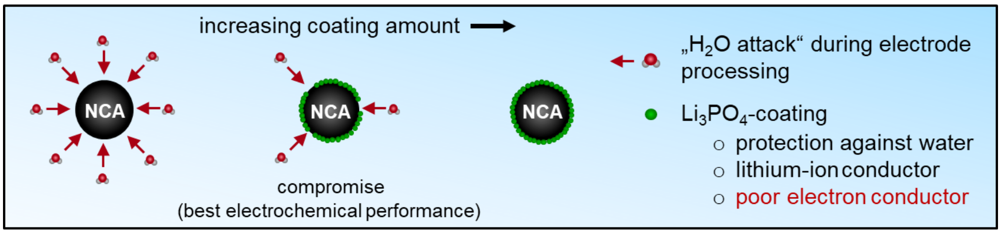

Figure 30: Illustration of the impact of the amount of lithium phosphate coating on the aqueous electrode manufacturing process and cell performance. The figure was reprinted from reference [167] (open access article distributed under the terms of the Creative Commons Attribution 4.0 License (CC BY, http://creativecommons.org/licenses/by/4.0/)).

---

[*] For aqueous processed electrodes the additional deposition of water-induced leached species on the surface of NCA particles during electrode drying is likely and might further increase the initial overvoltage. The impact of water-induced leached species on the electrochemical performance has to be clarified in further studies.

Uncoated particles are completely unprotected during aqueous electrode processing. As a consequence, the NCA particles are massively damaged resulting in electrochemical inactive cells. In contrast, NCA particles coated with a too high amount of lithium phosphate are relatively well protected during aqueous processing. However, the electronic resistance through the particles surface is remarkably increased for these particles. As a result, for a Li_3PO_4 coating, a compromise has to be made between protection during the water-based electrode manufacturing process and a sufficient electronic conductivity through the particle surface during electrochemical cycling.

From the tested materials, this compromise seems to be the best reflected by c02-NCA. For this reason, the cycling performance of cells with water-based electrodes with c02-NCA was compared with that of cells with conventional NMP/PVDF-based electrodes containing pristine NCA and c02-NCA, respectively (Figure 31).

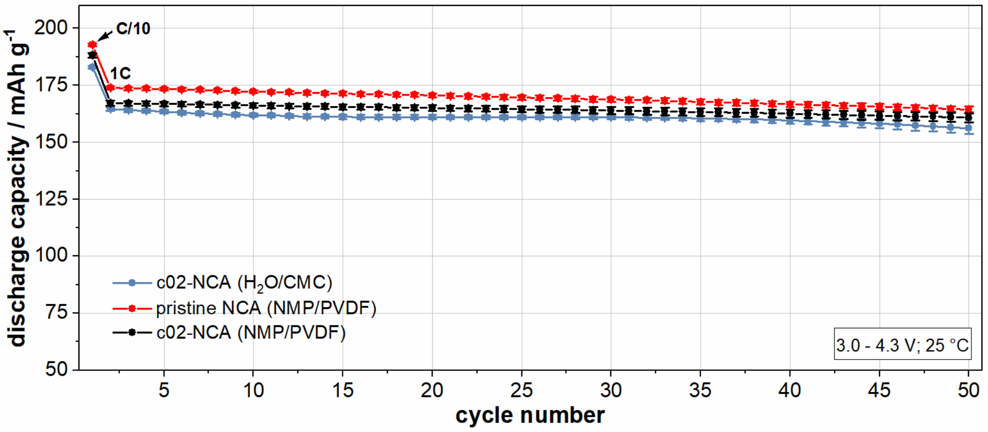

Figure 31: Average discharge capacity over cycle number of cells with H_2O/CMC- (c02-NCA) and NMP/PVDF-based electrodes (pristine NCA or c02-NCA). The values represent the average discharge capacity of three cells of each variant and the standard deviation is indicated by the error bars. The figure was adapted from reference [167] (open access article distributed under the terms of the Creative Commons Attribution 4.0 License (CC BY, http://creativecommons.org/licenses/by/4.0/)).

The cells with NMP-based electrodes and pristine NCA deliver the highest discharge capacity during the whole cycling procedure. For the cells with NMP/PVDF-electrodes in combination with c02-NCA the discharge capacity is slightly reduced. This result might be explained by the fact that the coating amount was optimized for an aqueous electrode process rather than a NMP-based one, where no protection against water exposure is required. The capacity of the cells with water-based electrodes and c02-NCA is approximately 5 – 10 mAh g^{-1} lower. As c02-NCA reflects a compromise coating amount (see Figure 30), a reduction in capacity compared to the NMP-variants was already expected. Interestingly, in terms of cycle life, the cells with the aqueous processed electrodes can easily compete with the cells containing the NMP-based electrodes.

Overall, the results shown above demonstrate that the coating amount is crucial to achieve the best results in terms of aqueous processability and electrochemical cell performance. Cells with water-based NCA electrodes and an optimized Li_3PO_4 coating can even compete with those containing conventional NMP-based electrodes.

3.3. Upscaling of modified NCA and evaluation of full cells

The results in sub-chapter 3.2 have demonstrated that the surface modification of NCA particles with a lithium phosphate coating is a feasible strategy to achieve an enhanced protection of NCA during a water based electrode manufacturing process. However, the coating has only been performed with a lab scale process (illustrated in Figure 32a). Coating of cathode particles via a spray drying process enables a continuous process in an industrial scale. So far, this process has already been used in literature to produce e.g. Sr-doped $LaMnO_3$-coated $LiNi_{0.8}Co_{0.1}Mn_{0.1}O_2$[168], CuO-coated $Li_{1.2}Mn_{0.54}Co_{0.13}Ni_{0.13}O_2$[169] and $Li[Mn_{2-x-y}Co_xLi_y]O_4$-coated $Li(Li_{0.033}Mn_{1.967})O_4$[170]. In this sub-chapter, first the suitability of a spray drying process (illustrated in Figure 32b) to coat NCA particles with lithium phosphate is investigated.

Upscaling of Li_3PO_4-coated NCA

The optimized coating amount from sub-chapter 3.2 (0.0125 mmol g^{-1} – applied on c02-NCA) was chosen for this test. In the following text, the particles coated via the spray drying process are denoted as sd-NCA.

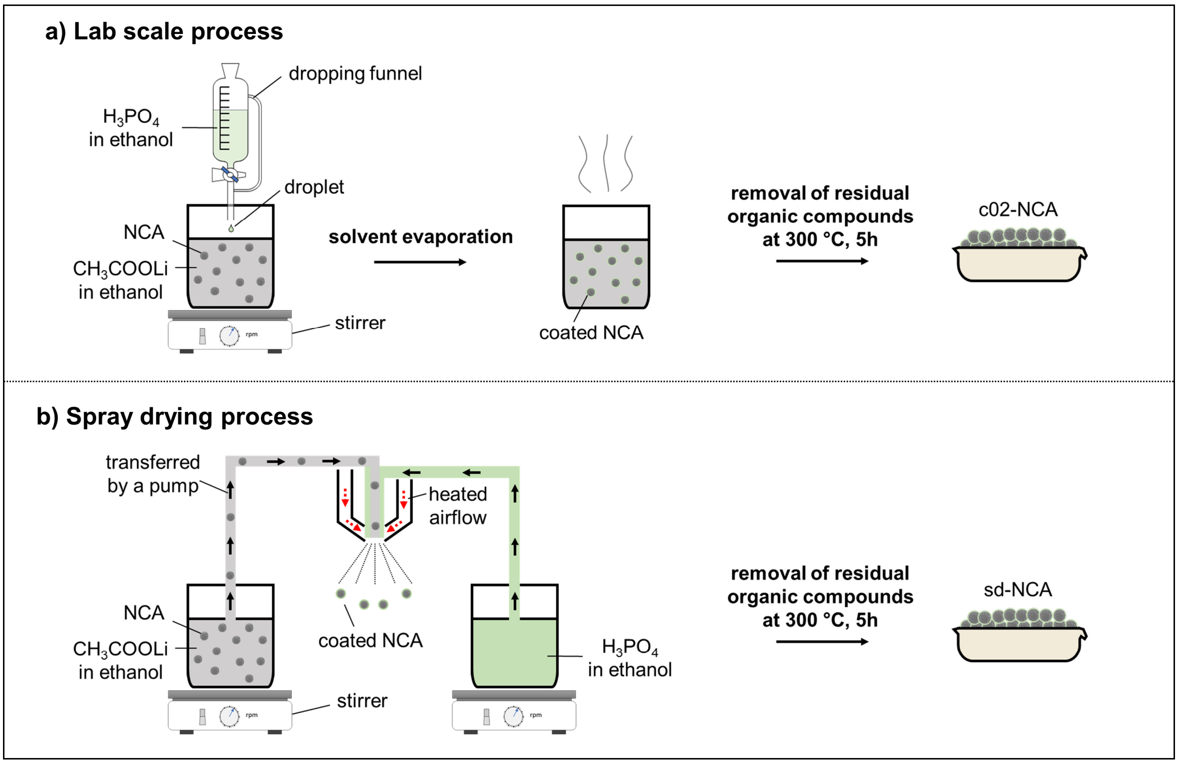

Figure 32: Illustration of the different processes that have been investigated to coat NCA particles with lithium phosphate (lab scale process from chapter 3.2 (a) and spray drying process (b)). The figure was adapted from reference [171] (open access article distributed under the terms of the Creative Commons Attribution 4.0 License (CC BY, http://creativecommons.org/licenses/by/4.0/)).

Figure 33 depicts SEM images of sd-NCA particles. By the selection of suitable process parameters, the raspberry-like secondary particles remain separated (Figure 33a) and no significant accumulation of coating material can be detected on the NCA surface indicating a rather homogenous coating (Figure 33b). TEM/EDS analysis was conducted on the cross-section of sd-NCA particles to investigate the coating in detail (Figure 33c). As expected, at position 2 (Pos. 2) the signals of the NCA bulk – Co, Ni and Al – can be recognized. In contrast, at the surface positions (Pos. 1 and Pos. 3) an additional phosphorus signal is detected confirming the successful surface coating. It is obvious that the phosphorus signal intensity at Pos. 3 is weaker compared to Pos. 1. Therefore, it can be concluded that the coating thickness varies slightly. Magnified pictures, which can be found in the supporting information of manuscript IV, demonstrate that the coating thickness is very thin being less than 10 nm at Pos. 1 (high intensity of the P-signal in the EDS spectrum). Moreover, the presence of some sulfur is also evident. Sulfur has been already found on the surface of pristine NCA (see manuscript II) and might stem from the NCA synthesis process where sulfate salts are often used as precursors.

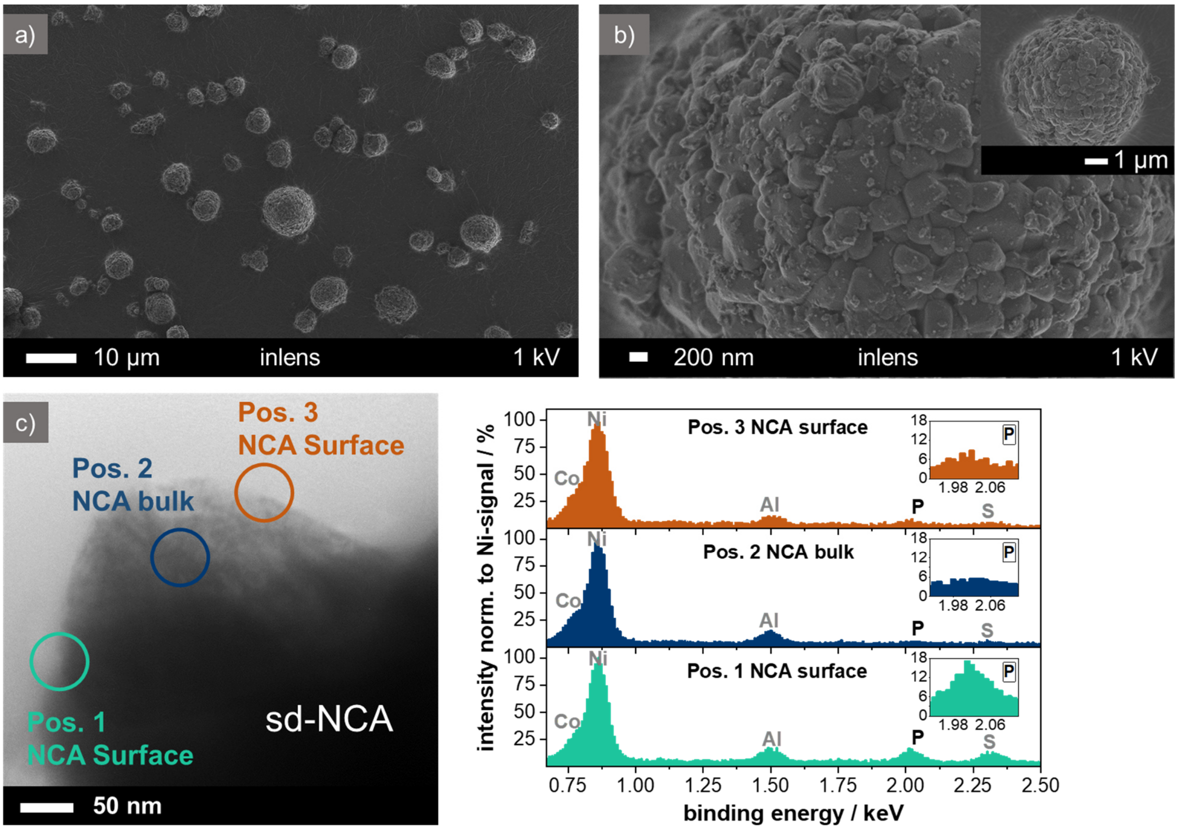

Figure 33: SEM images of sd-NCA in different magnifications (a, b). TEM/EDS analysis of the cross-section of sd-NCA (c). The figure was reprinted from reference [171] (open access article distributed under the terms of the Creative Commons Attribution 4.0 License (CC BY, http://creativecommons.org/licenses/by/4.0/)).

To investigate the electrochemical performance of sd-NCA particles and simultaneously the coatings ability to protect the NCA core against water attack, half cells with aqueous processed cathodes, analogous to those presented in chapter 3.2, were built. For comparison, the results of the cells with aqueous processed electrodes containing c02-NCA (prepared via the lab scale process) were reprinted from sub-chapter 3.2 (Figure 34).

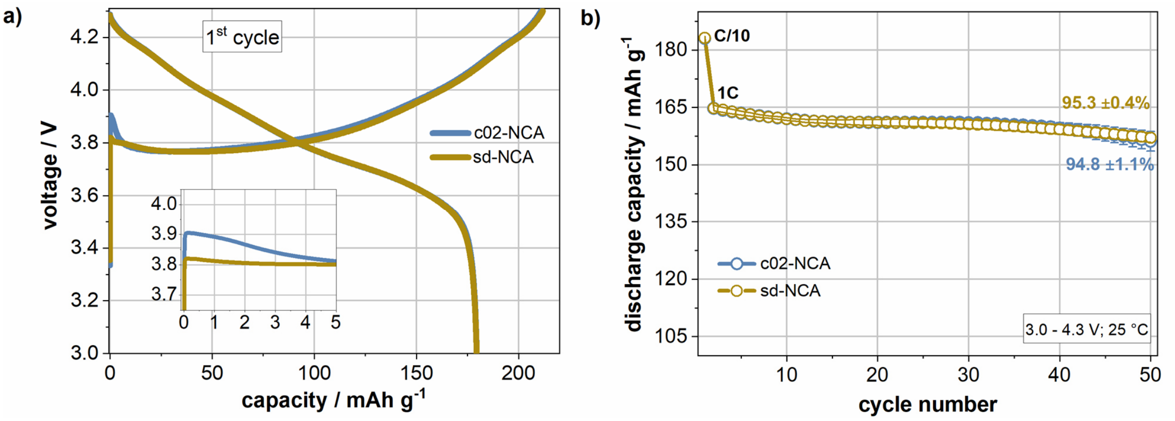

Figure 34: Voltage profile of the 1st formation cycle of a representative cell with c02-NCA and sd-NCA (a). Average discharge capacity over cycle number obtained during the cycling protocol of cells containing aqueous processed electrodes with c02-NCA and sd-NCA, respectively (b). The values in (b) represent the average discharge capacity of three cells of each variant and the associated standard deviation is indicated by the error bars. The data from the cells with c02-NCA were included as reference from sub-chapter 3.2. The figure was adapted from reference [171] (open access article distributed under the terms of the Creative Commons Attribution 4.0 License (CC BY, http://creativecommons.org/licenses/by/4.0/)).

In comparison to the c02-NCA cell variant, the initial overvoltage in the first formation cycle that correlates with the amount of water-induced surface species (see sub-chapter 3.1.2) is slightly lower for the cells with sd-NCA (Figure 34a).* This observation might be explained by the fact that for the spray drying route no additional solvent evaporation step is necessary (see Figure 32). Here, the time in which the cathode materials are in contact with air and might react with moisture is reduced. Moreover, the spray drying process as an automatic process enables a more defined precipitation of the coating on the particles surface as is achievable with the manual dropping funnel technique (lab scale process). The full formation data is available in the manuscript text (see manuscript IV).

The cycling data of these cells is shown in Figure 34b. The average discharge capacity of the cells with sd-NCA and c02-NCA is 183.2 mAh g^{-1}/164.8 mAh g^{-1} and 183.0 mAh g^{-1}/ 164.8 mAh g^{-1} in the first C/10 and 1C cycle, respectively. As such, the performance at the

---

*For aqueous processed electrodes the additional deposition of water-induced leached species on the surface of NCA particles during electrode drying is likely and might further increase the initial overvoltage.

beginning of the cycling is almost identical. Moreover, the cells deliver essential the same capacity retention after 50 cycles (cells with sd-NCA: 95.3 ± 0.4%; cells with c02-NCA: 94.8% ± 1.1%).

In sum, these results demonstrate, that using a spray drying process to coat NCA with lithium phosphate is a feasible and simple way to enable upscaling. Moreover, the behavior of this particles regarding the response to an aqueous electrode process is very comparable to that of particles coated with the lab-scale process.

To quantify the ability of the coating of the sd-NCA particles to protect the NCA core against water attack, the same water exposure experiment (two hours of water exposure) as presented in sub-chapter 3.1.2 was conducted. The obtained particles (denoted as sd-NCA-2h) were analyzed by means of TG-MS (Figure 35). For comparison, the TG-MS results obtained for pristine NCA particles that were exposed to water for the same period of time (NCA-2h, sub-chapter 3.1.2) were included as reference.

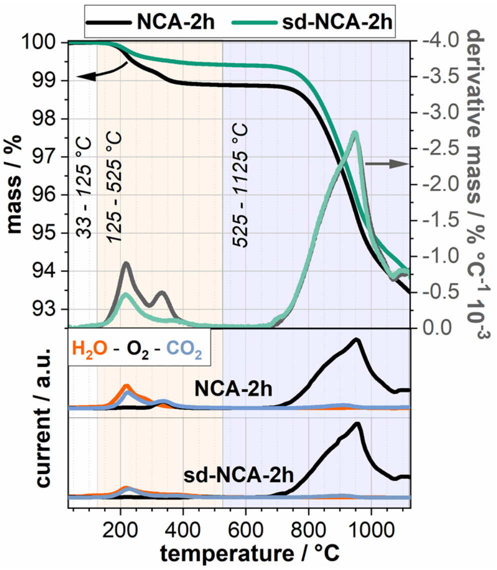

Figure 35: Thermogravimetric analysis coupled with mass spectrometry in the temperature range 33 °C – 1125 °C for sd-NCA-2h and NCA-2h (data reprinted from sub-chapter 3.1.2). The mass signals m/z = 18, m/z = 32 and m/z = 44 signals were assigned to H_2O, O_2 and CO_2, respectively. The intensity of the CO_2 signal was multiplied by a factor of 1.5. The figure was reprinted from reference [171] (open access article distributed under the terms of the Creative Commons Attribution 4.0 License (CC BY, http://creativecommons.org/licenses/by/4.0/)).

As shown in sub-chapter 3.1.2, newly formed water-induced surface species decompose in the temperature range 125 – 525 °C. Here, the mass loss for sd-NCA-2h is 0.6% and is clearly lower compared to the reference material NCA-2h (1.1%). As expected, the intensity of the mass signals of H_2O, O_2 and CO_2 is therefore lower for the sd-NCA-2h sample than for the

NCA-2h sample. As such, an almost two-fold reduction in amount of water-induced surface species was achieved by using sd-NCA compared to using pristine NCA. It is clear from the experiments that the use of sd-NCA does not completely prevent the formation of water-induced surface species. This aspect is likely related to the fact that the coating amount represents a compromise between protection against water and sufficient electronic conductivity through the particles surface as discussed in sub-chapter 3.2. Therefore, future studies, need to focus on the development and application of new coating materials that provide an even higher protection against water while still maintaining a good electrochemical performance.

Evaluation of the long-term performance of full cells

To this point, the electrochemical tests have been performed in a half cell configuration with a lithium metal anode.* To exclude that the massive lithium reservoir in a half cell configuration compensates lithium deficits (that arise during aqueous processing) and artificially prolongs the cycle life, cells in a full cell configuration with a graphite anode and aqueous processed sd-NCA cathode were built and evaluated. Figure 36 depicts the average discharge capacity that was obtained during 1C cycling for 1000 cycles.

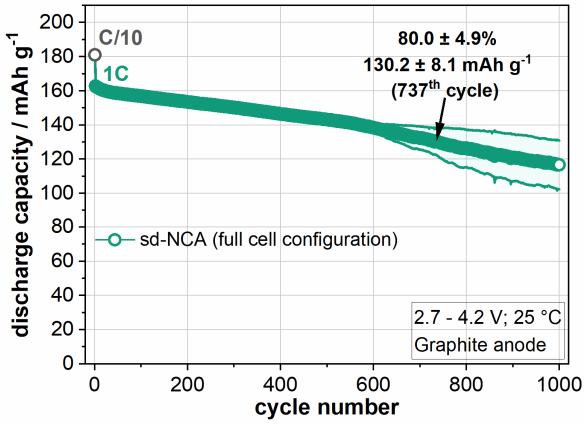

Figure 36: Long-term cycling performance of full cells containing a graphite anode and an aqueous processed sd-NCA cathode at 25 °C. The values represent the average discharge capacity of three cells and the associated standard deviation is indicated by the error bars. The figure was adapted from reference [171] (open access article distributed under the terms of the Creative Commons Attribution 4.0 License (CC BY, http://creativecommons.org/licenses/by/4.0/)).

In the C/10 cycle the cells deliver an average discharge capacity of 181.0 mAh g^{-1}. This value is quite close to the average value obtained in half cells at the same C-rate (183.2 mAh g^{-1},

---

*This configuration allows the electrochemical reactions of the cathode to be investigated in detail due to the known behavior of the lithium anode.

see Figure 34b) and indicates that no lithium reservoir is necessary to achieve such high capacity values. Moreover, the cells can be cycled for over 730 cycles at 1C before the generally-accepted end-of-life (EoL) criteria of 80% initial capacity is reached. For comparison, Table 4 shows the long-term cycling data that has been published in the literature for full cells with a graphite anode and an aqueous-processed cathode containing a layered oxide cathode material.

Table 4: Comparison of the long-term cycling performance reported for full cells with graphite anode and aqueous processed cathode containing layered oxide cathode materials. The table was adapted from reference [171] (open access article distributed under the terms of the Creative Commons Attribution 4.0 License (CC BY, http://creativecommons.org/licenses/by/4.0/)).

active material	capacity retention (capacity last cycle)	cycles	discharge C-Rate	voltage range, temperature	ref.
NCM111	~ 84% (104.0 mAh g^{-1}) ~ 70% (85.4 mAh g^{-1})	1000 2000	1C	2.75 V – 4.2 V, 20 °C	[121]
NCM111	95.7% (~ 123 mAh g^{-1}*)	311	1C	3.0 V – 4.2 V, 20 °C	[107]
NCM111	~ 88%* (~ 88 mAh g^{-1}*)	900	3C	3.0 V – 4.2 V, 23 °C	[106]
NCM111	~ 90%* (~ 118 mAh g^{-1}*)	500	1C	3.0 V – 4.2 V, 20 °C	[119]
NCM111	~ 99% (~ 17 Ah*)	500	1C	2.75 V – 4.1 V, 25 °C	[172]
NCM523	~ 81% (~ 115 mAh g^{-1})	500	1C	3.0 V – 4.2 V, not available	[173]
NCM523	79.5% (not available)	886	C/3	2.5 V – 4.2 V, 30 °C	[90]
NCM523	~ 76%* (~ 100 mAh g^{-1}*) ~ 70%* (~ 92 mAh g^{-1}*)	1000* 1425*	1C	2.8 V – 4.2 V, not available	[174]
NCM811	~ 70% (~ 131 mAh g^{-1}*)	1000	C/3	2.5 V – 4.2 V, 30 °C	[108]
NCA	~ 80% (~ 135 mAh g^{-1})†	~ 600†	C/3	3.0 V – 4.2 V, 30 °C	[175]
NCA	88.0% (143.2 mAh g^{-1}) 80.0% (130.2 mAh g^{-1}) 71.7% (116.7 mAh g^{-1})	500 737 1000	1C	2.7 V – 4.2 V, 25 °C	this work

*The value was calculated or determined from graphical data presented in the associated literature. This might lead to some variation from the actual value. †The long-term cycling performance was predicted by Hawley et al.[175] after measuring the cell performance for approx. 350 cycles at C/3.

From this table it is obvious, that the results of the full cells with sd-NCA can compete with those reported in literature so far. In particular, the high specific average discharge capacity even after 1000 cycles at 1C (116.7 mAh g^{-1}) is noteworthy. Full cells with aqueous processed NCM811 cathodes deliver a slightly higher specific discharge capacity after the same number of cycles (approx. 131 mAh g^{-1}). However, these results were obtained at a lower C-rate (C/3). Hawley et al. recently predicted that the EoL criterion of full cells containing water based cathodes with PAA-modified NCA is reached after approximately 600 cycles at C/3.[175] This is clearly earlier than for the full cells with sd-NCA. Some of the full cells with NCM111 or NCM523 demonstrate a comparable or better capacity retention, but deliver a lower capacity. Additionally, these electrodes were processed with cathode materials with a rather low fraction of nickel. These materials have been shown to be less sensitive to water as NCA (see sub-chapter 3.1).

The results demonstrate that through surface protection, aqueous processing of even very water-sensitive cathode materials such as NCA can be enabled. As suggested above, a further focus on the development and application of coating materials seems to be the key to enable a sustainable widespread electrode production for nickel-rich layered oxide cathode materials in the future.

4. Summary and outlook

4.1. Summary and outlook (ENG)

Summary

The implementation of a water-based cathode manufacturing process is attractive, given the prospect of improved sustainability of future lithium-ion batteries. However, the sensitivity of many cathode materials to water poses a huge challenge.

Within the scope of this work, a correlation between the water sensitivity of cathode materials from the class of layered oxides and their elemental composition was identified. In particular for the cathode material $LiNi_{0.8}Co_{0.15}Al_{0.05}O_2$ (NCA), the processes taking place in aqueous medium were clarified in detail. Based on this knowledge, the surface of NCA particles could be specifically modified, which led to a reduced water sensitivity. As a result, the electrochemical performance of cells with water-based NCA cathodes was significantly improved and a remarkable long-term cycling performance was achieved.

The present work contributes to a deeper understanding of the water sensitivity of cathode materials and at the same time presents a promising approach to overcome this obstacle. Consequently, this work advances the successful widespread realization of water-based cathode manufacturing.

The major findings of this work are summarized below:

<u>Correlation between water sensitivity and elemental composition</u>

Within the scope of this work, different cathode materials from the class of layered oxides ($LiNi_{0.33}Co_{0.33}Mn_{0.33}O_2$ (NCM111), $LiNi_{0.6}Co_{0.2}Mn_{0.2}O_2$ (NCM622), $LiNi_{0.8}Co_{0.1}Mn_{0.1}O_2$ (NCM811) and $LiNi_{0.8}Co_{0.15}Al_{0.05}O_2$ (NCA)) were compared in terms of their response to an aqueous electrode manufacturing process. It was demonstrated that the water sensitivity correlates directly with the elemental composition of the cathode material: Cathode materials with an increased amount of nickel are particularly sensitive to water. This is reflected in a significant leaching of lithium ions (detected via ICP-OES). In detail, the concentration of lithium ions increased in the order NCM111 < NCM622 < NCM811 < NCA and is correlated with the increase in the pH value into the alkaline region. The latter aspect can lead to the corrosion of the current collector during the electrode manufacturing process.

While only lithium ions were detected for NCM-type cathode materials when exposed to water, aluminum leaching was additionally observed for the cathode material NCA. In addition to nickel-driven lithium loss mechanisms, aluminum-related lithium loss mechanisms in an aqueous medium were proposed for NCA. These provide an explanation for the comparatively high lithium leaching from NCA.

The implications of water exposure on the cathode materials were also directly reflected in the electrochemical performance. Compared to cells with reference electrodes (manufactured by using the conventional *N*-methyl-2-pyrrolidone(NMP)-based process), the cells containing aqueous-processed electrodes with NCM-type cathode materials deliver a lower capacity. This was attributed to the loss of lithium and the degradation of the active materials in aqueous medium. The cycling performance of cells with water-based electrodes and the low-nickel NCM111 was found to be relatively comparable to NMP-variant cells. In contrast, the cells with water-based electrodes and the nickel-rich NCM cathode materials NCM622 and NCM811 degraded significantly faster than their reference cells. The situation was even exacerbated for cells with water-based NCA electrodes. These cells delivered only negligible capacity in the specified voltage range. Overall, NCA was identified as the most water-sensitive material from those tested, which is why further investigations focused on this cathode material.

Detailed clarification of the processes taking place when NCA is exposed to water

The processes that occur when NCA is exposed to water were clarified in detail using various analytical techniques (XRD, TG-MS, XPS, SEM/EDS). These can be summarized as the following:

1. Dissolution of surface impurities (e.g. Li_2CO_3) that are already present on the pristine NCA particles.
2. Continuous leaching of lithium and aluminum ions from the NCA active material structure and subsequent formation of species such as Li_2CO_3, LiOH and $LiAl_2(OH)_7 \cdot x\, H_2O$.
3. Continuous formation of surface species (e.g. nickel carbonate- and NiOOH-like species).

To investigate the impact of the water-induced surface species (see process 3.) on the electrochemical performance, cells with NMP-based electrodes containing pristine or water-exposed NCA particles were manufactured and evaluated with various electrochemical techniques (galvanostatic measurements, cyclic voltammetry, impedance spectroscopy). It was demonstrated that the water-induced surface species form a barrier layer that impedes the extraction of lithium ions from the active material structure when these cells are charged. This is reflected in a pronounced initial overvoltage in the first charge cycle. When the overvoltage is higher, more surface species have formed during the water exposure. Therefore, it can be concluded that if a critical amount of surface species is formed, the initial overvoltage cannot be overcome and the cells are electrochemically inactive. This phenomenon has been observed for cells with NCA electrodes manufactured via the water-based process. In addition to the initial overvoltage, a reduced initial discharge capacity was detected with increasing water exposure time due to the water-induced degradation of the active material particles. In the subsequent cycles, the capacity recovers at least partially via a reversed H^+-/Li^+-exchange mechanism. However, the complete regeneration cannot be achieved due to irreversible structure damage of NCA. Furthermore, side reactions involving the water-induced surface species lead to an accelerated cell degradation. To enable the successful aqueous processing of NCA, it is therefore essential to modify the surface of NCA with a protective coating.

Surface modification of NCA particles to prevent the direct contact with water

The newly-gained knowledge and previously established characterization techniques enabled the modification of the surface of NCA particles with a lithium phosphate coating in such a way that both the pH value in aqueous medium and the formation of water-induced surface species were reduced. In a comprehensive analysis it was demonstrated that the coating amount is the decisive factor and that a compromise has to be made in the case of a lithium phosphate coating. The particles should be as well-protected as possible during the aqueous electrode production, but sufficient electronic conductivity through the particle surface must also be guaranteed during cell operation. By optimizing the amount of lithium phosphate coating, cells with water-based NCA electrodes were able to be fabricated, which behaved electrochemically active and delivered a similar performance to that of cells with conventional NMP-based NCA electrodes. By transferring the laboratory-scale coating process to a continuous spray-drying process, a process suitable for industrial-scale production was successfully developed. In a final long-term cycling test, cells with graphite anodes and aqueous-processed NCA cathodes with an optimized amount of lithium phosphate coating showed an excellent electrochemical performance (80% capacity retention after 737 cycles at a C rate of 1C).

Outlook

The present work provides the basis for the further development of the water-based cathode manufacturing process. Here, one focus should be on the research of new coating materials, which provide an even more enhanced protection against water contact and at the same time have a positive effect on the performance of the battery.

With the increasing need to develop sustainable recycling processes for lithium-ion batteries, the water-based electrode manufacturing and the water sensitivity of cathode materials in general will move even more into the focus of future research. Many of the recycling processes that are currently being developed rely on water-based processes.[176,177] Therefore, it can be assumed that the recycling of aqueous processed electrodes becomes easier as the electrode material can be more quickly removed from the current collector due to the water-soluble binder ("design for recycling"). However, it can also be expected that water-sensitive cathode materials will be damaged by the contact with water during the recycling process. As a consequence, the resource-saving “direct recycling” process, where the recycled cathode material could be directly used in new batteries (after a regeneration step), would not be possible.[178,179] Instead, a costly chemical digestion and completely new synthesis of the cathode material would become necessary. It is therefore conceivable that the use of modified cathode materials could not only enable the implementation of an aqueous cathode manufacturing process, but also the direct use of the cathode material after a water-based recycling process. As such, a highly resource- and energy-efficient circular economy would be feasible (Figure 37):

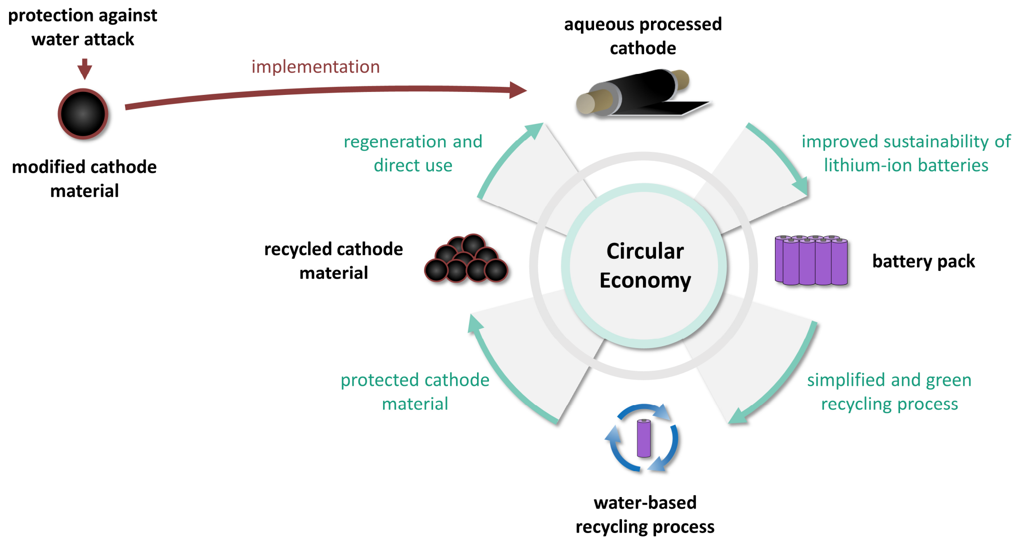

Figure 37: Illustration of a resource- and energy-efficient circular economy that could be enabled by the implementation of a modified cathode material.

4.2. Zusammenfassung und Ausblick (DE)

Zusammenfassung

Die Nachhaltigkeit zukünftiger Lithium-Ionen-Batterien kann durch die Implementierung eines wasserbasierten Herstellungsverfahrens für Kathoden verbessert werden. Die Wasserempfindlichkeit vieler Kathodenmaterialien stellt hierbei jedoch eine große Herausforderung dar.

Im Rahmen dieser Arbeit wurde ein Zusammenhang zwischen der Wasserempfindlichkeit von Kathodenmaterialien der Klasse der Schichtoxide und deren Elementzusammensetzung hergestellt. Insbesondere für das extrem wasserempfindliche Kathodenmaterial $LiNi_{0.8}Co_{0.15}Al_{0.05}O_2$ (NCA) wurden die im wässrigen Medium ablaufenden Prozesse detailliert aufgeklärt. Auf Basis dieser Erkenntnisse konnte die Oberfläche von NCA-Partikeln gezielt modifiziert und damit die Wasserempfindlichkeit reduziert werden. Infolgedessen konnte die elektrochemische Performance von Zellen mit wasserbasierten NCA-Kathoden signifikant verbessert und eine bemerkenswerte Langzeitperformance erzielt werden.

Die vorliegende Arbeit trägt somit zu einem tieferen Verständnis der Wasserempfindlichkeit von Kathodenmaterialien bei und liefert zugleich einen vielversprechenden Ansatz, um diese zu minimieren. So wird die erfolgreiche Realisierung der wässrigen Kathodenherstellung vorangetrieben.

Die wichtigsten Erkenntnisse dieser Arbeit werden im Folgenden noch einmal kurz zusammengefasst:

Zusammenhang zwischen Wasserempfindlichkeit und Elementzusammensetzung

Im Rahmen der Arbeit wurden verschiedene Kathodenmaterialien aus der Klasse der Schichtoxide ($LiNi_{0.33}Co_{0.33}Mn_{0.33}O_2$ (NCM111), $LiNi_{0.6}Co_{0.2}Mn_{0.2}O_2$ (NCM622), $LiNi_{0.8}Co_{0.1}Mn_{0.1}O_2$ (NCM811) und $LiNi_{0.8}Co_{0.15}Al_{0.05}O_2$ (NCA)) hinsichtlich ihrer Eignung für einen wasserbasierten Kathodenherstellungsprozess untersucht. Hierbei wurde gezeigt, dass ein direkter Zusammenhang zwischen Wasserempfindlichkeit und Elementzusammensetzung des Kathodenmaterials besteht: Kathodenmaterialien mit hohem Nickelanteil sind besonders empfindlich gegenüber Wasserkontakt. Dies spiegelte sich insbesondere in einer signifikanten Menge an ausgelaugten Lithium-Ionen (detektiert über ICP-OES) wider. Im Detail nahm die Lithium-Ionen-Konzentration in der Reihenfolge

NCM111 < NCM622 < NCM811 < NCA zu und korrelierte mit einem Anstieg des pH-Werts in den basischen Bereich. Letzterer Aspekt kann während des Elektroden-Herstellungsprozesses zur Korrosion des Stromableiters führen.

Während für NCM-Kathodenmaterialien bei Wasserkontakt nur Lithium-Ionen detektiert wurden, konnte für das Kathodenmaterial NCA zusätzlich Aluminiumauslaugung festgestellt werden. Neben Nickel-involvierten Lithiumverlust-Mechanismen wurden für NCA zusätzliche Aluminium-abhängige Lithiumverlust-Mechanismen im wässrigen Medium vorgeschlagen. Diese liefern eine Erklärung für die vergleichsweise hohe Lithiumauslaugung von NCA.

Die Auswirkungen von Wasserkontakt auf die Kathodenmaterialien spiegelten sich auch direkt in der elektrochemischen Performance wider. Im Vergleich zu Zellen mit Referenzelektroden (hergestellt über die konventionelle *N*-Methyl-2-pyrrolidon (NMP)-Route) wiesen die Zellen mit wässrig prozessierten Elektroden und NCM-Kathodenmaterialien eine geringere Kapazität auf. Dies wurde insbesondere auf den Lithiumverlust und die Degradation des Aktivmaterials in wässrigem Medium zurückgeführt. Die Zyklenleistung von Zellen mit wasserbasierten Elektroden und NCM111-Kathodenmaterial zeigte sich noch relativ vergleichbar mit der von Zellen und entsprechenden NMP-basierten NCM111-Elektroden. Im Gegensatz dazu degradierten die Zellen mit wasserbasiert hergestellten Elektroden und den nickelreichen NCM-Kathodenmaterialien NCM622 und NCM811 deutlich schneller als ihre Referenzzellen. Eine auffallend drastische Auswirkung des Wasserkontakts zeigte sich bei Zellen mit wässrig prozessierten NCA-Elektroden. Diese waren im vorgegebenen Spannungsbereich vollständig elektrochemisch inaktiv. Insgesamt stellte NCA somit das wasserempfindlichste Material dar, weshalb weitere Untersuchungen dieses Kathodenmaterial als Schwerpunkt hatten.

Detaillierte Aufklärung der Prozesse, die bei Kontakt von Wasser mit NCA auftreten

Die Vorgänge, die bei Kontakt von NCA mit Wasser auftreten, wurden mit verschiedenen Analysemethoden (XRD, TG-MS, XPS, REM/EDX) weiter aufgeklärt und lassen sich wie folgt zusammenfassen:

1. Lösen von Oberflächenverunreinigungen (z. B. Li_2CO_3), die sich bereits auf dem NCA-Ausgangsmaterial befinden.

2. Kontinuierliche Auslaugung von Lithium- und Aluminium-Ionen aus der NCA-Aktivmaterialstruktur und nachfolgende Bildung von Spezies wie z. B. Li_2CO_3, LiOH und $LiAl_2(OH)_7 \cdot x\ H_2O$.
3. Kontinuierliche Bildung von insbesondere nickelhaltigen Oberflächenspezies (u. a. Nickelcarbonat- und NiOOH-ähnliche Spezies).

Um den Einfluss der wasserinduzierten Oberflächenspezies (vgl. Prozess 3.) auf die elektrochemische Performance zu untersuchen, wurden Zellen mit NMP-basierten Elektroden, die unbehandelte bzw. wasserausgesetzte NCA-Partikel enthielten, hergestellt und mithilfe verschiedener Methoden (galvanostatisches Laden/Entladen, Cyclovoltammetrie, Impedanzspektroskopie) charakterisiert. Dabei stellte sich heraus, dass die wasserinduzierten Oberflächenspezies eine Barriere bilden, die die Extraktion der Lithium-Ionen aus der Aktivmaterialstruktur beim Laden der Zelle erschwert. Dies spiegelt sich in einer ausgeprägten anfänglichen Überspannung im ersten Ladezyklus wider. Die Überspannung ist umso höher, je mehr Oberflächenspezies sich während der Wasserexposition gebildet haben. Daraus konnte abgeleitet werden, dass, sobald eine kritische Menge an Oberflächenspezies vorliegt, die resultierende hohe Überspannung nicht mehr überwunden werden kann und sich entsprechende Zellen elektrochemisch inaktiv verhalten. Dieser Fall wurde bei Zellen mit NCA-Elektroden, die über ein wasserbasiertes Verfahren hergestellt wurden, beobachtet. Neben der anfänglichen Überspannung wurde mit zunehmender Wasserexpositionsdauer – aufgrund der wasserinduzierten Degradation der Aktivmaterialpartikel – eine verringerte Entladekapazität festgestellt. Die Kapazität kann allerdings zumindest teilweise in den ersten Lade-/Entladezyklen über einen H^+-/Li^+-Austausch zurückgewonnen werden. Eine vollständige Regeneration erfolgt jedoch aufgrund irreversibler struktureller Schäden von NCA nicht. Außerdem führen Nebenreaktionen, an denen die wasserinduzierten Oberflächenspezies beteiligt sind, zu einer beschleunigten Zelldegradation. Für die erfolgreiche wässrige Verarbeitung von NCA ist deshalb die Oberflächenmodifikation mit einer Schutzschicht essentiell.

Oberflächenmodifikation von NCA-Partikeln zum Schutz vor direktem Wasserkontakt

Durch die neu gewonnenen Erkenntnisse und zuvor etablierten Charakterisierungsmethoden war es möglich, die Oberfläche von NCA-Partikeln mit einer Lithiumphosphat-Beschichtung so zu modifizieren, dass sowohl der pH-Wert in wässrigem Medium als auch die Bildung der wasserinduzierten Oberflächenspezies verringert wurde. In einer umfassenden

Analyse zeigte sich, dass die Beschichtungsmenge entscheidend ist und im Falle einer Lithiumphosphat-Beschichtung ein Kompromiss eingegangen werden muss: Einerseits sollen die Partikel während der wässrigen Elektrodenherstellung möglichst gut geschützt sein, andererseits muss während des Zellbetriebs auch eine ausreichende elektronische Leitfähigkeit durch die Partikeloberfläche gewährleistet sein. Durch die Optimierung der Lithiumphosphat-Beschichtungsmenge konnten Zellen mit wasserbasierten NCA-Elektroden hergestellt werden, die sich elektrochemisch aktiv verhielten und eine ähnliche Performance wie Zellen mit konventionellen NMP-basierten NCA-Elektroden aufwiesen. Durch die Übertragung des Labormaßstab-Beschichtungsprozesses auf einen kontinuierlichen Sprühtrocknungs-Prozess, konnte zudem ein Prozess, der für die industrielle Produktion geeignet ist, entwickelt werden. In einem abschließenden Langzeittest zeigten Zellen mit Graphit-Anoden und wässrig hergestellte NCA-Kathoden mit optimierter Lithiumphosphat-Beschichtungsmenge eine exzellente elektrochemische Performance (80 % Kapazitätserhalt nach 737 Zyklen bei einer C-Rate von 1C).

Ausblick

Die vorliegende Arbeit liefert die Grundlage für die Weiterentwicklung des wasserbasierten Herstellungsprozesses für Kathoden. Ein Fokus sollte hierbei auf der Erforschung neuer Beschichtungsmaterialien liegen, welche die Aktivmaterialpartikel noch besser vor Wasserkontakt schützen und gleichzeitig die Performance der Batterie positiv beeinflussen.

Auch mit der zunehmenden Entwicklung des nachhaltigen Recyclings von Lithium-Ionen-Batterien wird in Zukunft die wässrige Elektrodenherstellung und die Wasserempfindlichkeit von Kathodenmaterialien per se noch weiter in den Fokus der Forschung rücken. Viele der in der Entwicklung befindlichen Recycling-Verfahren setzen auf wasserbasierte Prozesse.[176,177] Einerseits kann davon ausgegangen werden, dass das Recyceln von wässrig hergestellten Elektroden erleichtert ist, da sich das Elektrodenmaterial aufgrund des wasserlöslichen Bindemittels leichter vom Stromableiter lösen lässt („Design for Recycling“). Anderseits muss damit gerechnet werden, dass die Kathodenmaterialien während des Recycling-Prozesses durch den Wasserkontakt geschädigt werden. Dies kann dazu führen, dass das besonders ressourcenschonende „Direct Recycling“ Verfahren, welches auf den direkten Einsatz des recycelten Kathodenmaterials in neuen Batterien abzielt (nach einem Regenerationsschritt), nicht möglich ist.[178,179] Stattdessen wäre dann eine aufwendige

Aufbereitung und Neusynthese des Kathodenmaterials erforderlich. Es wäre deshalb denkbar, dass die Verwendung neuer, modifizierter Kathodenmaterialien nicht nur die Implementierung einer wässrigen Kathodenherstellung erlaubt, sondern auch den direkten Einsatz des Kathodenmaterials nach einem wasserbasierten Recycling-Prozess ermöglicht. So wäre eine besonders ressourcen- und energieeffiziente Kreislaufwirtschaft („Circular Economy“) realisierbar.

References

[1] European Commission, "Communication from the Commission to the European Parliament, the European Council, the Council, the European Economic and Social Committee and the Committee of the Regions. The European Green Deal", to be found under https://eur-lex.europa.eu/resource.html?uri=cellar:b828d165-1c22-11ea-8c1f-01aa75ed71a1.0002.02/DOC_1&format=PDF (accessed in January 2021).

[2] A. Malhotra, B. Battke, M. Beuse, A. Stephan, T. Schmidt, *Renew. Sustain. Energy Rev.* **2016**, *56*, 705–721.

[3] A. Thielmann, A. Sauer, M. Schnell, R. Isenmann, M. Wietschel, "Technologie-Roadmap Stationäre Energiespeicher 2030", to be found under https://www.isi.fraunhofer.de/content/dam/isi/dokumente/cct/lib/TRM-SES.pdf (accessed in January 2021).

[4] W. Chen, J. Liang, Z. Yang, G. Li, *Energy Procedia* **2019**, *158*, 4363–4368.

[5] Y. Liang et al., *InfoMat* **2019**, *1*, 6–32.

[6] NobelPrize.org, "Press release: The Nobel Prize in Chemistry 2019", to be found under https://www.nobelprize.org/prizes/chemistry/2019/press-release/ (accessed in November 2020).

[7] A. Manthiram, *Nat. Commun.* **2020**, *11*, 1550.

[8] Bloomberg News, "A million-mile battery from China could power your electric car", to be found under https://www.bloomberg.com/news/articles/2020-06-07/a-million-mile-battery-from-china-could-power-your-electric-car (accessed in January 2021).

[9] M. S. Whittingham, *J. Power Sources* **2020**, *473*, 228574.

[10] S. S. Sharma, A. Manthiram, *Energy Environ. Sci.* **2020**, *13*, 4087–4097.

[11] D. Bresser, D. Buchholz, A. Moretti, A. Varzi, S. Passerini, *Energy Environ. Sci.* **2018**, *11*, 3096–3127.

[12] D. L. Wood III, J. Li, C. Daniel, *J. Power Sources* **2015**, *275*, 234–242.

[13] M. Zackrisson, L. Avellán, J. Orlenius, *J. Clean. Prod.* **2010**, *18*, 1519–1529.

[14] H. Liu, X. Cheng, Y. Chong, H. Yuan, J.-Q. Huang, Q. Zhang, *Particuology* **2021**, *57*, 56–71.

[15] G. W. Nam, N.-Y. Park, K.-J. Park, J. Yang, J. Liu, C. S. Yoon, Y.-K. Sun, *ACS Energy Lett.* **2019**, *4*, 2995–3001.

[16] S.-T. Myung, F. Maglia, K.-J. Park, C. S. Yoon, P. Lamp, S.-J. Kim, Y.-K. Sun, *ACS Energy Lett.* **2017**, *2*, 196–223.

[17] a) R. Younesi, G. M. Veith, P. Johansson, K. Edström, T. Vegge, *Energy Environ. Sci.* **2015**, *8*, 1905–1922; b) D. Aurbach, Y. Talyosef, B. Markovsky, E. Markevich, E. Zinigrad, L. Asraf, J. S. Gnanaraj, H.-J. Kim, *Electrochim. Acta* **2004**, *50*, 247–254;

[18] A. A. Heidari, H. Mahdavi, *Chem. Rec.* **2020**, *20*, 570–595.

[19] Y. Yuan, K. Amine, J. Lu, R. Shahbazian-Yassar, *Nat. Commun.* **2017**, *8*, 3313.

[20] O. Ramström, "Lithium-ion batteries. Scientific Background on the Nobel Prize in Chemistry 2019", to be found under https://www.nobelprize.org/uploads/2019/10/advanced-chemistryprize2019.pdf (accessed in January 2021).

[21] J.-K. Park (Ed.) *Principles and applications of lithium secondary batteries*, Wiley-VCH, Weinheim, **2012**.

[22] A. J. Bard, G. Inzelt, F. Scholz (Eds.) *Electrochemical dictionary*, Springer-Verlag, Berlin, Heidelberg, **2008**.

[23] A. J. Bard, L. R. Faulkner, *Electrochemical methods*. *Fundamentals and applications,* 2nd ed., John Wiley & Sons, New York, **2001**.

[24] W. Vielstich, C. H. Hamann, *Elektrochemie,* 4th ed., Wiley-VCH Verlag, Weinheim, **2005**.

[25] D. Linden, T. B. Reddy (Eds.) *Handbook of batteries,* 3rd ed., McGraw-Hill, New York, **2002**.

[26] J. Xiao et al., *Nat. Energy* **2020**, *5*, 561–568.

[27] Y. Zhang, Q. Tang, Y. Zhang, J. Wang, U. Stimming, A. A. Lee, *Nat. Commun.* **2020**, *11*, 1706.

[28] R. Jung, M. Metzger, F. Maglia, C. Stinner, H. A. Gasteiger, *J. Electrochem. Soc.* **2017**, *164*, A1361-A1377.

[29] W. Lee, S. Muhammad, C. Sergey, H. Lee, J. Yoon, Y.-M. Kang, W.-S. Yoon, *Angew. Chem. Int. Ed.* **2020**, *59*, 2578–2605.

[30] P. Kurzweil, O. K. Dietlmeier, *Elektrochemische Speicher*. *Superkondensatoren, Batterien, Elektrolyse-Wasserstoff, Rechtliche Rahmenbedingungen,* 2nd ed., Springer Vieweg, Wiesbaden, **2018**.

[31] A. Rougier, P. Gravereau, C. Delmas, *J. Electrochem. Soc.* **1996**, *143*, 1168–1175.

[32] P. Kalyani, N. Kalaiselvi, N. G. Renganathan, *J. Power Sources* **2003**, *123*, 53–60.

[33] T. Ohzuku, A. Ueda, M. Nagayama, *J. Electrochem. Soc.* **1993**, *140*, 1862–1870.

[34] M. Broussely, F. Perton, P. Biensan, J. M. Bodet, J. Labat, A. Lecerf, C. Delmas, A. Rougier, J. P. Pérès, *J. Power Sources* **1995**, *54*, 109–114.

[35] W. Liu, P. Oh, X. Liu, M.-J. Lee, W. Cho, S. Chae, Y. Kim, J. Cho, *Angew. Chem. Int. Ed.* **2015**, *54*, 4440–4457.

[36] M. Bianchini, M. Roca-Ayats, P. Hartmann, T. Brezesinski, J. Janek, *Angew. Chem. Int. Ed.* **2019**, *58*, 10434–10458.

[37] J. Zheng, Y. Ye, T. Liu, Y. Xiao, C. Wang, F. Wang, F. Pan, *Acc. Chem. Res.* **2019**, *52*, 2201–2209.

[38] C. Delmas, J. P. Pérès, A. Rougier, A. Demourgues, F. Weill, A. Chadwick, M. Broussely, F. Perton, P. Biensan, P. Willmann, *J. Power Sources* **1997**, *68*, 120–125.

[39] R. Kanno, H. Kubo, Y. Kawamoto, T. Kamiyama, F. Izumi, Y. Takeda, M. Takano, *J. Solid State Chem.* **1994**, *110*, 216–225.

[40] K.-S. Park, S.-H. Park, Y.-K. Sun, K.-S. Nahm, Y.-S. Lee, M. Yoshio, *J. Appl. Electrochem.* **2002**, *32*, 1229–1233.

[41] C.-H. Lu, L. Wei-Cheng, *J. Mater. Chem.* **2000**, *10*, 1403–1407.

[42] E. McCalla, G. H. Carey, J. R. Dahn, *Solid State Ion.* **2012**, *219*, 11–19.

[43] M. Bianchini, F. Fauth, P. Hartmann, T. Brezesinski, J. Janek, *J. Mater. Chem. A* **2020**, *8*, 1808–1820.

[44] T. Sata, *Ceram. Int.* **1998**, *24*, 53–59.

[45] T. Hatsukade, A. Schiele, P. Hartmann, T. Brezesinski, J. Janek, *ACS Appl. Mater. Interfaces* **2018**, *10*, 38892–38899.

[46] C. S. Yoon, M.-J. Choi, D.-W. Jun, Q. Zhang, P. Kaghazchi, K.-H. Kim, Y.-K. Sun, *Chem. Mater.* **2018**, *30*, 1808–1814.

[47] C.-C. Chang, N. Scarr, P. N. Kumta, *Solid State Ion.* **1998**, *112*, 329–344.

[48] M. Y. Song, I. H. Kwon, H. R. Park, D. R. Mumm, *Ceram. Int.* **2012**, *38*, 2443–2448.

[49] X. Lai, D. Gao, J. Bi, Y. Li, P. Cheng, C. Xu, D. Lin, *J. Alloys Compd.* **2009**, *487*, L30-L32.

[50] H. Li, N. Zhang, J. Li, J. R. Dahn, *J. Electrochem. Soc.* **2018**, *165*, A2985-A2993.

[51] C. S. Yoon, D.-W. Jun, S.-T. Myung, Y.-K. Sun, *ACS Energy Lett.* **2017**, *2*, 1150–1155.

[52] U.-H. Kim et al., *Energy Environ. Sci.* **2018**, *11*, 1271–1279.

[53] L. de Biasi, A. Schiele, M. Roca-Ayats, G. Garcia, T. Brezesinski, P. Hartmann, J. Janek, *ChemSusChem* **2019**, *12*, 2240–2250.

[54] W. Li, J. N. Reimers, J. R. Dahn, *Solid State Ion.* **1993**, *67*, 123–130.

[55] Generalic Eni, "EniG. Periodic Table of the Elements. Crystal systems and Bravais lattices", to be found under https://www.periodni.com/crystal-systems-and-bravais-lattices.html (accessed in October 2021).

[56] A. van der Ven, G. Ceder, *J. Power Sources* **2001**, *97-98*, 529–531.

[57] A. van der Ven, G. Ceder, M. Asta, P. D. Tepesch, *Phys. Rev. B* **2001**, *64*, 184307.

[58] H. Li, M. Cormier, N. Zhang, J. Inglis, J. Li, J. R. Dahn, *J. Electrochem. Soc.* **2019**, *166*, A429-A439.

[59] F. P. McGrogan, S. R. Bishop, Y.-M. Chiang, K. J. van Vliet, *J. Electrochem. Soc.* **2017**, *164*, A3709-A3717.

[60] J. Li, J. Harlow, N. Stakheiko, N. Zhang, J. Paulsen, J. Dahn, *J. Electrochem. Soc.* **2018**, *165*, A2682-A2695.

[61] K. Dokko, M. Nishizawa, S. Horikoshi, T. Itoh, M. Mohamedi, I. Uchida, *Electrochem. Solid-State Lett.* **2000**, *3*, 125.

[62] J. R. Dahn, E. W. Fuller, M. Obrovac, U. von Sacken, *Solid State Ion.* **1994**, *69*, 265–270.

[63] X. Feng, M. Ouyang, X. Liu, L. Lu, Y. Xia, X. He, *Energy Storage Mater.* **2018**, *10*, 246–267.

[64] P. Kalyani, N. Kalaiselvi, *Sci. Technol. Adv. Mater.* **2005**, *6*, 689–703.

[65] T. Toma, R. Maezono, K. Hongo, *ACS Appl. Energy Mater.* **2020**, *3*, 4078–4087.

[66] H. S. Liu, Z. R. Zhang, Z. L. Gong, Y. Yang, *Electrochem. Solid-State Lett.* **2004**, *7*, A190-A193.

[67] S. Ahmed, M. Bianchini, A. Pokle, M. S. Munde, P. Hartmann, T. Brezesinski, A. Beyer, J. Janek, K. Volz, *Adv. Energy Mater.* **2020**, *10*, 2001026.

[68] J. Xu, F. Lin, D. Nordlund, E. J. Crumlin, F. Wang, J. Bai, M. M. Doeff, W. Tong, *Chem. Commun.* **2016**, *52*, 4239–4242.

[69] D. P. Abraham, R. D. Twesten, M. Balasubramanian, J. Kropf, D. Fischer, J. McBreen, I. Petrov, K. Amine, *J. Electrochem. Soc.* **2003**, *150*, A1450-A1456.

[70] S. Hwang, W. Chang, S. M. Kim, D. Su, D. H. Kim, J. Y. Lee, K. Y. Chung, E. A. Stach, *Chem. Mater.* **2014**, *26*, 1084–1092.

[71] S. Sallis et al., *Appl. Phys. Lett.* **2016**, *108*, 263902.

[72] E. Cho, S.-W. Seo, K. Min, *ACS Appl. Mater. Interfaces* **2017**, *9*, 33257–33266.

[73] N. Zhang, J. Li, H. Li, A. Liu, Q. Huang, L. Ma, Y. Li, J. R. Dahn, *Chem. Mater.* **2018**, *30*, 8852–8860.

[74] a) Y.-K. Sun, D.-J. Lee, Y. J. Lee, Z. Chen, S.-T. Myung, *ACS Appl. Mater. Interfaces* **2013**, *5*, 11434–11440; b) T. Ohzuku, A. Ueda, M. Kouguchi, *J. Electrochem. Soc.* **1995**, *142*, 4033–4039;

[75] A. Manthiram, B. Song, W. Li, *Energy Storage Mater.* **2017**, *6*, 125–139.

[76] a) A. Ueda, T. Ohzuku, *J. Electrochem. Soc.* **1994**, *141*, 2010–2014; b) A. Rougier, I. Saadoune, P. Gravereau, P. Willmann, C. Delmas, *Solid State Ion.* **1996**, *90*, 83–90; c) D. Caurant, N. Baffier, B. Garcia, J. P. Pereira-Ramos, *Solid State Ion.* **1996**, *91*, 45–54;

[77] Y. Jin, S. Xu, Z. Li, K. Xu, W. Ding, J. Song, H. Wang, J. Zhao, *J. Electrochem. Soc.* **2018**, *165*, A2267-A2273.

[78] M. Guilmard, L. Croguennec, D. Denux, C. Delmas, *Chem. Mater.* **2003**, *15*, 4476–4483.

[79] a) Y.-I. Jang, B. Huang, H. Wang, D. R. Sadoway, G. Ceder, Y.-M. Chiang, H. Liu, H. Tamura, *J. Electrochem. Soc.* **1999**, *146*, 862–868; b) Y.-I. Jang, B. Huang, H. Wang,

G. R. Maskaly, G. Ceder, D. R. Sadoway, Y.-M. Chiang, H. Liu, H. Tamura, *J. Power Sources* **1999**, *81-82*, 589–593;

[80] E. Rossen, C. D. W. Jones, J. R. Dahn, *Solid State Ion.* **1992**, *57*, 311–318.

[81] Y. Koyama, Y. Makimura, I. Tanaka, H. Adachi, T. Ohzuku, *J. Electrochem. Soc.* **2004**, *151*, A1499-A1506.

[82] D. Caurant, N. Baffler, V. Bianchi, G. Grégoire, S. Bach, *J. Mater. Chem.* **1996**, *6*, 1149–1155.

[83] H. Arai, S. Okada, Y. Sakurai, J.-i. Yamaki, *J. Electrochem. Soc.* **1997**, *144*, 3117–3125.

[84] J. Li, C. Daniel, D. Wood, *J. Power Sources* **2011**, *196*, 2452–2460.

[85] R. Korthauer (Ed.) *Handbuch Lithium-Ionen-Batterien,* 1st ed., Springer Vieweg, Berlin, Heidelberg, **2013**.

[86] M. Sterner, I. Stadler (Eds.) *Energiespeicher - Bedarf, Technologien, Integration,* 2nd ed., Springer Vieweg, Berlin, **2017**.

[87] a) H. Zheng, R. Yang, G. Liu, X. Song, V. S. Battaglia, *J. Phys. Chem. C* **2012**, *116*, 4875–4882; b) Y. Lee, *Energies* **2019**, *12*, 658;

[88] W. B. Hawley, J. Li, *J. Energy Storage* **2019**, *25*, 100862.

[89] M. Schmitt, P. Scharfer, W. Schabel, *J. Coat. Technol. Res.* **2014**, *11*, 57–63.

[90] D. L. Wood III, J. D. Quass, J. Li, S. Ahmed, D. Ventola, C. Daniel, *Dry. Technol.* **2017**, *36*, 234–244.

[91] J. Malm, "Inclusion of Substances of Very High Concern in the candidate List (Decision of the European Chemicals Agency)", to be found under https://echa.europa.eu/documents/10162/2d6cdfd7-e924-45fa-85d4-4450a7b4bf5a (accessed in May 2020).

[92] J.-C. Juncker, "Regulations. Commission Regulation (EU) 2018/588 of 18 April 2018 amending Annex XVII to Regulation (EC) No 1907/2006 of the European Parliament and of the Council concerning the Registration, Evaluation, Authorisation and Restriction of Chemicals (REACH) as regards 1-methyl-2-pyrrolidone", to be found under https://eur-lex.europa.eu/legal-content/EN/TXT/PDF/?uri=CELEX:32018R0588&from=DE (accessed in May 2020).

[93] A. Hunt, N. Dale, Economic valuation in 1-Methyl-2-pyrrolidone (NMP) regulation, *OECD Environment Working Papers* **2018**, *131*, OECD Publishing, Paris.

[94] J. Li et al., *JOM* **2017**, *69*, 1484–1496.

[95] N. Susarla, S. Ahmed, D. W. Dees, *J. Power Sources* **2018**, *378*, 660–670.

[96] Z. Wang, N. Dupré, A.-C. Gaillot, B. Lestriez, J.-F. Martin, L. Daniel, S. Patoux, D. Guyomard, *Electrochim. Acta* **2012**, *62*, 77–83.

[97] F. De Giorgio, N. Laszczynski, J. von Zamory, M. Mastragostino, C. Arbizzani, S. Passerini, *ChemSusChem* **2017**, *10*, 379–386.

[98] M. Sun, H. Zhong, S. Jiao, H. Shao, L. Zhang, *Electrochim. Acta* **2014**, *127*, 239–244.

[99] H. Zhong, J. He, L. Zhang, *Mater. Res. Bull.* **2017**, *93*, 194–200.

[100] A. F. Léonard, N. Job, *Mater. Today Energy* **2019**, *12*, 168–178.

[101] J. He, H. Zhong, J. Wang, L. Zhang, *J. Alloys Compd.* **2017**, *714*, 409–418.

[102] Z. Han, H. Zhan, Y. Zhou, *Mater. Lett.* **2014**, *114*, 48–51.

[103] Z. P. Cai, Y. Liang, W. S. Li, L. D. Xing, Y. H. Liao, *J. Power Sources* **2009**, *189*, 547–551.

[104] W. Porcher, P. Moreau, B. Lestriez, S. Jouanneau, F. Le Cras, D. Guyomard, *Ionics* **2008**, *14*, 583–587.

[105] a) L. Geng, S. B. Foley, H. Dong, G. M. Koenig, *Energy Technol.* **2019**, *7*, 1801116; b) A. Kvasha, I. Urdampilleta, I. de Meatza, M. Bengoechea, J. A. Blázquez, L. Yate, O. Miguel, H.-J. Grande, *Electrochim. Acta* **2016**, *215*, 238–246;

[106] W. Bauer, F. A. Çetinel, M. Müller, U. Kaufmann, *Electrochim. Acta* **2019**, *317*, 112–119.

[107] N. Loeffler, G.-T. Kim, F. Mueller, T. Diemant, J.-K. Kim, R. J. Behm, S. Passerini, *ChemSusChem* **2016**, *9*, 1112–1117.

[108] M. Wood, J. Li, R. E. Ruther, Z. Du, E. C. Self, H. M. Meyer III, C. Daniel, I. Belharouak, D. L. Wood III, *Energy Storage Mater.* **2020**, *24*, 188–197.

[109] I. Doberdò, N. Löffler, N. Laszczynski, D. Cericola, N. Penazzi, S. Bodoardo, G.-T. Kim, S. Passerini, *J. Power Sources* **2014**, *248*, 1000–1006.

[110] C.-C. Li, J.-T. Lee, Y.-L. Tung, C.-R. Yang, *J. Mater. Sci.* **2007**, *42*, 5773–5777.

[111] J. Paulsen, J. Kim, WO2012107313A1, **2012**.

[112] D. Pritzl, T. Teufl, A. T. S. Freiberg, B. Strehle, J. Sicklinger, H. Sommer, P. Hartmann, H. A. Gasteiger, *J. Electrochem. Soc.* **2019**, *166*, A4056-A4066.

[113] S. Jeong, J. Kim, J. Mun, *J. Electrochem. Soc.* **2018**, *166*, A5038-A5044.

[114] I. A. Shkrob, J. A. Gilbert, P. J. Phillips, R. Klie, R. T. Haasch, J. Bareño, D. P. Abraham, *J. Electrochem. Soc.* **2017**, *164*, A1489-A1498.

[115] H. Liu, Y. Yang, J. Zhang, *J. Power Sources* **2006**, *162*, 644–650.

[116] N. V. Faenza, L. Bruce, Z. W. Lebens-Higgins, I. Plitz, N. Pereira, L. F. J. Piper, G. G. Amatucci, *J. Electrochem. Soc.* **2017**, *164*, A3727-A3741.

[117] R. Jung, R. Morasch, P. Karayaylali, K. Phillips, F. Maglia, C. Stinner, Y. Shao-Horn, H. A. Gasteiger, *J. Electrochem. Soc.* **2018**, *165*, A132-A141.

[118] J. Sicklinger, M. Metzger, H. Beyer, D. Pritzl, H. A. Gasteiger, *J. Electrochem. Soc.* **2019**, *166*, A2322-A2335.

[119] L. Ibing, T. Gallasch, P. Schneider, P. Niehoff, A. Hintennach, M. Winter, F. M. Schappacher, *J. Power Sources* **2019**, *423*, 183–191.

[120] M. Kuenzel, H. Choi, F. Wu, A. Kazzazi, P. Axmann, M. Wohlfahrt-Mehrens, D. Bresser, S. Passerini, *ChemSusChem* **2020**, *13*, 2650–2660.

[121] N. Loeffler, J. von Zamory, N. Laszczynski, I. Doberdo, G.-T. Kim, S. Passerini, *J. Power Sources* **2014**, *248*, 915–922.

[122] M. Kuenzel, D. Bresser, G.-T. Kim, P. Axmann, M. Wohlfahrt-Mehrens, S. Passerini, *ACS Appl. Energy Mater.* **2020**, *3*, 218–230.

[123] M. Bichon, D. Sotta, N. Dupré, E. de Vito, A. Boulineau, W. Porcher, B. Lestriez, *ACS Appl. Mater. Interfaces* **2019**, *11*, 18331–18341.

[124] W. B. Hawley, A. Parejiya, Y. Bai, H. M. Meyer III, D. L. Wood III, J. Li, *J. Power Sources* **2020**, *466*, 228315.

[125] J.-H. Kuo, C.-C. Li, *J. Electrochem. Soc.* **2020**, *167*, 100504.

[126] M. Kuenzel, R. Porhiel, D. Bresser, J. Asenbauer, P. Axmann, M. Wohlfahrt-Mehrens, S. Passerini, *Batter. Supercaps* **2020**, *3*, 155–164.

[127] M. Memm, A. Hoffmann, M. Wohlfahrt-Mehrens, *Electrochim. Acta* **2018**, *260*, 664–673.

[128] N. Laszczynski, J. von Zamory, J. Kalhoff, N. Loeffler, V. S. K. Chakravadhanula, S. Passerini, *ChemElectroChem* **2015**, *2*, 1768–1773.

[129] a) N. Laszczynski, A. Birrozzi, K. Maranski, M. Copley, M. E. Schuster, S. Passerini, *J. Mater. Chem. A* **2016**, *4*, 17121–17128; b) K. Notake, T. Gunji, H. Kokubun, S. Kosemura, Y. Mochizuki, T. Tanabe, S. Kaneko, S. Ugawa, H. Lee, F. Matsumoto, *J. Appl. Electrochem.* **2016**, *46*, 267–278; c) Y. Liu et al., *J. Appl. Electrochem.* **2019**, *49*, 99–110; d) T. Tanabe et al., *Electrochim. Acta* **2017**, *224*, 429–438; e) T. Tanabe et al., *Electrochim. Acta* **2017**, *258*, 1348–1355;

[130] D. V. Carvalho, N. Loeffler, M. Hekmatfar, A. Moretti, G.-T. Kim, S. Passerini, *Electrochim. Acta* **2018**, *265*, 89–97.

[131] Z. Chen, G.-T. Kim, D. Chao, N. Loeffler, M. Copley, J. Lin, Z. Shen, S. Passerini, *J. Power Sources* **2017**, *372*, 180–187.

[132] A. Kazzazi, D. Bresser, A. Birrozzi, J. von Zamory, M. Hekmatfar, S. Passerini, *ACS Appl. Mater. Interfaces* **2018**, *10*, 17214–17222.

[133] M. Yapa Abeywardana, N. Laszczynski, M. Kuenzel, D. Bresser, S. Passerini, B. Lucht, *Int. J. Electrochem. Sci.* **2019**, *2019*, 1–7.

[134] M. Kuenzel, D. Bresser, T. Diemant, D. V. Carvalho, G.-T. Kim, R. J. Behm, S. Passerini, *ChemSusChem* **2018**, *11*, 562–573.

[135] K. Kimura, T. Sakamoto, T. Mukai, Y. Ikeuchi, N. Yamashita, K. Onishi, K. Asami, M. Yanagida, *J. Electrochem. Soc.* **2018**, *165*, A16-A20.

[136] K. Kimura, K. Onishi, T. Sakamoto, K. Asami, M. Yanagida, *J. Electrochem. Soc.* **2019**, *166*, A5313-A5317.

[137] T. Watanabe et al., *RSC Adv.* **2020**, *10*, 13642–13654.

[138] a) C. Fear, D. Juarez-Robles, J. A. Jeevarajan, P. P. Mukherjee, *J. Electrochem. Soc.* **2018**, *165*, A1639-A1647; b) R. Guo, L. Lu, M. Ouyang, X. Feng, *Sci. Rep.* **2016**, *6*, 30248; c) H.-F. Li, J.-K. Gao, S.-L. Zhang, *Chin. J. Chem.* **2008**, *26*, 1585–1588; d) D. Ren, X. Feng, L. Lu, X. He, M. Ouyang, *Appl. Energy* **2019**, *250*, 323–332;

[139] a) B. Arabsalmanabadi, N. Tashakor, A. Javadi, K. Al-Haddad, *IECON 2018 - 44th Annual Conference of the IEEE Industrial Electronics Society* **2018**, 5731–5738; b) H. Min, W. Sun, X. Li, D. Guo, Y. Yu, T. Zhu, Z. Zhao, *Energies* **2017**, *10*, 709;

[140] A. Tomaszewska et al., *eTransportation* **2019**, *1*, 100011.

[141] H. Baumgärtel, *Electrochemistry*. *A Guide for Newcomers,* 1st ed., De Gruyter, Berlin, **2019**.

[142] N. Elgrishi, K. J. Rountree, B. D. McCarthy, E. S. Rountree, T. T. Eisenhart, J. L. Dempsey, *J. Chem. Educ.* **2018**, *95*, 197–206.

[143] R. Raccichini, M. Amores, G. Hinds, *Batteries* **2019**, *5*, 12.

[144] W. R. Browne, *Electrochemistry*, Oxford University Press, New York, **2018**.

[145] X. Huang, Z. Wang, R. Knibbe, B. Luo, S. A. Ahad, D. Sun, L. Wang, *Energy Technol.* **2019**, *7*, 1801001.

[146] T. Kim, W. Choi, H.-C. Shin, J.-Y. Choi, J. M. Kim, M.-S. Park, W.-S. Yoon, *J. Electrochem. Sci. Technol.* **2020**, *11*, 14–25.

[147] W. Choi, H.-C. Shin, J. M. Kim, J.-Y. Choi, W.-S. Yoon, *J. Electrochem. Sci. Technol.* **2020**, *11*, 1–13.

[148] A. R. C. Bredar, A. L. Chown, A. R. Burton, B. H. Farnum, *ACS Appl. Energy Mater.* **2020**, *3*, 66–98.

[149] a) M. Urquidi-Macdonald, S. Real, D. D. Macdonald, *Electrochim. Acta* **1990**, *35*, 1559–1566; b) D. D. Macdonald, *J. Electrochem. Soc.* **1985**, *132*, 2316; c) B. A. Boukamp, *Solid State Ion.* **1993**, *62*, 131–141;

[150] M. Hofmann, M. Kapuschinski, U. Guntow, G. A. Giffin, *J. Electrochem. Soc.* **2020**, *167*, 140512.

[151] J. Lin, Z. Wen, X. Xu, N. Li, S. Song, *Fusion Eng. Des.* **2010**, *85*, 1162–1166.

[152] M. Nayak, T. R. N. Kutty, V. Jayaraman, G. Periaswamy, *J. Mater. Chem.* **1997**, *7*, 2131–2137.

[153] J. P. Thiel, C. K. Chiang, K. R. Poeppelmeier, *Chem. Mater.* **1993**, *5*, 297–304.

[154] Y.-M. Tzou, S.-L. Wang, L.-C. Hsu, R.-R. Chang, C. Lin, *Appl. Clay Sci.* **2007**, *37*, 107–114.

[155] S.-L. Wang, C.-H. Lin, Y.-Y. Yan, M. K. Wang, *Appl. Clay Sci.* **2013**, *72*, 191–195.

[156] A. V. Besserguenev, A. M. Fogg, R. J. Francis, S. J. Price, D. O'Hare, V. P. Isupov, B. P. Tolochko, *Chem. Mater.* **1997**, *9*, 241–247.

[157] S. J. Beckerman, R. B. Ford, M. T. Nemeth, *Powder Diffr.* **1996**, *11*, 312–317.

[158] J. Gao, S. Shi, R. Xiao, H. Li, *Solid State Ion.* **2016**, *286*, 122–134.

[159] M. Hofmann, M. Kapuschinski, U. Guntow, G. A. Giffin, *J. Electrochem. Soc.* **2020**, *167*, 140535.

[160] H. Beyer, S. Meini, N. Tsiouvaras, M. Piana, H. A. Gasteiger, *Phys. Chem. Chem. Phys.* **2013**, *15*, 11025–11037.

[161] S. Solchenbach, M. Metzger, M. Egawa, H. Beyer, H. A. Gasteiger, *J. Electrochem. Soc.* **2018**, *165*, A3022-A3028.

[162] Z.-F. Tang, R. Wu, P.-F. Huang, Q.-S. Wang, C.-H. Chen, *J. Alloys Compd.* **2017**, *693*, 1157–1163.

[163] a) D.-J. Lee, B. Scrosati, Y.-K. Sun, *J. Power Sources* **2011**, *196*, 7742–7746; b) S. Xia, F. Li, F. Chen, H. Guo, *J. Alloys Compd.* **2018**, *731*, 428–436; c) J. Chen et al., *Electrochim. Acta* **2019**, *312*, 179–187;

[164] A. K. Padhi, K. S. Nanjundaswamy, J. B. Goodenough, *J. Electrochem. Soc.* **1997**, *144*, 1188–1194.

[165] a) H. H. Yudar, S. Pat, Ş. Korkmaz, S. Özen, Z. Pat, *J. Mater. Sci.: Mater. Electron.* **2017**, *28*, 14499–14503; b) J. Kim, H. Cha, H. Lee, P. Oh, J. Cho, *Batter. Supercaps* **2020**, *3*, 309–322;

[166] X. Bian, Q. Fu, X. Bie, P. Yang, H. Qiu, Q. Pang, G. Chen, F. Du, Y. Wei, *Electrochim. Acta* **2015**, *174*, 875–884.

[167] M. Hofmann, F. Nagler, M. Kapuschinski, U. Guntow, G. A. Giffin, *ChemSusChem* **2020**, *13*, 5962–5971.

[168] Y. Li, F. Lai, X. Zhang, H. Wang, Z. Chen, X. He, Q. Li, *J. Taiwan Inst. Chem. Eng.* **2019**, *102*, 225–232.

[169] B. Li, Y. Yu, J. Zhao, *J. Power Sources* **2015**, *275*, 64–72.

[170] J. L. Shui, B. Lin, W. L. Liu, P. H. Yang, G. S. Jiang, C. H. Chen, *Mater. Sci. Eng. B* **2004**, *113*, 236–241.

[171] M. Hofmann, F. Nagler, U. Guntow, G. Sextl, G. A. Giffin, *J. Electrochem. Soc.* **2021**, *168*, 060511.

[172] N. Loeffler, G.-T. Kim, S. Passerini, C. Gutierrez, I. Cendoya, I. de Meatza, F. Alessandrini, G. B. Appetecchi, *ChemSusChem* **2017**, *10*, 3581–3587.

[173] L. Ibing, T. Gallasch, A. Friesen, P. Niehoff, A. Hintennach, M. Winter, M. Börner, *J. Power Sources* **2020**, *475*, 228608.

[174] M. Bichon, D. Sotta, E. de Vito, W. Porcher, B. Lestriez, *J. Power Sources* **2021**, *483*, 229097.

[175] W. B. Hawley, H. M. Meyer III, J. Li, *Electrochim. Acta* **2021**, *380*, 138203.

[176] A. Wolf et al., *Chem. Eng. Process.* **2021**, *160*, 108310.

[177] D. Horn, J. Zimmermann, R. Stauber, Gutfleisch O., "New efficient Recycling Process for Li-ion Batterie", to be found under https://mediatum.ub.tum.de/doc/1462984/1462984.pdf (acessed in February 2021).

[178] S. Sloop, L. Crandon, M. Allen, K. Koetje, L. Reed, L. Gaines, W. Sirisaksoontorn, M. Lerner, *Sustain. Mater. Techno.* **2020**, *25*, e00152.

[179] G. Harper et al., *Nature* **2019**, *575*, 75–86.

Abbreviations

Chemicals

CMC	Carboxymethyl cellulose
DEC	Diethyl carbonate
DMC	Dimethyl carbonate
EC	Ethylene carbonate
LCO	$LiCoO_2$
LFP	$LiFePO_4$
LMO	$LiMn_2O_4$
LNO	$LiNiO_2$
LiFSI	$LiN(SO_2F)_2$
LTO	$Li_4Ti_5O_{12}$
NCM111	$LiNi_{0.33}Co_{0.33}Mn_{0.33}O_2$
NCM622	$LiNi_{0.6}Co_{0.2}Mn_{0.2}O_2$
NCM811	$LiNi_{0.8}Co_{0.1}Mn_{0.1}O_2$
NCA	$LiNi_{0.8}Co_{0.15}Al_{0.05}O_2$
NMP	*N*-methyl-2-pyrrolidone
PAA	Polyacrylic acid
PVDF	Polyvinylidene fluoride
SBR	Styrene-butadiene rubber

Characterization techniques

ATR	Attenuated total reflectance
EDS	Energy-dispersive X-ray spectroscopy
EIS	Electrochemical impedance spectroscopy
FTIR	Fourier-transform infrared spectroscopy
ICP-OES	Inductively coupled plasma optical emission spectrometry
PEIS	Potentiostatic electrochemical impedance spectroscopy
SEM	Scanning electron microscope
TEM	Transmission electron microscope
TG-MS	Thermogravimetric analysis with coupled mass spectrometry
XRD	X-ray diffraction
XPS	X-ray photoelectron spectroscopy

Further abbreviations

CATL	Contemporary Amperex Technology
CC	Constant current
CE	Counter electrode
C. E.	Coulombic efficiency

CV	Constant voltage
DC	Direct current
DNEL	Derived no-effect level
EoL	End of life
EU	European Union
EV	Electric vehicle
fcc	Face centered cubic
H1	Hexagonal phase 1
H2	Hexagonal phase 2
H3	Hexagonal phase 3
HEV	Hybrid electric vehicle
LDHs	Layered double hydroxides
LIB	lithium-ion battery
M	Monoclinic phase
ODH	Oxygen dumbbell hop
PHEV	Plug-in hybrid electric vehicle
R	Rhombohedral
RE	Reference electrode
REACH	Regulation concerning the Registration, Evaluation, Authorization and Restriction of chemicals
SOC	State of charge
SVHC	Substances of very high concern
TSH	Tedrahedral site hop
WE	Working electrode

Symbols

a	Activity
C	Capacitor/capacitance
E	Equilibrium potential
E^0	Standard electrode potential
E_{anode}	Potential of the anode
$E_{cathode}$	Potential of the cathode
f	Frequency
F	Faraday constant
fcc	Face centered cubic
i	Current
i_a	Anodic current
i_c	Cathodic current
i(t)	Time-dependent current
i_m	Maximum current

L	Inductor/inductance
m	Mass
n	Number of moles
Q	Capacity
Q_{charge}	Charge capacity
Q_{CPE}	Constant phase element
$Q_{discharge}$	Charge capacity
Q_N	Capacity after N charge/discharge cycles
Q_p	Pratical capacity
Q_s	Specific capacity
Q_t	Theoretical capacity
R	Universal gas constant or resistor/resistance
T	Temperature
t	Time
v	Volume
V	Voltage
V_0	Equilibrium voltage
$V_{discharge}$	Discharge Voltage
V_m	Maximum voltage
V(t)	Time-dependent voltage
$\tilde{V}$	Mean voltage
W	Warburg impedance
z	Number of electrons
$Z(\omega)$	Impedance
Z`	Real part of the impedance
Z``	Imaginary part of the impedance
IZI	Magnitude of the impedance
Z_R	Impedance of a resistor
Z_C	Impedance of a capacitor
Z_L	Impedance of an inductor
ϕ	Phase angle
η	Overpotential
η_{con}	Concentration polarisation
η_{ct}	Charge transfer polarisation
η_{ohm}	Ohmic polarization
σ	Warburg coefficient
ω	Angular frequency

List of figures

List of tables

Acknowledgment

First of all, I would like to thank Prof. Dr. Gerhard Sextl for the supervision and assessment of my PhD thesis and the great opportunity to conduct this work in the professional and trustful atmosphere at the Fraunhofer Institute for Silicate Research.

Further, I would like to say thank you to Dr. Guinevere Giffin and Dr. Uwe Guntow. Your support and guidance throughout this time helped me to develop professionally as well as personally. Without your support, this work would not have been possible.

Moreover, I would like to thank all my colleagues at the Fraunhofer R&D center for electromobility Bavaria (FZEB) for the friendly working atmosphere, great collaboration, helpful discussions and technical support. I enjoyed working with every one of you. A special thanks goes here to Martina Kapuschinski, who instructed me in laboratory techniques right from the beginning, worked with me in several projects and always supported me throughout this time. At this point, I also would like to thank all my doctoral colleagues, Begüm Bozkaya, Philip Daubinger, Lukas Gold, Mara Göttlinger, Felix Nagler, Lukas Niklaus, Sven Macher, Matthias Rumpel, Mario Weller, Andreas Wolf and Paul Wulfert-Holzmann. Thank you for your support and the fun and fruitful discussions that we had.

Thank you goes also to my former students Alexander Buckel, Felix Nagler, Christian Piesold and Lukas Wald for their passionate work during their internships or time as research assistants. I hope you had as much fun working with me as I did with you. I wish you all the best for your future.

I want to express my gratitude to the Federal Ministry of Education and Research of Germany and the Bavarian Ministry of Economic Affairs and Media, Energy and Technology for funding the project NeW-Bat (grant no. 033R174A) and the Fraunhofer R&D Center for Electromobility Bavaria (grant no. 43-6629/86), respectively, and thus the creation of an environment in which my thesis could be developed successfully.

Furthermore, I would like to thank Doris Hanselmann, Johannes Prieschl and Dr. Benjamin Schug from the group of Particle Technology for technical support and scientific discussion regarding the coating of cathode materials. Additionally I would like to thank Sibylle Endres, Nadja Keidel, Richard Olsowski, Dr. Alexander Reinholdt, Angelika Schmitt and Werner

Stracke from the group of Applied Analytics for the measurements carried out and the joint discussions.

For encouraging words, scientific exchange or just having a coffee break together or sharing stories, I would like to thank Matteo Groß, Rainer Jahn, Matthias Klein, Caroline Kopittke, Katharina Lang, Katharina Lieberth, Nils Lindemann, Jochen Löblein, Jennifer Maxein and Andreas Räder.

Finally, my biggest thanks go to my love Yvonne and my family, who have always supported and motivated me. Thank you for being the way you are and for being part of my life.

Scientific contributions

Research articles

- M. Hofmann, M. Kapuschinski, U. Guntow, G. A. Giffin
  Implications of Aqueous Processing for High Energy Density Cathode Materials: Part I. Ni-Rich Layered Oxides
  J. Electrochem. Soc. **2020**, *167*, 140512.

- M. Hofmann, M. Kapuschinski, U. Guntow, G. A. Giffin
  Implications of Aqueous Processing for High Energy Density Cathode Materials: Part II. Water-Induced Surface Species on $LiNi_{0.8}Co_{0.15}Al_{0.05}O_2$
  J. Electrochem. Soc. **2020**, *167*, 140535.

- M. Hofmann, F. Nagler, M. Kapuschinski, U. Guntow, G. A. Giffin
  Surface Modification of $LiNi_{0.8}Co_{0.15}Al_{0.05}O_2$ *Particles via* Li_3PO_4 *Coating to Enable Aqueous Electrode Processing*
  ChemSusChem **2020**, *13*, 5962 – 5971.

- M. Hofmann, F. Nagler, U. Guntow, G. Sextl, G. A. Giffin
  Long-Term Cycling Performance of Aqueous Processed Ni-rich $LiNi_{0.8}Co_{0.15}Al_{0.05}O_2$ *Cathodes*
  J. Electrochem. Soc. **2021**, *168*, 060511.

Patents

- G. A. Giffin, M. Hofmann, M. Kapuschinski, U. Guntow, H. Chang, F. Nietfeld, T. Soczka-Guth
  Beschichtetes Elektrolytmaterial, Verfahren zu dessen Herstellung, sowie dessen Verwendung
  DE 10 2020 204 801, **2020**.

Talks

- M. Hofmann, F. Nagler, M. Kapuschinski, U. Guntow, G. A. Giffin
  Overcoming Obstacles of the Aqueous Processing of Ni-rich Layered Oxide Cathode Materials
  Korea Institute of Energy Research (KIER), Daejeon, South Korea, **18.10.2019**

Poster

- M. Hofmann, M. Kapuschinski, W. Stracke, U. Guntow, G. A. Giffin
  Synthesis and Characterization of $LiNi_xMn_{2-x}O_4$ *for Use in High-voltage Core-shell Cathode Materials*
  27th ATC 2018: Industrial Inorganic Chemistry – Materials and Processes, Frankfurt am Main, Germany, **22.02.2018 – 23.02.2018**
- M. Hofmann, U. Guntow, G. A. Giffin
  Implications of Aqueous Processing for High Energy-density Cathode Materials
  Kraftwerk Batterie – Advanced Battery Development for Automotive and Utility Applications and their Electric Power Grid Integration, Münster, Germany, **10.04.2018 – 11.04.2018**
- M. Hofmann, C. Piesold, A. Buckel, M. Kapuschinski, U. Guntow, G. A. Giffin
  Overcoming Obstacles in the Aqueous Processing of High Energy-density Cathode Materials
  Kraftwerk Batterie/Advanced Battery Power, Aachen, Germany, **03.04.2019 – 04.04.2019**
- M. Hofmann, F. Nagler, M. Kapuschinski, U. Guntow, G. A. Giffin
  Overcoming obstacles in the aqueous electrode processing of Ni-rich Layered-Oxide Cathode Materials
  SwissBatteryDays, Online Conference, **15.02.2021 – 17.02.2021**

Appendixes

I. Manuscripts

a. M. Hofmann, M. Kapuschinski, U. Guntow, G. A. Giffin, Implications of Aqueous Processing for High Energy Density Cathode Materials: Part I. Ni-Rich Layered Oxides. *J. Electrochem. Soc.* **2020**, *167*, 140512.

b. M. Hofmann, M. Kapuschinski, U. Guntow, G. A. Giffin, Implications of Aqueous Processing for High Energy Density Cathode Materials: Part II. Water-Induced Surface Species on $LiNi_{0.8}Co_{0.15}Al_{0.05}O_2$. *J. Electrochem. Soc.* **2020**, *167*, 140535.

c. M. Hofmann, F. Nagler, M. Kapuschinski, U. Guntow, G. A. Giffin, Surface Modification of $LiNi_{0.8}Co_{0.15}Al_{0.05}O_2$ Particles via Li_3PO_4 Coating to Enable Aqueous Electrode Processing. *ChemSusChem* **2020**, *13*, 5962 – 5971.

d. M. Hofmann, F. Nagler, U. Guntow, G. Sextl, G. A. Giffin, Long-Term Cycling Performance of Aqueous Processed Ni-rich $LiNi_{0.8}Co_{0.15}Al_{0.05}O_2$ Cathodes. *J. Electrochem. Soc.* **2021**, *168*, 060511.

II. Individual contributions to the manuscripts

Appendixes

I. Manuscripts

a. M. Hofmann, M. Kapuschinski, U. Guntow, G. A. Giffin, Implications of Aqueous Processing for High Energy Density Cathode Materials: Part I. Ni-Rich Layered Oxides. *J. Electrochem. Soc.* **2020**, *167*, 140512.

b. M. Hofmann, M. Kapuschinski, U. Guntow, G. A. Giffin, Implications of Aqueous Processing for High Energy Density Cathode Materials: Part II. Water-Induced Surface Species on $LiNi_{0.8}Co_{0.15}Al_{0.05}O_2$. *J. Electrochem. Soc.* **2020**, *167*, 140535.

c. M. Hofmann, F. Nagler, M. Kapuschinski, U. Guntow, G. A. Giffin, Surface Modification of $LiNi_{0.8}Co_{0.15}Al_{0.05}O_2$ Particles via Li_3PO_4 Coating to Enable Aqueous Electrode Processing. *ChemSusChem* **2020**, *13*, 5962 – 5971.

d. M. Hofmann, F. Nagler, U. Guntow, G. Sextl, G. A. Giffin, Long-Term Cycling Performance of Aqueous Processed Ni-rich $LiNi_{0.8}Co_{0.15}Al_{0.05}O_2$ Cathodes. *J. Electrochem. Soc.* **2021**, *168*, 060511.

Journal of The Electrochemical Society, 2020 **167** 140512

Implications of Aqueous Processing for High Energy Density Cathode Materials: Part I. Ni-Rich Layered Oxides

Michael Hofmann, Martina Kapuschinski, Uwe Guntow, and Guinevere A. Giffin[z]

Fraunhofer R&D Center Electromobility, Fraunhofer Institute for Silicate Research ISC, 97082 Wuerzburg, Germany

Combining the use of nickel-rich layered oxide cathode materials with the implementation of aqueous electrode processing can pave the way to cost-reduced and environmentally friendly electrodes and simultaneously increase the energy density of cells. Herein, $LiNi_{0.33}Co_{0.33}Mn_{0.33}O_2$ (NCM111), $LiNi_{0.6}Co_{0.2}Mn_{0.2}O_2$ (NCM622), $LiNi_{0.8}Co_{0.1}Mn_{0.1}O_2$ (NCM811) and $LiNi_{0.8}Co_{0.15}Al_{0.05}O_2$ (NCA) were evaluated in terms of their response to aqueous processing under the same conditions to facilitate a direct comparison. The results illustrate that mainly nickel driven processes lead to lithium leaching which is combined with the increase of the pH value in the alkaline region. For NCA an additional aluminum-involving lithium leaching mechanism is assumed, which could explain the highest amount of leached lithium and the additional detection of aluminum. Electrochemical tests show a reduced capacity for cells containing water-based electrodes compared to reference cells for the NCM-type materials which increases during the first cycles indicating a reversible Li^+/H^+-exchange mechanism. In contrast, the NCA cells were completely electrochemically inactive making NCA the most water sensitive material tested in this report. By comparing the cycling performance of cells containing aqueous processed electrodes, a more pronounced capacity fade for nickel-rich cathode materials as compared to their reference cells can be observed.

[DOI: 10.1149/1945-7111/abc033]

Manuscript submitted September 1, 2020; revised manuscript received September 29, 2020. Published October 21, 2020.

Supplementary material for this article is available online

The further development of electric and hybrid-electric vehicles (EVs, HEVs) is a decisive step towards sustainable mobility in an effort to drastically reduce emissions of greenhouse gases and other pollutants. For electromobility, lithium-ion batteries (LIBs) are considered to be, as of yet, the most promising battery technology, as they have a relatively high energy density.[1] However, improvements still need to be made in terms of safety, costs and environmentally friendly manufacturing of LIBs to meet consumer and industrial demands. One way to address both the cost and environmental impact of LIB production is to implement aqueous processing of high energy density cathode materials during electrode fabrication. This would facilitate the substitution of conventional, poorly recyclable, fluorinated binders like polyvinylidene fluoride (PVDF) and the volatile and carcinogenic organic solvent N-methyl-2-pyrrolidone (NMP) with a suitable water-soluble binder and water as a solvent to lower the costs and implement greener manufacturing.[2] One viable aqueous binder is the sodium salt of carboxymethylcellulose (CMC) which exhibits an excellent electrochemical stability and is already used in the production of state-of-the-art graphite anodes.[3–5] Water-based electrode manufacturing for the cathode materials remains troublesome, as the dispersing of the active material in water has specific drawbacks, like lithium leaching from the cathode structure, surface degradation, deposition of surface impurities and an increase in pH of the electrode slurry, which can lead to the corrosion of the aluminum current collector.[6–12]

Layered oxide cathode materials like $Li(Ni,Co,Mn)O_2$ (NCM) and $Li(Ni,Co,Al)O_2$ (NCA) are currently considered to be the material of choice for EVs and HEVs.[13] Materials with a high nickel and low cobalt content have the advantage of relatively low manufacturing costs accompanied with a high theoretical capacity and operation voltage.[13–15] Aqueous processing has been investigated for a variety of different layered oxides such as NCM111,[3,5–7,9,10,16–27] NCM424,[28] NCM523,[25,29–35] NCM622,[25,27] NCM811,[12,25,36–38] Li-/Mn-rich NCM[39–44] and NCA.[6,7,33,45–49] However, it is often difficult to compare the materials in terms of their processibility in an aqueous environment due to different treatment parameters. Therefore, in this study, different commercially available layered oxides are evaluated in terms of their use in aqueous electrode processing. These materials were compared in terms of water-induced metal leaching and time dependent pH evolution. Furthermore, the electrochemical performance of CMC-based electrodes with conventional NMP/PVDF-based was compared.

Experimental

Cathode materials.—Commercial $LiNi_{0.33}Co_{0.33}Mn_{0.33}O_2$ (NCM111, BASF), $LiNi_{0.6}Co_{0.2}Mn_{0.2}O_2$ (NCM622, MSE-Supplies), $LiNi_{0.8}Co_{0.1}Mn_{0.1}O_2$ (NCM811, MSE-Supplies) and $LiNi_{0.8}Co_{0.15}Al_{0.05}O_2$ (NCA, NAT-1050, TODA) were stored under inert atmosphere in a glovebox and used without any further modification.

Active material/water-suspensions.—The different active materials were added to deionized water (25 °C ± 2 °C; mass ratio active material:water = 0.33:1 = 15 g:45 g) and stirred continuously in a polypropylene bottle for two hours. The suspensions were subsequently filtered for the filtrate analysis. An additional sample of each active material was prepared according to the above-mentioned conditions but was additionally stored for a further week in water after the mixing procedure.

Electrode processing.—For the preparation of CMC-based electrodes, sodium carboxymethyl cellulose (Sigma-Aldrich, average Mw ~250,000, degree of substitution 0.9) was first dissolved in deionized water. The required amount of active material and conductive carbon (Imerys, Super C65) was added and the slurry was homogenized in a speedmixer (Hauschild GmbH & Co KG). The ratio of active material, conductive carbon and binder was adjusted to be 90:7:3. The slurries were casted on aluminum by the doctor-blade technique. The coated electrodes were immediately pre-dried at 80 °C for 30 min. Particular care was taken to ensure that the process time was the same for all materials. The pre-dried electrodes were calandered to 50% of initial electrode thickness to increase electrode density for cell assembly. Disc electrodes (16 mm in diameter) were immediately punched out of the electrode sheets and further dried under vacuum at 110 °C for 10 h. The mass loading of the electrodes was 12 ± 2 mg cm^{-2}.

For the sake of comparison, PVDF-based electrodes were prepared with the same active material/conductive carbon/binder ratio. PVDF (Solvay, Solef® 5130) was first dissolved in N-methyl-2-pyrrolidone (Sigma-Aldrich) overnight. The required amount of

---

[z] E-mail: guinevere.giffin@isc.fraunhofer.de

active material and conductive carbon (Imerys, Super C65) was added and the slurry was homogenized in a speedmixer (Hauschild GmbH & Co KG). The slurries were casted on aluminum by the doctor-blade technique. The coated electrodes were stored in a fume hood overnight and then pre-dried under vacuum at 80 °C for 2 h. The dried electrodes were calandered to 50% of initial electrode thickness. Disc electrodes (16 mm in diameter) were punched out of the electrode sheets and further dried under vacuum at 80 °C for 5 h.

Cell assembly and electrochemical measurements.—Cathode half-cells were prepared in a pouch bag configuration with metallic lithium (Sigma-Aldrich) on copper foil as counter electrode. Aluminum tabs (Targray) were used to connect the cathode electrodes, while copper-nickel tabs (Targray) were used for the lithium electrode. A single layer polyethylene membrane (Celgard, 2500) was utilized as the separator. For all cells, 1 mol l^{-1} LiPF$_6$ in EC:DMC 1:1 wt/wt (BASF, LP30) was used as the electrolyte. All pouch cells were assembled in an argon-filled glove box (MBraun). Three cells were built for each combination and the error bars in the figures represent the standard deviation.

The cells were cycled in a climate chamber (Memmert) at 25 °C with a battery cycler (Maccor, Series 4000). All cells were cycled with a lower cutoff of 3.0 V and an upper cutoff of 4.3 V. The charge was done in constant current-constant voltage (CCCV) mode with a current limitation in the CV-step of C/20, while the discharge was done in constant current (CC) mode. Prior to cycling, the cell formation was done with 5 cycles at C/10 relating to a current of 15.5 mA g^{-1} (NCM111), 17.8 mA g^{-1} (NCM622), 20.0 mA g^{-1} (NCM811) and 20.0 mA g^{-1} (NCA) in the voltage range between 3.0 V−4.3 V. The charge and the discharge were done in constant current (CC) mode. The capacity obtained from the last formation cycle was used to calculate the current for the C-rates of the cycling experiment. Cyclic voltammetry tests were carried out at a scanning rate of 0.05 mV s^{-1} between 2.7 V and 4.5 V in a climate chamber (Memmert) at 25 °C on a VMP300 galvanostat/potentiostat (BioLogic) starting at the open circuit voltage. The cell setup was the same as described above except that a lithium reference electrode was included in the pouch cell. Electrochemical impedance spectroscopy (EIS) analysis was carried out on the same workstation by applying an AC voltage amplitude of 5 mV over the frequency range from 1 MHz to 10 mHz.

Characterization methods.—ICP-OES analysis of the filtrate was conducted by using a Vista-Pro (Varian) spectrometer. The detection limits for lithium, manganese, aluminum, cobalt and nickel were 0.006 mg l^{-1}, 0.001 mg l^{-1}, 0.004 mg l^{-1}, 0.002 mg l^{-1} and 0.002 mg l^{-1}, respectively. pH measurements were carried out with a pH meter (WTW, pH 315i) using an electrode designed for the high alkaline range (WTW, SenTix®H) at a temperature of 25 ± 2 °C. The pH evolution was monitored during the entire stirring period. A further pH value was measured after the suspension had been stored for one additional week.

Results and Discussion

The metal ion concentrations in the filtrate of the aqueous cathode material suspensions after different water exposure durations were determined by means of ICP-OES. The comparison of the lithium leaching from the active materials after a water exposure time of two hours shows that the lithium content increases in the order NCM111 < NCM622 < NCM811 < NCA (Fig. 1a). NCA thus has, comparatively, the largest lithium loss. After one week the lithium content in the filtrate increases for all cathode materials. While the lithium content increase for NCM111 is only 25.6 mg l^{-1}, it is significantly higher for NCM622 (148.5 mg l^{-1}), NCM811 (356.4 mg l^{-1}) and NCA (566.9 mg l^{-1}).

The exact origin of the detected lithium is somewhat uncertain and might be a combination of different effects. Some of the literature reports about residual lithium compounds, such as lithium hydroxide or lithium carbonate, on the cathode surface stemming from unreacted precursors of the production process, while others suggest the formation of lithium surface species through the reaction of active oxygen species on the oxide surface with water and CO$_2$ molecules combined with the reduction of Ni^{3+} to Ni^{2+}.[50–52] Another explanation is a Li$^+$/H$^+$-exchange mechanism in the aqueous medium and concomitant formation of lithium hydroxide or lithium carbonate if CO$_2$ is accessible.[53] The latter mechanism should simultaneously lead to the partial formation of species such as NiOOH or CoOOH as recently reported for LiNiO$_2$,[54] LiNi$_{0.85}$Co$_{0.1}$Mn$_{0.05}$[11] and LiCoO$_2$.[55] By directly comparing NCM111, NCM622 and NCM811 with the same processing conditions, a clear trend for a higher leached lithium content with increased nickel content can be observed. These results are consistent with those of Wood et al. who investigated the time-dependent leaching behavior of different NCM-type cathode materials in aqueous media with different initial pH values, supporting the thesis of at least partial occurrence of one or both of the latter two mechanisms.[25] However, despite the same nickel content for NCM811 (LiNi$_{0.8}$Co$_{0.1}$Mn$_{0.1}$O$_2$) and NCA (LiNi$_{0.8}$Co$_{0.15}$Al$_{0.05}$O$_2$), NCA shows increased lithium leaching. Although NCA has a higher cobalt content than NCM811, cobalt-induced lithium leaching as a main driving force may be excluded since NCM111 (LiNi$_{0.33}$Co$_{0.33}$Mn$_{0.33}$O$_2$) has the highest cobalt content but shows the lowest lithium leaching. The most significant difference of NCM- and NCA-type materials is the presence of manganese or aluminum, respectively. Neither nickel nor cobalt ions could be detected in any of the filtrates (Table I). Although manganese ions could not be detected in the filtrate of the NCM-type

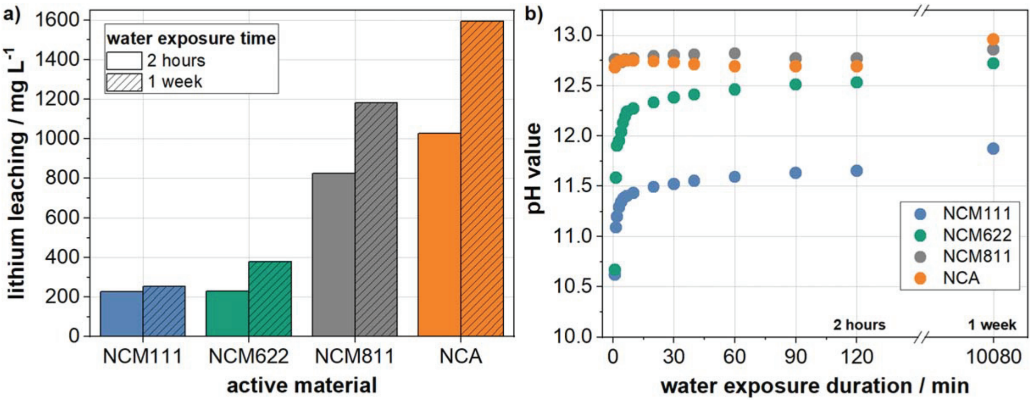

Figure 1. ICP-OES analysis of the lithium content in water after different water exposure times of the cathode materials (a) and time dependent pH evolution of the aqueous cathode material suspensions (b).

Table I. Metal ion concentration detected in the filtrate of active material/water suspensions after 2 h and 1 week water exposure.

Active material	water exposure	Li/mg l^{-1}	Ni/mg l^{-1}	Co/mg l^{-1}	Mn/mg l^{-1}	Al/mg l^{-1}
NCM111	2h	228.2	<0.002	<0.002	<0.001	N/A
	1w	253.8	<0.002	<0.002	<0.001	N/A
NCM622	2h	230.5	<0.002	<0.002	<0.001	N/A
	1w	379.0	<0.002	<0.002	<0.001	N/A
NCM811	2h	825.4	<0.002	<0.002	<0.001	N/A
	1w	1181.8	<0.002	<0.002	<0.001	N/A
NCA	2h	1027.3	<0.002	<0.002	N/A	192.3
	1w	1594.2	<0.002	<0.002	N/A	52.3

materials, aluminum was detected in the filtrate of the NCA suspensions. Recently, Hawley et al. also detected a significant amount of aluminum ions in the filtrate of NCA/water suspensions, while the amount of cobalt and nickel ions was small.[33] However, these observations were not discussed in detail. $LiAlO_2$, which may be considered as a type of substructure of NCA, can easily react with moisture. Beckerman et al. proposed a mechanism according to Eq. 1.[56]

$$4\ LiAlO_2 + 9\ H_2O + 2\ CO_2 \rightarrow Li_2Al_4(CO_3)(OH)_{12} \cdot 3H_2O + Li_2CO_3 \qquad [1]$$

The formation of $Li_2Al_4(CO_3)(OH)_{12} \cdot 3H_2O$ was also confirmed by Gao et al., who investigated, among others, the stability of α- and γ-$LiAlO_2$ with water.[57] Lin et al. proposed a reaction, where in the first step, the surface of $LiAlO_2$ reacts with water according to Eq. 2 forming AlO(OH), which can react in a second step to $LiAl_2(OH)_7 \cdot xH_2O$ (Eq. 3).[58]

$$LiAlO_2 + H_2O \rightarrow AlO(OH) + LiOH \qquad [2]$$

$$AlO(OH) + (2 + x)H_2O + LiOH \rightarrow LiAl_2(OH)_7 \cdot xH_2O \qquad [3]$$

Assuming that similar processes can occur for NCA upon water contact (in addition to nickel-driven lithium leaching reactions), this might explain the comparatively higher lithium leaching, as well as the detection of aluminum in the filtrate. Moreover, Al–O/Li–Al–O species were already found on the surface of NCA particles by Lebens-Higgins et al. albeit a different experimental context.[59] They investigated the surface of NCA using hard X-ray photoelectron spectroscopy methods and reported that this kind of species can be found on NCA from cells held at a potential of 3.6 V. When holding the potential at 4.5 V or higher they found that the amounts of Al–O/Li–Al–O species increased. However, it remains unclear why a higher content of aluminum can be detected in the filtrate after two hours water exposure than after one week. One possible explanation might be that with increasing time more insoluble aluminum species are formed on the NCA surface rather than dissolving into the filtrate. Further studies are necessary for clarification of this point. Overall, if the lithium that was detected in the filtrate comes not only from unreacted starting materials, but also from the active material itself, this should be reflected in reduced capacity in electrochemical tests. Moreover, since aluminum-doping is used to stabilize the NCA structure,[60] the loss of aluminum might lead at least partially to surface structure instability.

The evolution of the pH value over time in the aqueous cathode material suspensions was investigated (Fig. 1b). As soon as the active materials are in contact with water, a sharp increase in the pH into the alkaline range can be observed. The highest pH value is observed in the NCA and NCM811 suspensions, followed by NCM622 and NCM111. After about 60 min of water exposure, the pH values approach a limit that seems to be specific for each cathode material. A further, albeit minor, increase in the pH can be observed for all materials (highest for NCA) after one week of water contact. The hypothesis that a pH threshold value is reached would be consistent with the establishment of an equilibrium between Li^+ and H^+ ions on the cathode material surface. In Table II, the pH value after different immersion times (5 min, 30 min, 1 h, 2 h and 1 week) is displayed along with values reported in the literature. It should be taken into account that a direct comparison is difficult, since different treatment conditions can have a major impact on the results.[25] However, the trend shows a rising pH value with increasing nickel content which is consistent with the results of the lithium leaching presented above. A distinct difference of the pH values for NCA and NCM811 cannot be established from the overview, but this might be explained by the different treatment conditions.

To investigate the impact of the water exposure on the electrochemical performance, all of the active materials were handled with an aqueous electrode process and tested in half cells in a pouch bag configuration. Since the previous results presented here demonstrate that variation of water exposure time leads to significantly different results, particular care was taken to ensure that the process time was the same for all materials. Since Bauer et al. have shown that the active materials are most stable at their native pH, no acids were added to the slurry to adjust the pH value.[9] Therefore, some extent of aluminum corrosion is likely and should be noted. Nonetheless, cells with electrodes made without any pH modifier, from the work from Bauer et al. actually showed the most stable long-term performance.[9] For the sake of comparison, PVDF-based electrodes were prepared and investigated. Prior to a cycling test, a formation protocol consisting of five charge-/discharge-cycles with a comparable specific current (rate of C/10) for each active material was applied. The discharge capacity and coulombic efficiency can be found in Fig. 2. The initial average discharge capacity of the cells containing the NMP-based electrodes is 157.8 mAh g^{-1}, 176.8 mAh g^{-1}, 191.6 mAh g^{-1} and 194.4 mAh g^{-1} for NCM111, NCM622, NCM811 and NCA, respectively. These results are quite close to the expected values of ~155 mAh g^{-1} (NCM111), ~178 mAh g^{-1} (NCM622), ~200 mAh g^{-1} (NCM811) and ~200 mAh g^{-1} (NCA) from literature, confirming a good quality of the active materials and electrodes.[61–63] For the cells containing the aqueous processed NCM111-, NCM622- and NCM811-electrodes, the initial average discharge capacity is slightly reduced to 152.9 mAh g^{-1}, 168.8 mAh g^{-1} and 188.8 mAh g^{-1}, respectively. The reduced capacity at low current density indicates that the amount of lithium leached during water exposure originates, at least partially, from electrochemically active lithium from the active material structure. The observation of a lower initial discharge capacity of cells with H_2O/CMC-electrodes as compared to cells with NMP/PVDF-electrodes is in accordance with the previous literature. For NCM111, Memm et al. reported a specific discharge capacity of 152 mAh g^{-1} and 140 mAh g^{-1} for the PVDF- and CMC-based electrodes at 0.2 C, respectively.[17] Similar results for NCM111 can be found at Zhong et al.,[20] Soeda et al.,[23] Doberdó et al.[3] and Xu et al..[24] For NCM622[27] and NCM811[25] analogous results can be found. In contrast cells built with a CMC-based NCA-electrode show a negligible discharge capacity. This is kind of surprising since NCM811 and NCA have the same nickel content and leads to the conclusion that although the

Table II. pH values obtained for active material/water suspensions obtained after 5 min, 30 min, 1 h, 2 h and 1 week water exposure as well as several pH values reported in the literature.

Active material	pH after 5 min	pH after 30 min	pH after 1 h	pH after 2 h	pH after 1 week	Literature
NCM111	11.4	11.5	11.6	11.7	11.9	11.2,[32] a) 11.7,[6] b) 11.5,[10] * c) 11.5,[9] d) 12.2[25] * e) 10.5[23] f)
NCM622	12.1	12.4	12.5	12.5	12.7	12.1,[32] a) 12.0,[27] g) 12.7[25] * e)
NCM811	12.7	12.8	12.8	12.8	12.9	12.4,[80] h) 12.9[25] * e)
NCA	12.8	12.7	12.7	12.7	13.0	12.3,[48] i) 13.1,[6] b) 12.6,[66] * j) 12.5,[32] a) 12.5[33] * k)

*The value was determined from graphical data presented in the associated literature. This might lead to some variation from the actual value. a) suspension, 0.1:1 (active material:water ratio by weight), 60 min (time of recording). b) slurry, 5:1, N/A. c) suspension, 0.4:1, 100 min. d) slurry, N/A, 10 min. e) suspension, 2.33:1, 1 week. f) suspension, 0.02:1, N/A. g) suspension, 0.025:1, 60 min. h) suspension, 0.1:1, 25 min. i) suspension, N/A, N/A. j) suspension, 0.4:1, 40 min. k) suspension, N/A, 75 min.

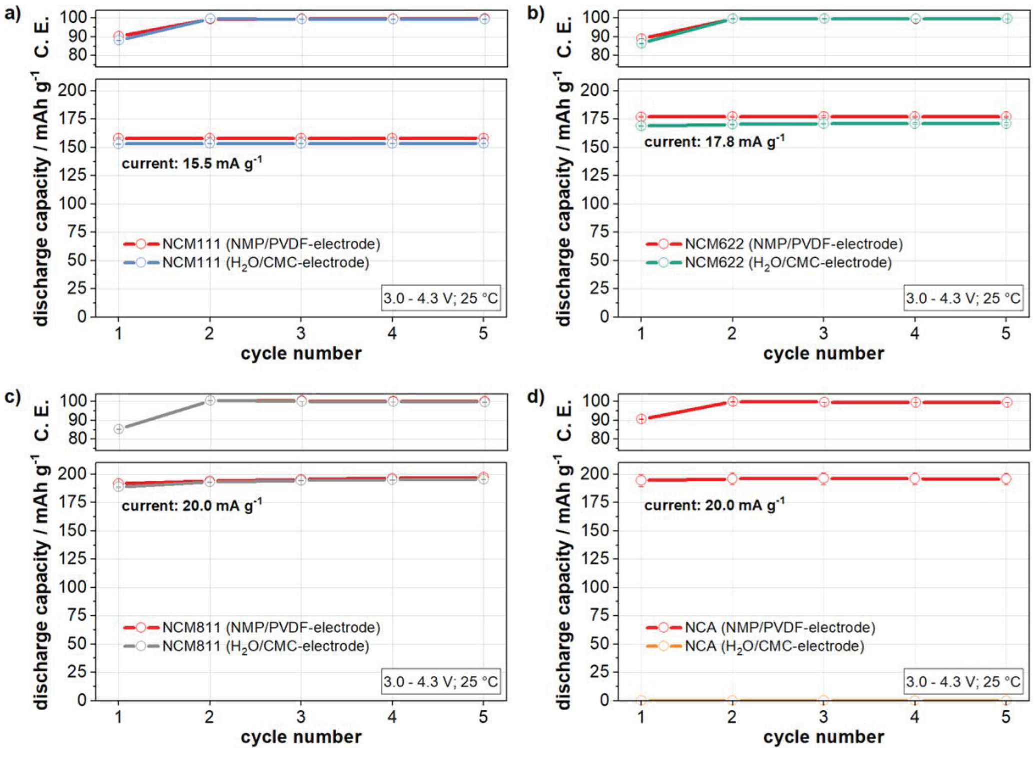

Figure 2. Discharge capacity and coulombic efficiency over cycle number obtained during the formation protocol applied to cells containing CMC- and PVDF-based electrodes (NCM111 (a), NCM622 (b), NCM811 (c), NCA (d)). The data represent the average specific discharge capacity and average coulombic efficiency of three cells and the error bars relate to the standard deviation between these cells. Due to the electrochemical inactivity of CMC-based NCA-electrodes no coulombic efficiency is shown for this variant.

nickel content is an important, it is not the only decisive reason for high-water sensitivity of NCA as already seen in the leaching tests above. Since the pH values of NCM811 and NCA are quite similar, aluminum corrosion can also be excluded as the deciding factor. Therefore, it is assumed that there is a direct correlation between the electrochemical inactivity of NCA and the increased lithium leaching combined with the detection of aluminum that was shown in the previous section. This may lead to a pronounced change of the

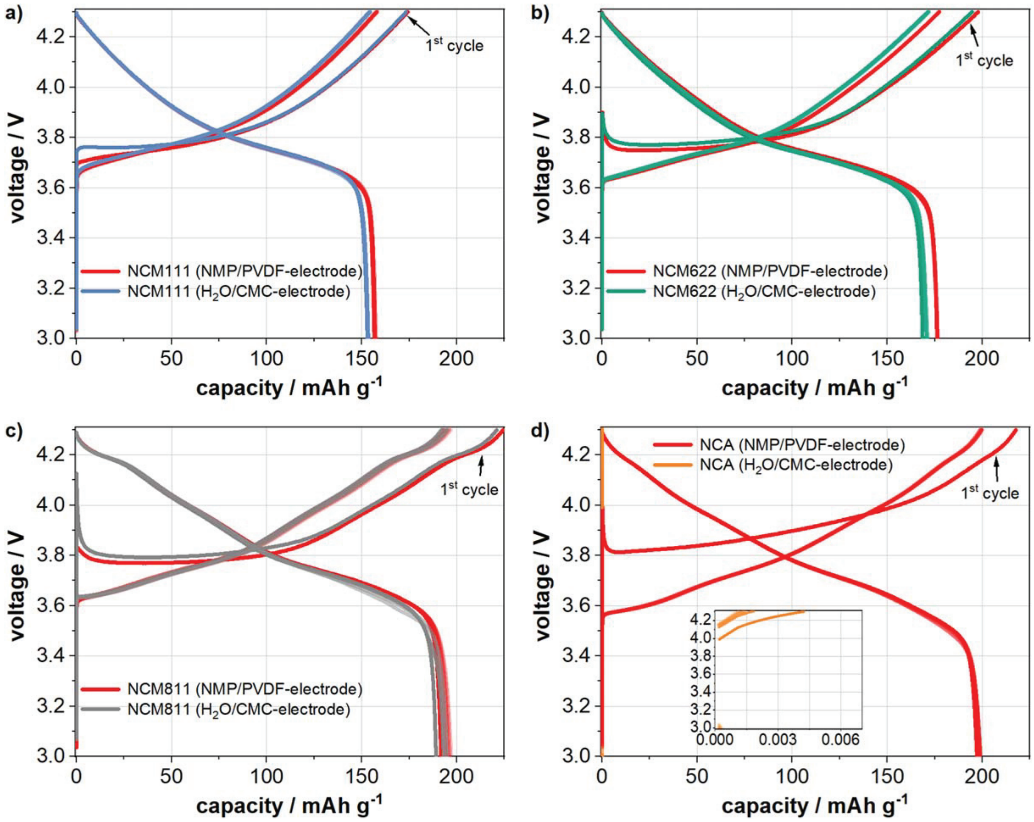

Figure 3. Voltage profiles of a representative cell of each cell combination obtained during the formation protocol (NCM111 (a), NCM622 (b), NCM811 (c), NCA (d) with inset of a magnified area of the voltage profile of a representative cell containing an aqueous-processed NCA electrode).

NCA surface structure through the formation of a layer which blocks the extraction of lithium ions. Moreover, these findings are supported by the results of Faenza et al., who observed electrochemical inactive cells when using ambient aged NCA as an active material.[64] It should be noted that, there is also literature showing electrochemically active cells with aqueous processed NCA electrodes even though the performance is for the most part for pristine NCA relatively poor.[33,45–48] Differences in the electrode manufacturing conditions (mixing process, binder-type, ratio of compounds, mixing time etc.) may be responsible for the varying results.

Over the five formation cycles, it is striking that the specific capacity slowly increases for all cells. As this effect can also be seen for the NMP-based variants, it can be at least partially explained as the volume expansion/contraction of the active materials during charge and discharge enables the electrolyte to reach active material that was previously not accessible. The increase in the discharge capacity for the NMP- vs. the H_2O-based cells from the 1st to the 5th formation cycles containing the NCM materials is 0.3 mAh g^{-1}/0.6 mAh g^{-1}, 0.1 mAh g^{-1}/2.2 mAh g^{-1} and 5.6 mAh g^{-1}/6.7 mAh g^{-1} for NCM111, NCM622 and NCM811, respectively. As such, the increase is higher for cells containing the water-based electrodes. This clearly supports a regeneration of the active material over cycling likely via a reverse Li^+-/H^+-exchange mechanism as proposed by Shkrob et al.[53] Nonetheless, the discharge capacity of the cells containing the water-based electrodes is still lower than their NMP-counterparts in the last formation cycle. Irreversible structural damage such as a reduction of Ni^{3+} to Ni^{2+} occurring during aqueous processing is also likely and would explain the lower capacity as the anode in the half cells provides a large lithium reservoir that would be more than sufficient to fully relithiate the active materials. When comparing the increase in capacity over cycling for the cells with water-based electrodes it is highest for NCM811 followed by NCM622 and NCM111 and therefore follows the nickel content. However, at this point it is unclear why the increase in capacity during formation for the cells with NMP-processed NCM811 electrodes is relatively high as compared to the NMP-based cells of NCM111 and NCM622. One possibility would be the fact that also during the NMP-based electrode manufacturing process and electrode pre-drying, the active material is in contact with ambient air for some time, which may have led to similar processes as in water. In this case, a regeneration process of the active material would be also observed for the NMP-processed material, similar to the observations by Jung et al. for one year aged NCM811.[65] The coulombic efficiency of the initial cycle for the NMP- vs H_2O-based cells is 90.26%/88.14%, 88.97%/86.47% and 85.40%/85.35% for NCM111, NCM622 and NCM811, respectively. The reduced efficiency also provides evidence for increased side reactions within the aqueous-processed cells. Assuming mechanisms upon water contact according to Liu et al. (spontaneous reduction of nickel)[51] or Shkrob et al. (Li^+/H^+-exchange),[53] both can lead to the formation of lithium carbonate. The latter one is known to be at least partially involved in gassing reactions in the first charge cycle and can therefore decrease the coulombic efficiency.[11,66–70] After the first cycle, the coulombic efficiency of both cell variants is quite similar. Unfortunately, these comparisons cannot be made for NCA, due to the electrochemically inactivity of the cells with water-based NCA-electrodes.

The voltage profiles of a representative cell of each variant are shown in Fig. 3. In accordance with the results shown above, the cells with CMC-based NCA electrodes show extreme polarization for all cycles. Comparing the voltage profiles of the NCM-based

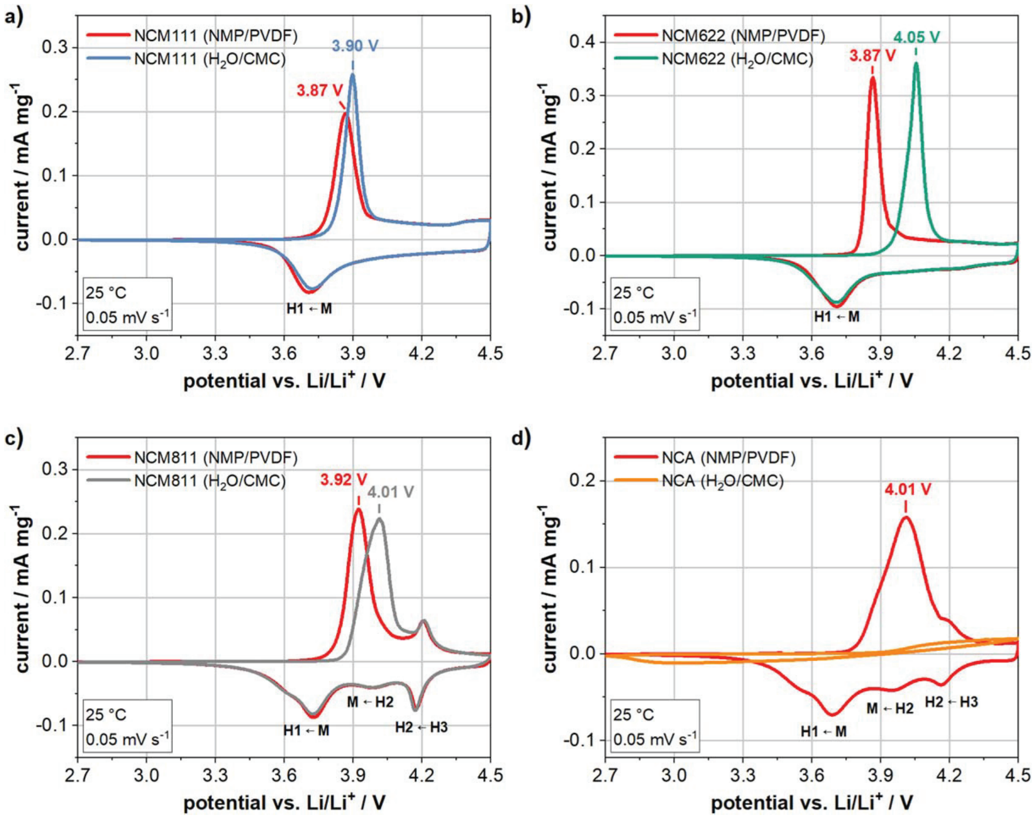

Figure 4. Cyclic voltammetry of a cell of each combination obtained in the first scan (NCM111 (a), NCM622 (b), NCM811 (c), NCA (d)).

cells, the polarization in the first charge cycle is always higher for the cells with aqueous-processed electrodes as compared to their NMP counterparts. While only a slight initial overvoltage can be seen for the aqueous-based NCM111 cells, this can be clearly recognized in the voltage profiles of NCM622 and NCM811-based cells. Many authors have observed an initial overvoltage for cells with layered active materials which is mostly attributed to the formation of a barrier layer formed by water contact, CO_2 or a combination of both which impedes the extraction of the lithium ions.[53,64,65] Therefore, the results for NCA may be explained by a thick surface layer that almost completely hinders lithium ion deinsertion and thus leads to the extreme cell polarization. In the following cycles, the polarization of the H_2O- and NMP-based cells for each material, except for NCA, is similar, although still marginally higher for the aqueous system.

Cyclic voltammetry was performed for each cell combination (Fig. 4). The experiments consisted of a voltage sweep from open circuit voltage to 4.5 V and a backward sweep to 2.5 V. In agreement with the initial overvoltages from the voltage profiles in Fig. 3, the first peak maximum of the current signal in the forward scan is shifted to slightly higher voltages for the NCM-type cells with water-based electrodes as compared to those with the NMP-based electrodes. In the reverse scan, this difference in overpotential is clearly reduced. In the case of NCM811, the overpotential differences seen in the first peak of the forward scan were already essentially eliminated by the second peak of the forward scan (4.2 V, attributed to the phase transition of a hexagonal phase (H2) to another hexagonal phase (H3)).[71–73] It should be noted that for materials with lower nickel content such as NCM111 and NCM622, the only transition detected is that associated with the change from a monoclinic phase (M) to a hexagonal phase (H1).[73] There is no peak maximum present for the water-based NCA cell leading to the conclusion that even an overvoltage of more than 500 mV as compared to the reference system is not enough to overcome a possible barrier layer.

Impedance spectra were recorded after the formation protocol and the results are shown in form of a Nyquist and Bode plot in Figs. 5 and S1 (available online at stacks.iop.org/JES/167/140512/mmedia), respectively. All Nyquist plots show a high-frequency intercept with the x-axis and an inclined line at low frequencies due to the ohmic resistances within the cell (R_s) and solid-state diffusion, respectively. For all cells with CMC-based electrodes (except the NCA-variant) three semicircles can be observed. Three semicircles have often been reported in literature when the impedance spectra were recorded at higher state of charge.[74–78] The associated resistances have been mostly assigned, from high to low frequencies, to the surface film impedance (R_f), the electronic properties of the active material or a combination of charge transfer resistance at the metallic lithium/electrolyte interface along with the electronic conductivity of the active material (R^*) and the charge transfer impedance at the cathode/electrolyte interface (R_{ct}). In contrast, three semicircles are hard to discern for the cells with the NMP-based electrodes. However, the presence of three semicircles seems to be supported by the Bode plots and the first two semicircles may be simply overlapped in the Nyquist plot (Fig. S1). The differences might be attributed to the different binder-types and therefore a different interaction behavior with the active material. Therefore, it is hard to differentiate between water- and binder-induced influences on the impedance spectra. R_{ct} is higher for the cells containing CMC-electrodes than the reference cells. This may be attributed to a degradation of the active materials during aqueous processing,

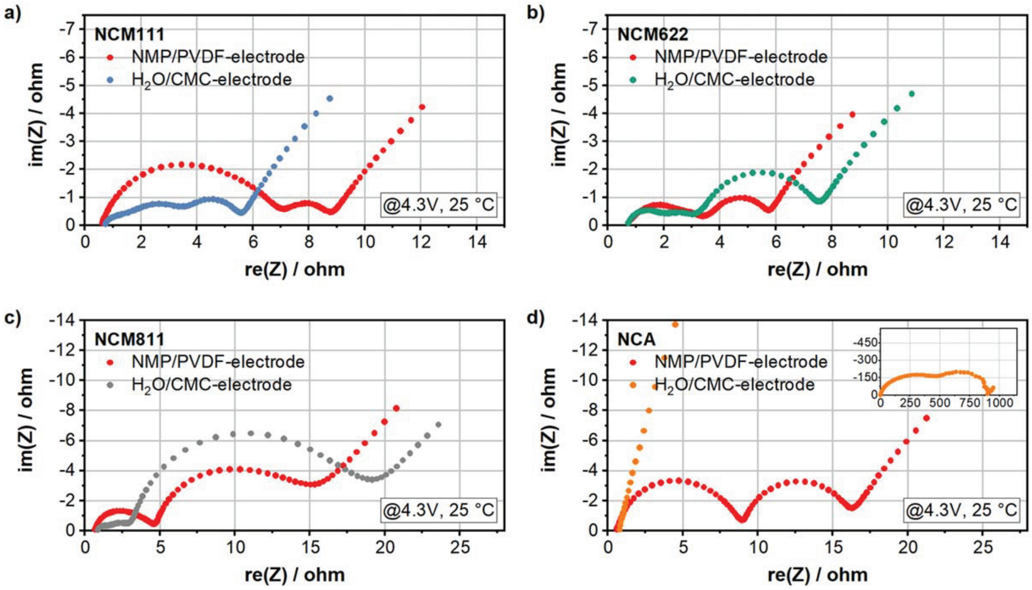

Figure 5. Nyquist plots of cells containing NMP- or H_2O-based electrodes at 4.3 V obtained after the formation protocol. The inset in (d) represents the impedance spectrum of a cell containing an aqueous processed NCA-electrode.

which may explain the slightly higher polarization in the last formation cycle(s) (Fig. 3). Interestingly, although the total impedance is higher for the cells with water-based electrodes and the active materials with higher nickel content, the total impedance for the cells with NCM111 is lower for the H_2O-variant compared to its NMP-counterpart. This difference might be attributed to the more detrimental effects of water on the nickel-rich materials. The overall impedance of the cell with aqueous-processed NCA electrode is on

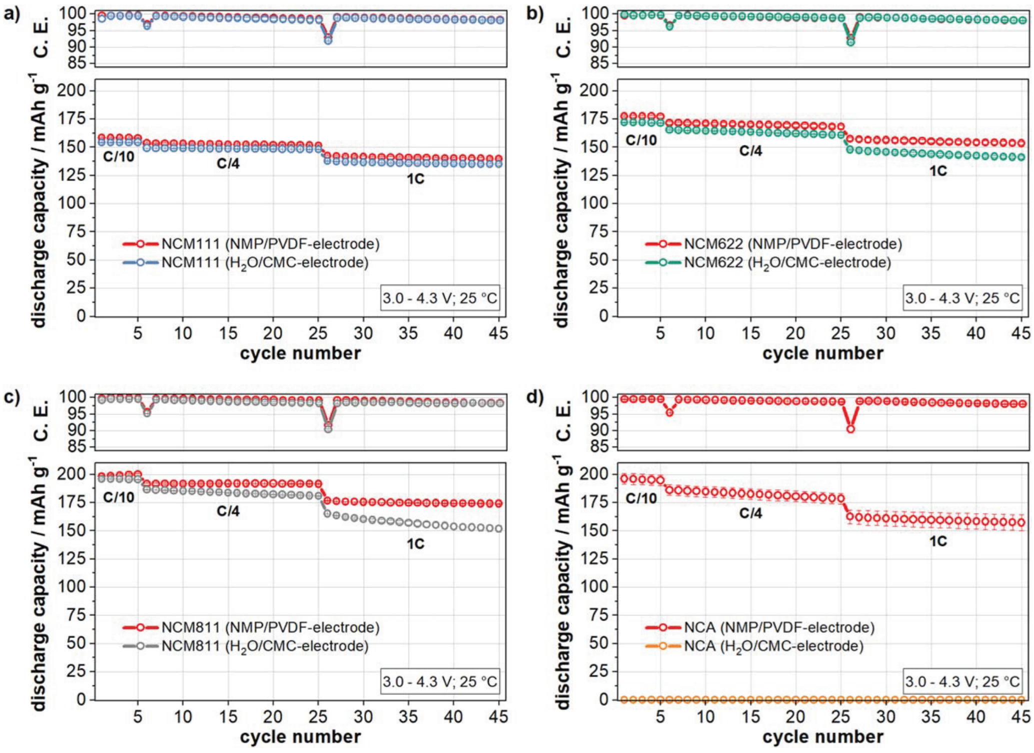

Figure 6. Cycle performance of CMC- and PVDF-based electrodes (NCM111 (a), NCM622 (b), NCM811 (c), NCA (d)). The data represent the average specific discharge capacity and average coulombic efficiency of three cells and the error bars relate to the standard deviation between these cells. Due to the electrochemical inactivity of CMC-based NCA-electrodes no coulombic efficiency is shown for this variant.

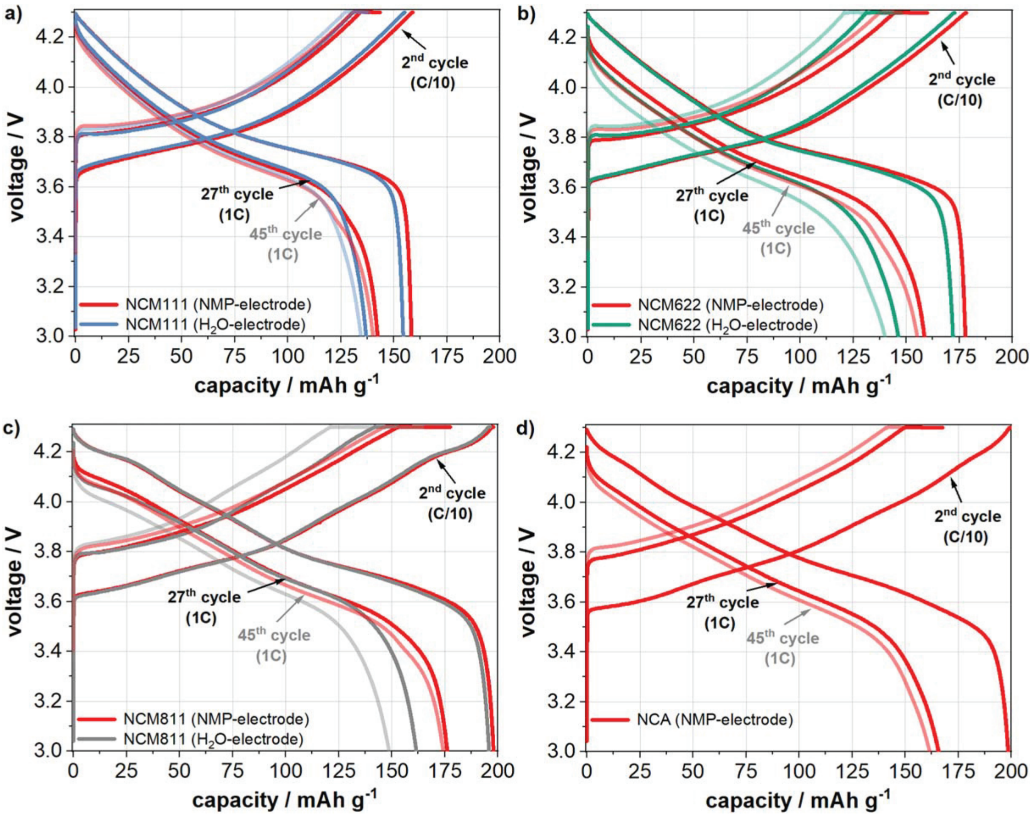

Figure 7. Voltage profiles in the 2nd, 27th and 45th cycle (lighter color corresponds to a higher cycle number) of a representative cell of each combination obtained during rate performance test (NCM111 (a), NCM622 (b), NCM811 (c), NCA (d)). Due to the electrochemical inactivity of CMC-based NCA-electrodes no voltage profiles are shown for this variant.

the order of two orders of magnitude higher than all of the other cells. This is consistent with the high overpotential of NCA cells with a water-based electrode. Therefore, the extraction of lithium ions from the NCA structure cannot be initiated in the voltage ranges examined. As noted above, the origin of the overpotential is thought to be in a thick surface layer formed during water contact. Further studies are necessary to clarify this point.

After formation, a rate performance test was performed. The average discharge capacity and coulombic efficiency is depicted in Fig. 6. The average discharge capacity remains higher for the NMP-cells as compared to the cells with aqueous processed electrodes during the whole test. As expected, the cells with water-based NCA-electrodes again did not show any electrochemical activity during cycling. The NMP-processed NCA electrodes show good cyclability, which suggests that the challenges lie with the processing rather than the NCA active material itself. When comparing the NCM cells, the performance of the cells with NCM111/CMC electrodes is similar to the reference cells irregardless of the current density. In contrast, the cells with the nickel-rich cathode materials (NCM622 and NCM811) show increased capacity fading after water-based processing especially upon cycling with increased current densities (1C). The capacity retention is 95.3%/97.5% (NCM622) and 92.0%/98.6% (NCM811) related to the first and last 1C-cycle for the CMC- and PVDF-based variant, respectively. Interestingly, Sicklinger et al. have shown that upon contact with ambient air basic surface contaminants such as nickel carbonate species can be formed on especially nickel-rich NCMs, which can react with EC-containing electrolytes leading to enhanced capacity fade.[79] The capacity fade, which is more pronounced with NCM811, supports the mechanisms according to the report above.

The voltage profiles in the 2nd (C/10), 27th (1C) and 45th (1C) cycle are shown in Fig. 7. As with the voltage profiles from the formation cycles, the cell polarization at low currents (C/10) is almost independent of the processing solvent for each active material (excluding the cells with the water-based NCA electrodes). For aqueous-based NCM622 and NCM811 cells, the polarization increases with increasing cycle number at high current densities (1C) relative to the NMP-based cells. As noted above, this effect is likely related to increased side-reactions between the EC-based electrolyte and the nickel-rich materials. Interestingly, this effect is not evident with NCM111, which indicates that a water-based process with CMC as a binder is, in principle, possible for active materials with a lower sensitivity against water and might even help to obtain higher capacity retention as it was already observed in the literature.[3] This statement is naturally dependent on the ability to control other effects, such as aluminum corrosion, during aqueous processing.

Conclusions

In this study, different layered oxides (NCM111, NCM622, NCM811 and NCA) were evaluated in terms of their response to aqueous processing under the same conditions to facilitate a direct comparison. The time-dependent metal leaching of the different layered oxides in water shows that the lithium leaching is more pronounced for active materials with higher nickel content. In the case of NCA, aluminum and a disproportionately high amount of lithium as compared to NCM811 is leached. This suggests that in addition to the nickel-driven reactions, NCA also undergoes degradation mechanisms involving aluminum that might lead to further lithium loss. More studies are needed to further clarify this point. For the materials with higher lithium leaching, more basic pH values are also observed and a specific limit is reached for each individual cathode material.

The electrochemical performance of cells containing aqueous-processed electrodes was compared with cells containing NMP-based electrodes. All cells with water-based electrodes show a lower capacity as compared to their NMP counterparts. Therefore, the leached lithium of the active material upon contact with water must at least partially come from the active material structure and not only from remaining surface impurities from the material synthesis. In the first cycles a pronounced increase in the capacity of the electrochemically active cells with water-based electrodes is observed, which indicates a partial regeneration of water-exposed layered cathode materials possibly via a reversed Li^+/H^+-mechanism. The changes at the material surface due to lithium leaching and other mechanisms during aqueous processing results in an increased initial overvoltage which likely impedes the extraction of lithium ions during the first cycle. A decrease in the overvoltage in the subsequent cycles illustrates that the damage may be, at least, partially repaired, assuming that a sufficient lithium source, as would be the case in a half-cell configuration, is present to replace the leached lithium. In the case of NCA, however, the structural changes result in a highly resistive layer that results in an increase in the initial overvoltage ($>$500 mV as compared to the NMP-processed reference cells) and renders the cells essentially inactive. The cycling experiments show an increased capacity fading for the cells with nickel-rich water-based electrodes likely due to increased side reactions from water-induced surface species. Taken together, the results demonstrate that NCM111 is the least sensitive and NCA is the most sensitive to aqueous-processing of the materials in this study.

Based on the direct comparison of the different active materials, it is clear that aqueous electrode processing is proving to be increasingly challenging, particularly with the current move to higher nickel-content active materials. Approaches to mitigate processing-related effects, such as suitable surface coatings, are urgently needed for the feasible implementation of a water-based electrode fabrication process. It seems that the presence of aluminum in the active material, at least in the case of NCA, exacerbates the situation. For future cathode materials such as NCA with a further increased nickel content or possibly even quaternary layered nickel-rich oxides with NCMA-structure, the role of aluminum in water-induced degradation processes needs to be clarified. In the second part of this work, the water-induced surface changes of NCA will be examined in more detail, including the affect of these changes on the electrochemical performance in order to elucidate the origin of the high water sensitivity of NCA.

Acknowledgments

The leaching tests were performed as part of the project NeW-Bat (grant no. 033R174A) which was funded by the Federal Ministry of Education and Research of Germany. Furthermore, the authors acknowledge the financial support from the Bavarian Ministry of Economic Affairs and Media, Energy and Technology for funding the Fraunhofer R&D Center for Electromobility Bavaria (grant no. 43-6629/86).

ORCID

Guinevere A. Giffin https://orcid.org/0000-0002-2303-9560

References

1. T. M. Bandhauer, S. Garimella, and T. F. Fuller, *J. Electrochem. Soc.*, **158**, R1 (2011).
2. D. L. Wood III, J. Li, and C. Daniel, *J. Power Sources*, **275**, 234 (2015).
3. I. Doberdò, N. Löffler, N. Laszczynski, D. Cericola, N. Penazzi, S. Bodoardo, G.-T. Kim, and S. Passerini, *J. Power Sources*, **248**, 1000 (2014).
4. J.-H. Lee, Y.-M. Choi, U. Paik, and J.-G. Park, *J. Electroceram.*, **17**, 657 (2006).
5. N. Loeffler, J. von Zamory, N. Laszczynski, I. Doberdo, G.-T. Kim, and S. Passerini, *J. Power Sources*, **248**, 915 (2014).
6. B. C. Church, D. T. Kaminski, and J. Jiang, *J. Mater. Sci.*, **49**, 3234 (2014).
7. S. Y. Li and B. C. Church, *Mater. Corros.*, **67**, 978 (2016).
8. D. Bresser, D. Buchholz, A. Moretti, A. Varzi, and S. Passerini, *Energy Environ. Sci.*, **11**, 3096 (2018).
9. W. Bauer, F. A. Çetinel, M. Müller, and U. Kaufmann, *Electrochim. Acta*, **317**, 112 (2019).
10. N. Loeffler, G.-T. Kim, F. Mueller, T. Diemant, J.-K. Kim, R. J. Behm, and S. Passerini, *ChemSusChem*, **9**, 1112 (2016).
11. D. Pritzl, T. Teufl, A. T. S. Freiberg, B. Strehle, J. Sicklinger, H. Sommer, P. Hartmann, and H. A. Gasteiger, *J. Electrochem. Soc*, **166**, A4056 (2019).
12. R. Sahore, D. L. Wood III, A. Kukay, K. M. Grady, J. Li, and I. Belharouak, *ACS Sustainable Chem. Eng.*, **8**, 3162 (2020).
13. W. Li, E. M. Erickson, and A. Manthiram, *Nat. Energy*, **5**, 26 (2020).
14. S.-T. Myung, F. Maglia, K.-J. Park, C. S. Yoon, P. Lamp, S.-J. Kim, and Y.-K. Sun, *ACS Energy Lett.*, **2**, 196 (2017).
15. J. Kim, H. Lee, H. Cha, M. Yoon, M. Park, and J. Cho, *Adv. Energy Mater.*, **8**, 1702028 (2018).
16. F. A. Çetinel and W. Bauer, *Bull. Mater. Sci.*, **37**, 1685 (2014).
17. M. Memm, A. Hoffmann, and M. Wohlfahrt-Mehrens, *Electrochim. Acta*, **260**, 664 (2018).
18. N. Loeffler, T. Kopel, G.-T. Kim, and S. Passerini, *J. Electrochem. Soc*, **162**, A2692 (2015).
19. N. Loeffler, G.-T. Kim, S. Passerini, C. Gutierrez, I. Cendoya, I. de Meatza, F. Alessandrini, and G. B. Appetecchi, *ChemSusChem*, **10**, 3581 (2017).
20. H. Zhong, M. Sun, Y. Li, J. He, J. Yang, and L. Zhang, *J. Solid State Electrochem.*, **20**, 1 (2016).
21. A. Kvasha, I. Urdampilleta, I. de Meatza, R. Colombo, P. Ulmann, M. Gulas, C. Gutierrez, M. Bengoechea, J. A. Blazquez, O. Miguel, and H.-J. Grande, *ECS Trans.*, **73**, 325 (2016).
22. D. V. Carvalho, N. Loeffler, G.-T. Kim, M. Marinaro, M. Wohlfahrt-Mehrens, and S. Passerini, *Polymers*, **8**, 276 (2016).
23. K. Soeda, M. Yamagata, and M. Ishikawa, *ECS Trans.*, **64**, 13 (2015).
24. J. Xu, S.-L. Chou, Q.-F. Gu, H.-K. Liu, and S.-X. Dou, *J. Power Sources*, **225**, 172 (2013).
25. M. Wood, J. Li, R. E. Ruther, Z. Du, E. C. Self, H. M. Meyer III, C. Daniel, I. Belharouak, and D. L. Wood III, *Energy Storage Mater.*, **24**, 188 (2020).
26. L. Ibing, T. Gallasch, P. Schneider, P. Niehoff, A. Hintennach, M. Winter, and F. M. Schappacher, *J. Power Sources*, **423**, 183 (2019).
27. K. V. Sangappillai, *Master Thesis: Aqueous Coating for Li-ion Batteries—Investigation of high energy (high Ni) cathodes*, University of Picardy Jules Verne (2017), https://www.researchgate.net/publication/338209588_Umicore_Advanced_coatings_on_High_energy_Li-ion_battery_Cathodes_for_enhanced_Water_Processability_Korea.
28. Z. Chen, G.-T. Kim, D. Chao, N. Loeffler, M. Copley, J. Lin, Z. Shen, and S. Passerini, *J. Power Sources*, **372**, 180 (2017).
29. Z. Du, J. Li, M. Wood, C. Mao, C. Daniel, and D. L. Wood III, *Electrochim. Acta*, **270**, 54 (2018).
30. Z. Du, K. M. Rollag, J. Li, S. J. An, M. Wood, Y. Sheng, P. P. Mukherjee, C. Daniel, and D. L. Wood III, *J. Power Sources*, **354**, 200 (2017).
31. M. Bichon, D. Sotta, N. Dupré, E. de Vito, A. Boulineau, W. Porcher, and B. Lestriez, *ACS Appl. Mater. Interfaces*, **11**, 18331 (2019).
32. A. N. Jansen, S. E. Trask, B. J. Polzin, W. Lu, O. Kahvecioglu Feridun, G. K. Krumdick, S. D. Hellring, M. Stewart, and B. Kornish, *New Aqueous Binders for Lithium-ion Batteries* (2016), https://publications.anl.gov/anlpubs/2018/01/141061.pdf.
33. W. B. Hawley, A. Parejiya, Y. Bai, H. M. Meyer III, D. L. Wood III, and J. Li, *J. Power Sources*, **466**, 228315 (2020).
34. J. Li, Y. Lu, T. Yang, D. Ge, D. L. Wood III, and Z. Li, *iScience*, **23**, 101081 (2020).
35. L. Ibing, T. Gallasch, A. Friesen, P. Niehoff, A. Hintennach, M. Winter, and M. Börner, *J. Power Sources*, **475**, 228608 (2020).
36. J.-H. Kuo and C.-C. Li, *J. Electrochem. Soc*, **167**, 100504 (2020).
37. A. Kukay, R. Sahore, A. Parejiya, W. B. Hawley, J. Li, and D. L. Wood III, *J. Colloid Interface Sci.*, **581**, 635 (2021).
38. S. Pedaballi and C.-C. Li, *J. Power Sources*, **472**, 228552 (2020).
39. Q. Wu, S. Ha, J. Prakash, D. W. Dees, and W. Lu, *Electrochim. Acta*, **114**, 1 (2013).
40. T. Zhao, Y. Meng, R. Ji, F. Wu, L. Li, and R. Chen, *J. Alloys Compd.*, **811**, 152060 (2019).
41. N. Laszczynski, J. von Zamory, J. Kalhoff, N. Loeffler, V. S. K. Chakravadhanula, and S. Passerini, *ChemElectroChem*, **2**, 1768 (2015).
42. A. Kazzazi, D. Bresser, A. Birrozzi, J. von Zamory, M. Hekmatfar, and S. Passerini, *ACS Appl. Mater. Interfaces*, **10**, 17214 (2018).
43. S. Zhang et al., *Adv. Energy Mater.*, **7**, 1601066 (2016).
44. K. Notake, T. Gunji, H. Kokubun, S. Kosemura, Y. Mochizuki, T. Tanabe, S. Kaneko, S. Ugawa, H. Lee, and F. Matsumoto, *J. Appl. Electrochem.*, **46**, 267 (2016).
45. T. Tanabe et al., *Electrochim. Acta*, **258**, 1348 (2017).
46. Y. Liu et al., *J. Appl. Electrochem.*, **49**, 99 (2019).
47. K. Kimura, K. Onishi, T. Sakamoto, K. Asami, and M. Yanagida, *J. Electrochem. Soc*, **166**, A5313 (2019).

48. K. Kimura, T. Sakamoto, T. Mukai, Y. Ikeuchi, N. Yamashita, K. Onishi, K. Asami, and M. Yanagida, *J. Electrochem. Soc*, **165**, A16 (2018).
49. M. Hofmann, F. Nagler, M. Kapuschinski, U. Guntow, and G. A. Giffin, *ChemSusChem*, **13** (2020).
50. H. S. Liu, Z. R. Zhang, Z. L. Gong, and Y. Yang, *Electrochem. Solid-State Lett.*, **7**, A190 (2004).
51. H. Liu, Y. Yang, and J. Zhang, *J. Power Sources*, **162**, 644 (2006).
52. J. Paulsen and J. Kim, *High nickel cathode material having low soluble base content*, US20140054495A1 (2014).
53. I. A. Shkrob, J. A. Gilbert, P. J. Phillips, R. Klie, R. T. Haasch, J. Bareño, and D. P. Abraham, *J. Electrochem. Soc*, **164**, A1489 (2017).
54. T. Toma, R. Maezono, and K. Hongo, *ACS Appl. Energy Mater.*, **3**, 4078 (2020).
55. S. Jeong, J. Kim, and J. Mun, *J. Electrochem. Soc*, **166**, A5038 (2019).
56. S. J. Beckerman, R. B. Ford, and M. T. Nemeth, *Powder Diffr.*, **11**, 312 (1996).
57. J. Gao, S. Shi, R. Xiao, and H. Li, *Solid State Ion.*, **286**, 122 (2016).
58. J. Lin, Z. Wen, X. Xu, N. Li, and S. Song, *Fusion Eng. Des.*, **85**, 1162 (2010).
59. Z. Lebens-Higgins et al., *ECS Trans.*, **80**, 197 (2017).
60. Z. W. Lebens-Higgins et al., *Sci. Rep.*, **9**, 17720 (2019).
61. M. Ruttert, V. Siozios, M. Winter, and T. Placke, *ACS Appl. Energy Mater.*, **3**, 743 (2020).
62. F. Friedrich, B. Strehle, A. T. S. Freiberg, K. Kleiner, S. J. Day, C. Erk, M. Piana, and H. A. Gasteiger, *J. Electrochem. Soc*, **166**, A3760 (2019).
63. N. Nitta, F. Wu, J. T. Lee, and G. Yushin, *Mater. Today*, **18**, 252 (2015).
64. N. V. Faenza, L. Bruce, Z. W. Lebens-Higgins, I. Plitz, N. Pereira, L. F. J. Piper, and G. G. Amatucci, *J. Electrochem. Soc.*, **164**, A3727 (2017).
65. R. Jung, R. Morasch, P. Karayaylali, K. Phillips, F. Maglia, C. Stinner, Y. Shao-Horn, and H. A. Gasteiger, *J. Electrochem. Soc*, **165**, A132 (2018).
66. J. Kim, Y. Hong, K. S. Ryu, M. G. Kim, and J. Cho, *Electrochem. Solid-State Lett.*, **9**, A19 (2006).
67. R. Jung, M. Metzger, F. Maglia, C. Stinner, and H. A. Gasteiger, *J. Electrochem. Soc*, **164**, A1361 (2017).
68. S. E. Renfrew, L. A. Kaufman, and B. D. McCloskey, *ACS Appl. Mater. Interfaces*, **11**, 34913 (2019).
69. C. Wang, L. Shao, X. Guo, X. Xi, L. Yang, C. Huang, C. Zhou, H. Zhao, D. Yin, and Z. Wang, *ACS Appl. Mater. Interfaces*, **11**, 44036 (2019).
70. S. E. Renfrew and B. D. McCloskey, *ACS Appl. Energy Mater.*, **2**, 3762 (2019).
71. W. Li, J. N. Reimers, and J. R. Dahn, *Solid State Ion.*, **67**, 123 (1993).
72. S.-U. Woo, C. S. Yoon, K. Amine, I. Belharouak, and Y.-K. Sun, *J. Electrochem. Soc*, **154**, A1005 (2007).
73. J.-H. Kim, K.-J. Park, S. J. Kim, C. S. Yoon, and Y.-K. Sun, *J. Mater. Chem. A*, **7**, 2694 (2019).
74. X.-Y. Qiu, Q.-C. Zhuang, Q.-Q. Zhang, R. Cao, Y.-H. Qiang, P.-Z. Ying, and S.-G. Sun, *J. Electroanal. Chem.*, **687**, 35 (2012).
75. M. M. Loghavi, M. Askari, M. Babaiee, and A. Ghasemi, *J. Electroanal. Chem.*, **841**, 107 (2019).
76. U. Nisar, R. Amin, R. Essehli, R. A. Shakoor, R. Kahraman, D. K. Kim, M. A. Khaleel, and I. Belharouak, *J. Power Sources*, **396**, 774 (2018).
77. P. Liu, L. Xiao, Y. Chen, and H. Chen, *Ceram. Int.*, **45**, 18398 (2019).
78. X.-Y. Qiu, Q.-C. Zhuang, Q.-Q. Zhang, R. Cao, P.-Z. Ying, Y.-H. Qiang, and S.-G. Sun, *Phys. Chem. Chem. Phys.*, **14**, 2617 (2012).
79. J. Sicklinger, M. Metzger, H. Beyer, D. Pritzl, and H. A. Gasteiger, *J. Electrochem. Soc*, **166**, A2322 (2019).
80. X. Xiong, Z. Wang, P. Yue, H. Guo, F. Wu, J. Wang, and X. Li, *J. Power Sources*, **222**, 318 (2013).

Implications of Aqueous Processing for High Energy Density Cathode Materials
Part I: Ni-rich Layered Oxides

Michael Hofmann, Martina Kapuschinski, Uwe Guntow and Guinevere A. Giffin[z]
Fraunhofer R&D Center Electromobility, Fraunhofer Institute for Silicate-Research,
Neunerplatz 2, 97082 Wuerzburg, Germany
[z]E-mail: guinevere.giffin@isc.fraunhofer.de

Supporting Information

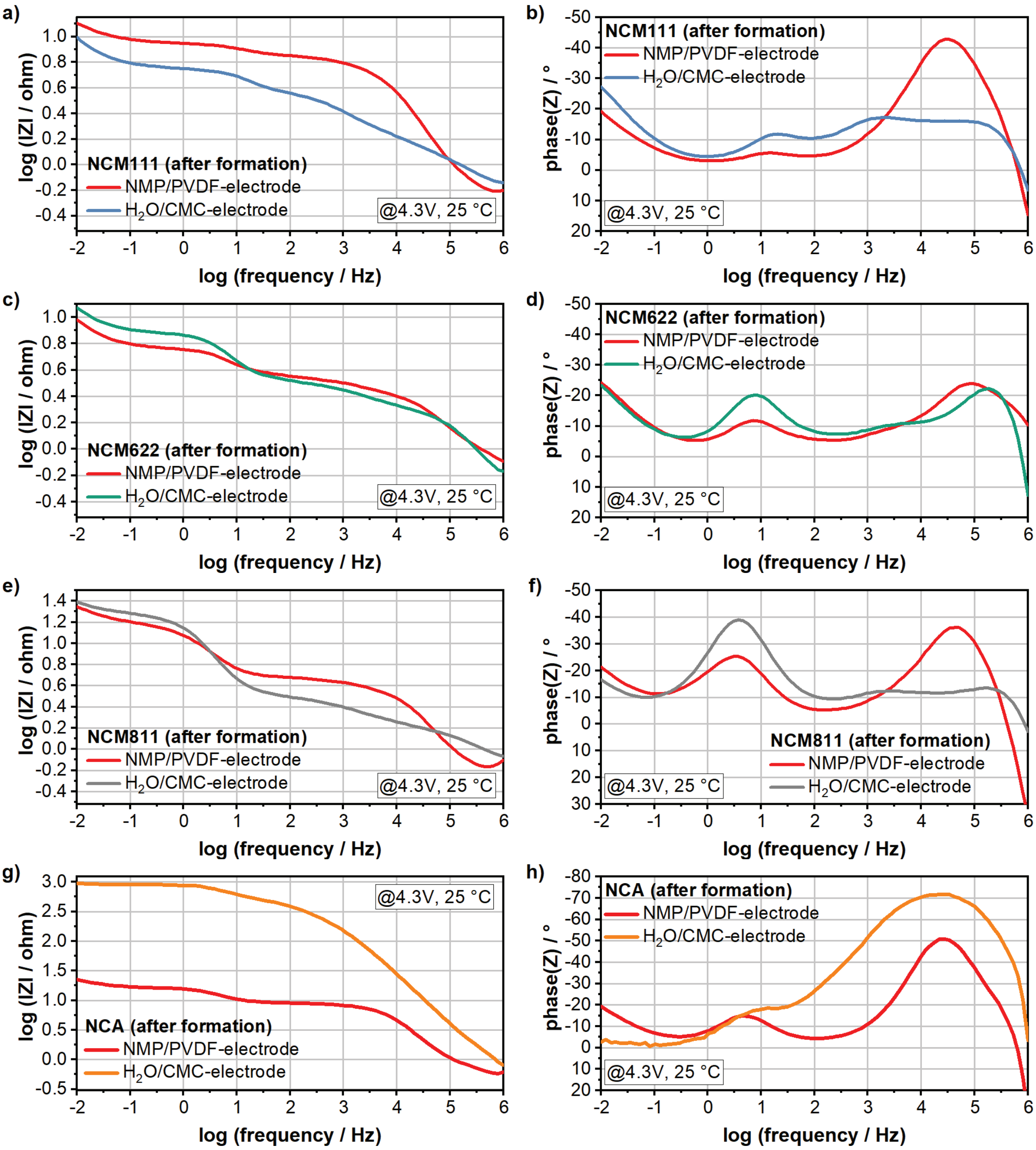

Figure S1 Bode plots of cells containing NMP- or H_2O-based electrodes obtained from impedance spectroscopy after the formation protocol at 4.3 V.

Appendixes

I. Manuscripts

a. M. Hofmann, M. Kapuschinski, U. Guntow, G. A. Giffin, Implications of Aqueous Processing for High Energy Density Cathode Materials: Part I. Ni-Rich Layered Oxides. *J. Electrochem. Soc.* **2020**, *167*, 140512.

b. M. Hofmann, M. Kapuschinski, U. Guntow, G. A. Giffin, Implications of Aqueous Processing for High Energy Density Cathode Materials: Part II. Water-Induced Surface Species on $LiNi_{0.8}Co_{0.15}Al_{0.05}O_2$. *J. Electrochem. Soc.* **2020**, *167*, 140535.

c. M. Hofmann, F. Nagler, M. Kapuschinski, U. Guntow, G. A. Giffin, Surface Modification of $LiNi_{0.8}Co_{0.15}Al_{0.05}O_2$ Particles via Li_3PO_4 Coating to Enable Aqueous Electrode Processing. *ChemSusChem* **2020**, *13*, 5962 – 5971.

d. M. Hofmann, F. Nagler, U. Guntow, G. Sextl, G. A. Giffin, Long-Term Cycling Performance of Aqueous Processed Ni-rich $LiNi_{0.8}Co_{0.15}Al_{0.05}O_2$ Cathodes. *J. Electrochem. Soc.* **2021**, *168*, 060511.

Journal of The Electrochemical Society, 2020 **167** 140535

Implications of Aqueous Processing for High Energy Density Cathode Materials: Part II. Water-Induced Surface Species on $LiNi_{0.8}Co_{0.15}Al_{0.05}O_2$

Michael Hofmann, Martina Kapuschinski, Uwe Guntow, and Guinevere A. Giffin[z]

Fraunhofer R&D Center Electromobility, Fraunhofer Institute for Silicate-Research, 97082 Wuerzburg, Germany

Aqueous electrode manufacturing of nickel-rich layered oxide cathode materials poses a significant challenge due to their high water sensitivity. $LiNi_{0.8}Co_{0.15}Al_{0.05}O_2$ (NCA) has been shown to be particularly sensitive not only to water during processing, but also ambient air. In an effort to further clarify the processes that occur when NCA is in contact with water, the active material was investigated after different durations of water exposure. The results show that a differentiation has to been made between the surface impurities already present on NCA in the pristine state, water-induced surface species and water-induced leached species. The results demonstrate that the water-induced surface species can be mainly attributed to chemisorbed CO_2, nickel carbonate and NiOOH-like species but also smaller amounts of newly-formed aluminum and cobalt compounds. The water-induced leached species were assigned to lithium and aluminum-containing species. Water-induced surface species lead to a severe deterioration of the cells due to the resistive nature of these moieties and their involvement in side reactions during cycling. It is essential to find ways to suppress the formation of these species for the successful implementation of aqueous processing for NCA and likely nickel-rich cathode materials in general.

[DOI: 10.1149/1945-7111/abc6ca]

Manuscript submitted September 1, 2020; revised manuscript received October 30, 2020. Published November 11, 2020.

Supplementary material for this article is available online

In recent years, nickel-rich layered oxides have been identified as promising cathode materials due to their high capacity and operation voltage for batteries in electric vehicles (EVs) to meet the consumer demands for longer driving ranges.[1,2] This group of cathode materials includes, among others, $Li(Ni,Co,Al)O_2$ (NCA), which is already part of Panasonic batteries in EVs used by Tesla.[1,3] NCA is related to $LiNiO_2$, where a fraction of the nickel cations have been replaced by cobalt and aluminum cations. While aluminum ions, which are redox inactive, enhance the thermal stability of delithiated layered oxides, cobalt ions stabilize the alternating layered structure.[4–6] Due to the high capacity of around 200 mAh g^{-1} combined with an average voltage of 3.7 V, cells with NCA can provide high energy density.[7]

One drawback of NCA is that it is known to be very sensitive to moisture which can result in a drastic deterioration of the electrochemical performance.[8] Upon storage in ambient air or wet conditions, detrimental surface species are formed which have been reported to be mainly Li_2CO_3, LiOH or $LiHCO_3$.[8–13] As a result, it is difficult to imagine that aqueous electrode processing, which has the potential for more environmentally-friendly and cost-effective electrode production, can replace the conventional *N*-methyl-2-pyrrolidone-based process, at least when unmodified NCA is used.[14] Nonetheless, by protecting the NCA surface with a suitable coating, the performance of cells containing aqueous-processed NCA electrodes can be remarkably improved.[15–20] The coating approach is one of various strategies which have been used to improve aqueous processing of layered-oxide cathode materials in general. Other strategies present in the literature, such as the use of a carbon-coated current collector foil and the addition of oxidic additives or acids, aim to prevent aluminum corrosion which is induced when the slurry pH value exceeds 9.[21–23] Moreover, the type of waterborne binder has also been reported to significantly affect the cell performance.[24–27]

In Part I of these two publications, which evaluated different layered-oxide cathode materials such as NCM111, NCM622, NCM811 and NCA for use in an aqueous electrode manufacturing process, NCA was identified as the most water-sensitive active material.[14] Nickel-driven processes that lead to lithium leaching upon water contact have been proposed for all of the materials investigated. An additional degradation mechanism for NCA involving aluminum was suggested, which resulted in a negligible electrochemical performance.

In an effort to further elucidate the processes that take place when NCA is in contact with water, active material particles have been exposed to water for different durations and were investigated by X-ray diffraction (XRD), scanning electron microscopy (SEM), thermogravimetry coupled with mass spectrometry (TG-MS) and X-ray photoelectron spectroscopy (XPS). Moreover, the impact of water-induced surface species on the electrochemical performance was analyzed in detail by electrochemical cycling, cyclic voltammetry and impedance spectroscopy.

Experimental

Cathode material.—Commercial $LiNi_{0.8}Co_{0.15}Al_{0.05}O_2$ (NCA, NAT-1050, TODA) was stored in a dry argon atmosphere and used without further modification.

Aqueous NCA suspensions.—$LiNi_{0.8}Co_{0.15}Al_{0.05}O_2$ was added to deionized water (25 °C ± 2 °C; mass ratio NCA:water = 1:3) and continuously stirred for 2 h. The suspension was then filtered; the resulting NCA powder and the filtrate were dried separately at 110 °C for 16 h. This NCA and filtrate are denoted as NCA-2 h and filtrate-2 h, respectively. Additional NCA samples were prepared in the same manner as NCA-2h and stored in water for further six hours (NCA-8h), and a week (NCA-1w) after the mixing procedure.

Electrode processing.—For the preparation of electrodes, PVDF (Solvay, Solef® 5130) was first dissolved in *N*-methyl-2-pyrrolidone (Sigma-Aldrich) overnight. The active material and conductive carbon (Imerys, Super C65) were added and the slurry was homogenized in a speedmixer (Hauschild & Co KG). The ratio of active material, conductive carbon and binder was 92:4:4. The resulting slurries were casted on aluminum foil (20 μm) by the doctor-blade technique. The coated electrodes were stored in a fume hood overnight and then pre-dried under vacuum at 80 °C for 2 h. The dried electrodes were calandered to 50% of initial electrode thickness. Disc electrodes (16 mm in diameter) were cut from the electrode sheets and further dried under vacuum at 80 °C for 5 h. The mass loading was 11 ± 1 mg cm^{-2}.

---

[z] E-mail: guinevere.giffin@isc.fraunhofer.de

Cell assembly and electrochemical measurements.—Cathode half-cells were assembled with metallic lithium (Sigma-Aldrich) on copper foil as the counter electrode in a pouch bag configuration. Aluminum tabs and copper-nickel tabs (Targray) were used to connect the cathode and lithium electrode, respectively. 1 mol l^{-1} $LiPF_6$ in EC:DMC 1:1 wt/wt (BASF, LP30) was utilized as the electrolyte and a single layer polyethylene membrane (Celgard, 2500) was used as the separator. All cells were built in an argon-filled glove box (MBraun, O_2 and $H_2O < 1$ ppm). Three cells were made for each combination and the error bars in the figures represent the standard deviation.

The cells were cycled with a battery cycler (Maccor, Series 4000) in a climate chamber (Memmert) at 25 °C. The lower and upper cutoff was 3.0 V and 4.3 V, respectively. A constant current-constant voltage (CCCV) mode with a current limitation in the CV-step of C/20 was used for the charging process, while a constant current (CC) mode was used for discharge. The formation protocol involved five CC cycles (both charge and discharge) at 20.0 mA g^{-1}. To calculate the current for the cycling experiments, the capacity obtained from the last formation cycle was used.

Cyclic voltammetry was carried out between 2.7 V and 4.5 V with a scan rate of 50 μV s^{-1} on a VMP300 galvanostat/potentiostat (BioLogic) in a climate chamber (Memmert) at 25 °C. A three-electrode pouch cell with lithium as a reference electrode was used. Electrochemical impedance spectroscopy (EIS) analysis was also carried out on a VMP300 galvanostat/potentiostat (BioLogic) with an amplitude of 5 mV in the frequency range from 1 MHz to 10 mHz.

Characterization methods.—Powder XRD patterns were recorded between 10° and 80° 2θ with a step size of 0.002° and a 10 mm aperture on a PANalytical Empyrean series 2 diffractometer with a Cu-source (Cu–K_α: $\lambda = 0.1540598$ nm). Rietveld refinement of the data of filtrate-2h was conducted by using the HighScore Plus 4.6a software (PANalytical). In total four phases were used in the refinement, LiOH (PDF-no. 98-002-7543), $LiOH{\cdot}H_2O$ (PDF-no. 98-000-9138), Li_2CO_3 (PDF-no. 98-006-9133) and $LiAl_2(OH)_7{\cdot}2H_2O$ (PDF-no. 98-007-2979). The surface morphology was investigated by using a high-resolution ZEISS Auriga 60 scanning electron microscope (Carl Zeiss Microscopy GmbH) equipped with an energy-dispersive X-ray spectroscopy detector. Thermogravimetric analysis (NETZSCH STA 449C Jupiter®) with coupled mass spectrometry (NETZSCH QMS 403C Aëolos®) was conducted between 33 °C and 1125 °C in argon with a heating rate of 10 K min^{-1} and using the m/z range from 10 to 200. Throughout the rest of this work, the term H_2O signal, O_2 signal and CO_2 signal will represent m/z = 18, m/z = 32 and m/z = 44 signal, respectively. XPS spectra of NCA-p and NCA-2 h were recorded using a Surface Science Instruments S-Probe X-ray photoelectron spectrometer equipped with a monochromatic Al-K_α X-ray source. Prior to the measurement, the powder were embedded in indium foil. All spectra were calibrated with the C_{1s} peak at 284.6 eV.

Results and Discussion

Analysis of pristine and water-exposed NCA.—The crystallographic structure of pristine (NCA-p) and water-exposed NCA (NCA-2 h and NCA-1w) was examined by XRD (Fig. S1 is available online at stacks.iop.org/JES/167/140535/mmedia). The peaks of each sample can be assigned to a layered α-$NaFeO_2$ structure.[28] A clear splitting of the peak pairs (006)/(102) and (108)/(110) is observed and the I_{003}/I_{004} ratio is determined to be around 1.6, which indicates a well-crystallized structure with low Li^+/Ni^{2+} cation mixing.[29,30] No new species or phase changes could be detected for NCA-2 h and NCA-1w, indicating that the bulk structure of the cathode material remains intact even after water exposure.

Scanning electron microscopy (Fig. 1) was used to examine the surface of NCA in the pristine state, and after two hours and one week water exposure. The secondary particles show a raspberry-like structure with a diameter of around 5 μm. In the magnified images, it can be clearly seen that increased water exposure results in changes at the active material surface. While the surface is smooth for pristine NCA, a fine particulate layer is formed on the surface of the water-exposed samples, which seems to be the most pronounced for NCA-1w. A similar observation was made by Wang et al. for NCA-exposed to moisturized air.[8] In that case, a surface film that grew with exposure time was attributed to the formation of Li_2CO_3.

Thermogravimetric analysis with coupled mass spectrometry was performed to examine the composition of the surface species before and after water exposure (Fig. 2a). The mass loss curves can be found in Fig. S2a. The results were divided into three temperature regions (I: 33 °C–125 °C, II: 125 °C–525 °C and III: 525 °C–1125 °C) analogous to that presented by Sicklinger et al. for data from NCM111 and NCM811 upon storage in moisturized air.[31]

For all samples, there is no mass loss detected in region I. A significant mass loss for NCA-2h (1.1%) and NCA-1w (1.5%) can be detected in region II that increases with prolonged water exposure duration. For NCA-p, the first mass loss occurs in region III at an

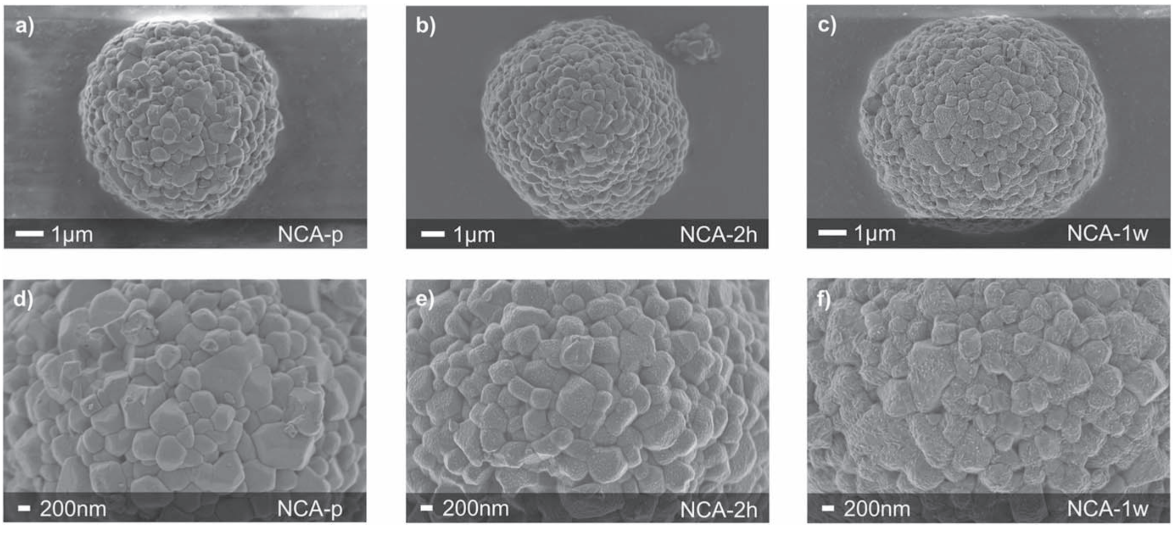

Figure 1. SEM images showing NCA pristine (a, d; NCA-p) and after different water exposure durations (b, e; NCA-2h; c, f; NCA-1w).

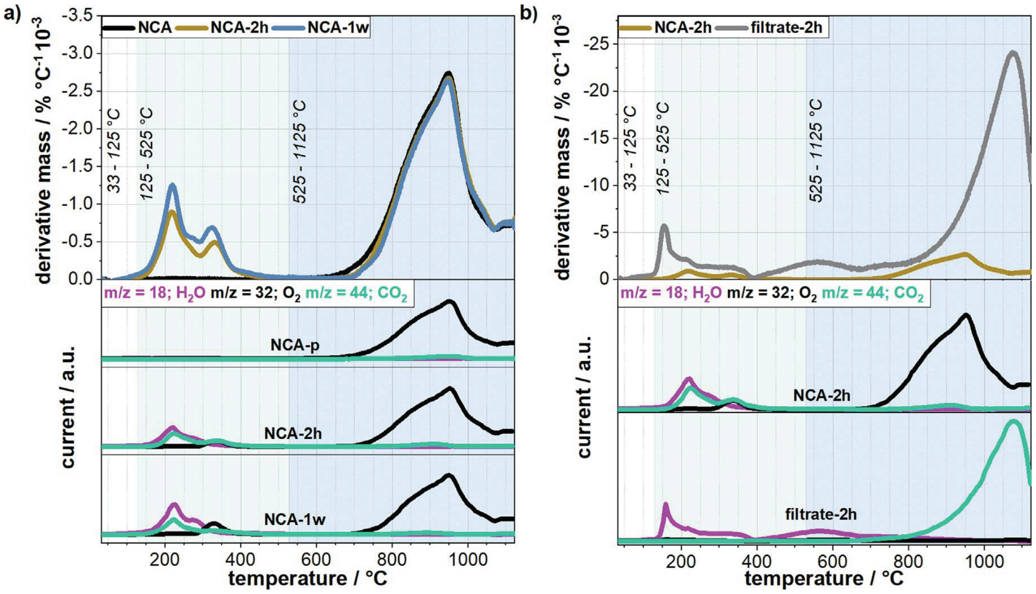

Figure 2. Derivative mass curves for NCA-p/NCA-2h/NCA-1w (a) and NCA-2h/filtrate-2h (b) in the temperature range 33 °C–1125 °C and associated m/z = 18, m/z = 32 and m/z = 44 signals, which were assigned to H_2O, O_2 and CO_2, respectively. The intensity of the mass signal m/z = 44 was multiplied by a factor of 1.5.

onset temperature of ~700 °C. A slightly lower weight decrease is observed in region III for the water-exposed variants (NCA-2h : 5.5%; NCA-1w: 5.3%) than for NCA-p (5.7%). The temperature-dependent mass signals m/z =18, m/z = 32 and m/z = 44 are depicted for all samples in Fig. 2a (bottom). These three m/z signals were assigned to the release of H_2O, O_2 and CO_2, respectively. As with the thermogravimetric results, there are no peaks in the m/z curves in region I. In contrast, in region II H_2O, O_2 and CO_2 signals can be detected for NCA-2h and NCA-1w. For both samples, the first onset of the H_2O and CO_2 signals is ~145 °C. Two peak maxima at ~220 °C/~275 °C and ~220 °C/~330 °C can be found for the H_2O signal and CO_2 signal, respectively. Furthermore, a peak maximum of the O_2 signal lays at ~330 °C in region II. In the last temperature region (III), a significant increase of the O_2 signal and a small CO_2 signal can be detected for all samples.

For a detailed interpretation, these results were compared to data reported in previous literature. Pure Li_2CO_3 has been shown to decompose in argon with the release of CO_2 between 650 °C and 1100 °C.[31,32] Therefore, the small CO_2 signal detected in region III is assigned to the decomposition of Li_2CO_3. Li_2CO_3, even on pristine NCA, is a plausible surface species as it can be used as a precursor for the active material synthesis and small amounts may remain.[33] Interestingly, the intensity of the CO_2 signal decreases from NCA-p to NCA-2h and the signal is negligible for NCA-1w. This correlates well with the lower mass loss for the water-exposed samples in region III. It should be noted that the NCA-2h and NCA-1w samples were obtained after filtering the aqueous NCA/water suspensions. Therefore, this trend may result from an at least partial dissolution of surface Li_2CO_3 (from synthesis) which is enhanced with longer water-exposure time. The pronounced O_2 signal in region III is assigned to the thermal decomposition of the NCA structure. It is known that layered oxide cathode materials decompose at high temperatures (>600 °C) and release oxygen.[31]

Region II is thought to be of specific interest, since a mass loss and m/z signals in this temperature range were only detected for the water-exposed NCA samples. Moreover, water-induced species seem to be continually formed during water exposure since the mass loss is higher for NCA-1w than for NCA-2h. The thermal decomposition of Li(NiCoAl)O_2 powder stored in ambient atmosphere was examined by Faenza et al. and Wu et al.[9,13] Faenza et al. assigned the mass loss detected in the temperature range of region II to the decomposition of $LiHCO_3$ (150 °C–350 °C) and LiOH (350 °C–450 °C). Wu et al. proposed the decomposition of LiOH and Li_2CO_3 starting at 220 °C (although they noted that this temperature is much lower than that for crystalline LiOH and Li_2CO_3). Neither group conducted a coupled mass spectrometry analysis. The decomposition of pure LiOH in argon has been reported to start at around 400 °C and is accompanied by the release of H_2O.[31,32] Since no H_2O signal has been observed around 400 °C, the presence of LiOH is essentially excluded here. Coupled TG/MS data has not been found for $LiHCO_3$. Furthermore, it is unclear from the published literature if this species is stable as a solid at standard conditions.[34] Interestingly, mass loss and the same mass fragment peaks have been observed at similar temperatures in reports with structurally-related layered oxide compounds such as Li(NiCoMn)O_2 and $LiNiO_2$ that have been exposed to ambient air or water.[31,35,36] For instance, Pritzl et al. investigated the effects of washing of NCM851005 particles in degassed water.[35] In the temperature range of region II, they detected two subsequent H_2O-signals with peak maxima at ~180 °C and ~250 °C as well as a maximum in the O_2 signal at ~310 °C. The results were attributed to the thermal decomposition of a NiOOH-like structure formed due to H^+-/Li^+-exchange in the water-exposed NCM. The reported signal sequence is quite similar to that detected for NCA-2h and NCA-1w (H_2O: ~220 °C and ~275 °C, O_2: ~330 °C (peak maxima)). Moreover, this assignment is also supported by a report of Toma et al., where a $Li_{1-x}H_xNiO_2$ structure for ambient air exposed $LiNiO_2$ was proposed on the basis of thermal (significant mass loss between 200 °C–320 °C) and chemical analysis.[36] The stepwise mechanism of the thermal decomposition of pure NiOOH can be found in various publications.[37–39] For example, Hamdan et al. explained that the thermal decomposition of NiOOH begins with water loss from the material surface (0 °C–120 °C), followed by water loss between the NiOOH interlayers (120 °C–280 °C). The final step of the NiOOH decomposition as shown in Eq. 1 occurs between 280 °C–400 °C.

$$2\,\mathrm{NiOOH} \rightarrow 2\,\mathrm{NiO} + \mathrm{H_2O} + 1/2\,\mathrm{O_2} \qquad [1]$$

No mass loss was detected at temperatures lower than 110 °C here as all the samples were pre-dried before the measurement at 110 °C for 16 h in air. In principle, the formation of CoOOH, which has already been reported for washed $LiCoO_2$, would also be conceivable, but a decomposition temperature between 250 °C–270 °C along with the release of O_2 and H_2O would be expected for this species.[40–42] However, due to the comparatively low proportion of cobalt in the NCA structure, these signals might have an intensity that is too low to be clearly detected.

A plausible explanation can be found for the CO_2-signal at ∼330 °C in the report by Sicklinger et al.[31] In this case, a peak maximum for the CO_2 signal at ∼335 °C was detected for NCM111 and NCM811 which was more pronounced for the ambient-stored samples. It was suggested that this signal originates from the decomposition of nickel carbonate species. The formation of nickel carbonate species was also proposed by Jung et al. when analyzing NCM811 stored in ambient air using Raman spectroscopy.[43] The origin of the CO_2 signal at ∼220 °C is a little more difficult to explain. For example it has been reported that chemisorbed CO_2 with mixed carbon-oxygen coordination on NiO has a CO_2 desorption temperature of 240 °C.[44] Moreover, Visbal et al. reported the successful removal of chemisorbed CO_2 species on NCA at a temperature of 250 °C.[45] Although further studies are needed to clarify this point in more detail, this feature could also be associated with chemisorbed CO_2. It should be noted that only components that decompose in the temperature range analyzed above with sufficient signal intensity are identified and thus other surface species may also be present. At the same time it is necessary to note that these results refer to the contact of the cathode material with deionized water. For an aqueous electrode slurry, additional components (additives, binders, etc) are used that can for example modify the pH value and might therefore lead to the formation of other surface species. To investigate the influence of other slurry components further studies are necessary, which is beyond the scope of this work.

NCA-p and NCA-2h were analyzed by XPS to further elucidate the surface composition before and after water exposure. The relative amount of surface lithium for NCA-2h is approximately half that of NCA-p (Table S1). This result is consistent with the dissolution of residual lithium compounds such as lithium carbonate and with the assumption that a Li^+/H^+-exchange occurs when NCA is exposed to water.

The XPS spectra of the O 1s signal can be found in Fig. 3a. Three peaks centered at binding energies of 528.8 eV, 531.2 eV and 533.2 eV can be detected for NCA-p. Based on previous literature, these peaks can be assigned to NCA lattice oxygen (O^{2-}), carbonate and hydroxide species ($O_{CO3}2-$, $_{OH}-$) and adsorbed oxygen containing species ($O_{adsorbed}$), respectively.[9,46,47] The intensity of the latter signal clearly increases in the spectrum of NCA-2h, indicating an increased amount of adsorbed species. In contrast, the signal intensity of O^{2-} is rather unaffected by water-exposure. It should be noted that a O^{2-} signal for NiOOH (a species proposed based on the TG-MS analysis above) is expected around 528.7–529.5 eV and therefore, in the same region as the NCA lattice oxygen.[47,48] As such, it is hard to discern between O^{2-} from NCA and possible newly-formed NiOOH-species. The signal at around 531 eV is mostly assigned in literature to lithium carbonate species on NCA.[9,12] At first glance, due to the solubility of lithium carbonate in water, a decrease in this signal for NCA-2h is expected. Interestingly, the intensity of this signal remains nearly the same. This might be explained by the fact that signals of nickel carbonate and NiOOH (both species proposed based on the TG-MS analysis above) around 531.6 eV[49] and 530.8–532.4 eV,[47,48] respectively, are expected to increase.

The spectra of both samples obtained in the Ni 2p region are depicted in Fig. 3b. For pristine NCA, Haasch and Abraham detected the $2p_{3/2}$ and $2p_{1/2}$ signals centered at a binding energy of 855.2 eV and 872.6 eV.[46] This is in good agreement with the signals detected for NCA-p at 855.0 eV and 872.3 eV. However, at least one other nickel species might be present even on NCA-p as further lower intensity peaks at higher binding energy (Ni'' $2p_{3/2}$: 857.0 eV, Ni'' $2p_{1/2}$: 874.3 eV) can be detected. The intensity of these signals increases for NCA-2h. For NiOOH, the Ni $2p_{3/2}$ signal is expected at a binding energy of around 855.3 eV[48] and therefore cannot be differentiated from the Ni $2p_{3/2}$ signal for NCA. In contrast, the $2p_{3/2}$ signal for nickel carbonate has been reported at a higher binding energy of 856.8 eV.[49] Therefore, the signals at higher binding energy, supported by the TG-MS results, were assigned to nickel carbonate species. Interestingly, in the report by Jung et al. on ambient-aged NCM811, a shift of the Ni $2p_{3/2}$ signal towards higher binding energy compared to the fresh NCM811 has been observed, but could not be explained.[43] It is possible that the peak shift in their study might be also related to nickel carbonate as they were able to detect such species on the ambient-aged NCM811 sample by Raman spectroscopy, as described in the previous section.

The spectra obtained in the Al 2p and Co 2p region can be found in Figs. S3a, S3b. For NCA-p, one Al 2p signal was detected and, based on previous literature, assigned to aluminum from the NCA structure.[46,50] For NCA-2h, a second aluminum signal (Al'' 2p) is clearly observable at 75.8 eV. For $Al(OH)_3$ and AlOOH species, Lindsay et al. reported binding energies in the range of 74.7 eV–75.7 eV.[51] The latter compound has been proposed to be formed upon water contact in Part I.[14] Additional signals can be found for NCA-2h in the cobalt region at 782.9 eV (Co'' $2p_{3/2}$) and 797.9 eV (Co'' $2p_{1/2}$) which might be attributed to $Co(OH)_2$. In a work on the electrochemical oxidation of Co metal in alkaline

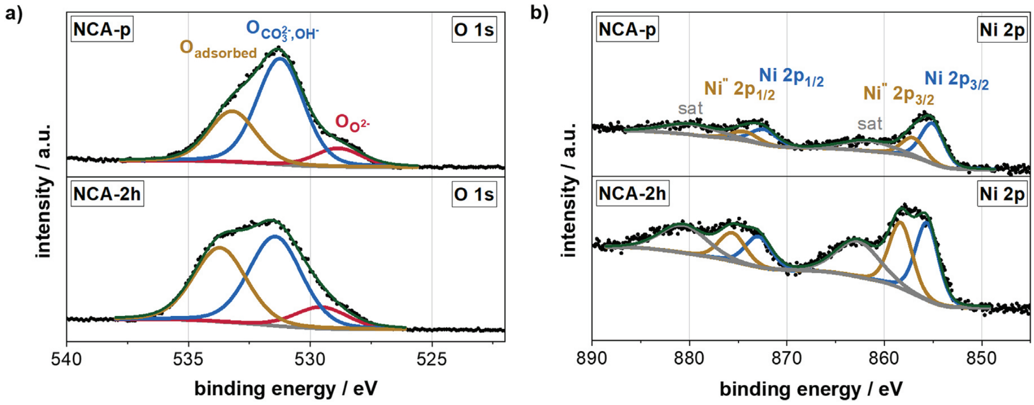

Figure 3. XPS spectra of NCA-p and NCA-2h recorded in the O 1s (a) and Ni 2p (b) region.

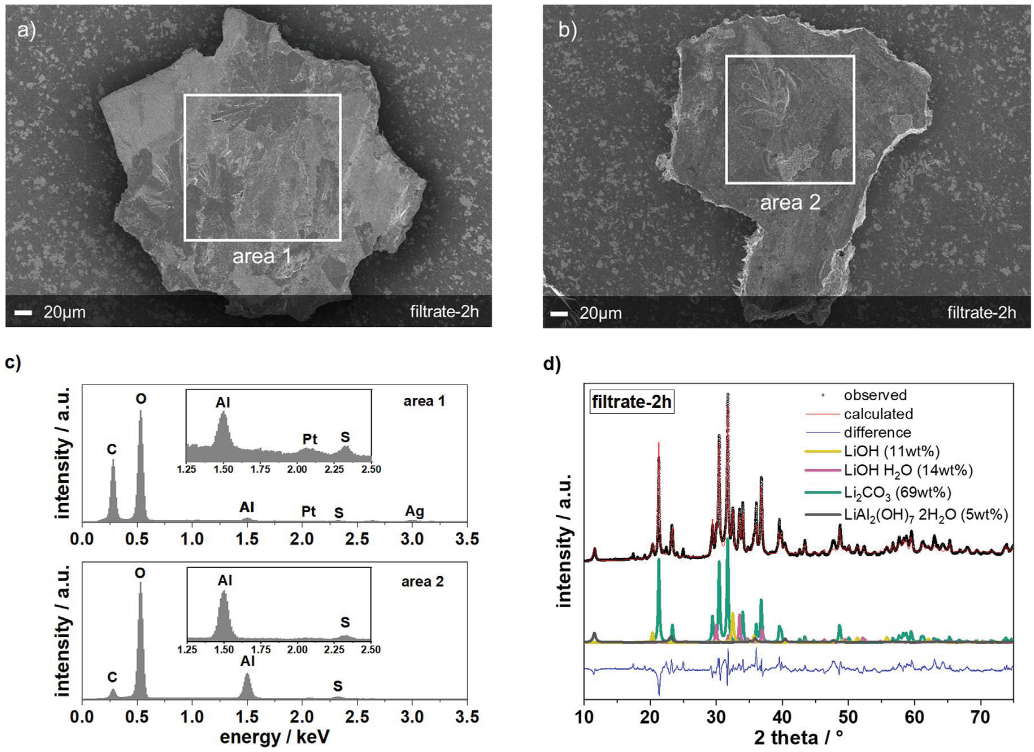

Figure 4. SEM images of filtrate-2h (a), (b) and associated EDS-spectra (c). XRD spectrum of filtrate-2h and Rietveld refinement (d).

conditions by Han et al., $Co(OH)_2$ was the only cobalt-containing compound with a $2p_{3/2}$ signal above 781.0 eV.[52] As the Al- and Co-compounds only represent a small fraction of the surface species, as would be expected given the high nickel content in the NCA structure, the TG-MS analysis were attributed to nickel-containing species. Finally, the detection of a S $2p_{3/2}$ (168.9 eV) and S $2p_{1/2}$ (170.9 eV) signal for NCA-p, which is not observed for NCA-2h , is noteworthy (Fig. S3c) . Sulfate salts are often used as precursors for the synthesis of layered-oxide cathode materials.[53–55] Therefore, it is possible that the pristine NCA had traces of, e.g., residual lithium sulfate on the surface which would dissolve upon contact of the NCA particles with water. A sulfur signal was also evident in the XPS data of Haasch and Abraham for NCA from the same supplier.[46] It should be noted that the surface properties of the pristine particle (including possible precursor residues) depend on the manufacturing process (nature and mixing of the metal precursors, particle size, storage conditions, etc.) and can therefore vary from sample to sample.

Based on the TG-MS and XPS data, the species formed on the NCA surface upon water contact and decomposing below 500 °C are mainly attributed to chemically-adsorbed CO_2, nickel carbonates and NiOOH-like species. New water-induced aluminum- and cobalt-species were evident from XPS data, but seem to be only present in smaller amounts.

Analysis of the filtrate.—In Part I of these two publications, it was shown that significant amounts of lithium and also aluminum was detected by ICP-OES in the filtrate of NCA-water suspensions, but no nickel or cobalt was detected.[14] The water-induced surface species described above were mainly assigned to nickel compounds. Therefore, it is assumed that in the context of aqueous electrode processing, there must be a clear differentiation between species formed on the active materials surface and leached species. To clarify this aspect, the TG-MS results of NCA-2h were compared to those of the dried filtrate-2h as shown in Fig. 2b. The mass loss curve for filtrate-2h can be found in Fig. S2b.

The m/z signals show that the compounds on the particle surface and in the filtrate differ. The highest mass loss for filtrate-2h is seen in region III and associated with a release of CO_2 starting at ∼800 °C. This signal is at least partially attributed to the decomposition of lithium carbonate,[31,32] which in the filtrate might stem from: 1) the dissolution of lithium carbonate from the pristine active materials surface (as described above); 2) newly formed Li_2CO_3 built in a multistep mechanism starting with spontaneous reduction of Ni^{3+} to Ni^{2+} accompanied by the reaction of active oxygen with water and CO_2; or 3) from lithium liberated during a proton-exchange process upon water contact which forms lithium hydroxide and can further react with CO_2 to lithium carbonate.[14,56–58] The H_2O signal with an onset of around ∼400 °C is associated to the thermal decomposition of lithium hydroxide.[32,43] The H_2O signals arising at ∼150 °C might be related to removal of crystal water of lithium hydroxide[59] and/or the loss of water followed by stepwise condensation of different OH groups in aluminum compounds such as $LiAl_2(OH)_7 \times H_2O$.[60] The latter compounds were proposed to be built upon the contact of NCA with water in Part I.[14]

A SEM/EDS analysis was conducted on filtrate-2h to provide further evidence for the composition of the filtrate species. In Figs. 4a and 4b SEM images of two different filtrate-2h particles are depicted. Both samples show different bright areas within the large particles, indicating that a mixture of compounds is present. The associated EDS spectra can be found in Fig. 4c. The elements C, O and Al can be clearly detected in both spectra. Moreover, a sulfur signal with relatively low intensity can be detected, which is in accordance with the XPS results shown above. It should be noted that the Ag and Pt signal in area 1 stems from the SEM/EDS sample preparation process. Furthermore, the detection of lithium via EDS is

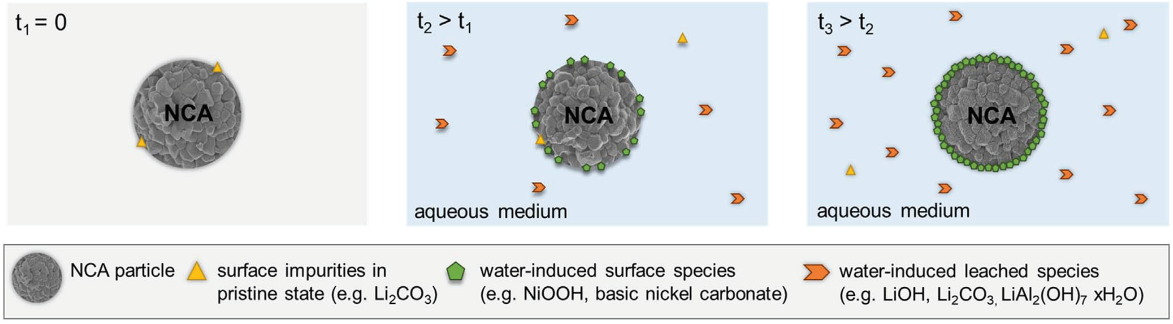

Figure 5. Proposed evolution of surface and leached species on NCA during prolonged water exposure.

not possible due to the low energy of Li-K_α X-rays (at least with the equipment used here). However, the presence of lithium was already demonstrated by ICP-OES analysis in Part I.[14]

The XRD analysis of the dried filtrate further supports the assignments made above. The main peaks can be assigned to Li_2CO_3, LiOH and $LiOH{\cdot}H_2O$ (Fig. 4d). Moreover, the presence of $LiAl_2(OH)_7 \cdot 2H_2O$ seems to be plausible. The phase quantification by Rietveld refinement of the crystalline part of filtrate-2 h yields 11% of LiOH, 14% of $LiOH{\cdot}H_2O$, 69% of Li_2CO_3 and 5% of $LiAl_2(OH)_7{\cdot}2H_2O$. However, from the difference curve it is clear that also other phases (e.g. sulfur containing compounds) could be present in the filtrate since not all of the reflections can be attributed to the refined phases. Nonetheless, it can be assumed that the weight percentages of these phases are rather small due to the low intensity of the unassigned peaks.

Summary of physical and chemical characterization results.—In summary, when NCA is exposed to water, e.g. during aqueous processing, the following processes occur: 1) the removal of surface impurities (e.g. Li_2CO_3) from the pristine NCA; 2) the water-induced leaching of lithium and aluminum that can be detected in water (forming e.g. LiOH, Li_2CO_3, $LiAl_2(OH)_7 \times H_2O$); and 3) the formation of water-induced surface species (e.g. NiOOH, basic nickel carbonate). These three processes are illustrated in Fig. 5. The involvement of aluminum in the leaching process is particularly noteworthy and may be at least partially responsible for the extreme moisture sensitivity of NCA as it may destabilize the surface structure. In comparison, there were no transition metals in the filtrate of various NCM materials in Part I.[14] This is likely at least partially responsible for the better electrochemical performance of these materials as compared to NCA.

Impact of water-induced surface species on the electrochemical performance.—The influence of the water-induced surface species on the electrochemical performance was investigated using pristine (NCA-p) and water-exposed NCA (NCA-2h, NCA-8h and NCA-1w) that was processed in conventional NMP/PVDF-based slurries. Water-based processing was not used for the further investigation presented here as the overvoltage in the results presented in Part I was so high that the cells were essentially electrochemically inactive.[14] The results obtained during the formation cycles are depicted in Fig. 6. Figure 6a shows the specific discharge capacity over the cycle number. The average specific discharge capacity is highest for the cells with NCA-p during the whole formation protocol followed by the cells of NCA-2h , NCA-8h and NCA-1w, which deliver 192.0 mAh g^{-1}, 189.4 mAh g^{-1}, 187.8 mAh g^{-1} and 180.9 mAh g^{-1} in the last formation cycle, respectively. The lower capacity with increasing water exposure duration is not surprising, since the water-induced changes lead to at least a partial modulation of the original active material surface structure and thus a reduced storage of lithium ions. The discharge capacity increases from the 1st to the 5th formation cycle by 3.1 mAh g^{-1}, 3.0 mAh g^{-1}, 4.0 mAh g^{-1} and 7.6 mAh g^{-1} for the cells with NCA-p, NCA-2 h, NCA-8 h and NCA-1w, respectively. As this effect can also be observed for NCA-p, it can be at least partially associated with the generation of more accessible active material surface area from cycle to cycle induced by the expansion and contraction of the cathode particles during charge and discharge.[14] This effect is most pronounced for the cells with NCA-1w, which was exposed to water the longest. As such, this result, along with the assumption that water-induced NiOOH-surface species form, might be an indicator for a regeneration of the active material via a reverse Li^+-/H^+-exchange mechanism as proposed by Shkrob et al.[56] However, the release of protons can simultaneously result in a side reaction with the $LiPF_6$-containing electrolyte, which leads to enhanced cell degradation during cycling.[61] The associated coulombic efficiencies are shown in Fig. 6b. It is striking that the initial coulombic efficiency is lower for NCA-p (88.7%) as compared to the water-exposed NCAs (≈93%), which suggests less side reactions occur in the first cycle. Xu et al. also observed higher initial coulombic efficiencies for cells containing washed $LiNi_{0.83}Co_{0.13}Mn_{0.04}O_2$ than those with the original active material.[62] This result was attributed to the removal of lithium carbonate remaining from the synthesis. These species are known to be at least partially involved in gassing reactions in the first cycle.[8,35,63–66] However, it should be noted that in the case of aqueous-electrode processing, where no filtration step is involved, as was carried out in the water-exposure experiments here, dissolved surface lithium carbonate from the synthesis process and leached species would still be present within the electrode. After the first cycle, the coulombic efficiency is highest for NCA-p during the whole formation protocol. This may be attributed to increased side reactions in the cells containing the water-exposed NCA involving protons from a reversed Li^+-/H^+-exchange or side reactions involving the water-induced surface species.[31,61]

The exposure of NCA to water also significantly influences the shape of the voltages profiles (Figs. 6c and 6d). As soon as the charge current is applied, an initial overvoltage can be detected in the first cycle, which is most pronounced for the cells with NCA-1w followed by NCA-8h , NCA-2h and NCA-p. Therefore, the overvoltage seems to be dependent on the water-exposure time and thus likely the amount of water-induced surface species. Similar phenomena were previously reported and were ascribed to a barrier layer on the active material surface that impeded the extraction of lithium ions.[9,43,56] The initial overvoltage of the cell containing NCA-1w (inset of Fig. 6c) is quite close to the cut-off voltage of 4.3 V. This is consistent with the electrochemical inactivity of NCA cells with aqueous-processed electrodes in Part I, where the initial overvoltage quickly exceeded the cut-off voltage.[14] The voltage directly drops for the cells with NCA-p and then increases slowly to the cut-off voltage of 4.3 V after the initial overvoltage. In contrast, the cells with NCA-2h , NCA-8h and NCA-1w show further fluctuations in the voltage profile, which suggest further side reactions in the first cycle. It seems, however, the surface layer is either modified or partially removed such that lithium intercalation/deintercalation pathways are (re)formed since the overvoltage is

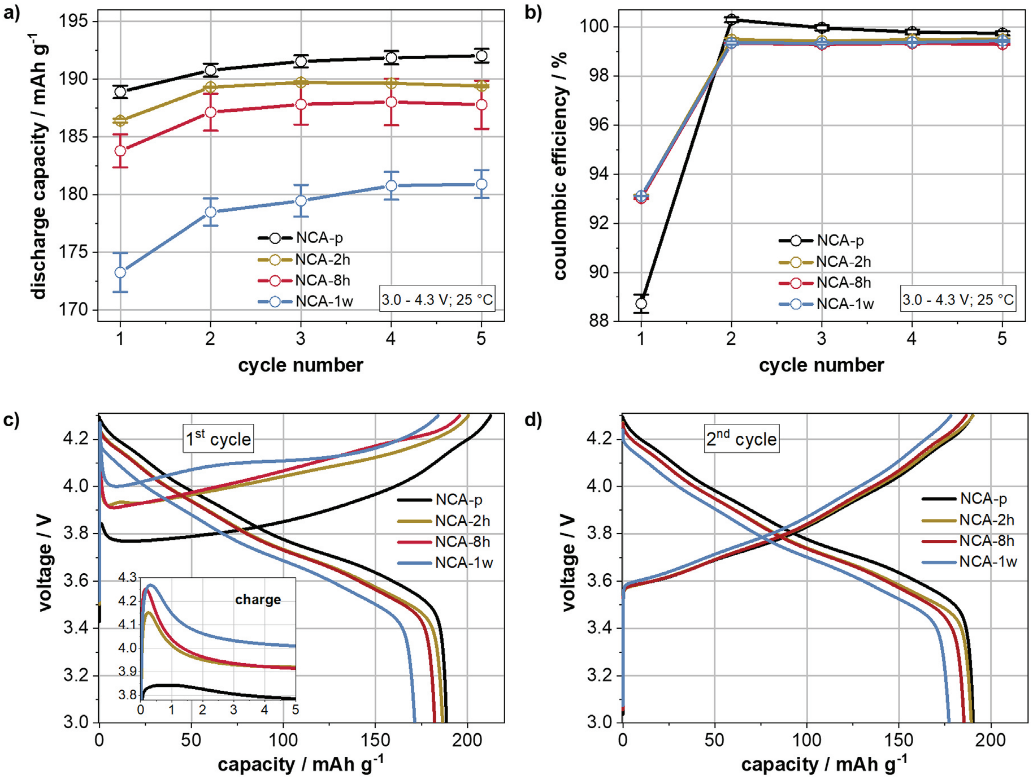

Figure 6. Results of the formation cycles for cells with NMP-processed electrodes containing NCA-p, NCA-2h, NCA-8h and NCA-1w: discharge capacity over formation cycle number (a), coulombic efficiency over formation cycle number (b) and voltage profiles of a representative cell of each combination in the 1st and 2nd cycle (c), (d). The data in (a) and (b) are the average specific discharge capacity of three cells and the error bars relate to the standard deviation between these cells.

significantly reduced in the second cycle. The cell polarization remains higher in the second cycle for the cells with NCA-2h, NCA-8h and NCA-1w, thus suggesting that the surface effects are not completely reversible.

Cyclic voltammetry measurements were exemplary conducted for cells with NCA-p, NCA-2h and NCA-1w between 2.7 V and 4.5 V (Fig. 7). The typical phase transitions of NCA, i.e. hexagonal (H1) to monoclinic (M), monoclinic (M) to hexagonal (H2) and hexagonal (H2) to hexagonal (H3) can be detected in the 2nd and 3rd cycle (and the reverse scan in the 1st cycle).[67–69] The forward scan in the first cycle differs significantly for all three materials. The maximum of the current signal is detected at 3.97 V, 4.22 V and 4.39 V for the cells with NCA-p, NCA-2h and NCA-1w, respectively. The shift of this current signal to higher voltages with prolonged water exposure follows the trend of the initial overvoltage in the first formation cycle (Fig. 6c), thus supporting the conclusion that the amount of surface species increases with prolonged water exposure. Furthermore, the phase transitions are at least partially overlapped for NCA-2h and NCA-1w in the 2nd and 3rd cycles (Figs. 7b and 7c). This might be associated with a more impeded lithium insertion and extraction with water-exposed NCA particles that slows the electrochemical processes. Interestingly, a slight shift in the onset of the first oxidation peak to lower voltages for NCA-1w can be observed from the 2nd to the 3rd cycle. This might be related to a partial regeneration of the active material surface structure as discussed above.

To further elucidate the electrochemical performance, impedance spectra were recorded after the formation for cells containing

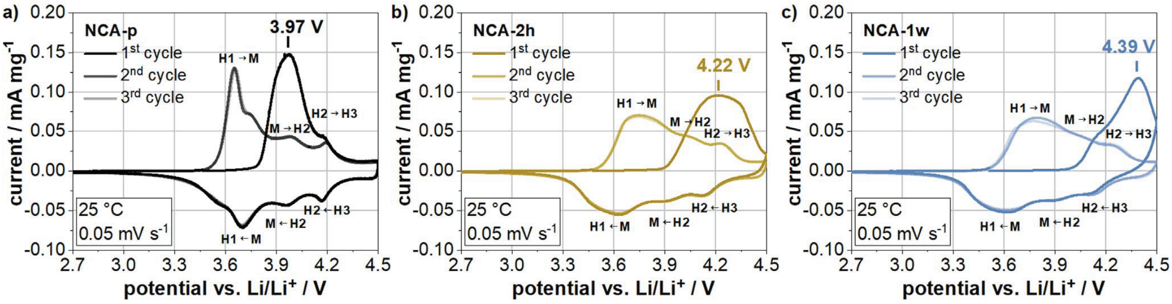

Figure 7. Cyclic voltammetry measurements at a scan rate of 0.05 mVs^{-1} between 2.7 V and 4.5 V for three cycles of cells containing NCA-p (a), NCA-2h (b) and NCA-1w (c).

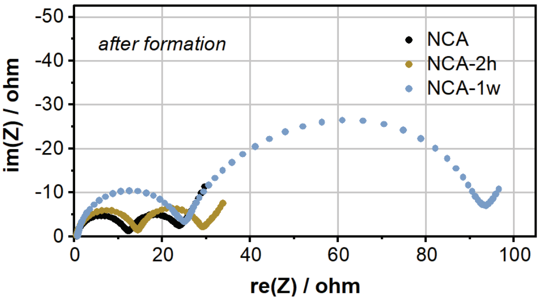

Figure 8. Electrochemical impedance spectra of cells containing NMP-based electrodes with NCA-p, NCA-2h and NCA-1w at 4.3 V after the formation protocol.

NCA-p, NCA-2h and NCA-1w (Fig. 8). The Nyquist plot from each cell has a high frequency intersection with the *x*-axis, followed by two semicircles and an inclined line at low frequencies. These features are associated with ohmic resistances within the cell (R_s), surface film impedance (R_f)/surface film capacitance, charge transfer impedance (R_{ct})/double layer capacitance and solid-state diffusion, respectively.[70] The associated Bode plots can be found in Fig. S4. It should be noted that in Part I of these two publications, three semicircles were identified in the Nyquist plot of cells with water-based electrodes, but were rather difficult to discern for the cells with NMP-based electrodes.[14] The differences may have resulted from the different binders and therefore different interactions with the cathode material. Here, the presence of a third semicircle should also not be excluded (in cells with NMP-based electrodes). However, as a third semicircle is difficult to clearly discern with the eye, the interpretation was carried out with only two semicircles. The fit model and the values obtained for R_s, R_f, and R_{ct} can be found in Fig. S5 and Table S2, respectively. As expected, R_s is similar for all cell variants. The impedance associated with both semicircles, i.e. with R_f and R_{ct}, increases from NCA-p to NCA-2h and NCA-1w. The increase in impedance demonstrates the resistive nature of the water-induced surface species, but might also be influenced by the deposition of electrolyte decomposition products resulting from the reaction of surface species with the electrolyte. A similar trend was also reported by You et al. when comparing the impedance spectra of cells containing electrodes with fresh and ambient air-exposed $LiNi_{0.94}Co_{0.06}O_2$ cells, which was attributed to aging-induced passive layers on the active material surface.[71]

The cells shown in Fig. 6 were cycled between 3.0 V and 4.3 V with an initial C/10 cycle and subsequent cycles at 1C. The cycling data is shown in Fig. 9 and Fig. S6. The average discharge capacity decreases in the order NCA-p > NCA-2h > NCA-8h > NCA-1w (Fig. 9a). The cells with NCA-p show a relatively stable cycling behavior, while the degradation of the cells with water-exposed NCA occurs much faster. This observation is consistent with the results of Wu et al. for air-exposed NCA as compared to fresh NCA and suggests that the water-induced surface species are involved in more side reactions which lead to the cell degradation.[13] The cell degradation is also reflected in the capacity retention, which is 94.5%, 80.9% 80.8% and 76.6% for cells with NCA-p, NCA-2h, NCA-8 h and NCA-1w, respectively. As expected from the results above, the cell polarization remains highest for the cells containing NCA-1w electrodes followed by NCA-8h, NCA-2h and NCA-p, which can be seen particularly when the current rate is increased from C/10 to 1C (Figs. 9b, 9c). The increased polarization has a direct impact on the capacity in the CC and CV charge steps. During

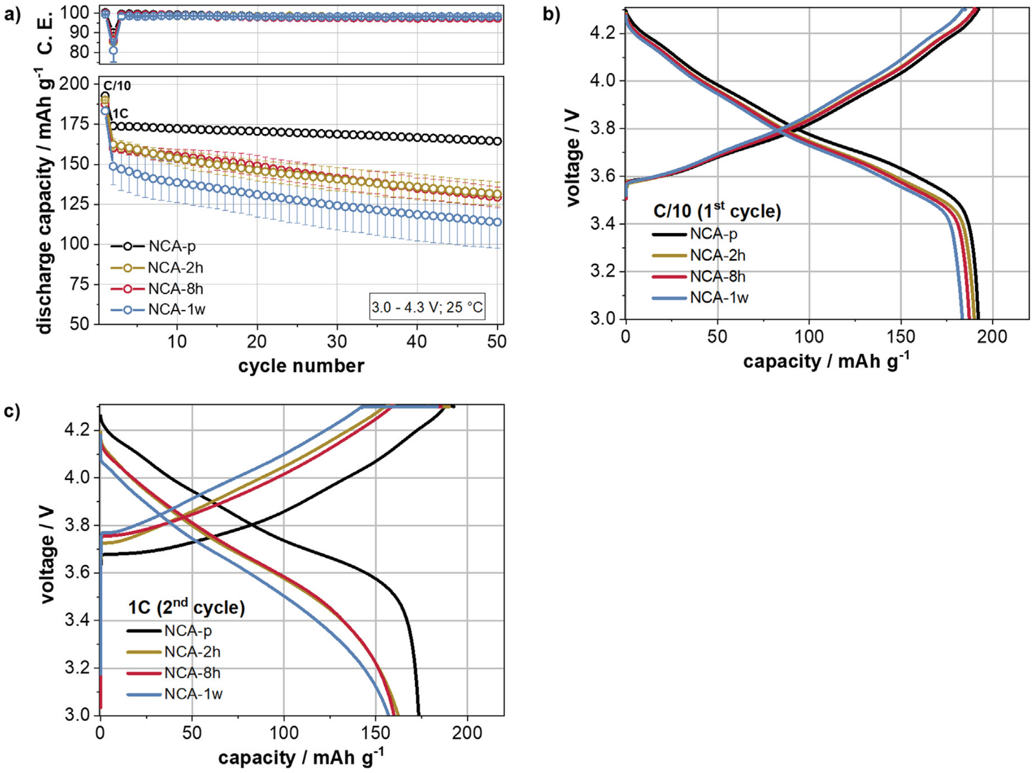

Figure 9. Cycle performance of half-cells containing NMP-processed cathodes with NCA-p, NCA-2h, NCA-8h and NCA-1w (a). Corresponding voltage profiles of a representative cell of NCA-p, NCA-2h, NCA-8h and NCA-1w at low (C/10, (b)) and high (1C, (c)) current rate. The data in (a) represent the average specific discharge capacity of three cells and the error bars relate to the standard deviation between these cells.

cycling the capacity in the CC step decreases and in the CV step increases more pronounced for the cells with water-exposed NCA (Fig. S6). This indicates that the damage of NCA upon water contact not only impacts the initial cycles, but leads to further cell degradation in the subsequent cycles.

Conclusions

Through the investigation of water-exposed NCA particles, new surface species, the amount of which seem to increase with exposure time, have been detected. These water-induced surface species are mainly assigned to chemisorbed CO_2, basic nickel carbonate and NiOOH-like species and lower amounts of newly-formed aluminum and cobalt species. In addition, water-induced leaching occurs primarily in the form of Li_2CO_3, LiOH and notably also aluminum compounds. In the context of aqueous processing, the water-induced surface species remain at the active material surface, while the leached species would likely deposit on the surface of the other electrode components as well. In particular, the involvement of aluminum in the leaching process may cause an enhanced destabilization of the NCA surface, which would explain the high water-sensitivity of NCA compared to NCM materials as shown in Part I of this work.[14]

Cells with water-exposed NCA show a high initial overvoltage in the first cycle, a decreased capacity and higher cell polarization most likely due to the resistive nature of the water-induced surface species and the degradation of the NCA structure at the particle surface. As a consequence, an aqueous electrode manufacturing process would likely result in an even higher amount of water-induced surface species, along with the deposition of the water-induced leached species. As such, the lithium ion insertion and extraction would be almost completely impeded, which explains the negligible performance of cells with water-based NCA-electrodes (as observed in Part I).[14] Moreover, it is assumed that a Li^+-/H^+-exchange occurs for NCA in aqueous medium due to the detection of NiOOH-like species and a continuous increase of the discharge capacity in the first cycles, which is most pronounced for the cells with NCA with longest water exposure duration. This effect of water exposure can be partially reversed. However, a full regeneration of water-exposed NCA during cycling does not occur and further side reactions involving the water-induced surface species lead to severe deterioration of the electrochemical performance reflected in a low capacity retention of 76.6% for cells with NCA exposed to water for one week as compared to 94.5% for cells with pristine NCA. Although these results, at first glance, suggest that aqueous processing of NCA is not promising, it is likely that modification of the particle surface to control or suppress the formation of water-induced species may provide a solution to the challenges discussed here.

Acknowledgments

The contributions of Felix Nagler (Fraunhofer ISC) for scientific discussion and support for Rietveld refinement and of Angelika Schmitt (Fraunhofer ISC) for the XPS measurements are gratefully acknowledged. The SEM analysis and electrochemical tests were performed as part of the project NeW-Bat (grant no. 033R174A) which was funded by the Federal Ministry of Education and Research of Germany. The authors further acknowledge the financial support from the Bavarian Ministry of Economic Affairs and Media, Energy and Technology for funding the Fraunhofer R&D Center for Electromobility Bavaria FZEB (grant no. 43-6629/86).

ORCID

Guinevere A. Giffin https://orcid.org/0000-0002-2303-9560

References

1. W. Li, E. M. Erickson, and A. Manthiram, *Nat. Energy*, **5**, 26 (2020).
2. S. S. Zhang, *Energy Storage Mater.*, **24**, 247 (2020).
3. J. Kim, H. Lee, H. Cha, M. Yoon, M. Park, and J. Cho, *Adv. Energy Mater.*, **8**, 1702028 (2018).
4. D. Caurant, N. Baffier, B. Garcia, and J. P. Pereira-Ramos, *Solid State Ion.*, **91**, 45 (1996).
5. M. Guilmard, L. Croguennec, D. Denux, and C. Delmas, *Chem. Mater.*, **15**, 4476 (2003).
6. M. Bianchini, M. Roca-Ayats, P. Hartmann, T. Brezesinski, and J. Janek, *Angew. Chem. Int. Ed.*, **58**, 10434 (2019).
7. N. Nitta, F. Wu, J. T. Lee, and G. Yushin, *Mater. Today*, **18**, 252 (2015).
8. C. Wang, L. Shao, X. Guo, X. Xi, L. Yang, C. Huang, C. Zhou, H. Zhao, D. Yin, and Z. Wang, *ACS Appl. Mater. Interfaces*, **11**, 44036 (2019).
9. N. V. Faenza, L. Bruce, Z. W. Lebens-Higgins, I. Plitz, N. Pereira, L. F. J. Piper, and G. G. Amatucci, *J. Electrochem. Soc*, **164**, A3727 (2017).
10. S.-W. Song, G. Zhuang, and P. Ross, *J. Electrochem. Soc.*, **151**, A1162 (2004).
11. K. Matsumoto, R. Kuzuo, K. Takeya, and A. Yamanaka, *J. Power Sources*, **81–82**, 558 (1999).
12. A. Grenier, H. Liu, K. M. Wiaderek, Z. W. Lebens-Higgins, O. J. Borkiewicz, L. F. J. Piper, P. J. Chupas, and K. W. Chapman, *Chem. Mater.*, **29**, 7345 (2017).
13. N. Wu, H. Wu, J.-K. Kim, X. Liu, and Y. Zhang, *ChemElectroChem*, **5**, 78 (2018).
14. M. Hofmann, M. Kapuschinski, U. Guntow, and G. A. Giffin, *J. Electrochem. Soc.*, **167**, 140512 (2020).
15. M. Hofmann, F. Nagler, M. Kapuschinski, U. Guntow, and G. A. Giffin, *ChemSusChem*, **13** (2020).
16. Y. Liu et al., *J. Appl. Electrochem.*, **49**, 99 (2019).
17. T. Tanabe et al., *Electrochim. Acta*, **258**, 1348 (2017).
18. K. Kimura, K. Onishi, T. Sakamoto, K. Asami, and M. Yanagida, *J. Electrochem. Soc*, **166**, A5313 (2019).
19. K. Kimura, T. Sakamoto, T. Mukai, Y. Ikeuchi, N. Yamashita, K. Onishi, K. Asami, and M. Yanagida, *J. Electrochem. Soc*, **165**, A16 (2018).
20. T. Watanabe et al., *RSC Adv.*, **10**, 13642 (2020).
21. I. Doberdò, N. Löffler, N. Laszczynski, D. Cericola, N. Penazzi, S. Bodoardo, G.-T. Kim, and S. Passerini, *J. Power Sources*, **248**, 1000 (2014).
22. M. Memm, A. Hoffmann, and M. Wohlfahrt-Mehrens, *Electrochim. Acta*, **260**, 664 (2018).
23. W. Bauer, F. A. Çetinel, M. Müller, and U. Kaufmann, *Electrochim. Acta*, **317**, 112 (2019).
24. D. Bresser, D. Buchholz, A. Moretti, A. Varzi, and S. Passerini, *Energy Environ. Sci.*, **11**, 3096 (2018).
25. L. Ibing, T. Gallasch, P. Schneider, P. Niehoff, A. Hintennach, M. Winter, and F. M. Schappacher, *J. Power Sources*, **423**, 183 (2019).
26. K. Soeda, M. Yamagata, and M. Ishikawa, *ECS Trans.*, **64**, 13 (2015).
27. S. Pedaballi and C.-C. Li, *J. Power Sources*, **472**, 228552 (2020).
28. Z. Wang, H. Liu, J. Wu, W.-M. Lau, J. Mei, H. Liu, and G. Liu, *RSC Adv.*, **6**, 32365 (2016).
29. H. Li, P. Zhou, F. Liu, H. Li, F. Cheng, and J. Chen, *Chem. Sci.*, **10**, 1374 (2019).
30. C. Song, W. Wang, H. Peng, Y. Wang, C. Zhao, H. Zhang, Q. Tang, J. Lv, X. Du, and Y. Dou, *Appl. Sci.*, **8**, 378 (2018).
31. J. Sicklinger, M. Metzger, H. Beyer, D. Pritzl, and H. A. Gasteiger, *J. Electrochem. Soc*, **166**, A2322 (2019).
32. H. Beyer, S. Meini, N. Tsiouvaras, M. Piana, and H. A. Gasteiger, *Phys. Chem. Chem. Phys.*, **15**, 11025 (2013).
33. Y. Matsubara, M. Ueda, I. Hidetoshi, and F. Tadashi, *Lithium/nickel/cobalt Composite Oxide, Process for Preparing the Same, And Cathode Active Material for Rechargeable Battery*, WO1998006670A1 (1998), https://patents.google.com/patent/WO1998006670A1/en.
34. Y. Duan, B. Zhang, D. C. Sorescu, J. Karl Johnson, E. H. Majzoub, and D. R. Luebke, *J. Phys. Condens. Matter.*, **24**, 325501 (2012).
35. D. Pritzl, T. Teufl, A. T. S. Freiberg, B. Strehle, J. Sicklinger, H. Sommer, P. Hartmann, and H. A. Gasteiger, *J. Electrochem. Soc*, **166**, A4056 (2019).
36. T. Toma, R. Maezono, and K. Hongo, *ACS Appl. Energy Mater.*, **3**, 4078 (2020).
37. M. S. Hamdan, Riyanto, and M. R. Othman, *Int. J. Electrochem. Sci.*, **8**, 4747 (2013), http://www.electrochemsci.org/papers/vol8/80404747.pdf.
38. T. S. Horányi, *Thermochim. Acta*, **137**, 247 (1989).
39. J. Pan, Y. Sun, P. Wan, Z. Wang, and X. Liu, *Electrochem. Commun.*, **7**, 857 (2005).
40. J. Yang, H. Liu, W. N. Martens, and R. L. Frost, *J. Phys. Chem. C*, **114**, 111 (2010).
41. Z. P. Xu and H. C. Zeng, *J. Mater. Chem.*, **8**, 2499 (1998).
42. S. Jeong, J. Kim, and J. Mun, *J. Electrochem. Soc*, **166**, A5038 (2019).
43. R. Jung, R. Morasch, P. Karayaylali, K. Phillips, F. Maglia, C. Stinner, Y. Shao-Horn, and H. A. Gasteiger, *J. Electrochem. Soc*, **165**, A132 (2018).
44. M. Hasmizam Razali, U. Ismail, M. Zul Helmi Mohd Rozaini, and M. Yusoff, *Orient. J. Chem.*, **33**, 1864 (2017).
45. H. Visbal, S. Fujiki, Y. Aihara, T. Watanabe, Y. Park, and S. Doo, *J. Power Sources*, **269**, 396 (2014).
46. R. T. Haasch and D. P. Abraham, *Surf. Sci. Spectra*, **26**, 14003 (2019).
47. B. P. Payne, M. C. Biesinger, and N. S. McIntyre, *J. Electron. Spectros. Relat. Phenomena*, **175**, 55 (2009).
48. A. N. Mansour and C. A. Melendres, *Surf. Sci. Spectra*, **3**, 271 (1994).
49. Y. Ji, M. Ma, X. Ji, X. Xiong, and X. Sun, *Front. Chem. Sci. Eng.*, **12**, 467 (2018).
50. Y. Lu et al., *ACS Sustainable Chem. Eng.*, **8**, 14975 (2020).
51. J. R. Lindsay, H. J. Rose, W. E. Swartz, P. H. Watts, and K. A. Rayburn, *Appl. Spectrosc.*, **27**, 1 (1973).
52. Y. Han, S. Axnanda, E. J. Crumlin, R. Chang, B. Mao, Z. Hussain, P. N. Ross, Y. Li, and Z. Liu, *J. Phys. Chem. B*, **122**, 666 (2018).
53. H. Watanabe, D. Morita, M. Yamamoto, K. Koga, A. Kajiyama, H. Masukuni, H. Sadamura, R. Masaki, and K. Matsumoto, *A Nickel-Nickel Composite Oxide Particle Powder and A Method for Producing The Same, A Positive Electrode Active Material Particle Powder For A Nonaqueous Electrolyte Battery, A Method for*

Producing the Same, And a Nonaqueous Electrolyte Battery, TWI568068B (2017), https://patents.google.com/patent/TWI568068B/en.

54. M. Yamamoto, D. Nishikawa, K. Ishizaki, O. Sasaki, and H. Sadamura, *Positive Electrode Active Substance Precursor Particles, Positive Electrode Active Substance Particles and Non-Aqueous Electrolyte Secondary Battery*, US20160111725A1 (2016), https://patents.google.com/patent/US20160111725A1/en.
55. C. Wu, C. Tan, L. Yan, D. Huang, R. Chen, Z. Zhang, C. Yuan, and H. Luo, *Methods For Preparing Nickel-Cobalt-Aluminum Precursor Material And Cathode Material With Gradient Distribution Of Aluminum Element*, EP3297072B1 (2019), https://patents.google.com/patent/EP3297072B1/en.
56. I. A. Shkrob, J. A. Gilbert, P. J. Phillips, R. Klie, R. T. Haasch, J. Bareño, and D. P. Abraham, *J. Electrochem. Soc*, **164**, A1489 (2017).
57. H. S. Liu, Z. R. Zhang, Z. L. Gong, and Y. Yang, *Electrochem. Solid-State Lett.*, **7**, A190 (2004).
58. J. Paulsen and J. Kim, *High Nickel Cathode Material Having Low Soluble Base Content* (2017), https://patents.google.com/patent/US20140054495A1/en.
59. J. Kim, H. Kang, K. Hwang, and S. Yoon, *Molecules*, **24**, 4624 (2019).
60. O. D. Pavel, R. Zăvoianu, R. Bîrjega, and E. Angelescu, *Mater. Res. Bull.*, **45**, 1106 (2010).
61. S. Solchenbach, M. Metzger, M. Egawa, H. Beyer, and H. A. Gasteiger, *J. Electrochem. Soc*, **165**, A3022 (2018).
62. S. Xu, X. Wang, W. Zhang, K. Xu, X. Zhou, Y. Zhang, H. Wang, and J. Zhao, *Solid State Ion.*, **334**, 105 (2019).
63. J. Kim, Y. Hong, K. S. Ryu, M. G. Kim, and J. Cho, *Electrochem. Solid-State Lett.*, **9**, A19 (2006).
64. R. Jung, M. Metzger, F. Maglia, C. Stinner, and H. A. Gasteiger, *J. Electrochem. Soc*, **164**, A1361 (2017).
65. S. E. Renfrew, L. A. Kaufman, and B. D. McCloskey, *ACS Appl. Mater. Interfaces*, **11**, 34913 (2019).
66. S. E. Renfrew and B. D. McCloskey, *ACS Appl. Energy Mater.*, **2**, 3762 (2019).
67. L. Zhang, J. Fu, and C. Zhang, *Nanoscale Res. Lett.*, **12**, 376 (2017).
68. B. Huang, X. Li, Z. Wang, H. Guo, and X. Xiong, *Ceram. Int.*, **40**, 13223 (2014).
69. Y. Chen, P. Li, S. Zhao, Y. Zhuang, S. Zhao, Q. Zhou, and J. Zheng, *RSC Adv.*, **7**, 29233 (2017).
70. X. Li, J. Liu, M. N. Banis, A. Lushington, R. Li, M. Cai, and X. Sun, *Energy Environ. Sci.*, **7**, 768 (2014).
71. Y. You, H. Celio, J. Li, A. Dolocan, and A. Manthiram, *Angew. Chem. Int. Ed.*, **57**, 6480 (2018).

Implications of Aqueous Processing for High Energy Density Cathode Materials Part II: Water-induced Surface Species on $LiNi_{0.8}Co_{0.15}Al_{0.05}O_2$

Michael Hofmann, Martina Kapuschinski, Uwe Guntow and Guinevere A. Giffin[z]
Fraunhofer R&D Center Electromobility, Fraunhofer Institute for Silicate-Research,
Neunerplatz 2, 97082 Wuerzburg, Germany
[z]E-mail: guinevere.giffin@isc.fraunhofer.de

Supporting Information

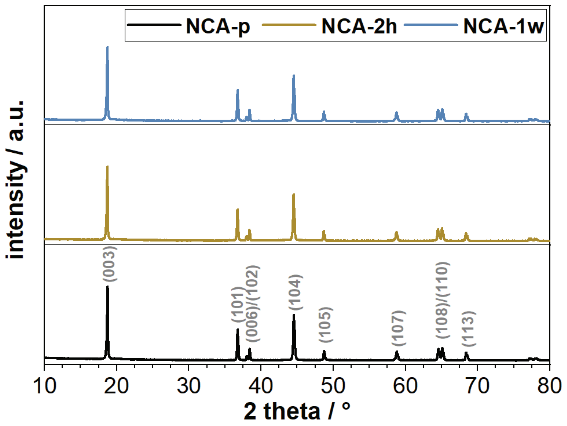

Figure S1 XRD pattern of pristine (NCA-p) and water exposed (NCA-2h and NCA-1w) NCA particles.

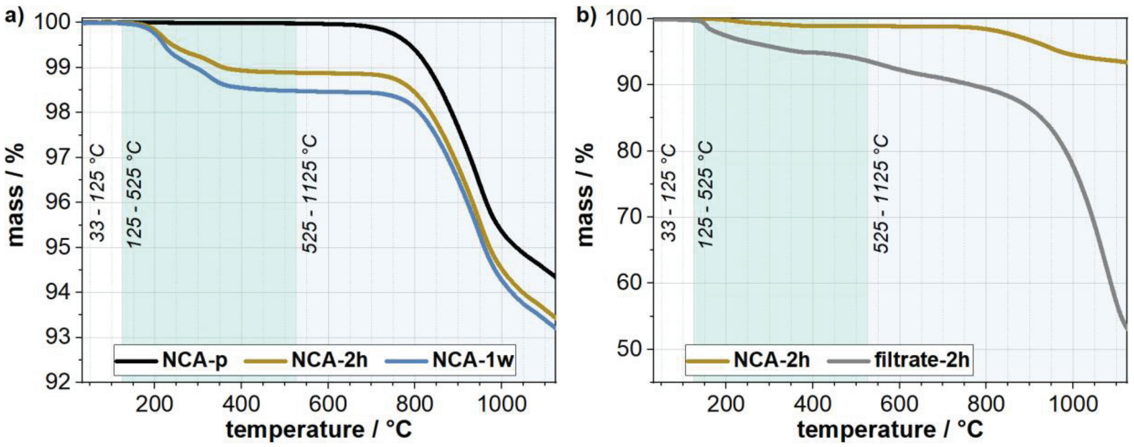

Figure S2 Thermogravimetric analysis in the temperature range 33 °C – 1125 °C of NCA-p/NCA-2h/NCA-1w (a) and NCA-2h/filtrate-2h (b).

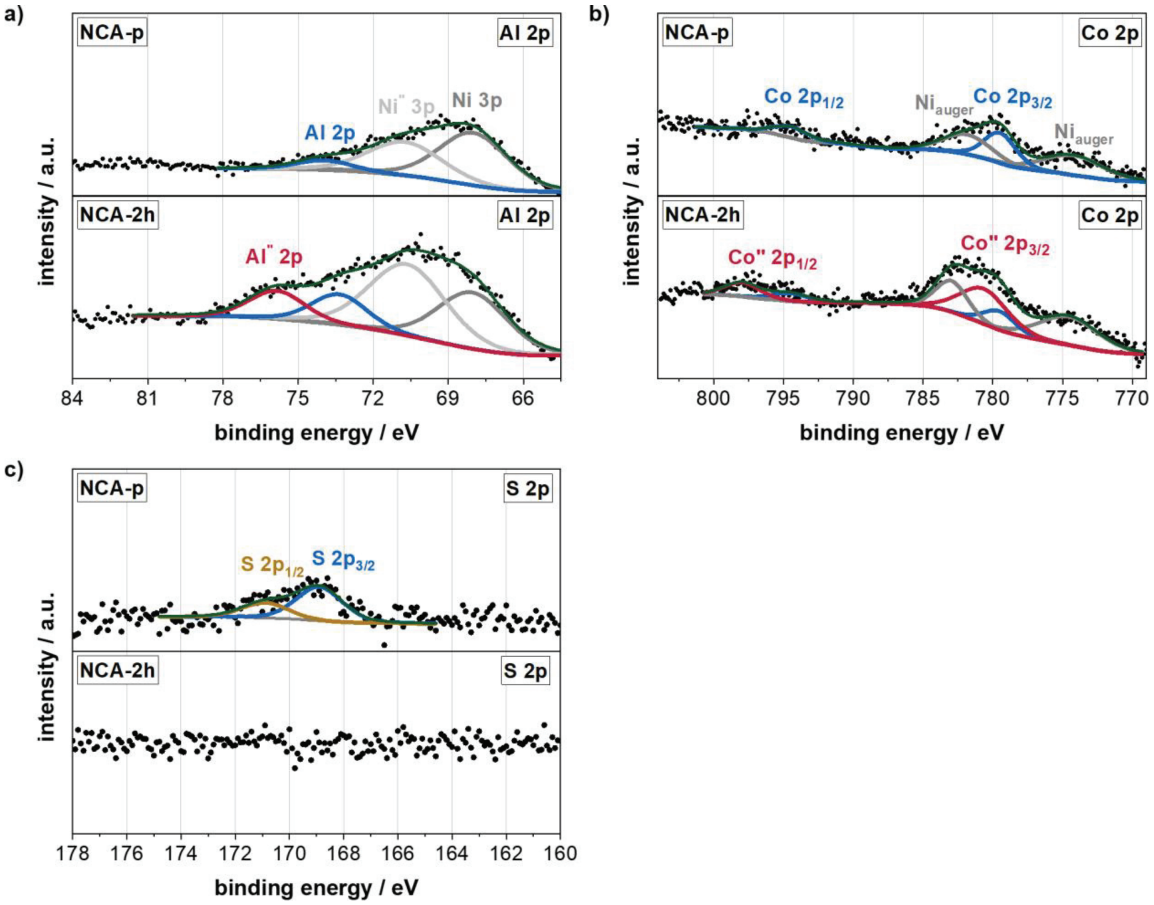

Figure S3 XPS spectra of NCA-p and NCA-2h recorded in the Al 2p (a), Co 2p (b) and S 2p (c) region.

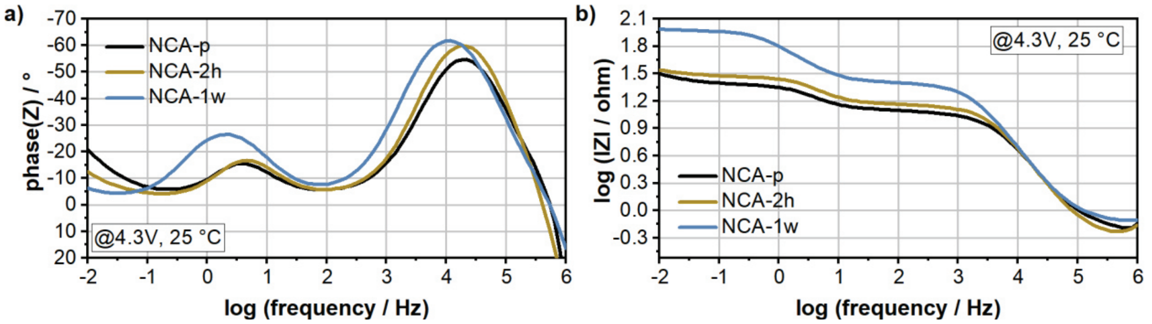

Figure S4 Bode plots of cells containing NCA-p, NCA-2h and NCA-1w obtained from impedance spectroscopy after the formation protocol at 4.3 V.

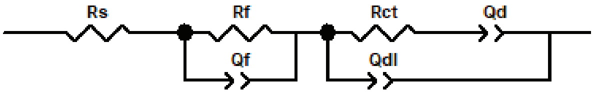

Figure S5 Equivalent circuit model used to fit the EIS spectra. The elements are attributed to ohmic resistances within the cell (resistor R_s), surface film impedance and capacitance (RCPE-element Rf, Qf), charge transfer impedance and double layer capacitance (RCPE-element Rct, Qct) and solid-state diffusion (CPE-element Qd).

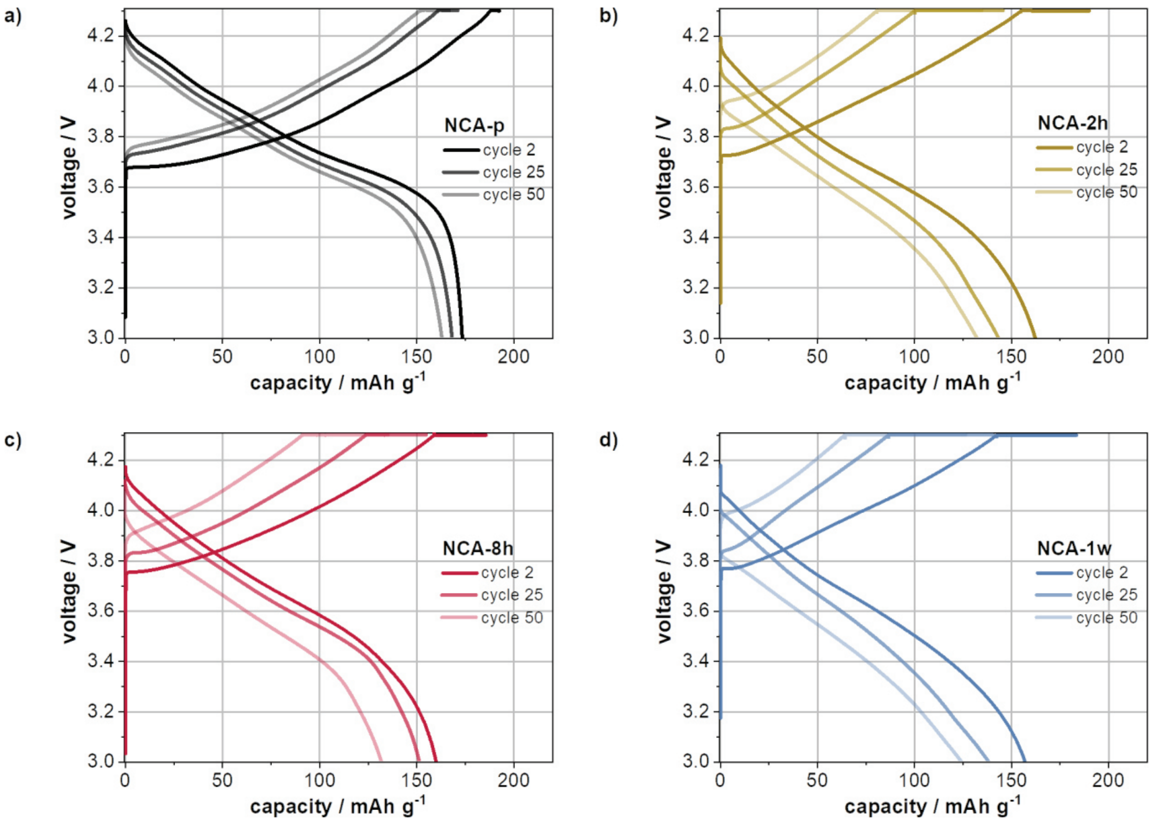

Figure S6 Voltage profiles of a representative cell of NCA-p (a), NCA-2h (b), NCA-8h (c) and NCA-1w (d) during 1C cycling.

Table S1 Relative surface concentration of the elements Li, Ni, Co, O, C and S on NCA-p and NCA-2h. The concentration was calculated from the Li 1s, Ni $2p_{3/2}$, Co $2p_{1/2}$, O 1s, C 1s and S 2p signal. As the Al 2p signal is overlapped with the Ni 3p signal, a reliable value could not be calculated for aluminum.

sample	Li [at%]	Ni [at%]	Co [at%]	O [at%]	C [at%]	S [at%]
NCA-p	21.22	3.87	0.22	50.56	23.02	1.12
NCA-2h	10.52	7.49	0.54	54.85	26.60	-

Table S2 Fitting results of EIS for cells containing NCA-p, NCA-2h and NCA-1w after formation.

cell	R_s [Ω]	[%]	R_f [Ω]	[%]	R_{ct} [Ω]	[%]
NCA-p	0.68	± 0.76	11.40	± 0.41	12.42	± 1.53
NCA-2h	0.60	± 1.16	13.50	± 0.64	15.36	± 2.26
NCA-1w	0.81	± 0.44	23.77	± 0.27	71.75	± 0.57

Appendixes

I. Manuscripts

a. M. Hofmann, M. Kapuschinski, U. Guntow, G. A. Giffin, Implications of Aqueous Processing for High Energy Density Cathode Materials: Part I. Ni-Rich Layered Oxides. *J. Electrochem. Soc.* **2020**, *167*, 140512.

b. M. Hofmann, M. Kapuschinski, U. Guntow, G. A. Giffin, Implications of Aqueous Processing for High Energy Density Cathode Materials: Part II. Water-Induced Surface Species on $LiNi_{0.8}Co_{0.15}Al_{0.05}O_2$. *J. Electrochem. Soc.* **2020**, *167*, 140535.

c. M. Hofmann, F. Nagler, M. Kapuschinski, U. Guntow, G. A. Giffin, Surface Modification of $LiNi_{0.8}Co_{0.15}Al_{0.05}O_2$ Particles via Li_3PO_4 Coating to Enable Aqueous Electrode Processing. *ChemSusChem* **2020**, *13*, 5962 – 5971.

d. M. Hofmann, F. Nagler, U. Guntow, G. Sextl, G. A. Giffin, Long-Term Cycling Performance of Aqueous Processed Ni-rich $LiNi_{0.8}Co_{0.15}Al_{0.05}O_2$ Cathodes. *J. Electrochem. Soc.* **2021**, *168*, 060511.

ChemSusChem
Full Papers
doi.org/10.1002/cssc.202001907
Chemistry Europe
European Chemical Societies Publishing

Surface Modification of $LiNi_{0.8}Co_{0.15}Al_{0.05}O_2$ Particles via Li_3PO_4 Coating to Enable Aqueous Electrode Processing

Michael Hofmann,[a] Felix Nagler,[a] Martina Kapuschinski,[a] Uwe Guntow,[a] and Guinevere A. Giffin*[a]

The successful implementation of an aqueous-based electrode manufacturing process for nickel-rich cathode active materials is challenging due to their high water sensitivity. In this work, the surface of $LiNi_{0.8}Co_{0.15}Al_{0.05}O_2$ (NCA) was modified with a lithium phosphate coating to investigate its ability to protect the active material during electrode production. The results illustrate that the coating amount is crucial and a compromise has to be made between protection during electrode processing and sufficient electronic conductivity through the particle surface. Cells with water-based electrodes containing NCA with an optimized amount of lithium phosphate had a slightly lower specific discharge capacity than cells with conventional *N*-methyl-2-pyrrolidone-based electrodes. Nonetheless, the cells with optimized water-based electrodes could compete in terms of cycle life.

Introduction

Lower overall battery costs and environmental impact of current and next-generation lithium-ion battery production are two critical aspects in the development of lithium-ion batteries. The implementation of a water-based manufacturing process seems to be a promising approach to address these points. It can lower the electrode production costs and therefore the overall battery price. At the same time, it would improve the environmental benignity of battery production.[1] The use of an aqueous process would enable the elimination of the mutagenic and toxic solvent *N*-methyl-2-pyrrolidone (NMP), which, as of yet, remains an integral component of state-of-the-art cathode electrode processing. From an environmental perspective, the regulations concerning the use of NMP in the US[2] and Europe[3] have been made more stringent. From a cost perspective, a water-based process should allow savings in terms of the solvent/binder prices, along with reduced investment and operation costs for the production plant.[1,4,5]

Despite the advantages, aqueous processing for the cathode materials is still problematic as metal leaching from the cathode active material and the resultant highly alkaline slurries lead to the production of surface impurities, a delithiated subsurface, and aluminum current collector corrosion, which have a detrimental effect on the electrochemical performance.[1,6–15] Various strategies with diverse cathode materials have been developed to improve aqueous-manufactured electrodes, wherein the modification of the active material by applying surface coatings seems to be very promising.[6–11,16]

$LiNiCoAlO_2$ (NCA) has attracted significant attention as a cathode active material because of its high energy density.[17] However, NCA is known to be extremely sensitive to moisture,[15,18–20] making it a difficult candidate for the aqueous electrode processing. According to the results in the literature, it is assumed that aqueous processing of NCA will not be successful without additional surface modifications, prior to electrode fabrication[10,11] or in situ surface modification during processing[8,9] or in a combination of both.[21]

The strong P–O-bonding energy in the PO_4^{3-} ion gives metal phosphates high structural stability against chemical attack.[22–24] Various phosphate coatings such as $Ni_3(PO_4)_2$,[25] $FePO_4$,[26] $LiMnPO_4$,[27] $MgHPO_4$,[28] $BiPO_4$,[29] $Li_{1.3}Al_{0.3}Ti_{1.7}(PO_4)_3$,[30] Li_3PO_4,[23,31] $Co_3(PO_4)_2$,[32,33] $LiFePO_4$,[34] and $AlPO_4$[31,33,35] have been studied on NCA and resulted in improved electrochemical performance. However, to the best of the authors' knowledge, a phosphate-coated NCA has never been used in a combination with a water-based electrode manufacturing process. Amongst the phosphate coatings mentioned above, Li_3PO_4 is relatively easy to synthesize and, in contrast to other metal phosphates such as $Ni_3(PO_4)_2$, $Co_3(PO_4)_2$, $BiPO_4$, $FePO_4$, $MgHPO_4$, and $AlPO_4$, a lithium-ion conductor.[36,37] The latter aspect might comparatively facilitate the migration of lithium ions through the particles surface.

Therefore, in this study, the surface of $LiNi_{0.8}Co_{0.15}Al_{0.05}O_2$ particles was modified by applying Li_3PO_4 coatings via a simple precipitation reaction. The modified particles are compared with pristine NCA in terms of their processability in water and their electrochemical performance in cells. Finally, the cycle stability of cells with electrodes prepared via an aqueous and the conventional NMP route as reference is investigated.

---

[a] *M. Hofmann, F. Nagler, M. Kapuschinski, Dr. U. Guntow, Dr. G. A. Giffin*
Fraunhofer Institute for Silicate Research ISC
Fraunhofer R&D Center Electromobility
Neunerplatz 2, 97082 Würzburg (Germany)
E-mail: guinevere.giffin@isc.fraunhofer.de

Supporting information for this article is available on the WWW under https://doi.org/10.1002/cssc.202001907

Results and Discussion

The lithium phosphate coating of NCA was carried out via a simple precipitation reaction. The chemical reaction is assumed to be as follows [Eq. (1)]:

$$3\,CH_3COOLi + H_3PO_4 \rightarrow Li_3PO_4 \downarrow + 3\,CH_3COOH \tag{1}$$

The coating process was done using ethanol as a solvent to reduce contact of the active material with water in order to minimize pre-damage of the particle during the coating process.

X-ray diffraction (XRD) of the pristine and lithium phosphate-coated powders was performed to determine if the coating had an effect on the NCA bulk crystal structure (Figure S1). All peaks of the pristine NCA can be assigned to a layered α-$NaFeO_2$ structure with $R3\,m$ space group with clear peak separations of the 006/012 and 108/110 reflections, indicating a highly ordered structure.[38] For the coated powder, no change in the XRD pattern and no impurity phase peaks were detected. Thus, the coating process does not affect the active material bulk structure. Peaks attributable to the diffraction pattern of Li_3PO_4 are not found in the XRD spectra of the coated samples, likely due to the low coating content.

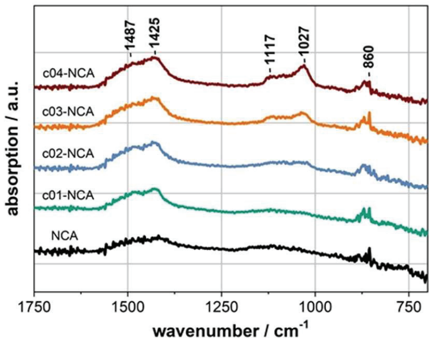

Figure 1. ATR-FTIR spectra of pristine and coated NCA particles.

To confirm the presence of lithium phosphate, the pristine and coated-NCA particles were characterized by attenuated total reflection Fourier-transform infrared (ATR-FTIR) spectroscopy. The magnified spectra (Figure 1) of the pristine and coated NCA particles show peaks around 860, 1425, and 1487 cm^{-1}, which can be assigned to the CO-bending, symmetric CO-stretching, and asymmetric CO-stretching vibrations, respectively.[19] These peaks can be attributed to carbonate species, which are often detected on the surface of layered Ni-rich oxides and can be formed by various processes.[39–41] For the coated samples, two additional peaks evolve with increasing coating content at around 1027 and 1117 cm^{-1}. According to literature, these peaks can be assigned to asymmetric P–O stretching vibrations of PO_4^{3-} ions, thus confirming the presence of the phosphate coating.[42] In principle, for a free phosphate ion, which belongs to the T_d point group, only one signal for the triply degenerate asymmetric P–O stretching vibration in the range 1100–1000 cm^{-1} would be expected. However, the interaction of PO_4^{3-} with lithium cations or other ions can lower the symmetry and thus lead to peak splitting.[43] The full spectra are shown in Figure S2, but no additional signals are observable.

The morphology of pristine and coated NCA was investigated via scanning electron microscopy (SEM). Figure 2 displays the SEM images of pristine NCA (a–c) and c04-NCA (d–f). Both samples (a,d) have spherical secondary particles, which are between 5–10 µm in diameter, made up of small primary particles that are 100–500 nm in diameter. The magnified images (b,e) show a very smooth surface for pristine NCA and a surface with an increased roughness for the coated material c04-NCA. The energy-dispersive X-ray spectroscopy (EDS) mapping images show the elemental distribution on the particle surface (c,f). All the elements (Ni, Co, Al) of NCA show a homogenous distribution. Furthermore, phosphorus is also evenly distributed on c04-NCA, which also supports the conclusion of a successful phosphate coating.

It is well-known that the slurry pH increases into the highly alkaline region during a water-based cathode electrode manufacturing process, which can lead to corrosion of the aluminum substrate. Therefore, the pH values of the pristine and coated NCA particles in aqueous mixtures were measured over a period of 2 h (Figure S3). Note that the pH results of pristine NCA were published previously.[18] The pH of all samples rises almost

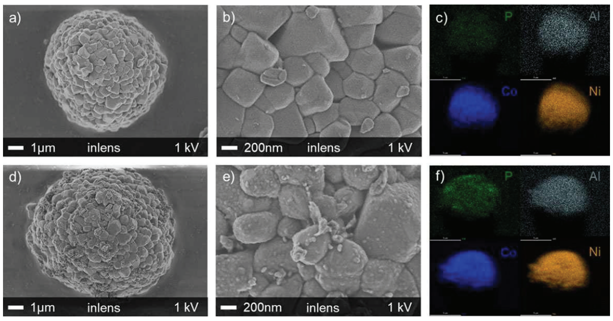

Figure 2. SEM images and EDS elemental mapping of pristine NCA (a–c) and c04-NCA (d–f).

instantaneously into the high alkaline region and then stabilizes after around 30 min. The pH value for pristine NCA is 12.69 after 2 h. This end pH value decreases with increased coating amount to 12.55, 12.43, 12.36, and 11.97 for c01-NCA, c02-NCA, c03-NCA, and c04-NCA, respectively. Since the pH value has a logarithmic dependency on the H_3O^+-ion concentration, the differences in the pH measured result in a reduction of the OH^--ion concentration by a factor of more than 7 for c04-NCA. However, since all the pH values are higher than 9 and therefore beyond the regime where aluminum is passivated, the formation of basic species is only reduced, and aluminum corrosion and the concomitant generation of hydrogen gas can be expected during the electrode processing according to Equations (2) and (3).[6,44]

$$Al_2O_3 + 2\,OH^- + 3\,H_2O \rightarrow 2\,[Al(OH)_4]^- \quad (2)$$

$$2\,Al + 2\,OH^- + 6\,H_2O \rightarrow 2\,[Al(OH)_4]^- + 3\,H_2 \quad (3)$$

Figure 3 displays photographs and SEM images of the top view of calandered aqueous-processed electrodes with pristine and coated NCA (c04-NCA). The data for the other electrodes (c01-NCA, c02-NCA, and c03-NCA) can be found in Figure S4. As expected from the pH measurements, all electrodes show large holes and cracks stemming from the formation of hydrogen gas bubbles during aluminum corrosion.[6] However, for the electrodes containing coated NCA, fewer holes are present (larger reduction for the electrodes with NCA with a higher coating amount), which suggests that the Al corrosion was at least partially suppressed. Moreover, this improvement can be also clearly seen with water-based electrodes with a higher mass loading, where electrode cracking caused by hydrogen evolution is known to be a major issue (Figure S5).[45] To fully compensate for the aluminum corrosion, a number of strategies present in the literature such as the addition of acids[14,46] or amphoteric oxidic additives,[47] CO_2 gas treatment,[8,9] and the use of carbon-coated aluminum foil[13] can be applied for further optimization. However, it should be noted that these approaches mitigate the consequences of water contact with the cathode material but do not prevent the origin of the problem from the beginning as is at least partially possible with a surface coating.

The electrochemical performance of cells containing the Li_3PO_4-coated NCA in aqueous-processed electrodes was investigated in pouch cells in a half-cell configuration. The results of the formation are depicted in Figure 4. Figure 4a,b shows the average discharge capacity, while Figure 4c,d shows the voltage profiles of the first and second cycle, respectively. In accordance with a previous report of the authors, the cells with pristine NCA particles have a negligible electrochemical performance due to a high overpotential that exceeds the cut-off voltage.[18] The corresponding voltage profiles illustrate the extreme polarization of the cells (Figure S6). These results were attributed to the formation of water-induced species, which cover the particle surface and severely hinder the extraction and insertion of lithium ions.[15] In contrast, all cells containing coated-NCA deliver a reasonable capacity, demonstrating a protective function of the Li_3PO_4 coating during the aqueous electrode processing. The initial specific discharge capacities are in the range of approximately 174–182 mAh g^{-1} at rate of C/10 with a coulombic efficiency of approximately 85 % (Figure 4a). As a comparison, the average specific discharge capacity value with NMP-processed electrodes containing pristine NCA is approximately 192 mAh g^{-1}. This result will be discussed in more detail later. Upon further cycling all cells show increasing specific discharge capacities with coulombic efficiencies above 99 %. The increasing capacity can be explained at least partially by a reversible Li^+/H^+-exchange as suggested by Shkrob et al.[48] This mechanism implies the formation of species such as NiOOH, which have been shown to be formed on the surface of water-exposed NCA in a previous report.[15] Moreover, mechanical stress induced by the volume expansion/contraction of NCA particles during lithium insertion and deinsertion might also contribute to the increase of capacity by enabling the electrolyte to wet previously not accessible pores.[18] The specific discharge capacity of the last formation cycle (5th cycle) is a maximum of 181.6 mAh g^{-1} for c02-NCA (Figure 4b). The capacity differs by less than 4 mAh g^{-1} between the four coated materials.

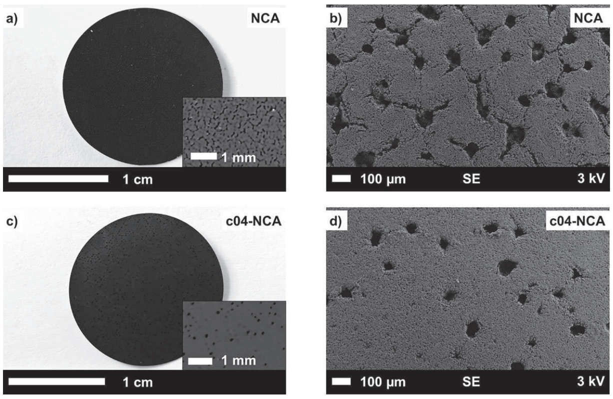

Figure 3. Photographs and SEM images of calandared aqueous-processed electrodes with pristine NCA (a,b) and c04-NCA (c,d).

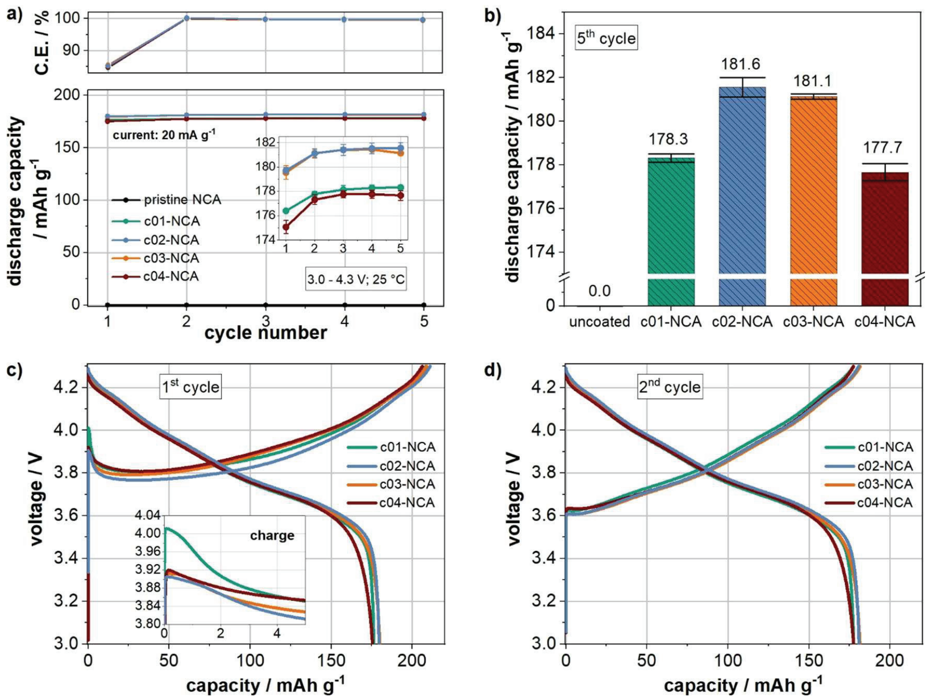

Figure 4. Results of the formation cycles of cells with aqueous-processed electrodes: discharge capacity over cycle number (a), discharge capacity in the last formation cycle (b), and voltage profiles of a representative cell of each combination in the first and second cycle (c,d). The data in (a) and (b) represent the average specific discharge capacity of three cells, and the error bars relate to the standard deviation between these cells.

The voltage profiles provide further information about the nature of the coating. The first and second cycle of a representative cell of each coated material is depicted in Figure 4c,d. All cells show an initial overvoltage as soon as the charge current is applied, which is the most pronounced for the cell with c01-NCA followed by c04-NCA, c03-NCA, and c02-NCA. The magnitude of the initial overvoltage has been reported to reflect the amount of water-induced surface species on NCA particles.[15] Moreover, various authors report a high initial overvoltage in cells containing nickel-rich active materials or electrodes that have been exposed to moisture, which was ascribed to degradation of the surface or deposition of surface species.[18,39,48,49] This can explain the high initial overvoltage for the lowest coating amount (c01-NCA), where the particles seem to be the least protected against the exposure to water. In contrast, the cells containing a slightly higher amount of Li_3PO_4 in the coating (c02-NCA) deliver the highest discharge capacity and lowest initial overvoltage. Finally, a coating amount that is “too high” results again in a higher initial overvoltage and lower discharge capacity as seen for c03-NCA and c04-NCA. In accordance with the literature, the overvoltage at the beginning of the charge cycle is no longer present in the second cycle, which was explained by at least partial decomposition of the surface species during the first cycle.[15,18,39,50] In an effort to better understand the different behavior of the cells during the formation, cells with c01-NCA, c02-NCA, and c04-NCA, as examples for a low, medium, and high Li_3PO_4 coating amount, were selected for cyclic voltammetry and impedance spectroscopy measurements. Figure 5a–c shows the cyclic voltammetry curves of the c01-NCA, c02-NCA, and c04-NCA electrodes in lithium half-cells at a scan rate of 0.05 mV s^{-1} between 2.7 and 4.5 V. The first cycle clearly differs from cycles two and three. In the first cycle, there is a main oxidation peak at 4.15, 3.99, and 4.05 V for the cells containing c01-NCA, c02-NCA, and c04-NCA, respectively. Thus, the voltage of this first peak is highest for electrodes with the lowest amount of coating (c01-NCA) followed by the highest (c04-NCA) and medium (c02-NCA) Li_3PO_4 coating amount. This trend is consistent with the order of the initial overvoltage observed in the first cycle of the galvanostatic formation (Figure 4c). In the second and third cycles, the characteristic redox pairs of NCA appear, which are attributed to the phase transitions from hexagonal (H1) to monoclinic (M), monoclinic (M) to hexagonal (H2), and hexagonal (H2) to hexagonal (H3) during lithium extraction.[51] Figure 5d shows the potential differences (ΔE) between the anodic and cathodic scans of the three redox pairs for each cell variant in the third cycle. While the cells with c02-NCA and c04-NCA show comparable ΔE values (lowest for c02-NCA), they are considerably higher than those for c01-NCA, indicating an increased cell polarization.[52]

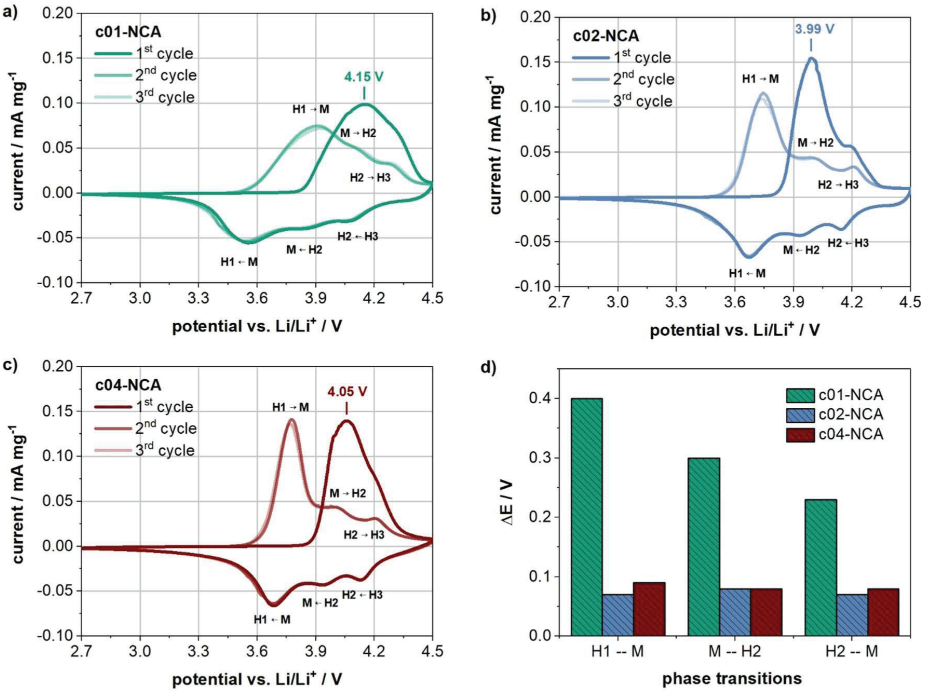

Figure 5. Cyclic voltammetry measurements at a scan rate of 0.05 mVs^{-1} between 2.7 and 4.5 V for three cycles of cells containing c01-NCA (a), c02-NCA (b), and c04-NCA (c), and potential differences (ΔE) of NCA redox pairs in the third cycle (d).

Another sign for an increased cell polarization for the lowest coating amount (c01-NCA) is that the anodic peaks for H1/M and M/H2 are not clearly separated, in contrast to the cells with c02-NCA and c04-NCA, but are partially overlapped.[53]

Electrochemical impedance spectroscopy was conducted after the formation cycles to gain more understanding of the effect of the amount of coating. The results obtained for c01-NCA, c02-NCA, and c04-NCA are depicted in Figure 6. For c01-NCA and c02-NCA, the Nyquist plots consist of four features, which are assigned based on studies of similar cathode materials in the literature as the following: a high-frequency intercept due to ohmic resistances within the cell (R_s), a first semicircle related to surface film impedance (R_f), a second semicircle related to charge-transfer impedance at medium-low frequencies (R_{ct}), and an inclined line ascribed to solid-state diffusion at low frequencies.[54] In addition, for c04-NCA a third semicircle appears in the mid-frequency region, which can be correlated based on previous literature to the charge-transfer resistance at the metallic lithium/electrolyte interface along with the electronic conductivity of the active material (R_*).[55] Therefore, a fit model with an additional element was used for c04-NCA (Figure S7, Table S1). For c01-NCA and c02-NCA, it is possible that contributions associated with R_f and R_* are superimposed in the first semicircle. However, as these contribu-

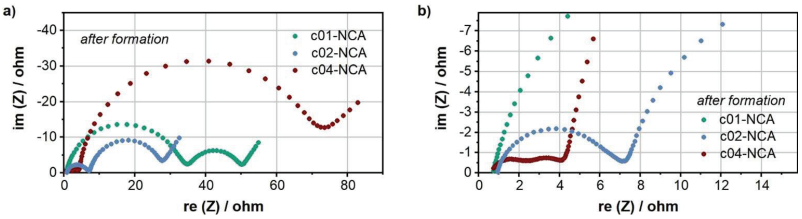

Figure 6. Electrochemical impedance spectra of cells containing c01-NCA, c02-NCA, and c04-NCA at 4.3 V after the formation protocol: full spectra (a) and magnified view of the high-frequency regime (b).

tions cannot be separated by the eye, they were fitted with a single element.

As expected, the ohmic resistance (R_s) is similar for all three cell types. However, the surface film impedance is much higher for the low coating variant (c01-NCA) as compared to the medium coating amount (c02-NCA) and is lowest for the high coating amount (c04-NCA). This result may suggest that as the amount of coating increases, the active material particles are better protected during aqueous electrode processing, and that negative effects of water contact such as delithiation, degradation of the active material structure, as well as the deposition of surface species are partially suppressed. In contrast, R_{ct} is lowest for c01-NCA, slightly higher for c02-NCA, and much higher for c04-NCA. According to literature, a thick or overly-dense coating of a material with poor electronic conductivity can increase the charge-transfer resistance.[30,54] Keeping in mind that lithium phosphate can also be used as a solid electrolyte[37] because of its low electronic conductivity, this implies that for a Li_3PO_4 coating a compromise between a reduction of the surface film resistance R_f and an increased charge transfer resistance R_{ct} has to be made, which seems to be the case with the medium coating amount (c02-NCA).

The cycling results of the various cells at 25 °C with an initial cycle at C/10 followed by 49 cycles at a rate of 1 C in the voltage range of 3.0–4.3 V are shown in Figure 7 and Figure S8. Not surprisingly, the cells containing the pristine NCA still do not deliver any capacity (Figure S8). At first glance, the electrochemical performance of the cells with coated NCA differ only marginally, and all show relatively stable cycling. The discharge capacities at 1 C are in the range of 145–165 mAh g^{-1} during the whole cycling procedure.

The cells with c02-NCA have a slightly higher discharge capacity than the other three coated NCA materials. The corresponding voltage profiles can be found in Figure 7a–d. The cell polarization is lowest for the cells with the coated materials c02-NCA followed by c03-NCA, c04-NCA, and c01-NCA, and increases with increasing cycle number. Moreover, the length of the CV-step, and thus the capacity delivered during the CV step, is the highest for the cells with c01-NCA. Specifically, the constant-voltage phase delivers approximately 17 % and 24 % of the capacity in the first and last 1 C cycle, respectively. In comparison, the capacity delivered in the CV step for the materials with a higher coating content is 4 %/8 %, 6 %/13 %, and 7 %/15 % for the first/last 1 C cycles of c02-NCA, c03-NCA, and c04-NCA, respectively. These results are consistent with those of Jung et al., who reported that the capacity obtained in the CV step was significantly higher in cells with NMC811 aged under ambient conditions as compared to cells with fresh NMC811.[39]

The impedance was also compared for the same materials as above after cycling (Figure 8). Unlike the results after the formation cycles, a clear semicircle for R_* is now also visible for c02-NCA. R_f after cycling increased by approximately the same factor for all cells, and the trend is the same as after formation (c04-NCA < c02-NCA < c01-NCA; Table S2). In contrast, R_{ct} significantly increases for c01-NCA over cycling by a factor of approx. 4, but it only slightly increases for c02-NCA and c04-NCA. According to the literature, a smaller increase for R_{ct} is consistent with reduced side reactions during cycling.[56] The

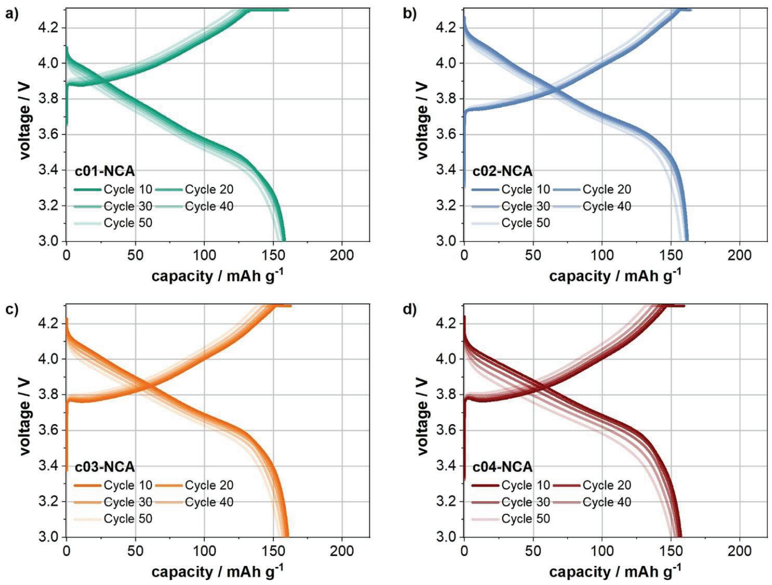

Figure 7. Voltage profiles of a representative cell of c01-NCA (a), c02-NCA (b), c03-NCA (c), and c04-NCA (d) during cycling.

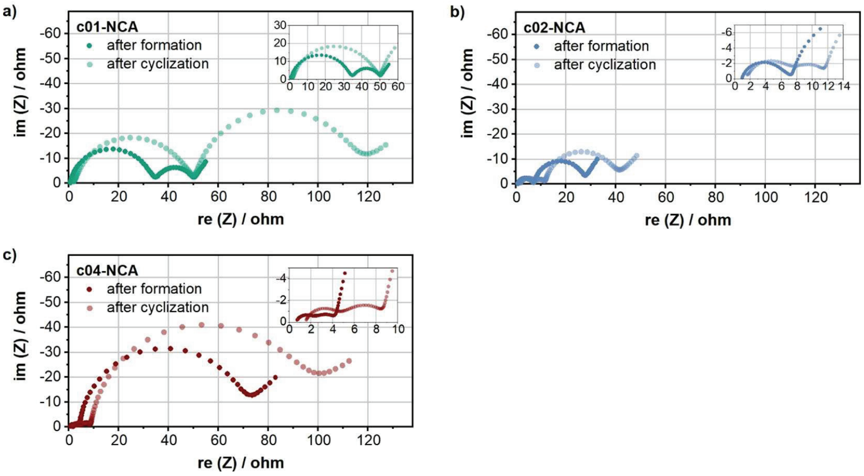

Figure 8. Comparison of electrochemical impedance spectra (a) of cells containing c01-NCA, c02-NCA, and c04-NCA at 4.3 V after formation and after cycling. The high-frequency region is magnified in the inset for each material.

origin for reduced side reactions may be explained by the following considerations. The coated materials c02-NCA and c04-NCA seem to be better protected against water exposure and therefore the deposition of surface species. These surface species may react with ethylene carbonate (EC)-containing electrolytes during cycling and lead to increased resistances.[40] Furthermore, an optimized coating layer might act as a barrier between NCA and the electrolyte, which may hinder electrolyte decomposition. This aging mechanism is known to be one of the major issues for Ni-rich layered cathode materials that leads to increased cell degradation.[57,58] This benefit has been already reported by different authors for a Li_3PO_4 coating used in combination with NMP-based electrode processing.[24,59,60] It should be noted that R_{ct} remains the highest for c04-NCA even after cycling, which, as mentioned before, is mainly attributed to the low electronic conductivity of the coating. It seems that to achieve the best electrochemical performance, c02-NCA is the coating amount of choice, at least from those tested, as reflected by the lowest overall impedance both after formation and after cycling.

Finally, the cell performance of the optimized water-based electrodes with c02-NCA was compared to that of cells containing conventional NMP/polyvinylidene fluoride (PVDF)-based electrodes with pristine NCA and c02-NCA. The data of the cells with NMP-electrodes with pristine NCA was previously published by these authors.[15] The formation results for the cells with the conventional electrodes are shown in Figures S9 and S10. During cycling (Figure 9a,b), the cells with NMP-processed electrodes containing pristine NCA deliver an average specific discharge capacity of 192.8 $mAh\,g^{-1}$ in the initial C/10 cycle and 174.0 $mAh\,g^{-1}$ in the first 1 C cycle. These values are slightly higher than for the cells with NMP-based electrodes containing c02-NCA (188.2 $mAh\,g^{-1}$ at C/10 and 167.2 $mAh\,g^{-1}$ at 1 C). In addition, the associated voltage profiles show an increased cell polarization for the NMP-based c02-NCA variant (Figure 9b). This might be explained by the presence of the coating that was optimized for an aqueous electrode manufacturing process rather than for an NMP/PVDF-based one. The latter does not require the protection of particles against water exposure and will likely also result in different cathode particle/binder interactions [PVDF vs. sodium carboxymethyl cellulose (CMC)].[1,61] Therefore, higher capacity values and lower cell polarization might be obtained by optimizing the coating amount for an NMP/PVDF based process, which is beyond the scope of this work. Compared to the NMP/PVDF variants, the capacity values of the cells with aqueous-processed c02-NCA electrodes are between 5–10 $mAh\,g^{-1}$ lower (183.0 $mAh\,g^{-1}$ at C/10 and 164.8 $mAh\,g^{-1}$ at 1 C). However, the capacity retention of these cells at 1 C is 94.8% and therefore slightly higher than the NMP-based variant with pristine NCA (94.5%). The cells with NMP-processed electrodes containing c02-NCA have an even higher capacity retention of 96.2%. These trends suggest that the Li_3PO_4 coating may provide additional protection against side reactions during cycling as it was reported in previous literature.[24,59,60] Another plausible interpretation for these differences is that for the cells with higher capacity values, where more lithium ions were extracted from the NCA structure (i.e., a higher state of charge), this can lead to enhanced degradation of the NCA particles and result in a more rapid deterioration of the cell performance.[57,62] Although there are different mechanisms to explain the differences in the capacity retention, the aqueous processing certainly plays a role in slightly lower retention of the cells with the aqueous-processed electrodes as compared to these with NMP-processed coated NCA. The coating amount with c02-NCA is a compromise, as described above. Therefore, the formation of a small amount of water-

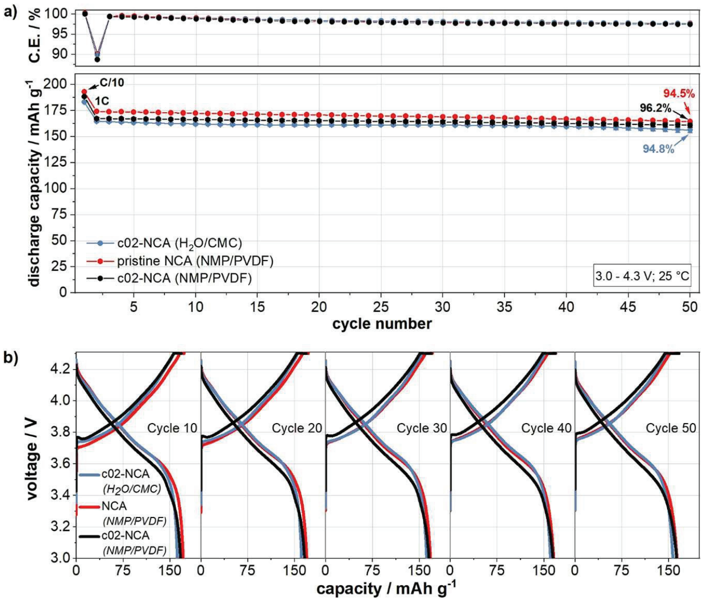

Figure 9. Cycle performance of aqueous- and NMP-processed cathodes (a) and corresponding voltage profiles of a representative cell of each combination (b). The aqueous-processed cathodes contain c02-NCA, while the conventional cathodes contain pristine NCA and c02-NCA, respectively. The data in (a) represent the average specific discharge capacity of three cells, and the error bars relate to the standard deviation between these cells.

induced surface species likely occurs even here, which may also contribute to additional side reactions.[15] Furthermore, an impact of the different binder properties of PVDF and CMC should be considered.[1,61] More studies are needed to clarify this point in detail.

Currently, the electrochemical performance of full cells containing optimized water-based NCA electrodes is under investigation to demonstrate long-term cycling stability, and an upscaling process for the coating procedure is developed.

Conclusions

By a simple precipitation reaction, $LiNiCoAlO_2$ (NCA) particles were coated with different amounts of lithium phosphate. The use of the coated NCA in aqueous electrode processing reduced the alkalinity of the slurry and thus the lithium leaching in water could be at least partially suppressed. In electrochemical testing, all cells with coated NCA showed good electrochemical performance. The results suggest that the coating amount is crucial to optimize the cell performance. A low coating amount leads to relatively poor protection of the NCA during aqueous processing. As a result, more pronounced structural damage and/or deposition of surface impurities occur, which is reflected by a high initial overvoltage in the first charge and an increased surface film impedance. In contrast, a lithium phosphate coating amount that is too high provides better protection against water but leads to increased electronic resistance. Therefore, a compromise has to be made between protection against water and sufficient electronic conductivity through the particle surface.

The best-performing cells containing aqueous-processed electrodes were compared with cells with *N*-methyl-2-pyrrolidone (NMP)-based electrodes. Although the NMP cells have slightly higher discharge capacities, the water-based variant can compete in terms of cycle life. Although further studies are needed, this work demonstrates that applying protective surface coatings on NCA particles can be a feasible way towards a successful implementation of an aqueous-based electrode processing for this water-sensitive material.

Experimental Section

Li_3PO_4 coating

Commercial $LiNi_{0.8}Co_{0.15}Al_{0.05}O_2$ (TODA, NAT-1050) was used as received. For the Li_3PO_4 coating, the appropriate amount of lithium acetate dihydrate (Sigma Aldrich, 98%) was dissolved in ethanol (20 g). NCA (10 g) was added and the suspension was homogenized for 10 min at room temperature. Dropwise, a solution consisting of phosphoric acid (Merck, 85 wt% in water) in 5 g ethanol was added within 15 min under vigorous stirring. The molar ratio between lithium acetate dihydrate and phosphoric acid was controlled to be 3:1. Next, the suspension was dried under reduced pressure, and the powder was annealed at 300 °C for 5 h in ambient atmosphere (heating rate: 5 °C min^{-1}) to remove residual organic compounds. To evaluate the effect of the coating, four different samples with varying Li_3PO_4-amounts per g NCA ($0.00625\ mmol\,g^{-1}$, $0.0125\ mmol\,g^{-1}$, $0.025\ mmol\,g^{-1}$, and $0.05\ mmol\,g^{-1}$) were prepared assuming that all precursors were totally converted to Li_3PO_4 after the coating process. The surface modified NCA-particles are referred to by increasing coating amount as c01-NCA, c02-NCA, c03-NCA, and c04-NCA, respectively.

Electrode processing

CMC (Sigma-Aldrich, mass average molar mass $\approx 250000\ g\,mol^{-1}$ with a degree of substitution of 0.9) and Super C65 (Imerys) were used as binder and conductive carbon, respectively. Slurries consisting of 92 wt% active material, 4 wt% CMC, and 4 wt% Super C65 in deionized water were prepared by the following steps: CMC was dissolved in deionized water using a laboratory shaker. After the addition of either the pristine or the coated NCA and Super C65, the mixture was homogenized by a speedmixer. Using the doctor-blade technique, the slurries were coated onto aluminum foil and then pre-dried at 80 °C for 30 min. The resulting electrode sheets were calandered (50% of initial electrode thickness), and disc electrodes with an area of $2.01\ cm^2$ were punched out (mass loading: $11 \pm 1\ mg\,cm^{-2}$). To remove residual moisture, the disc electrodes were dried under vacuum at 110 °C for 10 h.

To prepare NMP-based electrodes, PVDF (Solvay, Solef® 5130) was dissolved in NMP (Sigma-Aldrich) overnight. Then, the active material and conductive carbon (Imerys, Super C65) were added, and the mixture was homogenized in a speedmixer. The ratio of active material/conductive carbon/binder was kept the same as for the aqueous route. After casting the slurries on aluminum foil, the electrodes were stored in a fume hood overnight and pre-dried under vacuum (80 °C, 2 h). The dried electrode sheets were calendered to 50% of initial electrode thickness. Disc electrodes (16 mm in diameter) with a mass loading of $11 \pm 1\ mg\,cm^{-2}$ were punched out and dried under vacuum at 80 °C for 5 h.

Cell assembly and electrochemical measurements

Pouch cells with the NCA electrodes, lithium metal (Sigma-Aldrich) on a copper substrate as counter electrode, a polyethylene separator (Celgard 2500) and $1\ mol\,L^{-1}$ $LiPF_6$ in EC/DMC (dimethyl carbonate) 1:1 *w/w* (LP30, BASF) as electrolyte were assembled in an argon filled glovebox (MBraun). To contact the electrodes, aluminum tabs (Targray) and copper-nickel tabs (Targray) were used for the cathode and anode, respectively. To ensure data reliability three cells were prepared for each variant.

Charge/discharge tests were conducted on an electrochemical workstation (Maccor, Series 4000) in the voltage range of 3.0 to 4.3 V at 25 °C (climate chamber, Memmert). The cells were activated with a formation protocol consisting of five cycles at C/10 ($20\ mA\,g^{-1}$), whereby charge and discharge were done in constant-current mode (CC). The capacity of the 5th formation cycle was used to calculate the current for the cycling test, which consisted of one cycle at C/10 and 49 cycles at 1 C. Here, the charge was done with a constant-current constant-voltage (CCCV) process and discharge was carried out in the CC-mode. The CV-step was terminated at a current of C/20. Due to the low coating amount, the coated NCA particles were treated as pure active material for the specific capacity calculations. This may artificially reduce the actual specific capacity of the active material. Cyclic voltammetry tests and electrochemical impedance spectroscopy (EIS) were conducted on a VMP300 galvanostat/potentiostat (BioLogic). Impedance spectra were obtained by the perturbation of the cells with an AC voltage (amplitude: 5 mV) over the frequency range of 1 MHz to 10 mHz. Cyclic voltammograms were recorded between 2.7 and 4.5 V with a scan rate of $0.05\ mV\,s^{-1}$ at 25 °C (climate chamber, Memmert). For these measurements a lithium reference electrode was added to the cell setup described above.

Characterization methods

The crystal structures of the active material powders were analyzed by XRD (CuK_α: $\lambda = 0.1540598\ nm$; PANalytical Empyrean series 2) in the 2θ-range 10–80° (step size: 0.003°, aperture: 10 mm). ATR-FTIR analysis was performed using an Alpha II (Bruker) spectrometer with germanium crystal in the range of $700–4000\ cm^{-1}$. All spectra were recorded with 64 scans and a resolution of $2\ cm^{-1}$. The spectra were normalized to the largest peak. To measure the pH values a pH meter (pH 315i, WTW) equipped with a SenTix®H electrode (WTW) was used. The pristine or coated NCA was added to distilled water (mass ratio NCA/water = 1:3) and the pH evolution with continuous stirring by a magnetic stirrer (750 rpm) was monitored for 2 h. The surface morphology and elemental distribution was investigated by SEM (ZEISS Ultra 55, Carl Zeiss Microscopy GmbH) coupled with EDS.

Acknowledgements

The authors acknowledge the financial support from the Bavarian Ministry of Economic Affairs and Media, Energy and Technology for funding the Fraunhofer R&D Center for Electromobility Bavaria FZEB (Grant number: 43-6629/86). Open access funding enabled and organized by Projekt DEAL.

Conflict of Interest

The authors declare no conflict of interest.

Keywords: aqueous electrode processing · lithium-ion battery · lithium phosphate coating · Ni-rich cathode material · sustainable chemistry

[1] D. Bresser, D. Buchholz, A. Moretti, A. Varzi, S. Passerini, *Energy Environ. Sci.* **2018**, *11*, 3096–3127.
[2] United States Environmental Protection Agency (EPA), "Risk Evaluation for N-Methylpyrrolidone (NMP)". Available from https://www.epa.gov/assessing-and-managing-chemicals-under-tsca/risk-evaluation-n-methylpyrrolidone-nmp-0 (accessed June **2019**).
[3] European Parliament and the Council concerning the Registration, Evaluation, Authorisation and Restriction of Chemicals (REACH), "Commission regulation (EU) 2018/588 of April 2018". Avaible from https://eur-lex.europa.eu/legal-content/EN/TXT/PDF/?uri=CELEX:32018R0588&from=DE (accessed in June **2019**).
[4] S. F. Lux, F. Schappacher, A. Balducci, S. Passerini, M. Winter, *J. Electrochem. Soc.* **2010**, *157*, A320–A325.
[5] a) D. L. Wood, J. Li, C. Daniel, *J. Power Sources* **2015**, *275*, 234–242; b) S. Ahmed, P. A. Nelson, K. G. Gallagher, D. W. Dees, *J. Power Sources* **2016**, *322*, 169–178.
[6] M. Kuenzel, D. Bresser, T. Diemant, D. V. Carvalho, G.-T. Kim, R. J. Behm, S. Passerini, *ChemSusChem* **2018**, *11*, 562–573.
[7] N. Loeffler, G.-T. Kim, F. Mueller, T. Diemant, J.-K. Kim, R. J. Behm, S. Passerini, *ChemSusChem* **2016**, *9*, 1112–1117.
[8] K. Kimura, K. Onishi, T. Sakamoto, K. Asami, M. Yanagida, *J. Electrochem. Soc.* **2019**, *166*, A5313–A5317.
[9] K. Kimura, T. Sakamoto, T. Mukai, Y. Ikeuchi, N. Yamashita, K. Onishi, K. Asami, M. Yanagida, *J. Electrochem. Soc.* **2018**, *165*, A16–A20.

[10] Y. Liu, T. Tanabe, Y. Irii, F. Maki, T. Tsuda, T. Gunji, S. Ugawa, Y. Asai, H. Lee, T. Ohsaka, F. Matsumoto, *J. Appl. Electrochem.* **2019**, *49*, 99–110.
[11] T. Tanabe, Y. Liu, K. Miyamoto, Y. Irii, F. Maki, T. Gunji, S. Kaneko, S. Ugawa, H. Lee, T. Ohsaka, F. Matsumoto, *Electrochim. Acta* **2017**, *258*, 1348–1355.
[12] B. C. Church, D. T. Kaminski, J. Jiang, *J. Mater. Sci.* **2014**, *49*, 3234–3241.
[13] I. Doberdò, N. Löffler, N. Laszczynski, D. Cericola, N. Penazzi, S. Bodoardo, G.-T. Kim, S. Passerini, *J. Power Sources* **2014**, *248*, 1000–1006.
[14] W. Bauer, F. A. Çetinel, M. Müller, U. Kaufmann, *Electrochim. Acta* **2019**, *317*, 112–119.
[15] M. Hofmann, M. Kapuschinski, U. Guntow, G. A. Giffin, *unpublished results*, **2020**.
[16] a) K. Notake, T. Gunji, H. Kokubun, S. Kosemura, Y. Mochizuki, T. Tanabe, S. Kaneko, S. Ugawa, H. Lee, F. Matsumoto, *J. Appl. Electrochem.* **2016**, *46*, 267–278; b) N. Laszczynski, J. von Zamory, J. Kalhoff, N. Loeffler, V. S. K. Chakravadhanula, S. Passerini, *ChemElectroChem* **2015**, *2*, 1768–1773.
[17] a) Y. Xia, J. Zheng, C. Wang, M. Gu, *Nano Energy* **2018**, *49*, 434–452; b) J. Kim, H. Lee, H. Cha, M. Yoon, M. Park, J. Cho, *Adv. Energy Mater.* **2018**, *8*, 1702028; c) G. Berckmans, M. Messagie, J. Smekens, N. Omar, L. Vanhaverbeke, J. Van Mierlo, *Energies* **2017**, *10*, 1314; d) A. Purwanto, C. S. Yudha, U. Ubaidillah, H. Widiyandari, T. Ogi, H. Haerudin, *Mater. Res. Express* **2018**, *5*, 122001.
[18] M. Hofmann, M. Kapuschinski, U. Guntow, G. A. Giffin, *unpublished results*, **2020**.
[19] A. Grenier, H. Liu, K. M. Wiaderek, Z. W. Lebens-Higgins, O. J. Borkiewicz, L. F. J. Piper, P. J. Chupas, K. W. Chapman, *Chem. Mater.* **2017**, *29*, 7345–7352.
[20] a) N. V. Faenza, L. Bruce, Z. W. Lebens-Higgins, I. Plitz, N. Pereira, L. F. J. Piper, G. G. Amatucci, *J. Electrochem. Soc.* **2017**, *164*, A3727–A3741; b) Y. Lin, M. Xu, Y. Tian, W. Fan, Le Yu, W. Li, *Mater. Chem. Phys.* **2018**, *211*, 200–205; c) G. V. Zhuang, G. Chen, J. Shim, X. Song, P. N. Ross, T. J. Richardson, *J. Power Sources* **2004**, *134*, 293–297.
[21] T. Watanabe, K. Hirai, F. Ando, S. Kurosumi, S. Ugawa, H. Lee, Y. Irii, F. Maki, T. Gunji, J. Wu, T. Ohsaka, F. Matsumoto, *RSC Adv.* **2020**, *10*, 13642–13654.
[22] A. K. Padhi, K. S. Nanjundaswamy, J. B. Goodenough, *J. Electrochem. Soc.* **1997**, *144*, 1188–1194.
[23] Z.-F. Tang, R. Wu, P.-F. Huang, Q.-S. Wang, C.-H. Chen, *J. Alloys Compd.* **2017**, *693*, 1157–1163.
[24] J. Chong, S. Xun, J. Zhang, X. Song, H. Xie, V. Battaglia, R. Wang, *Chem. Eur. J.* **2014**, *20*, 7479–7485.
[25] D.-J. Lee, B. Scrosati, Y.-K. Sun, *J. Power Sources* **2011**, *196*, 7742–7746.
[26] a) S. Xia, F. Li, F. Chen, H. Guo, *J. Alloys Compd.* **2018**, *731*, 428–436; b) B. Huang, X. Li, Z. Wang, H. Guo, *Mater. Lett.* **2014**, *131*, 210–213.
[27] J. Duan, C. Wu, Y. Cao, K. Du, Z. Peng, G. Hu, *Electrochim. Acta* **2016**, *221*, 14–22.
[28] T. Chen, F. Wang, X. Li, X. Yan, H. Wang, B. Deng, Z. Xie, M. Qu, *Appl. Surf. Sci.* **2019**, *465*, 863–870.
[29] W. Liu, H. Guo, M. Qin, J. Deng, L. Xu, S. Yi, T. Hong, *ChemistrySelect* **2018**, *3*, 7660–7666.
[30] Y. Nie, W. Xiao, C. Miao, R. Fang, Z. Kou, D. Wang, M. Xu, C. Wang, *Electrochim. Acta* **2020**, *353*, 136477.
[31] X. Zhang, G. Liu, S. Li, H. Dong, H. Liu, J. Mei, *J. Electron. Mater.* **2019**, *48*, 4443–4451.
[32] a) K. S. Ryu, S. H. Lee, B. K. Koo, J. W. Lee, K. M. Kim, Y. J. Park, *J. Appl. Electrochem.* **2008**, *38*, 1385–1390; b) J. Kim, J. Lee, H. Ma, H. Y. Jeong, H. Cha, H. Lee, Y. Yoo, M. Park, J. Cho, *Adv. Mater.* **2018**, *30*, 1704309.
[33] Y.-R. Bak, Y. Chung, J.-H. Ju, M.-J. Hwang, Y. Lee, K.-S. Ryu, *J. New Mater. Electrochem. Syst.* **2011**, *14*, 203–207.
[34] J. Chen, L. Zhu, D. Jia, X. Jiang, Y. Wu, Q. Hao, X. Xia, Y. Ouyang, L. Peng, W. Tang, T. Liu, *Electrochim. Acta* **2019**, *312*, 179–187.
[35] R. Qi, J.-L. Shi, X.-D. Zhang, X.-X. Zeng, Y.-X. Yin, J. Xu, L. Chen, W.-G. Fu, Y.-G. Guo, L.-J. Wan, *Sci. China Chem.* **2017**, *60*, 1230–1235.
[36] a) J. Kim, H. Cha, H. Lee, P. Oh, J. Cho, *Batter. Supercaps* **2020**, *3*, 309–322; b) Y. Sakurai, A. Sakuda, A. Hayashi, M. Tatsumisago, *Solid State Ionics* **2011**, *182*, 59–63; c) Y. Kobayashi, H. Miyashiro, K. Takei, H. Shigemura, M. Tabuchi, H. Kageyama, T. Iwahori, *J. Electrochem. Soc.* **2003**, *150*, A1577–A1582.
[37] L. D. Prayogi, M. Faisal, E. Kartini, W. Honggowiranto, Z. Supardi, *AIP Conf. Proc.* **2016**, *1710*, 030047.
[38] Z. Wang, H. Liu, J. Wu, W.-M. Lau, J. Mei, H. Liu, G. Liu, *RSC Adv.* **2016**, *6*, 32365–32369.
[39] R. Jung, R. Morasch, P. Karayaylali, K. Phillips, F. Maglia, C. Stinner, Y. Shao-Horn, H. A. Gasteiger, *J. Electrochem. Soc.* **2018**, *165*, A132–A141.
[40] J. Sicklinger, M. Metzger, H. Beyer, D. Pritzl, H. A. Gasteiger, *J. Electrochem. Soc.* **2019**, *166*, A2322–A2335.
[41] J. Paulsen, J. Kim, "High nickel cathode material having low soluble base content" (US20140054495A1).
[42] a) X. Bian, Q. Fu, X. Bie, P. Yang, H. Qiu, Q. Pang, G. Chen, F. Du, Y. Wei, *Electrochim. Acta* **2015**, *174*, 875–884; b) H. Z. Zhang, Q. Q. Qiao, G. R. Li, X. P. Gao, *J. Mater. Chem. A* **2014**, *2*, 7454–7460.
[43] a) V. Laperche, S. J. Traina, Immobilization of Pb by Hydroxylapatite, *Adsorption of Metals by Geomedia* (Ed.: E. A. Jenne), Academic Press, San Diego **1998**; b) G. Babu, D. Bhuvaneswari, N. Kalaiselvi, N. Jayaprakash, P. Periasamy, *J. Sol-Gel Sci. Technol.* **2009**, *49*, 137–144.
[44] N. L. Sukiman, X. Zhou, N. Birbilis, A. E. Hughes, J. M. C. Mol, S. J. Garcia, X. Zhou, G. E. Thompson, Durability and Corrosion of Aluminium and Its Alloys: Overview, Property Space, Techniques and Developments, *Aluminium Alloys – New Trends in Fabrication and Applications* (Ed.: Z. Ahmad), InTech **2012**.
[45] R. Sahore, D. L. Wood, A. Kukay, K. M. Grady, J. Li, I. Belharouak, *ACS Sustainable Chem. Eng.* **2020**, *8*, 3162–3169.
[46] a) C.-C. Li, J.-T. Lee, Y.-L. Tung, C.-R. Yang, *J. Mater. Sci.* **2007**, *42*, 5773–5777; b) D. V. Carvalho, N. Loeffler, G.-T. Kim, M. Marinaro, M. Wohlfahrt-Mehrens, S. Passerini, *Polymer* **2016**, *8*, 276.
[47] M. Memm, A. Hoffmann, M. Wohlfahrt-Mehrens, *Electrochim. Acta* **2018**, *260*, 664–673.
[48] I. A. Shkrob, J. A. Gilbert, P. J. Phillips, R. Klie, R. T. Haasch, J. Bareño, D. P. Abraham, *J. Electrochem. Soc.* **2017**, *164*, A1489–A1498.
[49] a) H. S. Liu, Z. R. Zhang, Z. L. Gong, Y. Yang, *Electrochem. Solid-State Lett.* **2004**, *7*, A190–A193; b) Z. Chen, J. Wang, J. Huang, T. Fu, G. Sun, S. Lai, R. Zhou, K. Li, J. Zhao, *J. Power Sources* **2017**, *363*, 168–176.
[50] J. Xu, E. Hu, D. Nordlund, A. Mehta, S. N. Ehrlich, X.-Q. Yang, W. Tong, *ACS Appl. Mater. Interfaces* **2016**, *8*, 31677–31683.
[51] a) D. Y. Wan, Z. Y. Fan, Y. X. Dong, E. Baasanjav, H.-B. Jun, B. Jin, E. M. Jin, S. M. Jeong, *J. Nanomater.* **2018**, *2018*, 1–9; b) Y. Li, H. Yu, Y. Hu, H. Jiang, C. Li, *J. Energy Chem.* **2018**, *27*, 559–564; c) L. Zhang, J. Fu, C. Zhang, *Nanoscale Res. Lett.* **2017**, *12*, 376.
[52] J.-c. Zheng, Z. Yang, Z.-j. He, H. Tong, W.-j. Yu, J.-f. Zhang, *Nano Energy* **2018**, *53*, 613–621.
[53] Z. Tang, J. Bao, Q. Du, Y. Shao, M. Gao, B. Zou, C. Chen, *ACS Appl. Mater. Interfaces* **2016**, *8*, 34879–34887.
[54] X. Li, J. Liu, M. N. Banis, A. Lushington, R. Li, M. Cai, X. Sun, *Energy Environ. Sci.* **2014**, *7*, 768–778.
[55] U. Nisar, R. Amin, R. Essehli, R. A. Shakoor, R. Kahraman, D. K. Kim, M. A. Khaleel, I. Belharouak, *J. Power Sources* **2018**, *396*, 774–781.
[56] P. Zhou, Z. Zhang, H. Meng, Y. Lu, J. Cao, F. Cheng, Z. Tao, J. Chen, *Nanoscale* **2016**, *8*, 19263–19269.
[57] K.-J. Park, J.-Y. Hwang, H.-H. Ryu, F. Maglia, S.-J. Kim, P. Lamp, C. S. Yoon, Y.-K. Sun, *ACS Energy Lett.* **2019**, *4*, 1394–1400.
[58] C. S. Yoon, H.-H. Ryu, G.-T. Park, J.-H. Kim, K.-H. Kim, Y.-K. Sun, *J. Mater. Chem. A* **2018**, *6*, 4126–4132.
[59] C.-H. Jo, D.-H. Cho, H.-J. Noh, H. Yashiro, Y.-K. Sun, S. T. Myung, *Nano Res.* **2015**, *8*, 1464–1479.
[60] S. Chen, T. He, Y. Su, Y. Lu, L. Bao, L. Chen, Q. Zhang, J. Wang, R. Chen, F. Wu, *ACS Appl. Mater. Interfaces* **2017**, *9*, 29732–29743.
[61] S.-L. Chou, Y. Pan, J.-Z. Wang, H.-K. Liu, S.-X. Dou, *Phys. Chem. Chem. Phys.* **2014**, *16*, 20347–20359.
[62] a) D. Mohanty, K. Dahlberg, D. M. King, L. A. David, A. S. Sefat, D. L. Wood, C. Daniel, S. Dhar, V. Mahajan, M. Lee, F. Albano, *Sci. Rep.* **2016**, *6*, 26532; b) L. David, D. Mohanty, L. Geng, R. E. Ruther, A. S. Sefat, E. Cakmak, G. M. Veith, H. M. Meyer III, H. Wang, D. L. Wood III, *ChemElectroChem* **2019**, *6*, 5571–5580.

Manuscript received: August 10, 2020
Revised manuscript received: September 17, 2020
Accepted manuscript online: September 24, 2020
Version of record online: October 7, 2020

ChemSusChem

Supporting Information

Surface Modification of $LiNi_{0.8}Co_{0.15}Al_{0.05}O_2$ Particles via Li_3PO_4 Coating to Enable Aqueous Electrode Processing

Michael Hofmann, Felix Nagler, Martina Kapuschinski, Uwe Guntow, and Guinevere A. Giffin*

Author Contributions

M.H. Conceptualization:Lead; Investigation:Lead; Methodology:Lead; Writing - Original Draft:Lead
F.N. Investigation:Supporting; Methodology:Supporting
M.K. Investigation:Supporting
U.G. Conceptualization:Supporting; Funding acquisition:Lead; Investigation:Supporting; Methodology:Supporting; Supervision:Supporting; Writing - Review & Editing:Supporting
G.G. Conceptualization:Supporting; Investigation:Supporting; Methodology:Supporting; Supervision:Lead; Writing - Review & Editing:Lead

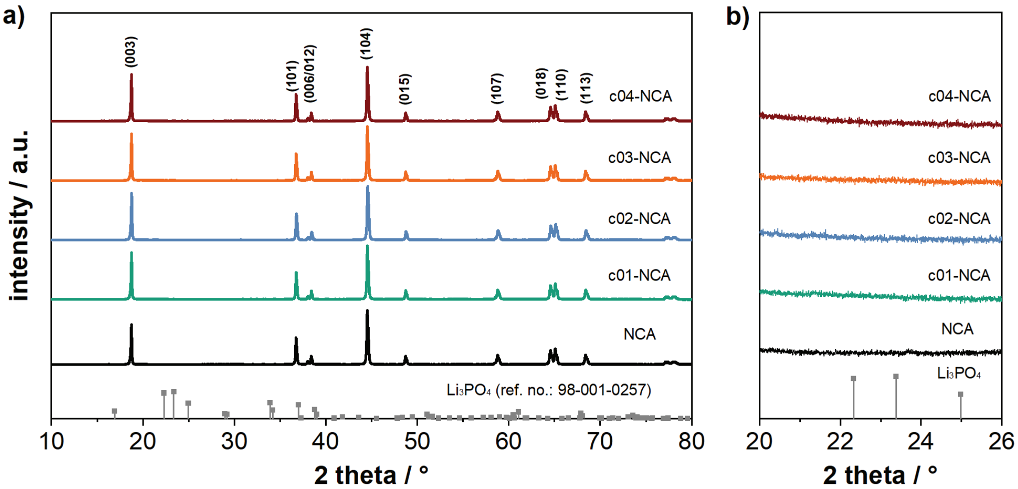

Figure S1 XRD patterns of pristine and coated NCA-particles (a), and a magnified 2θ range of 20 – 26 ° (b).

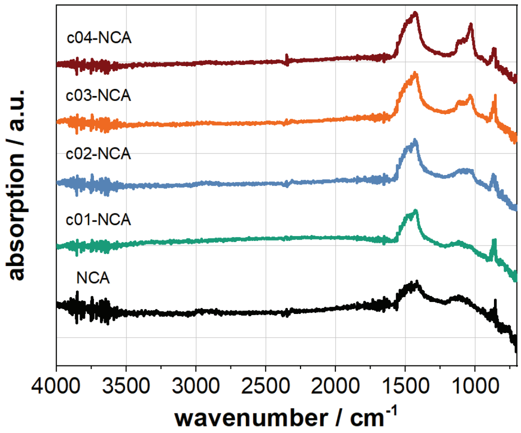

Figure S2 ATR-FT-IR spectra of pristine and coated NCA-particles.

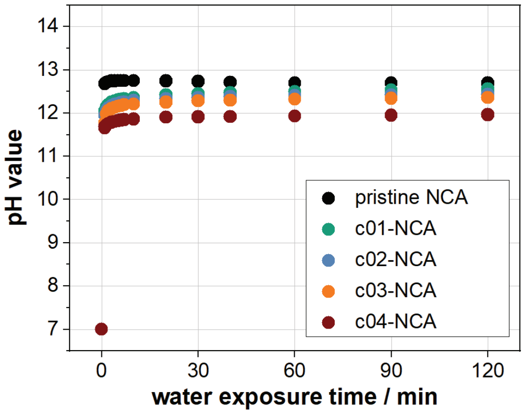

Figure S3 pH measurements of pristine and coated NCA-particles in water over a period of two hours.

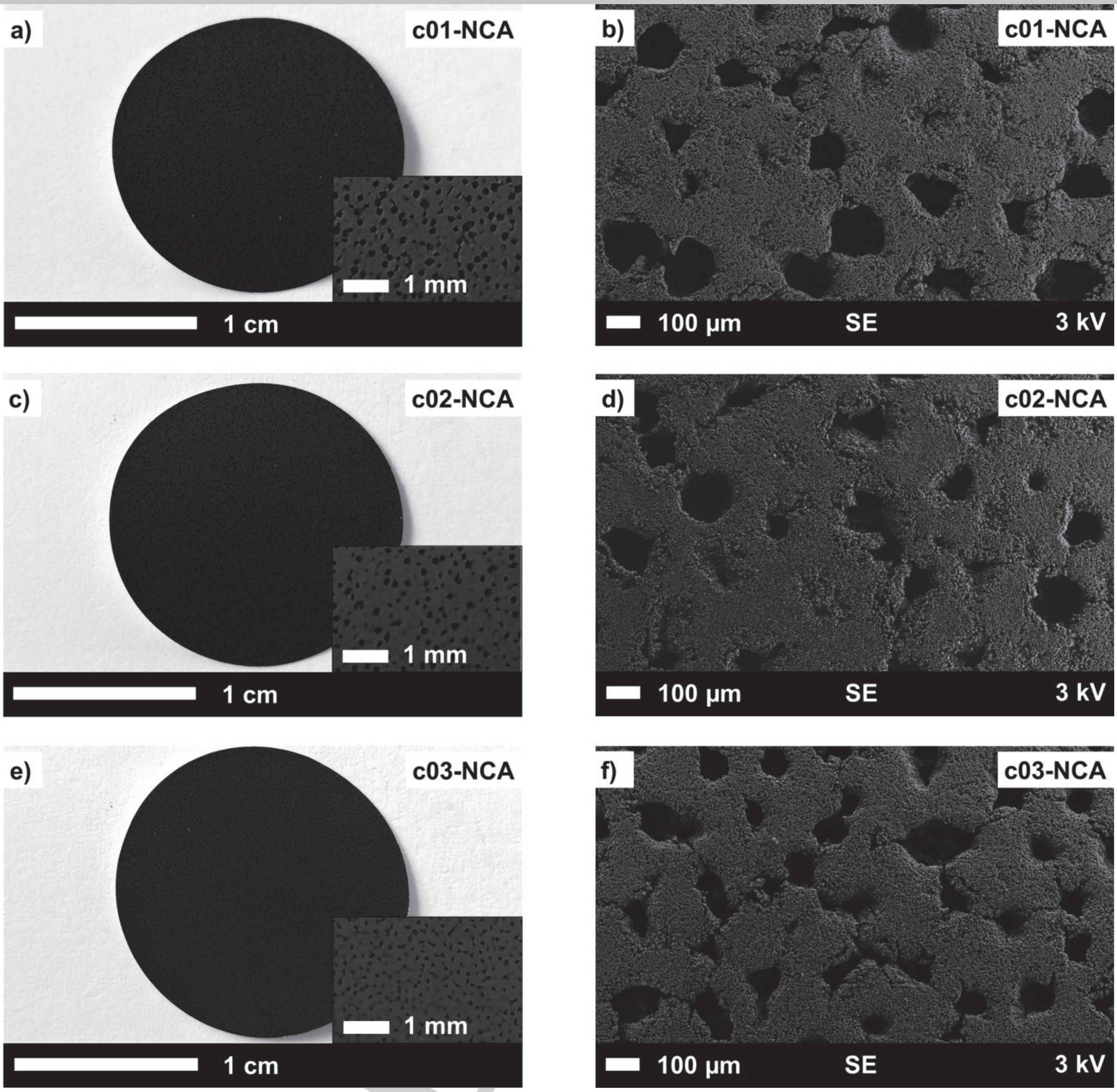

Figure S4 Photographs and SEM images of the top view of calandered aqueous-processed electrodes with c01-NCA (a, b), c02-NCA (c, d) and c03-NCA (e, f).

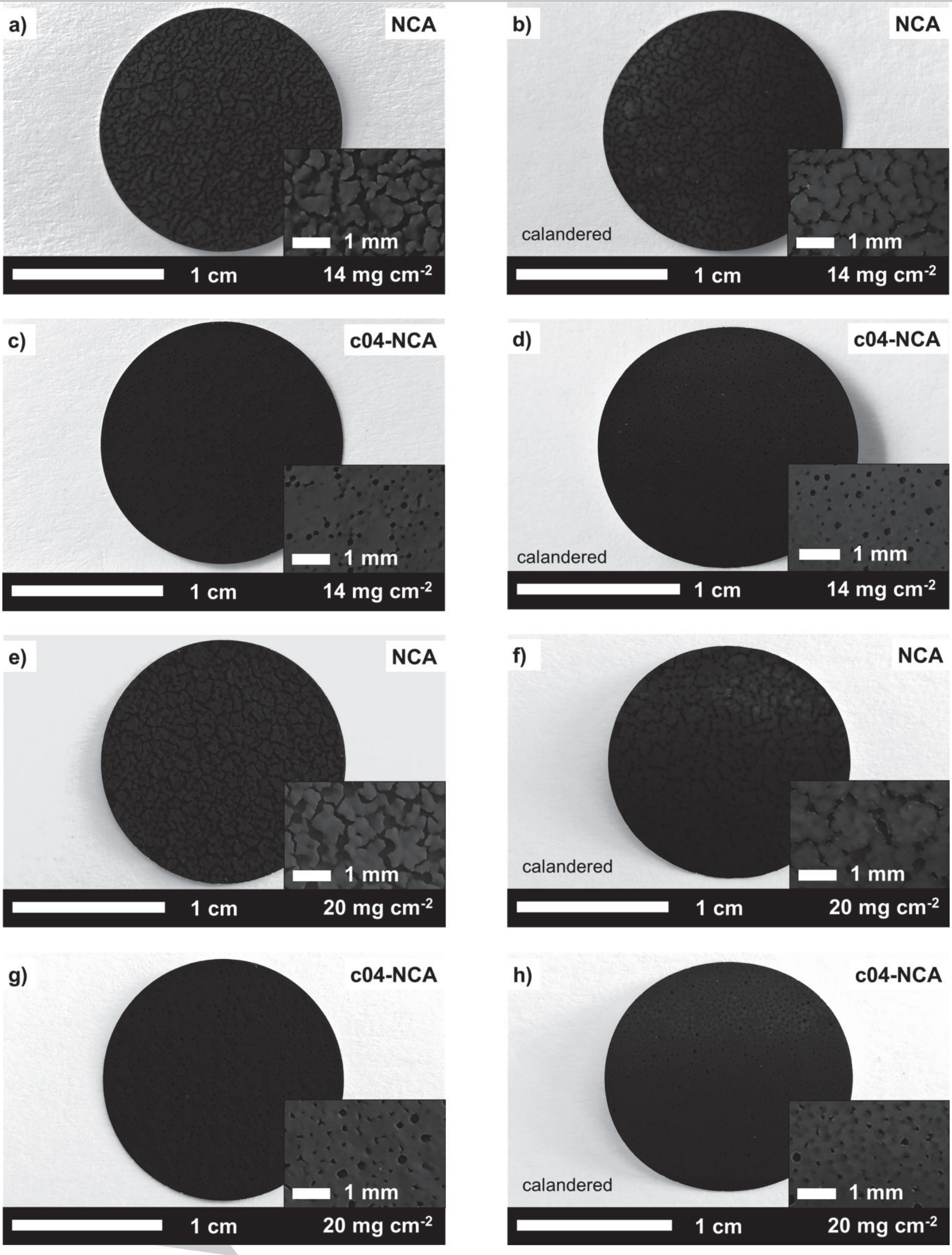

Figure S5 Photographs of uncalandered and calandared aqueous-processed electrodes with different mass loadings containing pristine NCA (a, b, e, f) and c04-NCA (c,d, g, h).

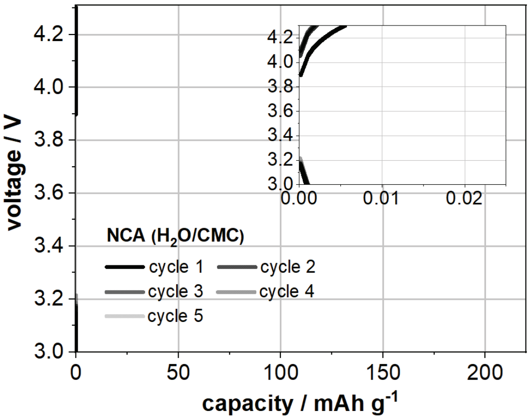

Figure S6 Voltage profiles during formation of a representative cell with aqueous-processed NCA electrodes.

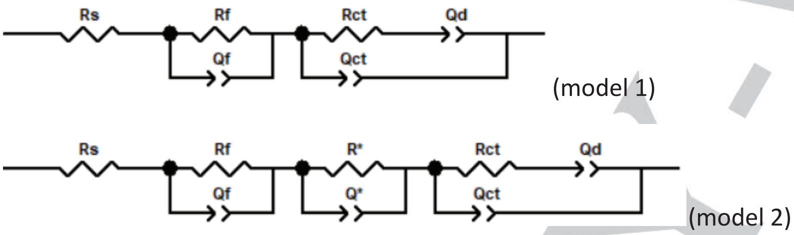

Figure S7 Equivalent circuit models used for fitting of EIS spectra. The various elements in model 1 are attributed to the following processes: ohmic resistances within the cell (resistor R_s), surface film impedance and capacity (RCPE-element Rf, Qf), charge transfer impedance and double layer capacity (RCPE-element Rct, Qct) and solid-state diffusion (CPE-element Qd). The additional RCPE-element (R*, Q*) in model 2 is used to describe the charge transfer process at the metallic lithium/electrolyte interface along with the electronic conductivity of the active material. The information which model was used for the fit can be found in Table S 1 and S 2.

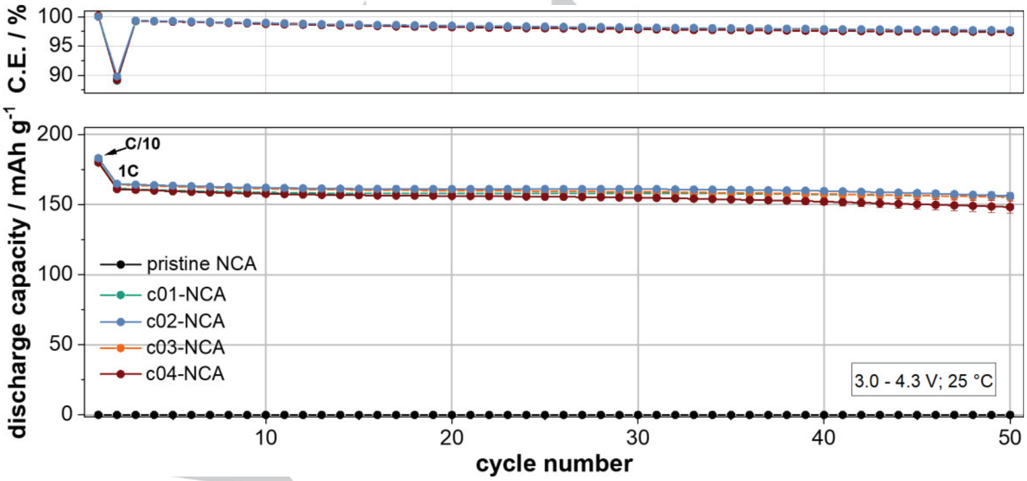

Figure S8 Cycling of half-cells with aqueous-processed electrodes between 3.0 – 4.3 V. The data represent the average specific discharge capacity of three cells and the error bars relate to the standard deviation between these cells.

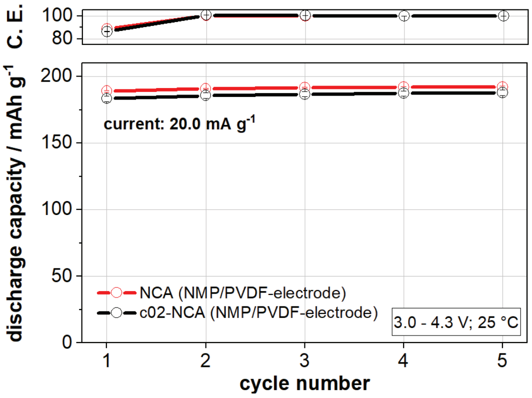

Figure S9 Discharge capacity during formation for cells with NMP-processed electrodes containing pristine NCA and c02-NCA, respectively.

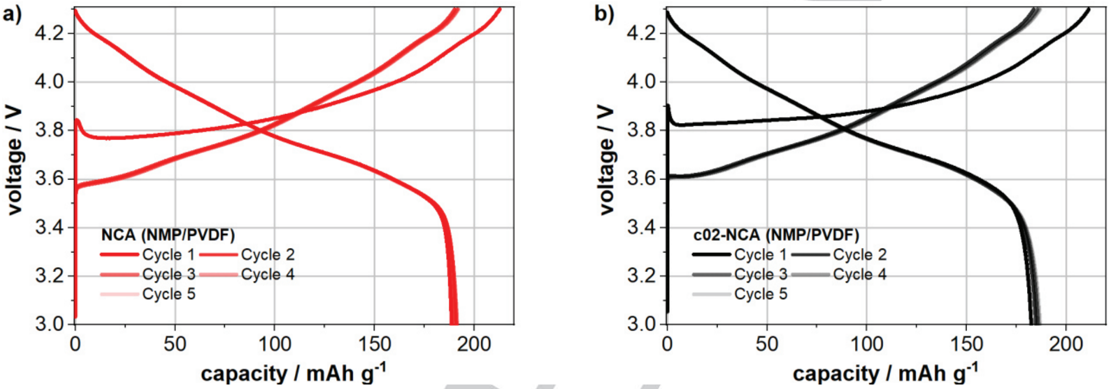

Figure S10 Voltage profiles during formation for a representative cell with NMP-processed electrodes containing pristine NCA (a) and c02-NCA (b).

Table S1 Fitting results of EIS for cells containing c01-NCA, c02-NCA and c04-NCA after formation.

cell	R_s [Ω]	[%]	R_f [Ω]	[%]	R_* [Ω]	[%]	R_{ct} [Ω]	[%]	fit model
c01-NCA	0.76	± 0.80	33.11	± 0.21	-	-	16.94	± 1.27	model 1
c02-NCA	0.93	± 1.98	6.08	± 0.91	-	-	21.44	± 1.87	model 1
c04-NCA	0.64	± 2.85	1.54	± 3.26	2.29	± 1.98	67.27	± 0.35	model 2

Table S2 Fitting results of EIS for cells containing c01-NCA, c02-NCA and c04-NCA after cycling.

cell	R_s [Ω]	[%]	R_f [Ω]	[%]	R_* [Ω]	[%]	R_{ct} [Ω]	[%]	fit model
c01-NCA	2.01	± 0.88	48.05	± 0.33	-	-	66.92	± 2.52	model 1
c02-NCA	1.53	± 0.38	5.85	± 0.54	4.44	± 0.92	28.00	± 0.33	model 2
c04-NCA	1.52	± 0.69	3.24	± 0.95	4.14	± 0.84	86.82	± 0.47	model 2

Appendixes

I. Manuscripts

a. M. Hofmann, M. Kapuschinski, U. Guntow, G. A. Giffin, Implications of Aqueous Processing for High Energy Density Cathode Materials: Part I. Ni-Rich Layered Oxides. *J. Electrochem. Soc.* **2020**, *167*, 140512.

b. M. Hofmann, M. Kapuschinski, U. Guntow, G. A. Giffin, Implications of Aqueous Processing for High Energy Density Cathode Materials: Part II. Water-Induced Surface Species on $LiNi_{0.8}Co_{0.15}Al_{0.05}O_2$. *J. Electrochem. Soc.* **2020**, *167*, 140535.

c. M. Hofmann, F. Nagler, M. Kapuschinski, U. Guntow, G. A. Giffin, Surface Modification of $LiNi_{0.8}Co_{0.15}Al_{0.05}O_2$ Particles via Li_3PO_4 Coating to Enable Aqueous Electrode Processing. *ChemSusChem* **2020**, *13*, 5962 – 5971.

d. M. Hofmann, F. Nagler, U. Guntow, G. Sextl, G. A. Giffin, Long-Term Cycling Performance of Aqueous Processed Ni-rich $LiNi_{0.8}Co_{0.15}Al_{0.05}O_2$ Cathodes. *J. Electrochem. Soc.* **2021**, *168*, 060511.

Journal of The Electrochemical Society, 2021 **168** 060511

Long-Term Cycling Performance of Aqueous Processed Ni-Rich $LiNi_{0.8}Co_{0.15}Al_{0.05}O_2$ Cathodes

Michael Hofmann, Felix Nagler, Uwe Guntow, Gerhard Sextl, and Guinevere A. Giffin[z]

[1]*Fraunhofer R&D Center Electromobility, Fraunhofer Institute for Silicate Research, 97082 Wuerzburg, Germany*

A lithium phosphate surface coating can protect water-sensitive $LiNi_{0.8}Co_{0.15}Al_{0.05}O_2$ (NCA) particles during aqueous electrode manufacturing. Herein, the coating process was performed by using a spray drying process, an easy method for upscaling. The coating provides enhanced protection against water that is reflected in a significantly reduced formation of detrimental water-induced surface species. As a consequence, full cells containing water-based electrodes with coated NCA and graphite anodes demonstrate good long-term 1C cycling performance with a capacity retention of 80% maintained after more than 730 cycles and a remaining capacity of approximately 130 mAh g^{-1}.

[DOI: 10.1149/1945-7111/ac054f]

Manuscript submitted March 6, 2021; revised manuscript received May 6, 2021. Published June 8, 2021.

Supplementary material for this article is available online

Switching from a *N*-Methyl-2-pyrrolidone (NMP)-based cathode electrode manufacturing process to a water-based process is attractive given the prospect of lower costs and lower environmental impact.[1,2] Moreover, as reported by various authors, aqueous cathode processing can also contribute to better electrochemical performance.[3–6] The superior performance of cells made with aqueous-processed electrodes, compared to their NMP-counterparts, is mostly attributed to beneficial effects associated with the binder properties.[2] However, for water-sensitive cathode materials such as nickel-rich layered oxides, these positive effects are negated by detrimental effects such as extreme metal leaching and the formation of water-induced surface species.[7–11] One cathode material belonging to this material class is Li(Ni,Co,Al)O_2 (NCA), which is an Al- and Co-substituted derivative of $LiNiO_2$ and can deliver high energy density.[12] Due to the extremely high water-sensitivity of NCA, the surface protection of this cathode material seems to be important for a successful implementation of a water-based electrode manufacturing process.[9] Numerous materials such as metal oxides, carbon, phosphates, carbonates, fluorinated compounds and organic polymers have been applied as a coating on the surface of NCA particles so far.[13–15] However, most of these coated NCA particles were only tested in the combination with a NMP-based electrode fabrication process. To date, the coating materials Li_2CO_3,[14,16] TiO_x,[17,18] a combination of both[19] and polyacrylic acid (PAA)[20] were investigated in an aqueous NCA electrode manufacturing process that all resulted in an improved electrochemical performance. In addition, this list was extended recently by the authors of this work, who reported the ability of a lithium phosphate coating to protect NCA against water.[21] It was demonstrated that the coating amount is crucial to achieve good electrochemical results and a compromise has to be made between sufficient protection against water and a low charge transfer resistance. An optimized coating amount led to a performance comparable to cells with NMP-based electrodes.

The coating of particles via a spray drying process enables a continuous process on an industrial scale.[22,23] This technique has already been used on the cathode side to produce CuO-coated $Li_{1.2}Mn_{0.54}Co_{0.13}Ni_{0.13}O_2$,[24] Sr-doped $LaMnO_3$-coated $LiNi_{0.8}Co_{0.1}Mn_{0.1}O_2$[25] and $Li[Mn_{2-x-y}Co_xLi_y]O_4$-coated $Li(Li_{0.033}Mn_{1.967})O_4$.[26] Herein, the lab scale coating process, previously reported,[21] is transferred to a spray drying process and the performance of half cells containing aqueous processed electrodes with spray dried material is compared to that of cells containing lab scale material. Furthermore, thermogravimetric analysis coupled with mass spectrometry (TG-MS) is used to evaluate the ability of the coating to reduce the formation of water-induced surface species, which have been shown to have a detrimental effect on the electrochemical performance.[9] The benefit of the lithium phosphate coating is further demonstrated through testing in lithium-ion full cells. The verification of the long-term cycling is a critical step as the lithium reservoir present in half cells, i.e. lithium metal counter electrode, might compensate a lithium deficit that resulted from lithium leaching during aqueous processing.

Experimental

Li_3PO_4 coating via spray drying.—Pristine $LiNi_{0.8}Co_{0.15}Al_{0.05}O_2$ (NCA, NAT-1050, TODA) was used as received. For the lithium phosphate coating, a solution consisting of 25.3 μl phosphoric acid (Merck, 85 wt% in water) in 65 g ethanol was prepared (A). Simultaneously, 114.8 mg lithium acetate dihydrate (Sigma Aldrich, 98%) were dissolved in 60 g ethanol and afterwards 30 g NCA were added (B). Both, the solution A and suspension B were stirred vigorously during the whole coating process. The molar ratio between lithium acetate dihydrate and phosphoric acid was fixed at 3:1, resulting in a coating amount of 0.0125 mmol Li_3PO_4 per gram NCA. Slight differences in the volume of solution A and suspension B were balanced by addition of ethanol. A and B were then transferred separately via two pumps (Ismatec) to a static mixer. Directly afterwards, the mixture of A and B was spray-dried with a mini spraydryer (Büchi, B-290). The inlet air temperature was chosen to be 120 °C and the outlet temperature 75 °C–85 °C. After spray-drying, the powder was annealed at 300 °C for 5 h in ambient atmosphere (heating rate: 5 K min^{-1}) to remove moisture and residual organic compounds. This coated NCA is denoted as sd-NCA. The laboratory scale lithium phosphate-coated NCA with the same coating amount, as was previously published, is used as a reference and is labelled as ls-NCA.[21]

Electrode processing and cell assembly.—The water-based cathode sheets were fabricated with 92 wt% sd-NCA, 4 wt% sodium carboxymethyl cellulose (CMC, Sigma-Aldrich, degree of substitution 0.9, average Mw ∼250,000) and 4 wt% conductive carbon (Imerys, Super C65). First, CMC was dissolved in deionized water overnight using a laboratory shaker (Heidolph, Vibramax 100). After addition of sd-NCA and conductive carbon, the slurry was homogenized several times over a period of one hour with a speedmixer (Hauschild GmbH & Co KG, DAC 400.1). The slurry was casted on aluminum foil (Korff, 20 μm thickness) by the doctor blade technique and the resulting electrodes were pre-dried at 80 °C for 30 min. The time between the addition of sd-NCA to the aqueous CMC solution and the end of the pre-drying step was two hours and

[z]E-mail: guinevere.giffin@isc.fraunhofer.de

approximately reflects the total time in which sd-NCA was in contact with water during this electrode manufacturing process. This time was used for the preparation of water-exposed sd-NCA (see Preparation of water-exposed sd-NCA). After the pre-drying step, the electrode sheets were calendered to 50% of their initial thickness and disc electrodes with 16 mm in diameter (2.01 cm^2, electrode density: ~ 1.7 g cm^{-3}, active mass loading: 11 ± 1.0 mg cm^{-2}) were punched out. The area capacity loading of these cathodes was calculated to approx. 2.0 mAh cm^{-2} by using the average practical capacity (~ 182 mAh g^{-1}) obtained in the last formation step of the half cell tests. The disc electrodes were further dried at 110 °C under vacuum for 10 h to ensure the removal of residual moisture. To study the effect of an extended slurry fabrication duration (i.e. increased water exposure time) on the cell performance, further electrode discs were prepared (2.01 cm^2, electrode density: ~ 1.7 g cm^{-3}, active mass loading: 12 ± 1.0 mg cm^{-2}) by applying the same slurry preparation protocol, except that the slurry was stored for additional two hours before the final mixing step. This procedure resulted in an extended (ext.) total time of approximately four hours of water-exposure. Half cells and full cells were prepared in a single-layer pouch bag configuration (pouch dimension: 56 mm × 83 mm) with metallic lithium (Sigma Aldrich, 20 mm × 20 mm) on a copper substrate or graphite anode discs (2.2 mAh cm^{-2}, 17 mm in diameter, Custom Cells Itzehoe GmbH), respectively. Copper-nickel tabs and aluminum tabs were used to connect the anode and cathode, respectively. The cells were assembled in an argon-filled glove box (MBraun, H_2O and $O_2 < 1$ ppm) using a single layer 25 μm microporous monolayer polypropylene membrane (Celgard, 2500) as separator. For the half cells, 1 mol l^{-1} $LiPF_6$ in ethylene carbonate (EC):dimethylene carbonate (DMC) 1:1 wt/wt (BASF, LP30) was added as electrolyte before sealing. For the full cells 1 mol l^{-1} $LiPF_6$ in EC:DMC 1:1 v/v + 2 wt% vinylene carbonate (Solvionic, 180 μl) was used. After assembling the cells, they were placed between two plates and fixed with clamps to apply a low undefined pressure to guarantee a good contact between tabs and electrodes. For all half cell and full cell tests, a minimum of three cells were built.

Electrochemical measurements.—The half cells and full cells were cycled at 25 °C in the voltage range 3.0–4.3 V and 2.7–4.2 V, respectively. Prior to cycling, the cells were allowed to rest for 12 h (half cells) and 16 h (full cells) at 25 °C to ensure complete electrolyte wetting. The cells were charged and discharged for five cycles (formation protocol). Both charge and discharge were performed in the constant current (CC) mode (current: 20.0 mA g^{-1}). The discharge capacity of the 5th formation cycle was used to calculate the current for the CC mode step in the long-term cycling test. The cycling protocol consisted of one cycle at C/10, followed by cycling at 1C. The charge step was performed in constant current (CC)-constant voltage (CV) mode (CV current limitation: C/20), whereas the discharge was done in constant current mode. The cycling of the half cells was ended after 50 cycles, while the full cells were cycled for 1000 cycles. For the calculation of the specific capacity, the sd-NCA particles were treated as pure active material due to the low amount of coating. As such, the actual specific capacity of the core material is artificially reduced.

Preparation of water-exposed sd-NCA.—The sd-NCA and deionized water were added to a polypropylene bottle in a mass ratio of 1:3 (sd-NCA:water). The suspension was continuously stirred for 2 h. After subsequent filtration, the resultant NCA powder was dried at 110 °C for 16 h. This NCA powder was denoted as sd-NCA-2 h.

Characterization methods.—Scanning electron microscopy (SEM) was performed at 1 kV with an inlens detector on a high-resolution ZEISS Ultra 55 scanning electron microscope (Carl Zeiss Microscopy GmbH). Transmission electron microscopy (TEM) was performed on a JEM-2011 microscope (Jeol LTd., Japan) equipped with an energy-dispersive X-ray spectroscopy (EDS) detector (Ametek/EDAX, USA). Prior to the measurement, the powder was embedded in a resin and a cross-section of sd-NCA particles was prepared with a Ar-ion beam milling technique using the Cryo Ion Slicer instrument IB-09060CIS (Jeol LTd., Japan). TG-MS analysis was conducted in argon on a Netzsch STA 449C Jupiter® in the temperature range 33 °C–1125 °C (heating rate: 10 K min^{-1}) coupled with a Netzsch QMS 403C Aëolos® in the m/z range from 10 to 200. Attenuated total reflectance Fourier-transform infrared spectroscopy (ATR-FTIR) was performed on an Alpha (Bruker) spectrometer equipped with germanium crystal in the wavenumber range 700–4000 cm^{-1} with 64 scans and a resolution of 2 cm^{-1}.

Results and Discussion

The amount of coating was chosen to be 0.0125 mmol Li_3PO_4 per gram NCA, which on the lab scale was shown to deliver the best electrochemical performance in a previous report.[21] The morphology of the sd-NCA particles was investigated by scanning electron microscopy (Figs. 1a, 1b). After the coating process, the raspberry-like secondary particles remain separated, confirming that the formation of larger agglomerates was avoided by the selection of suitable process parameters (Fig. 1a). SEM images of the uncoated NCA particles can be found in the literature.[9,21] The magnified images do not show accumulation of the coating material on the particle surface indicating a rather homogenously-distributed coating (Fig. 1b). TEM/EDS analysis was conducted on the cross-section of sd-NCA particles to confirm the formation of the phosphate coating layer. As expected, signals of nickel, cobalt and aluminum can be detected in the EDS spectrum of the sd-NCA bulk (Fig. 1c, Pos. 2). An additional phosphorus signal can be recognized in the EDS spectra recorded at the surface of sd-NCA (Pos. 1 and Pos. 3), which confirms the successful coating. While the phosphorus signal intensity at Pos. 1 is very intense, it is relatively weak at Pos. 3 and indicates some variation in the coating thickness. TEM images at Pos. 1 and Pos. 3 with a higher magnification were made to determine the range of the coating thickness (Fig. S1 available online at stacks.iop.org/JES/168/060511/mmedia). Even at Pos. 1 (intense phosphorus signal in the EDS spectrum), the coating thickness is less than 10 nm and demonstrates that the coating is very thin. Not only phosphorus, but also sulfur can be found on the surface of sd-NCA. Sulfur-containing species have been already detected on the surface of the pristine NCA by X-ray photoelectron spectroscopy in previous reports.[9,27] These have been proposed to be residues from the NCA synthesis process.[9]

The infrared spectrum of the sd-NCA particles provides further evidence of the presence of the phosphate coating (Fig. S2). Two peaks at around 1028 cm^{-1} and 1112 cm^{-1} can be detected, which can be assigned to the asymmetric P–O stretching vibrations of PO_4^{3-} ions.[28,29] Peaks around 866 cm^{-1}, 1428 cm^{-1} and 1483 cm^{-1} can also be detected, which have been already observed on the pristine material.[21] These peaks can be assigned to the CO-bending, symmetric CO-stretching and asymmetric CO-stretching vibrations, respectively, and might belong to residual lithium carbonate species from synthesis.[9,21,30]

For the electrochemical analysis, half cells with aqueous-processed cathode electrodes containing sd-NCA and a lithium metal anode were built in a pouch-cell configuration. For comparison, the data of cells with NCA coated with lithium phosphate via the lab scale route (ls-NCA, 0.0125 mmol Li_3PO_4 per gram NCA) from the previous report are included as a reference. 21 A visual comparison of the two different coating processes (lab scale vs spray drying process) is shown in Fig. 2. The detailed experimental conditions for the lab scale process can be found in the literature.[21]

The results from the formation protocol are depicted in Fig. 3. The cells with sd-NCA and ls-NCA deliver identical average discharge capacity and Coulombic efficiency values of 181.7 ± 0.2 mAh g^{-1}/99.6 ± 0.1% and 181.6 ± 0.4 mAh g^{-1}/99.6 ± 0.1% in the last formation cycle, respectively (Figs. 3a, 3b). Interestingly, the

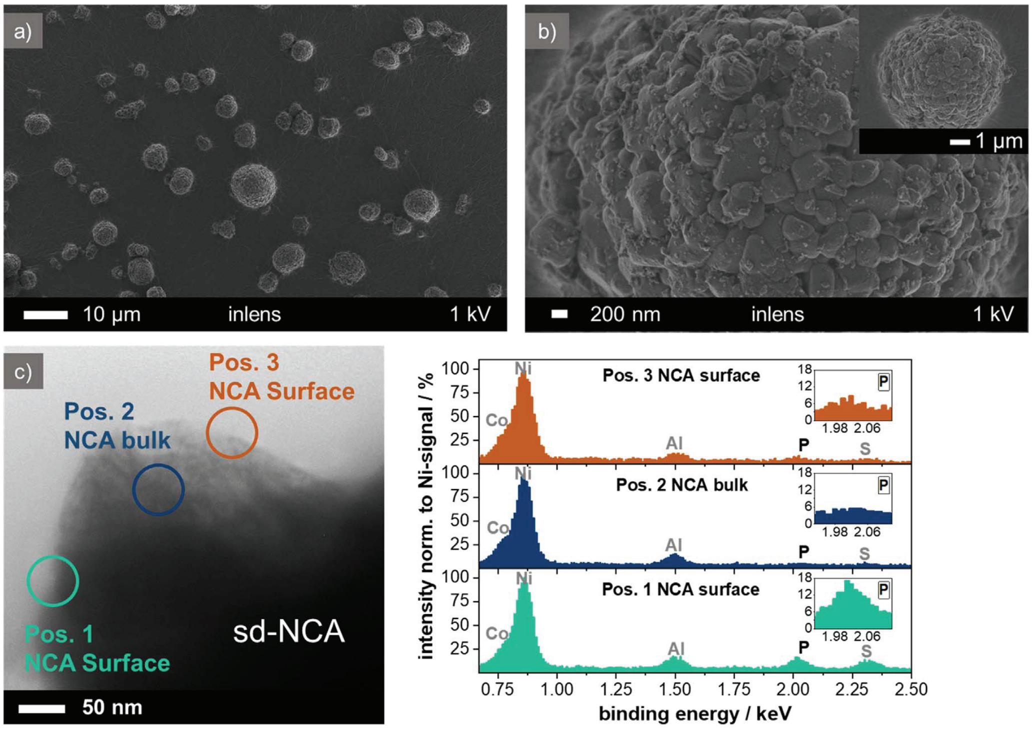

Figure 1. SEM images of sd-NCA with different magnifications (a), (b) and TEM/EDS analysis at the cross-section of sd-NCA.

height of the initial overvoltage in the first charge cycle is slightly lower for the cell with sd-NCA than that with the ls-NCA variant (Fig. 3c). The initial overvoltage has proven to be an indicator of the amount of surface species formed during water exposure.[9] Thus, the lower value suggests a slightly lower amount of water-induced surface species and therefore improved protection against water for sd-NCA. This effect might be related to a more defined precipitation of the coating on the NCA surface enabled by the automated spray drying process as compared to the manually-performed dropping funnel technique (lab scale process). In addition, no solvent evaporation step is necessary with spray drying, which accelerates the process and decreases the time in which the cathode particles are in contact with air. With respect to the latter aspect, it is well known that air-contact of pristine Ni-rich cathode materials leads to damage of the active material that is more pronounced for prolonged exposure duration.[31] For instance, preparing the small amount of 10 g of coated NCA via the lab scale process takes about 15 min for the dropping funnel process plus additional 30 min to evaporate the solvent. This time will further increase for a bigger batch size. In contrast, coating 10 g of NCA with the spray drying process takes less than 5 min and the process velocity is not influenced when the batch size is increased. In the second cycle, no further significant differences in the voltage profiles can be seen (Fig. 3d). While the initial Coulombic efficiency (ICE) is 84.7 ± 0.1% for the cells with sd-NCA, it is higher for those with ls-NCA (85.2 ± 0.1%). This result might be correlated with at least some differences in the surface properties of sd-NCA and ls-NCA as was already indicated by the differing initial overvoltage. In literature, a low ICE has mostly been assigned to irreversible reactions such as the decomposition of the electrolyte and the simultaneous formation of the solid electrolyte interphase (SEI) and cathode electrolyte interphase (CEI), respectively.[32] However, in recent years it has been demonstrated that the ICE is also affected by kinetic limitations during the discharge process. For instance, Kasnatscheew et al. were able to increase the ICE of NCM/graphite cells from 83.7% to 90.4% by applying a constant voltage step during the first discharge cycle.[33]

To examine the cycling performance, a program consisting of an initial C/10 cycle followed by 49 cycles at 1C rate in the voltage range 3.0–4.3 V was chosen. As with the results obtained during formation, both cell variants deliver essentially the same average discharge capacities of 183.2 ± 0.4 mAh g^{-1}/164.8 ± 0.7 mAh g^{-1} (sd−NCA) and 183.0 ± 0.5 mAh g^{-1}/ 164.8 ± 0.8 mAh g^{-1} (ls-NCA) in the initial C/10 cycle and first 1C cycle, respectively (Fig. 4a). The same applies for the average capacity retention after 50 cycles, which is 95.3 ± 0.4% and 94.8% ± 1.1% for the cells with sd-NCA and ls-NCA, respectively. As expected, the associated voltage profiles in the 2nd and 50th cycle are also nearly identical (Fig. 4b). Based on these results, the spray-drying process provides a simple and scalable process for coating NCA with lithium phosphate that results in very comparable electrochemical performance to the cells with lab-scale coated NCA at least during the cycling test conducted here.

To investigate the impact of an extended electrode fabrication duration (i.e. increased water exposure time) on the cell performance and as such the protection potential of the sd-NCA coating, further cathodes (ext.) were fabricated. With those electrodes, half cells were built and tested analogously to the cells presented above. The results are included in Figs. 3 and 4. It is striking that the average discharge capacity of these cells is about 4 mAh g^{-1} lower during the whole formation protocol compared to this of the cells with sd-NCA and the conventional electrodes (last formation cycle: 177.7 ± 0.3 mAh g^{-1} vs 181.7 ± 0.2 mAh g^{-1}). While the ICE of both cell variants is comparable (ICE: 84.4 ± 0.5% vs 84.7 ± 0.1%), the Coulombic efficiency in the last formation cycle is at least slightly lower for the cells containing the cathodes that were processed with the extended fabrication protocol (98.4 ± 0.9% vs 99.6 ± 0.1%). These results together with the slightly increased initial overvoltage in the first charge cycle indicate that the coating of sd-NCA cannot

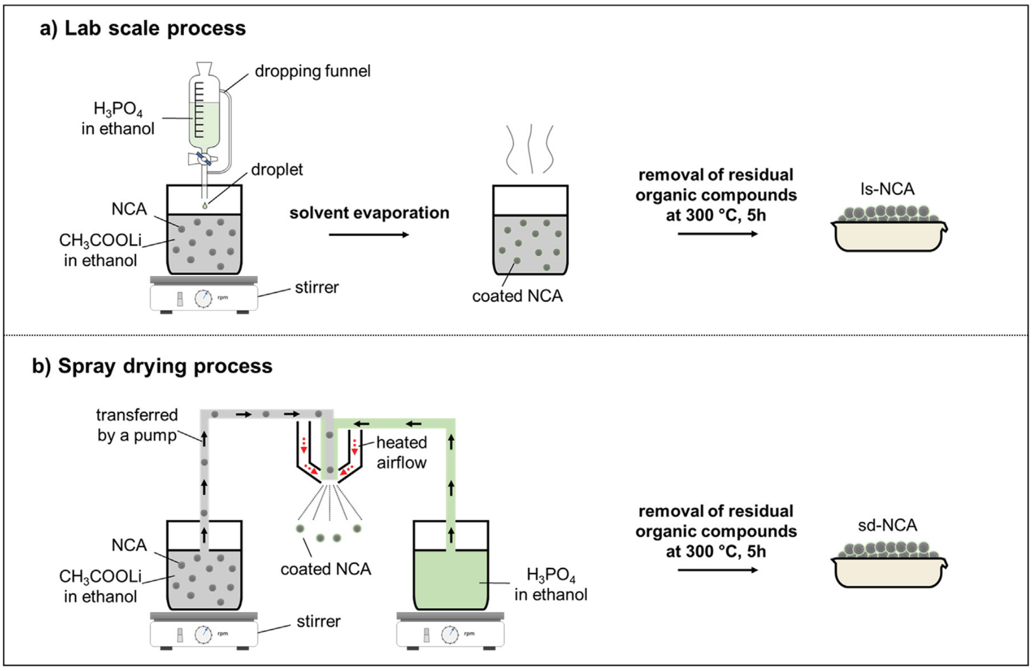

Figure 2. Illustration of the lithium phosphate coating process via the lab scale[21] (a) and spray drying (b) route.

completely prevent a continuous water-induced degradation of NCA. However, the influence of the prolonged slurry fabrication process used herein on the cell performance is rather low and more or less comparable results are still obtained during cycling. An interesting point for further studies would be now the investigation of the impact of a switch from the speedmixer process used herein to an industrial mixing process.

For a more in depth investigation of the protection potential of the coating of sd-NCA, a water exposure experiment was conducted. A water exposure time of two hours was chosen since this reflects approximately the time where the NCA material is in contact with water during the conventional aqueous electrode manufacturing process used herein. TG-MS analysis was conducted on the water exposed sd-NCA particles that are denoted as sd-NCA-2 h. The results are depicted in Fig. 5. For better clarification, the results were divided into three temperature regions (region I: 33 °C–125 °C, region II: 125 °C–525 °C, region III: 525 °C–1125 °C). The results obtained for pristine NCA particles exposed to water for the same period of time (NCA-2 h) are shown for comparison purposes.[9] The mass signals m/z = 18, m/z = 32 and m/z = 44 were assigned in accordance with previous literature to H_2O, O_2 and CO_2, respectively.[9,10,34,35] As expected, for both materials, no mass loss can be detected in region I as the samples were dried prior to the TG-MS measurement at 110 °C. The largest mass loss can be determined in region III (both samples: onset temperature of ~ 700 °C and mass loss of 5.5%). This loss of weight is accompanied by the release of O_2, indicating the thermal decomposition of the NCA structure.[9] Water-induced surface species such as chemically adsorbed CO_2, basic nickel carbonate and NiOOH-like compounds, which may form on NCA particles during aqueous processing, have been shown to decompose between 125 °C–525 °C.[9] While the mass loss for NCA-2 h in this temperature range is 1.1%, it is only 0.6% for sd-NCA-2 h. Simultaneously, the intensity of the mass signals of CO_2, H_2O and O_2 from sd-NCA-2 h in region II is significantly weaker than those arising from NCA-2 h. A detailed assignment of the mass signals to water-induced surface species can be found in previous literature.[9]

As the mass loss has been reduced by about one half, the results support the reduction of water-induced species for sd-NCA-2h and thus underline the protective function of the coating against water. It is obvious that the formation of the surface species was not completely suppressed, but only reduced. This is likely related to the coating amount that was optimized in the previous report at the lab-scale to deliver the best electrochemical cell performance rather than best protection ability.[21] Although a higher amount of Li_3PO_4 coating may more effectively reduce the water-induced species, it will have a negative effect on the cell performance by increasing the charge transfer resistance.[21]

To exclude effects attributed to the large lithium reservoir in a half cell configuration that compensates lithium deficits and artificially prolongs the cycle life, the water-based cathode electrodes containing sd-NCA were evaluated in a full cell configuration with graphite anode electrodes. The ICE of the full cells (Fig. S3a) is 79.3 ± 3.9% and therefore lower as compared to that of the associated half cells (84.7 ± 0.1%). The ICE of full cells is of particular interest as the lithium-inventory is fixed by the amount of cathode material and electrolyte. The origin of the lower ICE might be at least partially attributed to the different anodes (half cells: lithium metal, full cells: graphite). Regarding this point previous literature has shown that the ICE strongly depends on the type of anode material.[36] Vinylene carbonate was additionally present as additive in the electrolyte used for the full cells to guarantee the formation of a stable SEI on the graphite anode.[37] The choice of additive also plays a role for the ICE.[38] Further data from the formation cycles can be found in Fig. S3. Figure 6a depicts the mean discharge capacity of three full cells over 1000 cycles. Here, in the first cycle (C/10), a mean discharge capacity of 181.0 ± 2.6 mAh g^{-1} is obtained, which is very close to the value of the half cells at C/10 (Fig. 4). This clearly indicates that no lithium reservoir in form of a lithium metal anode is necessary to achieve these high capacity values. Over 730 cycles are possible before the generally accepted end-of-life (EoL) criteria of 80% initial capacity is reached (80.0 ± 4.9%) and after 1000 cycles the capacity retention is still 71.7 ± 8.7%. In accordance with these results, the associated mean discharge voltage (calculated using the

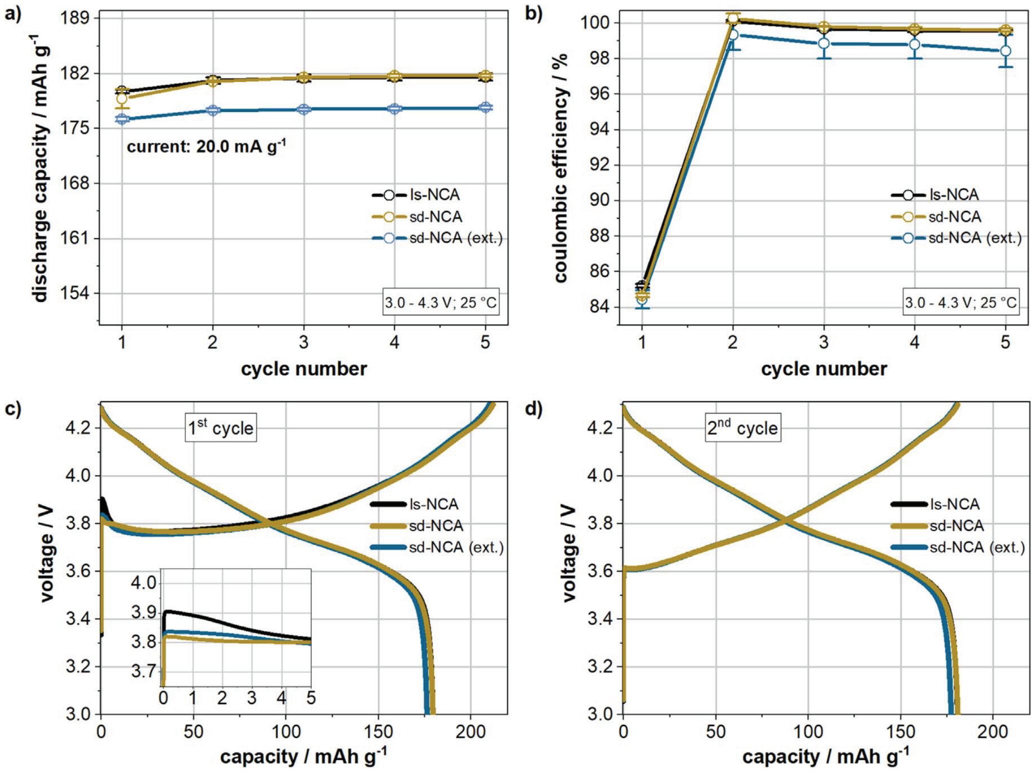

Figure 3. Results of the formation cycles of cells with aqueous-processed electrodes containing ls-NCA and sd-NCA, respectively, as well as of cells containing sd-NCA cathodes that were fabricated with an extended electrode manufacturing process (ext.): discharge capacity (a) and Coulombic efficiency (b) over cycle number; voltage profiles of a representative cell of each combination in the 1st (c) and 2nd cycle (d). The data in a and b represent the average specific discharge capacity of three cells and the error bars relate to the standard deviation between these cells. The data for the cells with ls-NCA are included for comparison from the previous publication.[21]

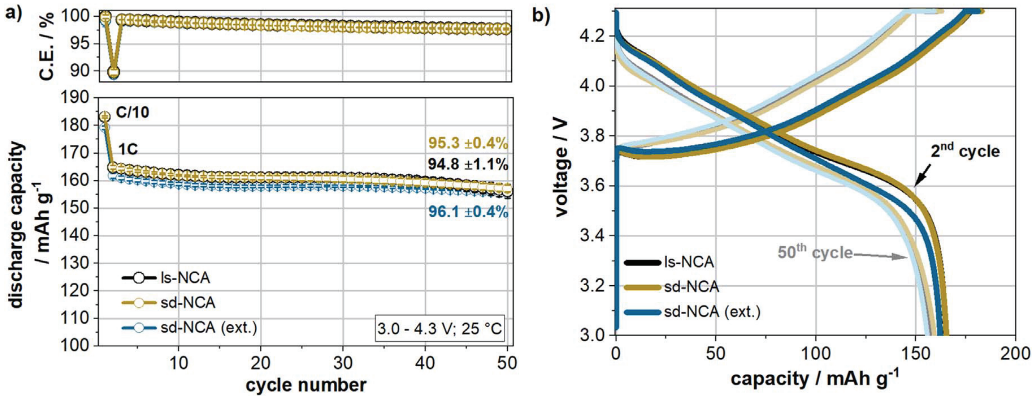

Figure 4. Cycling performance of cells containing ls-NCA and sd-NCA, respectively, as well as of cells containing sd-NCA cathodes that were fabricated with an extended electrode manufacturing process (ext.): Coulombic efficiency and discharge capacity over cycle number (a) and voltage profiles of a representative cell of each variant in the 2nd, 20th and 50th cycle (lighter color corresponds to a higher cycle number). The data in (a) represent the average specific discharge capacity of three cells and the error bars relate to the standard deviation between these cells. The data for ls-NCA is taken from Ref. 21.

formula $\widetilde{V}_{disch.} = \int V_{disch.}\, dq_{disch.}/\int dq_{disch.}$[39]) decreases only moderately in a relatively linear behavior with approx. 0.16 mV per cycle (Fig. 6b). This is similar to the value of 0.12 mV/cycle, which was reported for full cells containing graphite anodes and NMP-processed NCM811 cathodes and also resulted in a good capacity retention of 77–80% after 1000 cycles (0.2C, 3.0 V–4.5 V).[40] During the entire cycling test, the average Coulombic efficiency is above 99.7% (except in the second cycle due to the change of the C-Rate) indicating that only minor side reactions occur (Fig. 6c). Selected voltage profiles of a representative cell are depicted in Fig. 6d. Upon cycling the cell polarization increases only moderately.

To put these results into context, an overview of the long-term performance of full cells containing water-based electrodes with layered oxide cathode materials, which have been published in

Table I. Comparison of the long-term cycling performance of full cells containing an aqueous processed cathode with layered oxide cathode material and a graphite anode, which were published in previous literature.

Active material	capacity retention (capacity last cycle)	cycles	discharge C-Rate	voltage range, temperature	References
NCM111[a)]	~84% (104.3 mAh g^{-1}) ~70% (85.4 mAh g^{-1})	1000 2000	1C	2.75 V–4.2 V, 20 °C	41
NCM111[b)]	95.7% (~123 mAh g^{-1}[k)])	311	1C	3.0 V–4.2 V, 20 °C	42
NCM111[c)]	~88%[k)] (~88 mAh g^{-1}[k)])	900	3C	3.0 V–4.2 V, 23 °C	43
NCM111[d)]	~90%[k)] (~118 mAh g^{-1}[k)])	500	1C	3.0 V–4.2 V, 20 °C	44
NCM111[e)]	~99% (~17 Ah[k)])	500	1C	2.75 V–4.1 V, 25 °C	45
NCM523[f)]	~81% (~115 mAh g^{-1})	500	1C	3.0 V–4.2 V, not available	46
NCM523[g)]	79.5% (not available)	886	C/3	2.5 V–4.2 V, 30 °C	47
NCM523[h)]	~76%[k)] (~100 mAh g^{-1}[k)]) ~70%[k)] (~92 mAh g^{-1}[k)])	1000[k)] 1425[k)]	1C	2.8 V–4.2 V[k)], not available	48
NCM811[i)]	~70% (~131 mAh g^{-1}[k)])	1000	C/3	2.5 V–4.2 V, 30 °C	8
NCA[j)]	~80% (~135 mAh g^{-1})[l)]	~600[l)]	C/3	3.0 V–4.2 V, 30 °C	20
NCA	88.0% (143.2 mAh g^{-1}) 80.0% (130.2 mAh g^{-1}) 71.7% (116.7 mAh g^{-1})	500 737 1000	1C	2.7 V–4.2 V, 25 °C	this work

a) TODA (active material supplier), CMC (binder-type), none (slurry additives). b) TODA, CMC, H_3PO_4 (in situ Li_3PO_4 coating). c) BASF, CMC/fluorine acrylic copolymer latex binder, none. d) not available, CMC/polyacrylic acid (PAA)/polyethylene oxide (PEO), LiOH. e) not available, CMC/acrylic based latex binder, none. f) not available, CMC/PAA/PEO, LiOH. g) not available, CMC/latex binder, none. h) Umicore, CMC/latex binder, H_3PO_4 (in situ Li_3PO_4 coating). i) Targray, CMC/acrylic emulsion, none. j) TODA, CMC/PAA/fluorine acrylic hybrid latex binder, PAA (in situ PAA coating). k) The value was calculated or determined from graphical data presented in the associated literature. This might lead to some variation from the actual value. l) The long-term cycling performance was predicted by Hawley et al.[20] after measuring the cell performance for approx. 350 cycles at C/3.

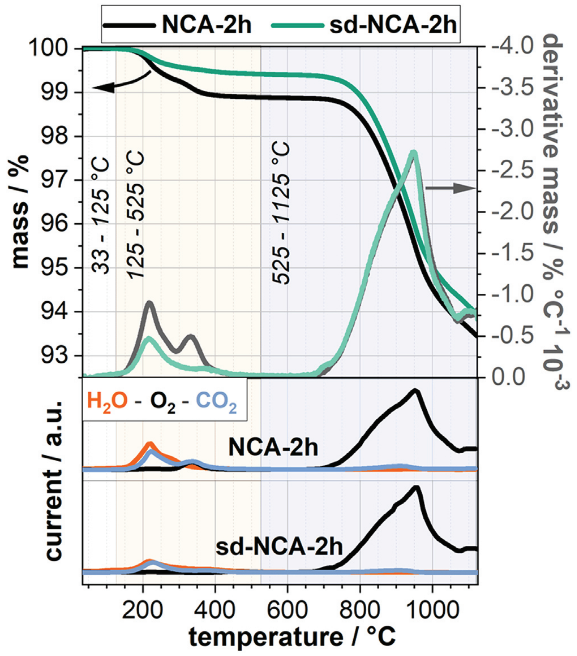

Figure 5. Thermogravimetric analysis of NCA-2 h and sd-NCA-2 h in the temperature range 33 °C–1125 °C and associated mass signals m/z = 18, m/z = 32 and m/z = 44 signals, which were assigned to H_2O, O_2 and CO_2, respectively. The intensity of the CO_2 signal was multiplied by a factor of 1.5. The data for NCA-2h is taken from Ref. 9.

previous literature, is given in Table I. From a comparison of these results, it is obvious that full cells with sd-NCA can compete with the performance obtained for full cells with other layered oxide materials. In particular, the high specific capacity even after long-term cycling at 1C is promising. In comparison, full cells with water-based NCM811-electrodes deliver slightly higher capacity values after 1000 cycles, but these results were obtained at C/3. Moreover, in a very recent report by Hawley et al. full cells containing aqueous-processed NCA cathodes were prepared.[20] Based on the electrochemical data obtained during approximately 350 cycles, the authors predicted that these cells will reach the EoL criterion after about 600 cycles. This is more than 100 cycles earlier than for the cells reported here, although the cells of Hawley et al. were cycled at a lower C-rate (C/3). Full cells with aqueous processed NCM111- or NCM523-electrodes have (at least partially) a comparable or better capacity retention, but deliver a lower capacity. Furthermore, layered oxides with a lower fraction of nickel are much less sensitive to water-exposure than NCA as demonstrated in a previous report of the current authors.[7] Overall, these results demonstrate that an aqueous electrode production process - also for the extremely water-sensitive NCA - might be successfully implemented by the selection of a suitable protective particle coating.

Conclusions

A simple upscaling process for lithium phosphate-coated NCA using a spray drying process has been successfully developed. Half cells with aqueous-processed electrodes containing the coated NCA show a comparable cell performance as cells containing NCA coated via a lab scale process with a capacity retention of 95.3 ± 0.4% and 94.8 ± 1.1% after 1C cycling for 50 cycles, respectively. TG-MS analyses demonstrate that the coated NCA particles show a significantly reduced amount of detrimental water-induced surface

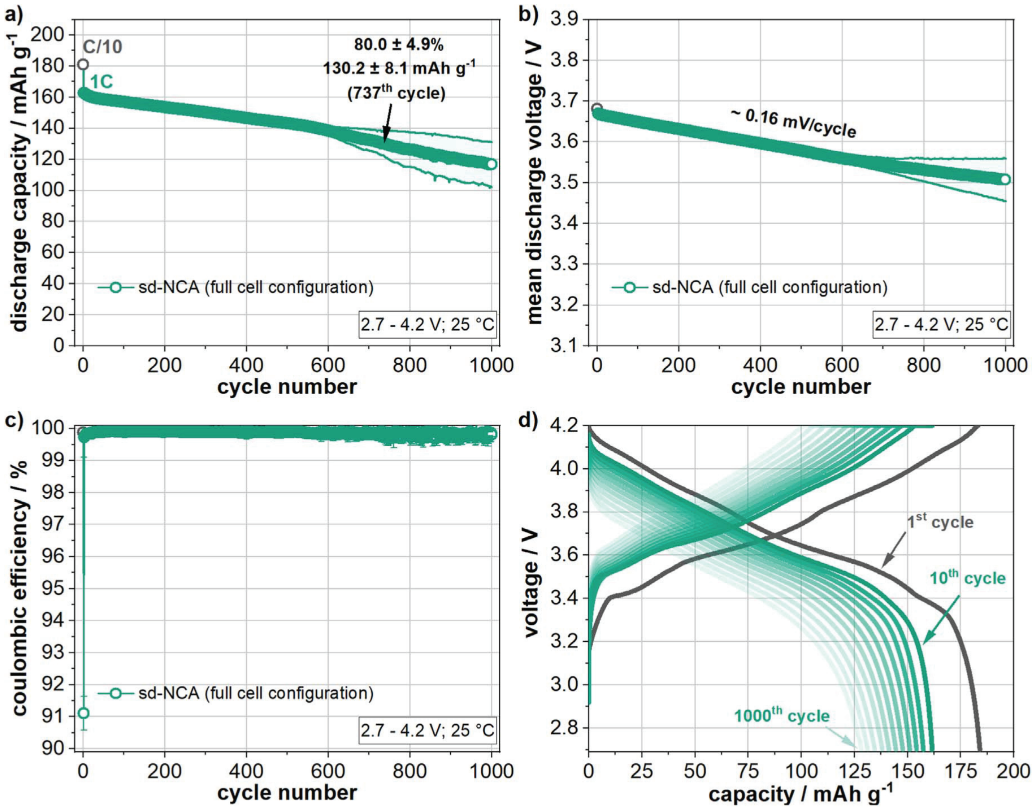

Figure 6. Discharge capacity (a), mean discharge voltage (b) and Coulombic efficiency (c) over cycle number of full cells containing aqueous processed electrodes with sd-NCA. The values represent the mean of three cells and the error bars correspond to the associated standard deviation (a)–(c). Voltage profiles of a representative full cell in the 1st, 10th, 100th, 200th, 300th, 400th, 500th, 600th, 700th, 800th, 900th and 1000th cycle (b) (lighter color corresponds to a higher cycle number).

species. The long-term cycling performance of full cells with the lithium phosphate-coated NCA is competitive with the best results published in the literature to date. The cells show excellent performance with a capacity retention of 80.0 ± 4.9% reached only after 737 cycles at 1C and a remaining capacity of 130.2 ± 8.1 mAh g^{-1}. This work demonstrates that a protective coating on NCA is a feasible solution to facilitate the successful implementation of aqueous processing for this extremely water sensitive cathode material. Focusing on the development of coating materials that can provide excellent protection against water and simultaneously beneficially impact the electrochemical performance seems to be a key to enable a sustainable widespread electrode production for nickel-rich layered oxide cathode materials in the future.

Acknowledgments

The authors acknowledge the financial support from the Bavarian Ministry of Economic Affairs and Media, Energy and Technology for funding the Fraunhofer R&D Center for Electromobility Bavaria FZEB (Grant number: 43-6629/86). The authors further acknowledge the following coworkers at Fraunhofer ISC: Johannes Prieschl and Benjamin Schug for fruitful scientific discussions and support; Martina Kapuschinski and Doris Hanselmann for technical support; Werner Stracke and Alexander Reinholdt for the TEM/EDS measurements.

ORCID

Michael Hofmann https://orcid.org/0000-0002-8164-6457
Guinevere A. Giffin https://orcid.org/0000-0002-2303-9560

References

1. D. L. Wood III, J. Li, and C. Daniel, *J. Power Sources*, **275**, 234 (2015).
2. D. Bresser, D. Buchholz, A. Moretti, A. Varzi, and S. Passerini, *Energy Environ. Sci.*, **11**, 3096 (2018).
3. W.-Y. Chou, Y.-C. Jin, J.-G. Duh, C.-Z. Lu, and S.-C. Liao, *Appl. Surf. Sci.*, **355**, 1272 (2015).
4. J. Li, R. Klöpsch, S. Nowak, M. Kunze, M. Winter, and S. Passerini, *J. Power Sources*, **196**, 7687 (2011).
5. F. de Giorgio, N. Laszczynski, J. von Zamory, M. Mastragostino, C. Arbizzani, and S. Passerini, *ChemSusChem*, **10**, 379 (2017).
6. Z. Chen, G.-T. Kim, D. Chao, N. Loeffler, M. Copley, J. Lin, Z. Shen, and S. Passerini, *J. Power Sources*, **372**, 180 (2017).
7. M. Hofmann, M. Kapuschinski, U. Guntow, and G. A. Giffin, *J. Electrochem. Soc.*, **167**, 140512 (2020).
8. M. Wood, J. Li, R. E. Ruther, Z. Du, E. C. Self, H. M. Meyer III, C. Daniel, I. Belharouak, and D. L. Wood III, *Energy Storage Mater.*, **24**, 188 (2020).
9. M. Hofmann, M. Kapuschinski, U. Guntow, and G. A. Giffin, *J. Electrochem. Soc.*, **167**, 140535 (2020).
10. I. Hamam, N. Zhang, A. Liu, M. B. Johnson, and J. R. Dahn, *J. Electrochem. Soc.*, **167**, 130521 (2020).
11. W. B. Hawley, A. Parejiya, Y. Bai, H. M. Meyer III, D. L. Wood III, and J. Li, *J. Power Sources*, **466**, 228315 (2020).
12. J. Kim, H. Lee, H. Cha, M. Yoon, M. Park, and J. Cho, *Adv. Energy Mater.*, **8**, 1702028 (2018).
13. C. M. Julien and A. Mauger, *Energies*, **13**, 6363 (2020).
14. K. Kimura, T. Sakamoto, T. Mukai, Y. Ikeuchi, N. Yamashita, K. Onishi, K. Asami, and M. Yanagida, *J. Electrochem. Soc.*, **165**, A16 (2018).
15. G. Hu, J. Fan, Y. Lu, Y. Zhang, K. Du, Z. Peng, L. Li, B. Zhang, Y. Shi, and Y. Cao, *ChemSusChem*, **13**, 5699 (2020).
16. K. Kimura, K. Onishi, T. Sakamoto, K. Asami, and M. Yanagida, *J. Electrochem. Soc.*, **166**, A5313 (2019).
17. Y. Liu et al., *J. Appl. Electrochem.*, **49**, 99 (2019).
18. T. Tanabe et al., *Electrochim. Acta*, **258**, 1348 (2017).
19. T. Watanabe et al., *RSC Adv.*, **10**, 13642 (2020).
20. W. B. Hawley, H. M. Meyer III, and J. Li, *Electrochim. Acta*, **380**, 138203 (2021).

21. M. Hofmann, F. Nagler, M. Kapuschinski, U. Guntow, and G. A. Giffin, *ChemSusChem*, **13**, 5962 (2020).
22. B. Vertruyen, N. Eshraghi, C. Piffet, J. Bodart, A. Mahmoud, and F. Boschini, *Materials*, **11**, 1076 (2018).
23. L. Xu, F. Zhou, B. Liu, H. Zhou, Q. Zhang, J. Kong, Q. Wang, and H. Liu, *Int. J. Electrochem.*, **2018**, 1 (2018).
24. B. Li, Y. Yu, and J. Zhao, *J. Power Sources*, **275**, 64 (2015).
25. Y. Li, F. Lai, X. Zhang, H. Wang, Z. Chen, X. He, and Q. Li, *J. Taiwan Inst. Chem. Eng.*, **102**, 225 (2019).
26. J. L. Shui, B. Lin, W. L. Liu, P. H. Yang, G. S. Jiang, and C. H. Chen, *Mater. Sci. Eng. B*, **113**, 236 (2004).
27. R. T. Haasch and D. P. Abraham, *Surf. Sci. Spectra*, **26**, 14003 (2019).
28. X. Bian, Q. Fu, X. Bie, P. Yang, H. Qiu, Q. Pang, G. Chen, F. Du, and Y. Wei, *Electrochim. Acta*, **174**, 875 (2015).
29. H. Z. Zhang, Q. Q. Qiao, G. R. Li, and X. P. Gao, *J. Mater. Chem. A*, **2**, 7454 (2014).
30. A. Grenier, H. Liu, K. M. Wiaderek, Z. W. Lebens-Higgins, O. J. Borkiewicz, L. F. J. Piper, P. J. Chupas, and K. W. Chapman, *Chem. Mater.*, **29**, 7345 (2017).
31. R. Jung, R. Morasch, P. Karayaylali, K. Phillips, F. Maglia, C. Stinner, Y. Shao-Horn, and H. A. Gasteiger, *J. Electrochem. Soc.*, **165**, A132 (2018).
32. J. Xiao et al., *Nat. Energy*, **5**, 561 (2020).
33. J. Kasnatscheew et al., *Phys. Chem. Chem. Phys.*, **18**, 3956 (2016).
34. J. Sicklinger, M. Metzger, H. Beyer, D. Pritzl, and H. A. Gasteiger, *J. Electrochem. Soc.*, **166**, A2322 (2019).
35. D. Pritzl, T. Teufl, A. T. S. Freiberg, B. Strehle, J. Sicklinger, H. Sommer, P. Hartmann, and H. A. Gasteiger, *J. Electrochem. Soc.*, **166**, A4056 (2019).
36. X. Li, X. Sun, X. Hu, F. Fan, S. Cai, C. Zheng, and G. D. Stucky, *Nano Energy*, **77**, 105143 (2020).
37. D. Aurbach, K. Gamolsky, B. Markovsky, Y. Gofer, M. Schmidt, and U. Heider, *Electrochim. Acta*, **47**, 1423 (2002).
38. J. Li, A. R. Cameron, H. Li, S. Glazier, D. Xiong, M. Chatzidakis, J. Allen, G. A. Botton, and J. R. Dahn, *J. Electrochem. Soc.*, **164**, A1534 (2017).
39. R. Jung, M. Metzger, F. Maglia, C. Stinner, and H. A. Gasteiger, *J. Electrochem. Soc.*, **164**, A1361 (2017).
40. F. Friedrich, B. Strehle, A. T. S. Freiberg, K. Kleiner, S. J. Day, C. Erk, M. Piana, and H. A. Gasteiger, *J. Electrochem. Soc.*, **166**, A3760 (2019).
41. N. Loeffler, J. von Zamory, N. Laszczynski, I. Doberdo, G.-T. Kim, and S. Passerini, *J. Power Sources*, **248**, 915 (2014).
42. N. Loeffler, G.-T. Kim, F. Mueller, T. Diemant, J.-K. Kim, R. J. Behm, and S. Passerini, *ChemSusChem*, **9**, 1112 (2016).
43. W. Bauer, F. A. Çetinel, M. Müller, and U. Kaufmann, *Electrochim. Acta*, **317**, 112 (2019).
44. L. Ibing, T. Gallasch, P. Schneider, P. Niehoff, A. Hintennach, M. Winter, and F. M. Schappacher, *J. Power Sources*, **423**, 183 (2019).
45. N. Loeffler, G.-T. Kim, S. Passerini, C. Gutierrez, I. Cendoya, I. de Meatza, F. Alessandrini, and G. B. Appetecchi, *ChemSusChem*, **10**, 3581 (2017).
46. L. Ibing, T. Gallasch, A. Friesen, P. Niehoff, A. Hintennach, M. Winter, and M. Börner, *J. Power Sources*, **475**, 228608 (2020).
47. D. L. Wood III, J. D. Quass, J. Li, S. Ahmed, D. Ventola, and C. Daniel, *Dry. Technol.*, **36**, 234 (2018).
48. M. Bichon, D. Sotta, E. de Vito, W. Porcher, and B. Lestriez, *J. Power Sources*, **483**, 229097 (2021).

Long-Term Cycling Performance of Aqueous Processed Ni-rich $LiNi_{0.8}Co_{0.15}Al_{0.05}O_2$ Cathodes

Michael Hofmann, Felix Nagler, Uwe Guntow, Gerhard Sextl and Guinevere A. Giffin[z]
Fraunhofer R&D Center Electromobility, Fraunhofer Institute for Silicate-Research,
Neunerplatz 2, 97082 Wuerzburg, Germany
[z]E-mail: guinevere.giffin@isc.fraunhofer.de

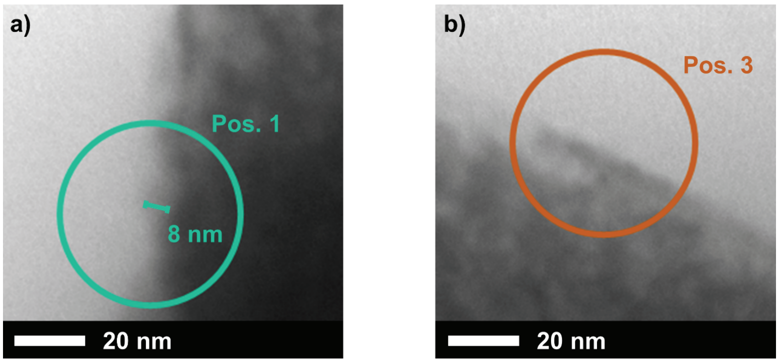

Figure S1 TEM images with higher magnification at Pos. 1 (a) and Pos. 3 (b). The coating thickness in (a) has been determined to be less than 10 nm. The coating thickness in (b) seems to be extremely thin so that it cannot be clearly determined with the TEM equipment available.

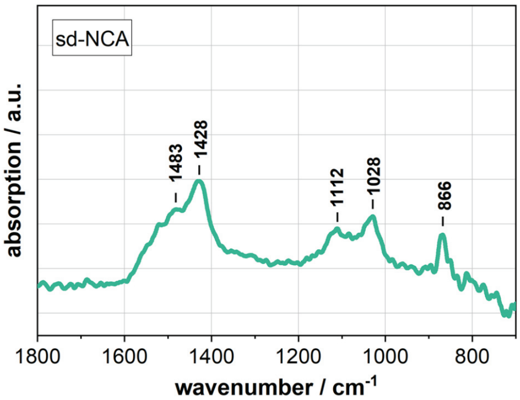

Figure S2 Infrared spectrum of NCA particles which were coated with lithium phosphate via a spray drying process (sd-NCA).

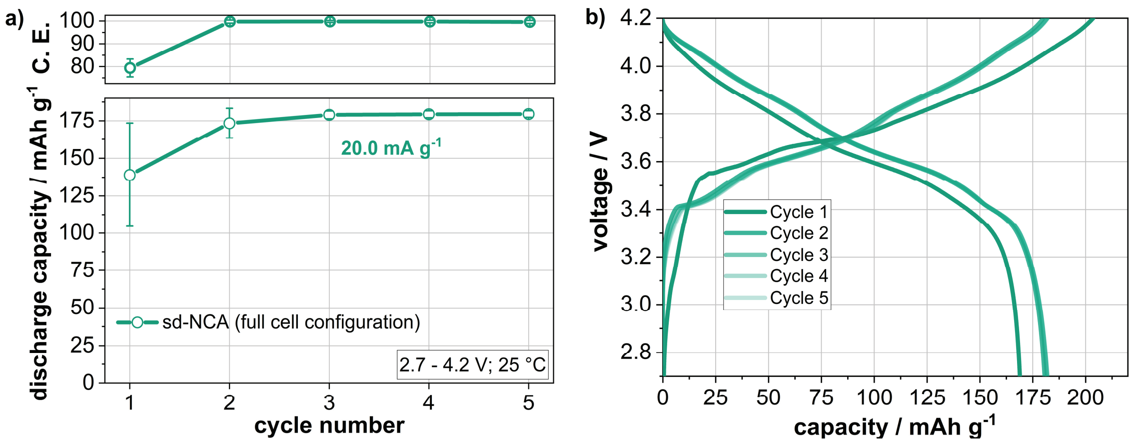

Figure S3 Results of the formation cycles of cells with full cell configuration containing aqueous processed electrodes with sd-NCA: discharge capacity and Coulombic efficiency over cycle number (a) and voltage profiles of a representative cell of each combination (b). The data in (a) represent the average specific discharge capacity of three cells and the error bars relate to the standard deviation between these cells.

Appendixes

II. Individual contributions to the manuscripts

Erklärung zur Autorenschaft

Implications of Aqueous Processing for High Energy Density Cathode Materials: Part I. Ni-Rich Layered Oxides, Michael Hofmann, Martina Kapuschinski, Uwe Guntow, Guinevere A. Giffin, Journal of the Electrochemical Society, 2020, 167, 140512.

Detaillierte Darstellung der Anteile an der Veröffentlichung (in %)
Angabe Autoren/innen (ggf. Haupt- / Ko- / korrespondierende/r Autor/in) mit Vorname Nachname (Initialen)

Michael Hofmann (M. H.), Martina Kapuschinski (M. K.), Uwe Guntow (U. G.), Guinevere A. Giffin (G. G.)

Autor	**M. H.**	**M. K.**	**U. G.**	**G. G.**								**∑ in Prozent**
Konzept	3%		1%	1%								5%
Präparation und Charakterisierung wässriger Kathodenmaterial-Suspensionen	14%	3%	2%	5%								24%
Elektrodenherstellung und Zellbau	6%	4%										10%
Elektrochemische Charakterisierung	16%		2%	13%								31%
Verfassen der Veröffentlichung	9%			6%								15%
Korrektur der Veröffentlichung			2%	8%								10%
Koordination der Veröffentlichung	1%			4%								5%
Summe	49%	7%	7%	37%								100%

Julius-Maximilians-
UNIVERSITÄT
WÜRZBURG

Fakultät für
CHEMIE UND
PHARMAZIE

Erklärung zur Autorenschaft

Implications of Aqueous Processing for High Energy Density Cathode Materials: Part II. Water-Induced Surface Species on $LiNi_{0.8}Co_{0.15}Al_{0.05}O_2$, Michael Hofmann, Martina Kapuschinski, Uwe Guntow, Guinevere A. Giffin, Journal of the Electrochemical Society, 2020, 167, 140535.

Detaillierte Darstellung der Anteile an der Veröffentlichung (in %)
Angabe Autoren/innen (ggf. Haupt- / Ko- / korrespondierende/r Autor/in) mit Vorname Nachname (Initialen)

Michael Hofmann (M. H.), Martina Kapuschinski (M. K.), Uwe Guntow (U. G.), Guinevere A. Giffin (G. G.)

Autor	**M. H.**	**M. K.**	**U. G.**	**G. G.**								**∑ in Prozent**
Konzept	3%		1%	1%								5%
Präparation und Charakterisierung der wasserausgesetzten NCA-Partikel bzw. des NCA-Filtrats	17%	4%	3%	9%								33%
Elektrodenherstellung und Zellbau	6%	2%										8%
Elektrochemische Charakterisierung	13%		2%	9%								24%
Verfassen der Veröffentlichung	11%			4%								15%
Korrektur der Veröffentlichung			1%	9%								10%
Koordination der Veröffentlichung	1%			4%								5%
Summe	51%	6%	7%	36%								100%

Julius-Maximilians-
UNIVERSITÄT
WÜRZBURG

Fakultät für
CHEMIE UND
PHARMAZIE

Erklärung zur Autorenschaft

Surface Modification of $LiNi_{0.8}Co_{0.15}Al_{0.05}O_2$ Particles via Li_3PO_4 Coating to Enable Aqueous Electrode Processing, Michael Hofmann, Felix Nagler, Martina Kapuschinski, Uwe Guntow, Guinevere A. Giffin, ChemSusChem, 2020, 13, 5962-5971.

Detaillierte Darstellung der Anteile an der Veröffentlichung (in %)
Angabe Autoren/innen (ggf. Haupt- / Ko- / korrespondierende/r Autor/in) mit Vorname Nachname (Initialen)

Michael Hofmann (M. H.), Felix Nagler (F. N.), Martina Kapuschinski (M. K.), Uwe Guntow (U. G.), Guinevere A. Giffin (G. G.)

Autor	**M. H.**	**F. N.**	**M. K.**	**U. G.**	**G. G.**							**∑ in Prozent**
Konzept	3%				2%							5%
Synthese und Charakterisierung von beschichteten NCA-Partikeln	17%	4%	3%	2%	2%							28%
Elektrodenherstellung und Zellbau	3%	4%	2%									9%
Elektrochemische Charakterisierung	15%	1%		2%	10%							28%
Verfassen der Veröffentlichung	11%				4%							15%
Korrektur der Veröffentlichung				1%	9%							10%
Koordination der Veröffentlichung	1%				4%							5%
Summe	50%	9%	5%	5%	31%							100%

Julius-Maximilians-
UNIVERSITÄT
WÜRZBURG

Fakultät für
CHEMIE UND
PHARMAZIE

Erklärung zur Autorenschaft

Long-Term Cycling Performance of Aqueous Processed Ni-rich $LiNi_{0.8}Co_{0.15}Al_{0.05}O_2$ Cathodes, Michael Hofmann, Felix Nagler, Uwe Guntow, Gerhard Sextl, Guinevere A. Giffin, Journal of the Electrochemical Society, 2021, 168, 060511.

Detaillierte Darstellung der Anteile an der Veröffentlichung (in %)
Angabe Autoren/innen (ggf. Haupt- / Ko- / korrespondierende/r Autor/in) mit Vorname Nachname (Initialen)

Michael Hofmann (M. H.), Felix Nagler (F. N.), Uwe Guntow (U. G.), Gerhard Sextl (G.S.), Guinevere A. Giffin (G. G.)

Autor	**M. H.**	**F. N.**	**U. G.**	**G. S.**	**G. G.**							**∑ in Prozent**
Konzept	3%		1%		1%							5%
Beschichtung von NCA-Partikeln über einen Sprühtrocknungsprozess sowie deren Charakterisierung	15%	3%	1%		8%							27%
Elektrodenherstellung und Zellbau	6%	3%										9%
Elektrochemische Charakterisierung	17%		3%		9%							29%
Verfassen der Veröffentlichung	12%				3%							15%
Korrektur der Veröffentlichung				5%	5%							10%
Koordination der Veröffentlichung	1%				4%							5%
Summe	54%	6%	5%	5%	30%							100%